MAGNETOM Flash

The Magazine of MRI

Issue Number 3/2011
RSNA Edition

SIEMENS

How I do it

Clinical

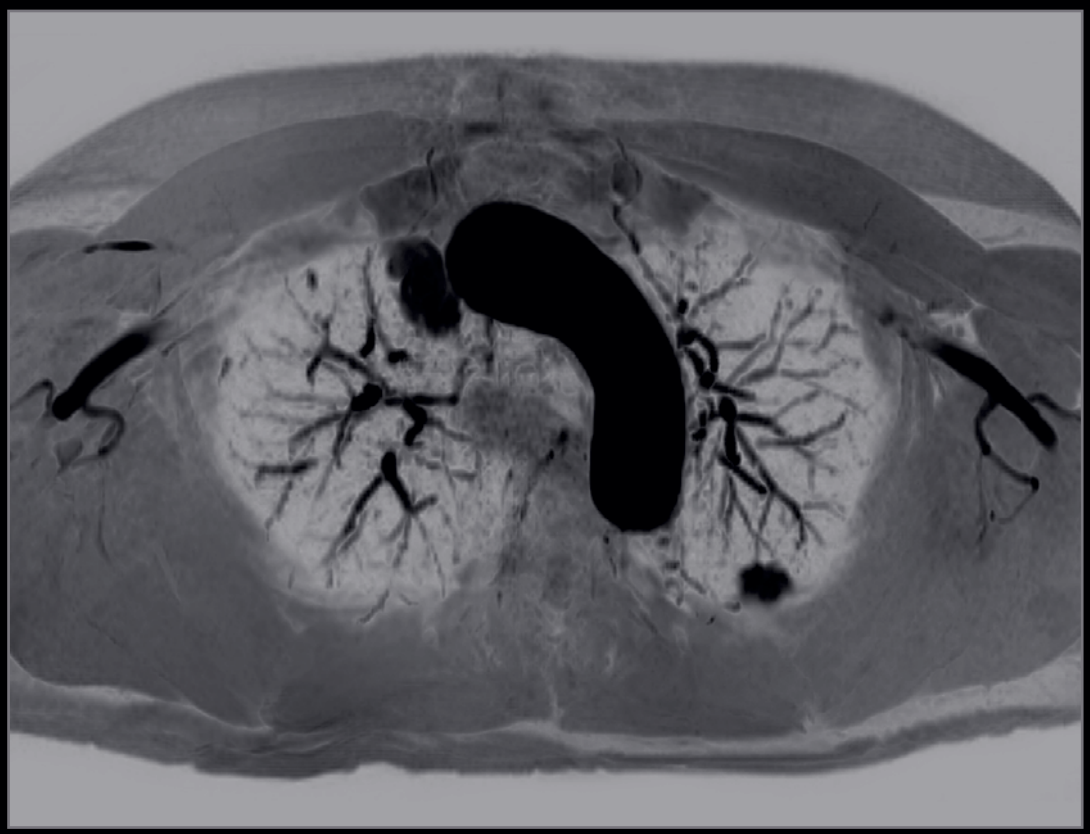

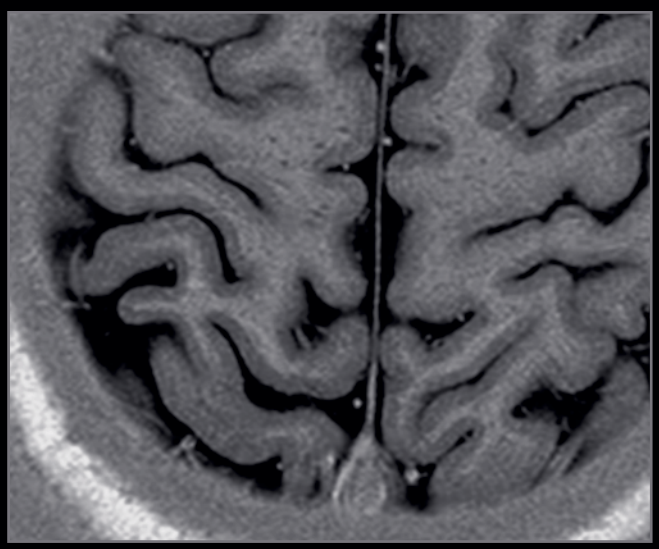

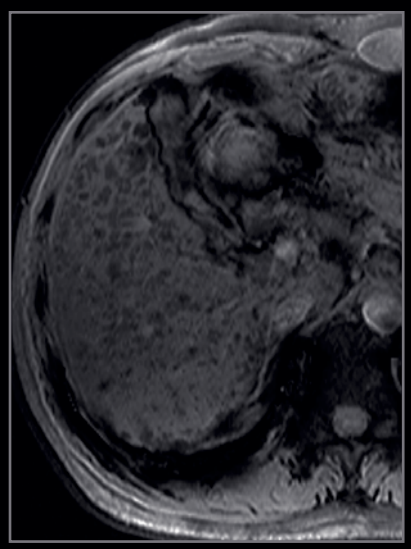

48

Matthias Lichy, M.D.
Editor-in-Chief

Dear Reader,

The first time of travelling to Chicago to attend the annual meeting of the Radiological Society of North America left me truly overwhelmed, not least by the huge number of people sharing their knowledge and experience in all fields of medical imaging.

There are only a few windows in the radiologist's calendar in which to exchange ideas with so many colleagues from all over the world. For this reason, the first week of December has now become a significant week in all our calendars.

However, even more than this, the RSNA is the largest platform for learning about the latest developments in imaging technology (and this applies for different imaging modalities) and how this technology influences our daily patient care. For several years now we have distributed a new issue of the MAGNETOM Flash at the RSNA (we even call it the "RSNA issue").

Sharing knowledge and showing how MR imaging technology influences patient diagnosis are what MAGNETOM Flash magazine is all about. This issue is no different.

Here you can read, for example, about how the Children's Hospital in Atlanta deals with imaging for surgical therapy planning of epilepsy in children*; about imaging protocols for imaging of the lumbosacral plexus at Johns Hopkins Hospital; and about the clinical reality of simultaneous MR/PET at the University Hospital of Tübingen. Of course, these are just three of many exciting and informative articles awaiting you on the following pages. They have inspired me, and I am sure they will inspire you.

Enjoy reading the latest issue of Flash!

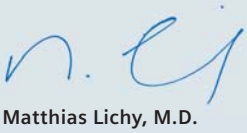

Matthias Lichy, M.D.

*MR scanning has not been established as safe for imaging fetuses and infants under two years of age. The responsible physician must evaluate the benefit of the MRI examination in comparison to other imaging procedures.

Editorial Board

We appreciate your comments.
Please contact us at magnetomworld.med@siemens.com

Antje Hellwich
Associate Editor

Wellesley Were
MR Business Development Manager Australia and New Zealand

Dr. Sunil Kumar S.L.
Senior Manager Applications, Canada

Christiane Bernhardt
Head Outbound Marketing Erlangen, Germany

Milind Dhamankar, M.D.
Sr. Director, MR Product Marketing, Malvern, PA, USA

Michelle Kessler
US Installed Base Manager Malvern, PA, USA

Gary R. McNeal, MS (BME)
Advanced Application Specialist, Cardiovascular MR Imaging Hoffman Estates, IL, USA

Peter Kreisler, PhD
Collaborations & Applications, Erlangen, Germany

Review Board

Okan **Ekinci**, MD, Center of Clinical Competence – Cardiology
Jens-Christoph **Georgi**, PhD, Global Marketing Manager Biograph mMR
Christian **Geppert**, PhD, Application Development Breast Applications
Wilhelm **Horger**, Application Development Oncology
Jürgen **Kampmeier**, PhD, MR/PET
Berthold **Kiefer**, PhD, Oncological and Interventional Applications
Lars **Lauer**, PhD, Orthopedic Applications
Heiko **Meyer**, PhD, Neuro Applications
Edgar **Müller**, Cardiovascular Applications
Silke **Quick**, Global Marketing Manager Women's Health
Ignacio **Vallines**, PhD, Global Marketing Manager Neurology and Orthopedics
Heike **Weh**, Clinical Data Manager
Lisa **Chuah**, PhD, Collaboration Manager MR Asean

Content

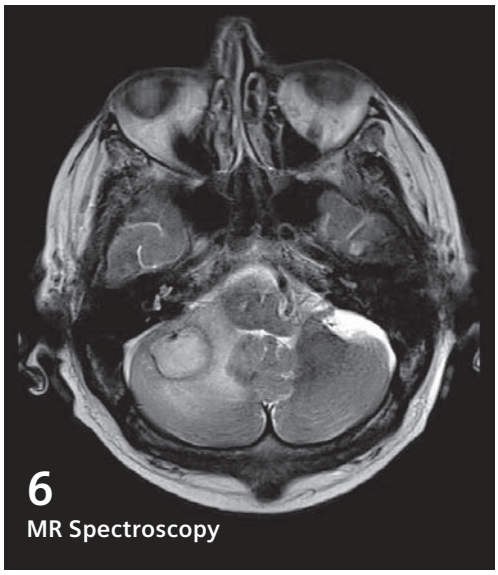

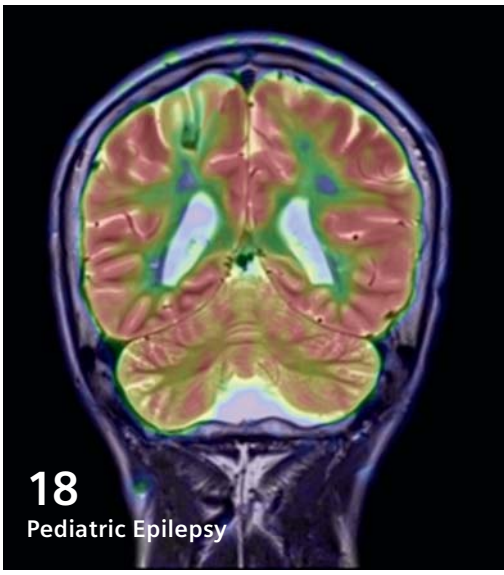

Further clinical information

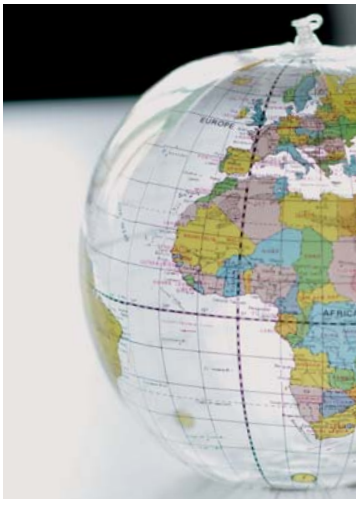

Visit the MAGNETOM World Internet pages at **www.siemens.com/magnetom-world** for further clinical information and talks by international experts.

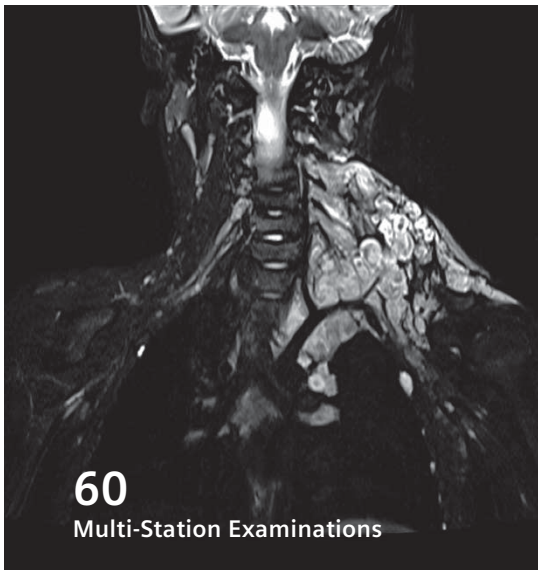

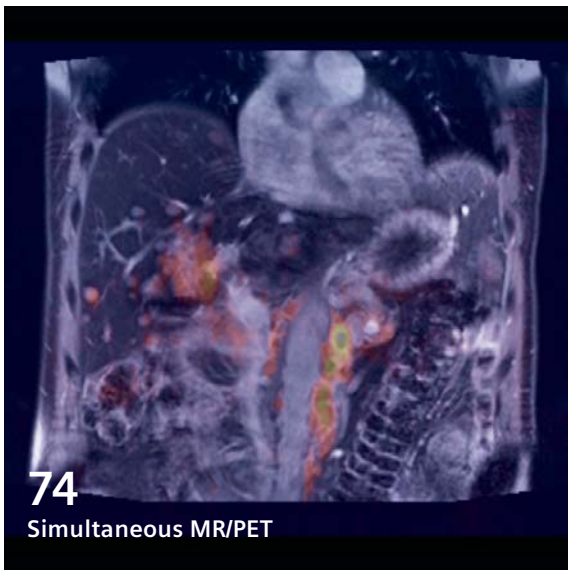

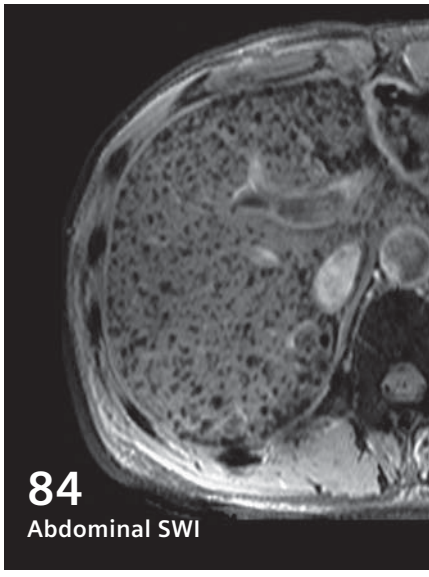

Case Reports: Cerebral Magnetic Resonance Spectroscopy at 1.5T and 3T

Marc Agzarian, BMBS (Hons), FRANZCR; Angela Walls, M.MedSc, B.App.Sc.Med Rad.

Division of Medical Imaging, Flinders Medical Centre, Bedford Park, South Australia, Australia

Introduction

This is a pictorial review of cerebral magnetic resonance spectroscopy (MRS) using a 1.5T MAGNETOM Aera system with software version *syngo* MR D11 and a 20-channel head and neck coil and a 3T MAGNETOM Trio system with software version *syngo* MR B15 and a 12-channel head matrix coil at Flinders Medical Centre, South Australia, Australia.
Magnetic resonance spectroscopy refers to the process of performing a chemical analysis in-vivo by the Fourier transform of the magnetic resonance signal from a voxel of tissue. Hydrogen nuclei (^{1}H protons) are used for clinical cerebral MRS. Proton spins in different molecules have slightly different Larmor frequencies. These differences are known as the chemical shift and are expressed in parts per million (ppm). Chemical shifts are usually referenced to the Larmor frequency of tetramethylsilane (TMS) which is given a chemical shift of zero ppm. All in-vivo molecules of interest have chemical shifts that increase their Larmor frequencies relative to TMS and are thus shown on the spectrogram to the left of zero.
Cerebral MRS can be acquired using two techniques, point resolved spectroscopy sequence (PRESS) and stimulated echo acquisition mode (STEAM). PRESS has become the most commonly used technique as it has a higher signal-to-noise ratio than STEAM. Both techniques can

Case 1: Right thalamic glioblastoma multiforme

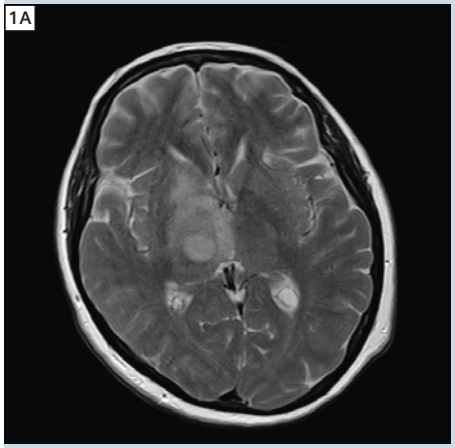

1A T2w TSE axial.

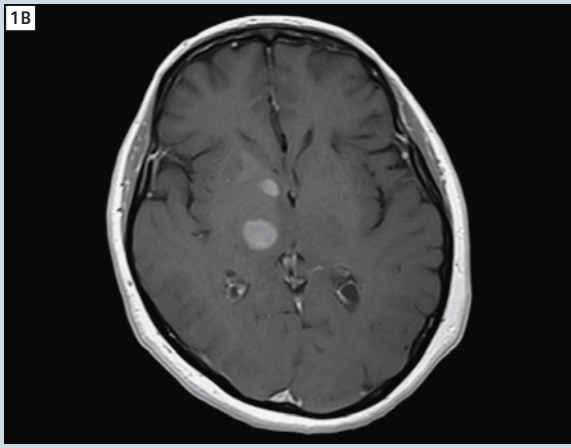

1B T1w SE post-gadolinium axial.

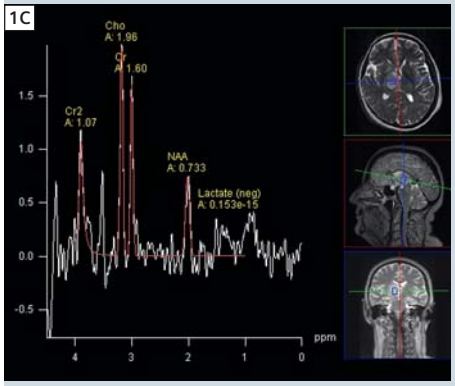

1C Multi-voxel PRESS MRS (TE 135 ms) within the lesion in the right thalamus.

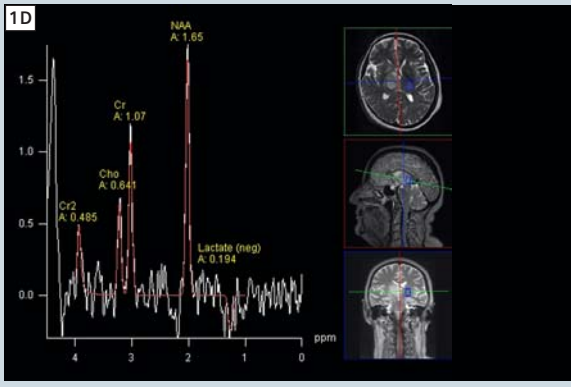

1D Multi-voxel PRESS MRS (TE 135 ms) within normally appearing left thalamus.

be used in either single-voxel or multi-voxel acquisitions. Single-voxel acquisitions provide a better quality spectrogram from just one region of interest at a time whereas multi-voxel acquisitions provide a lesser quality spectrogram from a grid of voxels acquired simultaneously. Multi-voxel MRS can be performed using PRESS or STEAM in 2D or 3D with additional phase encoding steps. Multi-voxel MRS is also known as chemical shift imaging (CSI) or magnetic resonance spectroscopic imaging (MRSI). Regardless of the technique and acquisition used, the essential requirement for MRS is exceptionally good magnetic field homogeneity.

Cerebral MRS is usually acquired at one or more of three different echo times, short (TE 30 – 35 ms), intermediate (TE 135 – 144 ms) and long (TE 270 – 288 ms). The short echo time is better at resolving the peaks of myoinositol, glutamine, glutamate and lipids whilst the long echo time tends to have less baseline noise. The intermediate echo time is used to confirm the presence of lactate as the lactate peak inverts.

Patient history

A 61-year-old female presented with a two week history of dysarthria and left sided weakness. Initial computed tomography (CT) scan revealed a faintly enhancing lesion within the right thalamus. MRI was performed to further characterize the lesion. The diagnosis of glioblastoma multiforme was confirmed with stereotactic biopsy.

Sequence details

Sagittal T1, axial PD, T2, T2 FLAIR, DWI, T1 and T1 post-gadolinium, coronal T2 and T1 post-gadolinium, 3D T1 MPRAGE post-gadolinium and multi-voxel PRESS MRS (TE 135 ms) were performed on our Siemens 1.5T MAGNETOM Aera scanner.

Imaging findings

A solitary, high T2 signal, intra-axial mass lesion is demonstrated within the right thalamus with mild surrounding vasogenic oedema (Fig. 1A). Multi-focal contrast enhancement is present (Fig. 1B). The MRS at an intermediate echo time (TE 135 ms) within the lesion clearly demonstrates a significant elevation of choline at 3.2 ppm relative to NAA at 2 ppm (Fig. 1C). This is in contrast to the normal MRS obtained from the left thalamus (Fig. 1D).

Discussion

Neoplasms display a characteristic MRS pattern, with an elevation of choline relative to NAA. This is the reverse of the normal situation in which NAA is the highest peak in the spectrum. Choline is a component of phospholipids and the increase in choline seen in neoplasms has been postulated to be the result of increased cell membrane turnover secondary to rapid cellular proliferation. A choline: NAA ratio of greater than 2.2 is highly suggestive of a neoplasm.

The key normal resonant peaks in cerebral MRS are N-acetyl-aspartate (NAA) at 2 ppm, creatine (Cr) at 3 ppm and 3.9 ppm and choline (Cho) at 3.2 ppm. Whilst there is some regional variation in the brain, the NAA peak is normally the highest in the spectrum.

Tips for performing cerebral MRS

On older generation MRI scanners, achieving high quality MRS was a difficult feat. With improved magnetic field homogeneities, higher field strengths and optimised software, performing MRS is no longer to be feared! At Flinders Medical Centre we routinely perform cerebral MRS using 2D multi-voxel PRESS CSI at an intermediate echo time (TE 135 ms). We have developed the following tips that have proven to work for a variety of pathologies and reduce operator dependance:

- Modify the volume of interest (VOI) size to best suit the lesion. We often use a 4 x 4 VOI to closely target a single lesion. Be sure to include some normal brain inside the VOI to aid in lesion diagnosis. A smaller VOI results in an improved shim and spectrum.
- Ensure the VOI avoids structures that will contaminate the baseline, such as skull, scalp, air, cerebrospinal fluid and major cerebral vessels.
- Do not be afraid to perform the spectroscopy in the coronal plane, particularly nearing the vertex.
- Ensure the VOI is planned according to an imaging slice. If not, perform a T2 localizer in the best plane and angle for the target lesion. Use 'copy image position' to ensure you have anatomical images during post-processing.
- Remember to use spatial saturation bands to cover the skull, scalp and vessels. We use six saturation bands positioned in 3D on all sides of the VOI. We found that if the saturation bands were positioned too close to the VOI we would get some baseline distortion. Leaving a buffer of one voxel's

width between the saturation bands and the VOI improves this significantly.
- Ensure 'fully excited volume' is selected. This option helps to attain homogenous excitation of all metabolites within the VOI, whilst suppressing interference from outside the VOI. This can be preset in your CSI protocol.
- Always perform MRS at the isocentre of the magnet.
- Ensure that your patient is comfortable, as their stillness is imperative.
- Post-processing is made easy through site defined defaults located in 'protocols'. Here we have preset exactly what we wish our spectra to show, including range, scale and peak information. This significantly reduces variability between operators.

Case 2: Right cerebellar abscess

Patient history

A 62-year-old male presented with a three week history of headache, atxia and diplopia. Initial CT scan revealed a ring enhancing lesion within the right cerebellar hemisphere. MRI was performed to further characterize the lesion. The diagnosis of a cerebral abscess was confirmed by the presence of pus at the time of operation and growth of *Staphylococcus aureus* on culture.

Sequence details

Sagittal T1 FLAIR, axial PD, T2, T2 FLAIR, DWI, T1 and T1 post-gadolinium, coronal T2 and T1 post-gadolinium, 3D T1 MPRAGE post-gadolinium and multi-voxel PRESS MRS (TE 135 ms) were performed on our Siemens 3T MAGNETOM Trio scanner.

Imaging findings

A solitary, ring enhancing, high T2 signal, intra-axial mass lesion is demonstrated within the right cerebellar hemisphere with surrounding vasogenic oedema (Figs. 2A, B). Uniformly restricted diffusion is present within the lesion, being hyperintense on DWI and hypointense on the ADC map (Figs. 2C, D). The MRS at an intermediate echo time (TE 135 ms) clearly demonstrates an elevated lipid and lacate peak at 1.3 ppm (Fig. 2E). Importantly, there is no significant elevation of choline at 3.2 ppm relative to NAA at 2 ppm.

Discussion

Cerebral abscess characteristically demonstrates a significantly elevated lipid and lactate peak without an elevation of choline relative to NAA on MRS. This allows MRS to reliably distinguish between cerebral abscesses and neoplasms. The uniform restricted diffusion is also typical of cerebral abscess. Thus, the combination of MRS and DWI allows the diagnosis of a cerebral abscess to be made with a high degree of certainty.

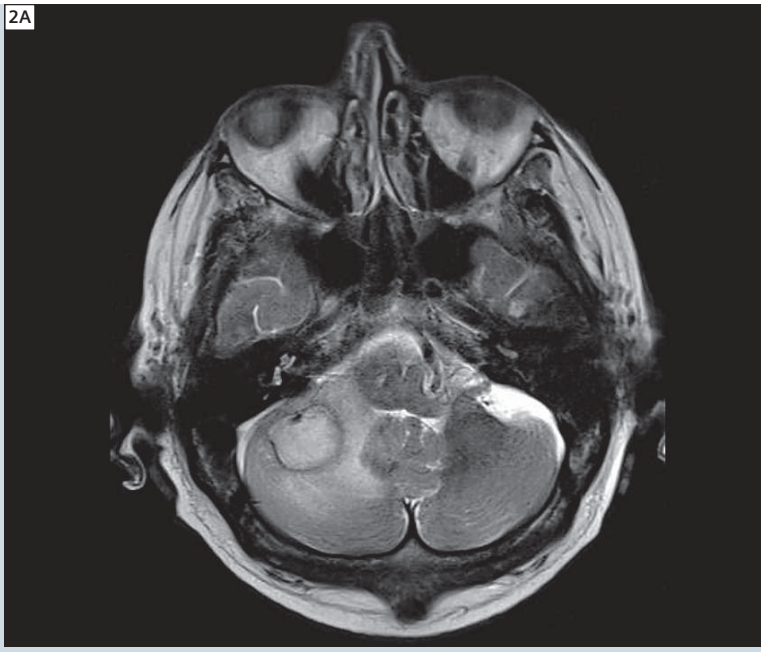

2A T2w TSE axial.

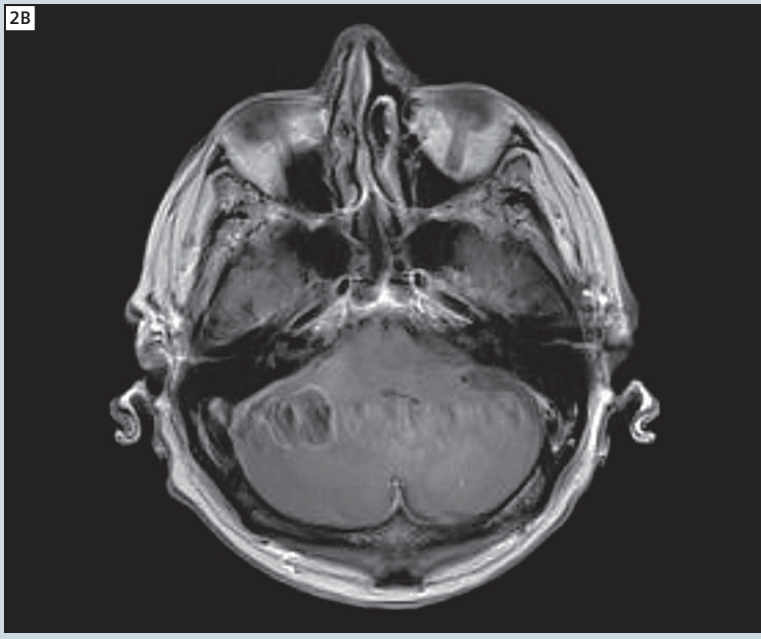

2B T1w SE post intravenous gadolinium axial.

MRS sequence details

The MRS sequence parameters for case 1, performed on our 1.5T MAGNETOM Aera were: 2D multi-voxel PRESS ^{1}H spectroscopy (csi_se_135), TR 1500 ms, TE 135 ms, 16 x 16 matrix, FOV 160 mm, slice thickness 15 mm, voxel size 10 x 10 x 15 mm, VOI 8 x 8, 4 averages, acquisition time 7:12 min. **The MRS sequence parameters for cases 2, 3 and 4,** performed on our 3T MAGNETOM Trio were: 2D multi-voxel PRESS ^{1}H spectroscopy (csi_se_135 or csi_se_270), TR 1700 ms, TE 135 ms or 270 ms, 16 x 16 matrix, FOV 160 mm, slice thickness 15 mm, voxel size 10 x 10 x 15 mm, VOI 4 x 4, 3 averages, acquisition time 6:53 min.

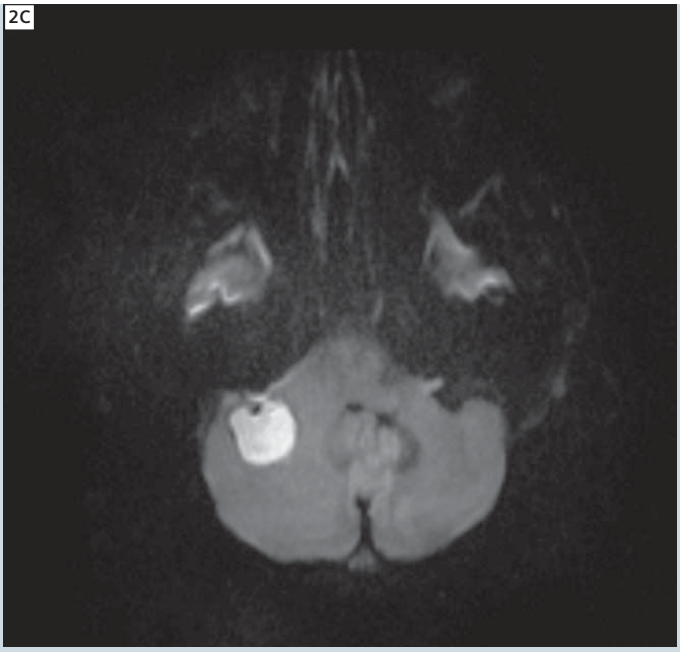

2C DWI axial.

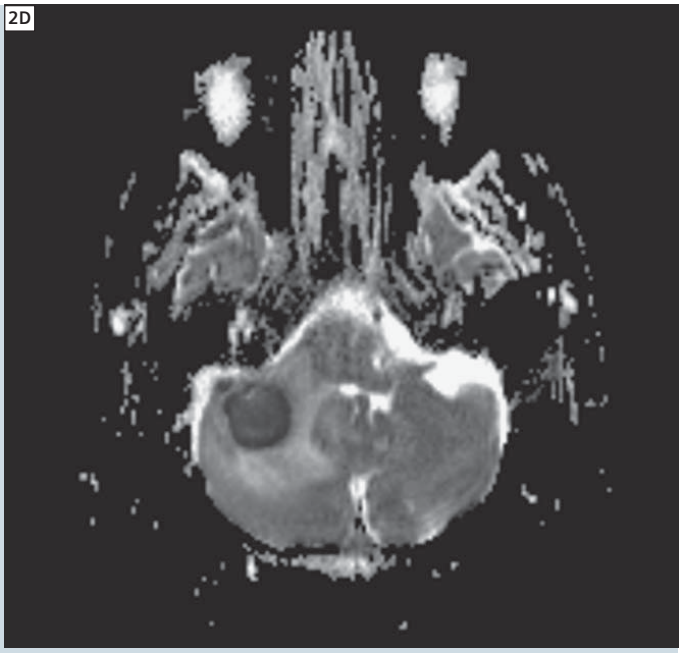

2D Corresponding ADC map.

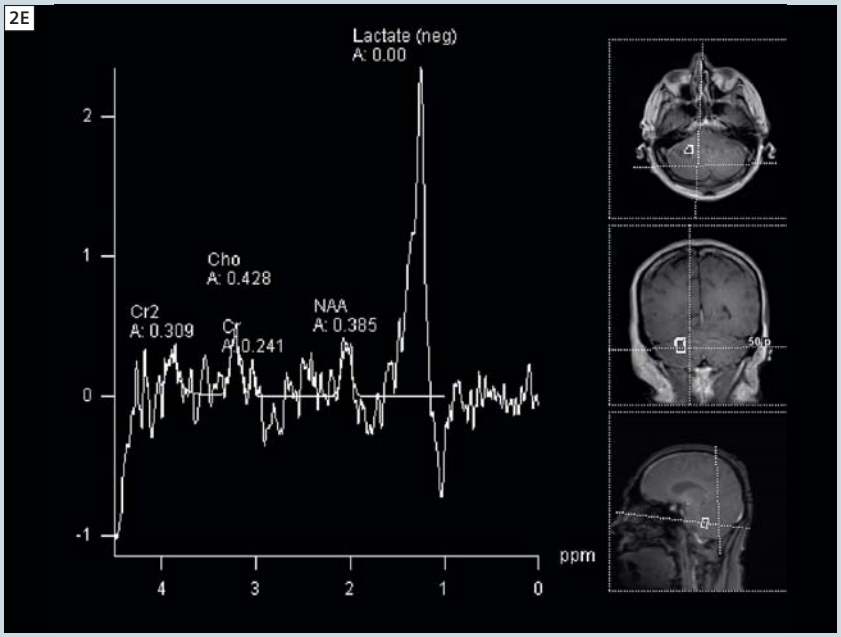

2E Multi-voxel PRESS MRS (TE 135 ms) within the lesion in the right cerebellum.

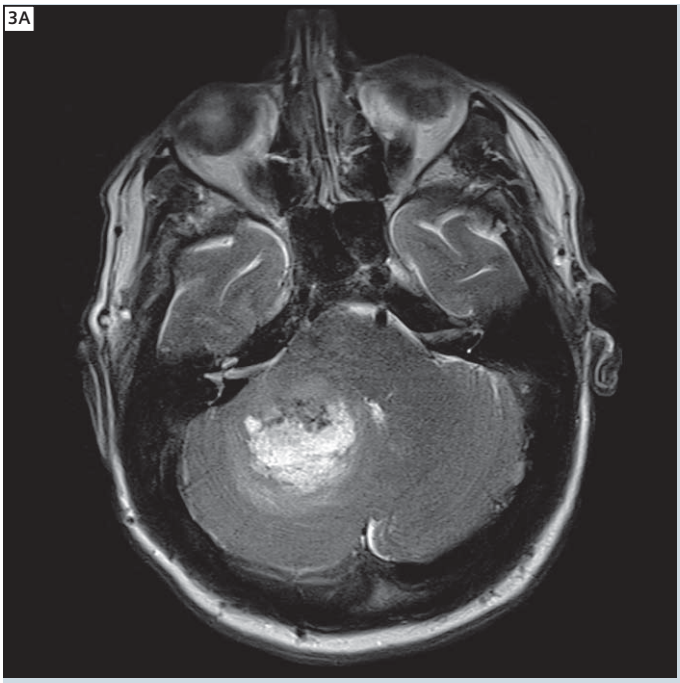

3A T2w TSE axial.

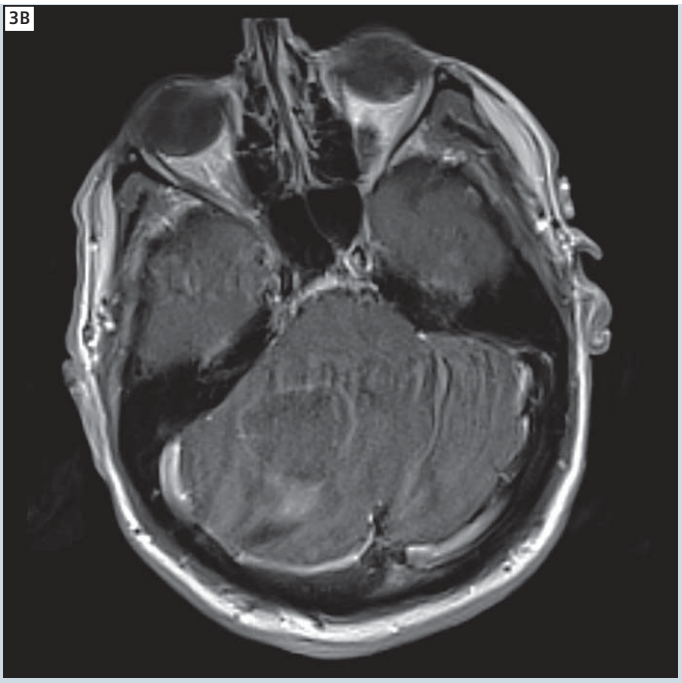

3B T1w SE post intravenous gadolinium axial.

Case 3:
Right cerebellar glioblastoma multiforme

Patient history

A 69-year-old male presented three days after a fall with progressively worsening headache. Initial CT scan revealed a ring enhancing lesion within the right cerebellar hemisphere. MRI was performed to further characterize the lesion. The diagnosis of glioblastoma multiforme was confirmed on excision biopsy.

Sequence details

Sagittal T1 FLAIR, axial PD, T2, T2 FLAIR, DWI, T1 and T1 post-gadolinium, coronal T2 and T1 post-gadolinium, 3D T1 MPRAGE post-gadolinium and multi-voxel PRESS MRS (TE 135 ms and TE 270 ms) were performed on our Siemens 3T MAGNETOM Trio scanner.

Imaging findings

A solitary, slightly irregular, ring enhancing, high T2 signal, intra-axial mass lesion is demonstrated within the right cerebellar hemisphere with mild surrounding vasogenic oedema (Figs. 3A, B). No restricted diffusion is present within the lesion, being hypointense on DWI and hyperintense on the ADC map, in keeping with T2 shine through (Figs. 3C, D). The MRS within the lesion, at a long echo time (TE 270 ms) clearly demonstrates a significant elevation of choline at 3.2 ppm relative to NAA at 2 ppm (Fig. 3E). An elevated lactate peak is also present at 1.3 ppm. The presence of lactate is confirmed with inversion of the peak when an intermediate echo time (TE 135 ms) is used (Fig. 3F). Importantly, MRS, at a long echo time (TE 270 ms) from white matter adjacent the lesion and largely outside of the surrounding vasogenic oedema, continues to demonstrate an abnormal elevation of choline relative to NAA (Fig. 3G).

Discussion

Magnetic resonance spectroscopy can be helpful in distinguishing a solitary primary cerebral neoplasm from a solitary cerebral metastatic deposit. The spectroscopic evaluation of the brain parenchyma outside of the lesion is the key in making this distinction. If, as in this case, there is an elevation of choline relative to NAA outside of the lesion, it is far more likely that the lesion represents a primary cerebral neoplasm. It is postulated that this is due to the infiltrative growth pattern of higher grade primary cerebral neoplasms. The lack of restricted diffusion in this case is in contrast to case 2.

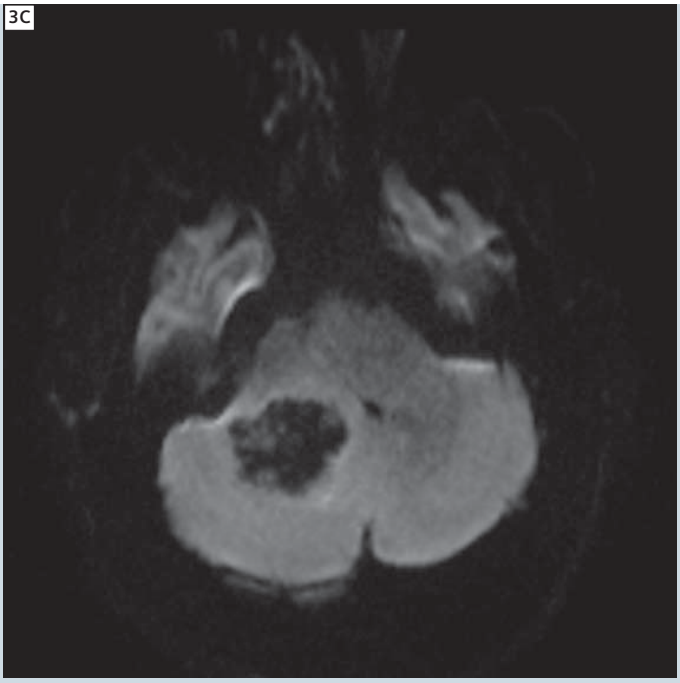

3C DWI axial.

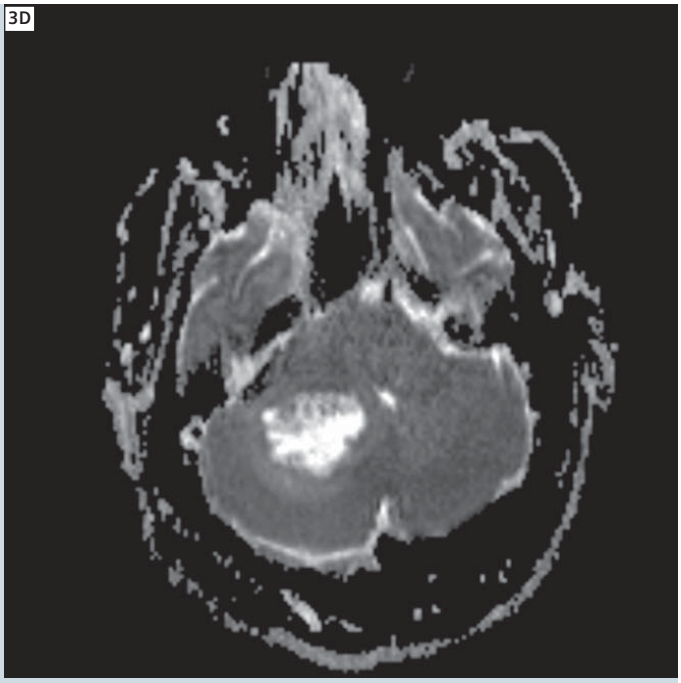

3D Corresponding ADC map.

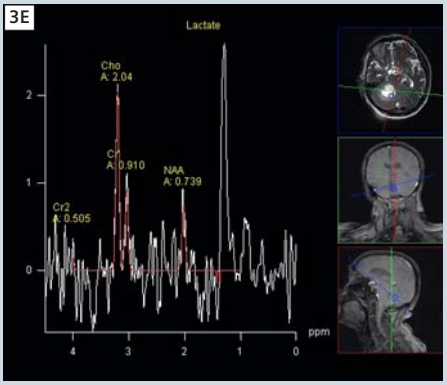

3E Multi-voxel PRESS MRS (TE 270 ms) within the lesion in the right cerebellum.

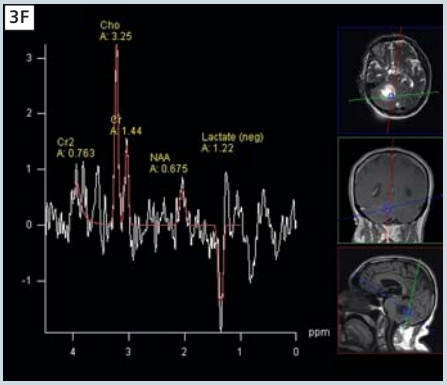

3F Multi-voxel PRESS MRS (TE 135 ms) within the lesion in the right cerebellum.

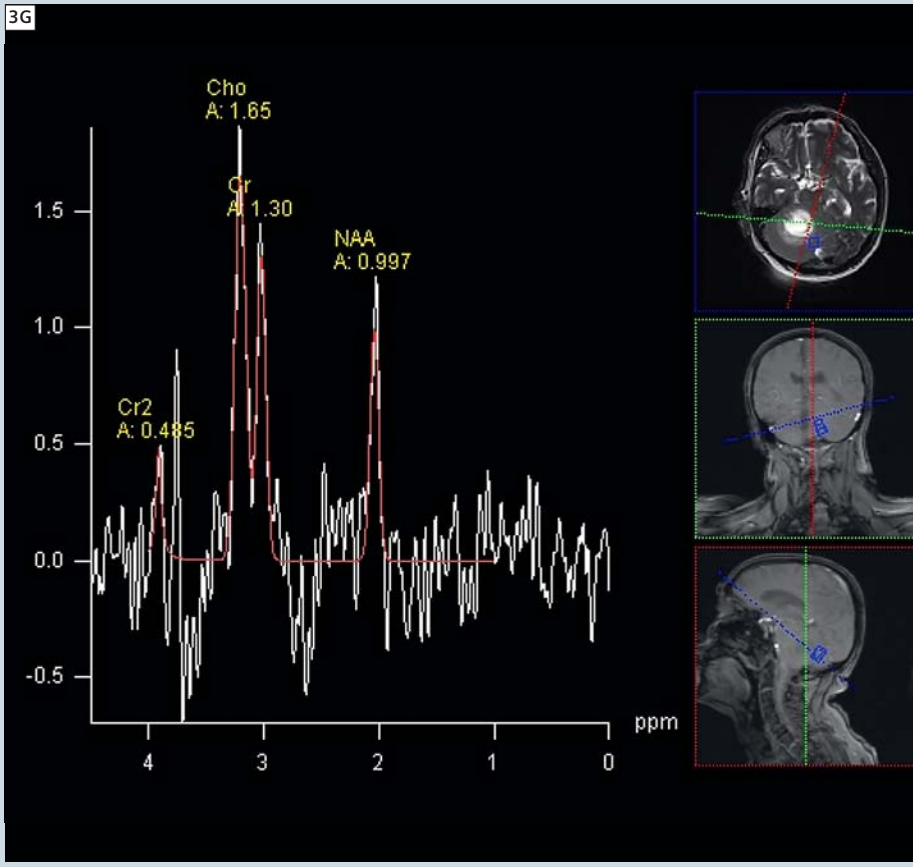

3G Multi-voxel PRESS MRS (TE 270 ms) adjacent the lesion in the right cerebellum.

Case 4: Right frontal lobe metastases

Patient history

A 50-year-old male presented with a two week history of progressively worsening headache. Initial CT scan revealed a ring enhancing lesion within the right frontal lobe. MRI was performed to further characterize the lesion. The diagnosis of metastatic adenocarcinoma was confirmed on excision biopsy.

Sequence details

Sagittal T1 FLAIR, axial PD, T2, T2 FLAIR, DWI, T1 and T1 post-gadolinium, coronal T2 and T1 post-gadolinium, 3D T1 MPRAGE post-gadolinium and multi-voxel PRESS MRS (TE 135 ms) were performed on our Siemens 3T MAGNETOM Trio scanner.

Imaging findings

A solitary ring enhancing, heterogeneous T2 signal, intra-axial mass lesion is demonstrated within the right frontal lobe with extensive surrounding vasogenic oedema (Figs. 4A, B). The MRS within the lesion, at an intermediate echo time (TE 135 ms) clearly demonstrates a significant elevation of choline at 3.2 ppm relative to NAA at 2 ppm (Fig. 4C). An elevated lipid and lactate peak is also present at 1.3 ppm. Importantly, MRS, at an intermediate echo time (TE 135 ms) from the white matter adjacent the lesion, within the surrounding vasogenic oedema, does not demonstrate an abnormal elevation of choline relative to NAA (Fig. 4D). A subsequently performed CT chest revealed a lobulated mass within the right upper lobe (Fig. 4E).

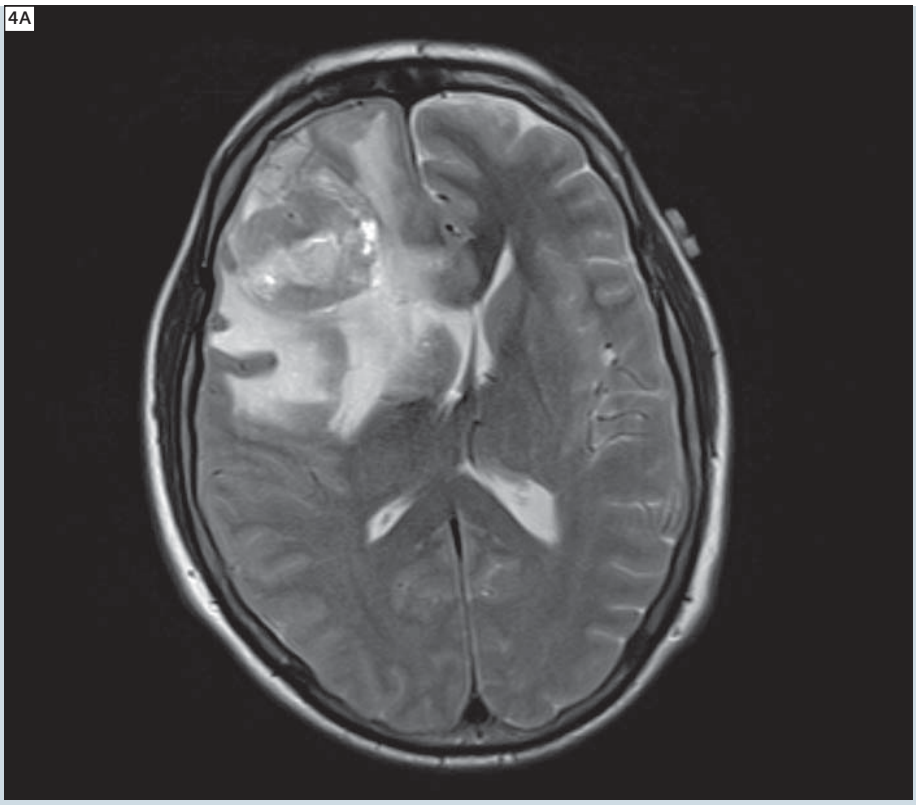

4A T2w TSE axial.

Discussion

In this case, the MRS from the brain parenchyma outside of the lesion does not demonstrate an elevation of choline relative to NAA, consistent with a solitary metastatic deposit. This is in contrast to case 3.

Case studies discussion

Magnetic resonance spectroscopy is a powerful technique that adds metabolic information to routine MRI brain examinations. As shown in these four cases, this additional information is useful in differentiating cerebral neoplasms from abscesses and distinguishing solitary primary cerebral neoplasms from solitary cerebral metastatic deposits. MRS is also beneficial in distinguishing radiation necrosis from recurrent tumor, diagnosing metabolic and mitochondrial disorders such as MELAS (mitochondrial encephalopathy lactic acidosis and stroke like episodes) and guiding the biopsy of lesions. Recent improvements in scanner hardware and software allow MRS to be performed reliably and quickly, facilitating its incorporation into routine clinical practice.

References

1 Horska A, Barker PB. Imaging of brain tumors: MR spectroscopy and metabolic imaging. Neuroimag Clin N Am 2010;20:293-310. Review.
2 Al-Okaili RN, Krejza J, Wang S, Woo JH, Melhem ER. Advanced MR imaging techniques in the diagnosis of intraaxial brain tumors in adults. Radiographics 2006;26:S173–S189. Review.
3 Barker PB, Bizzi A, De Stafano N, Gullapalli RP, Lin DDM. Clinical MR spectroscopy: techniques and applications. Cambridge University Press, Cambridge, 2010.

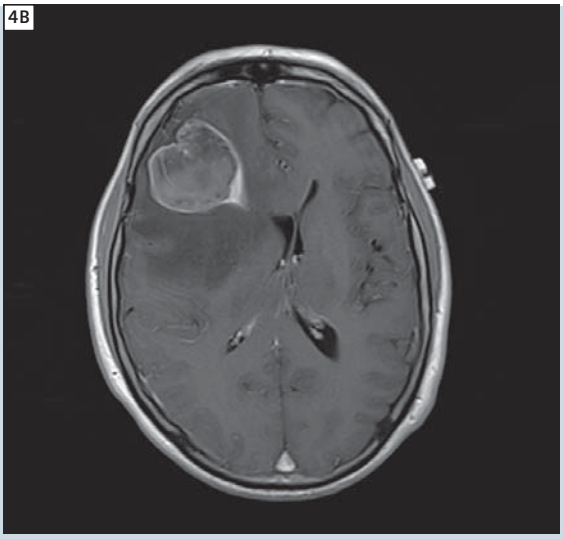

4B T1w SE post intravenous gadolinium axial.

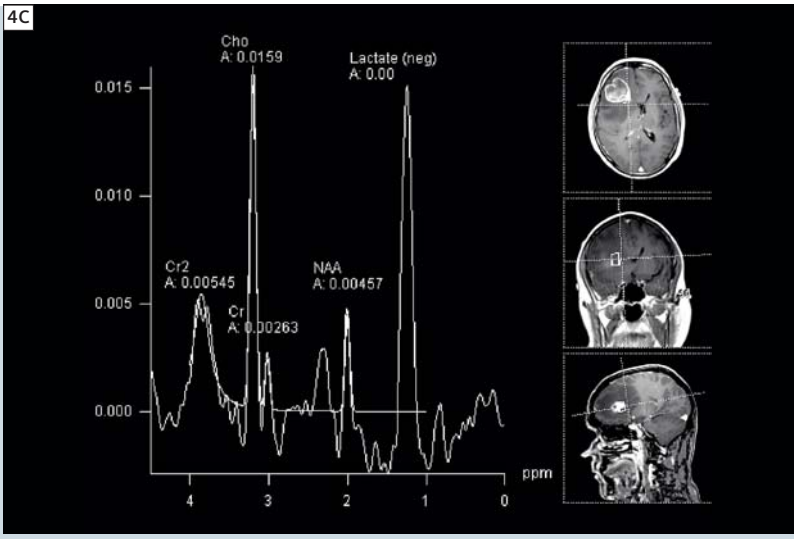

4C Multi-voxel PRESS MRS (TE 135 ms) within the lesion in the right frontal lobe.

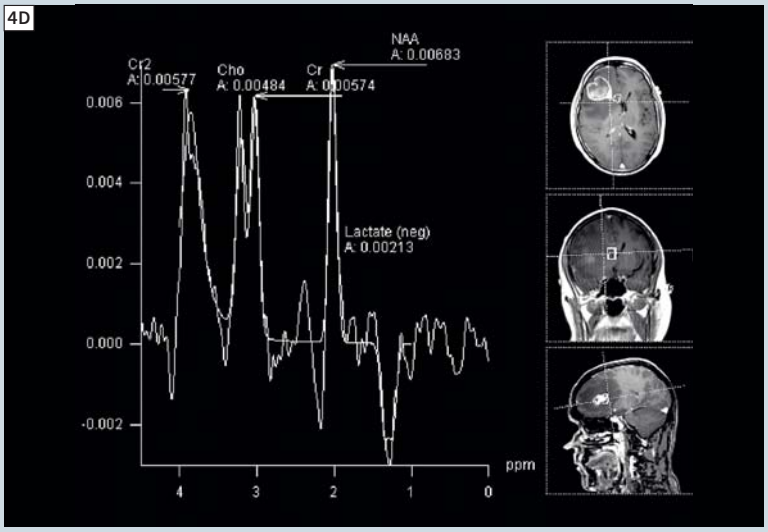

4D Multi-voxel PRESS MRS (TE 135 ms) adjacent the lesion in the right frontal lobe.

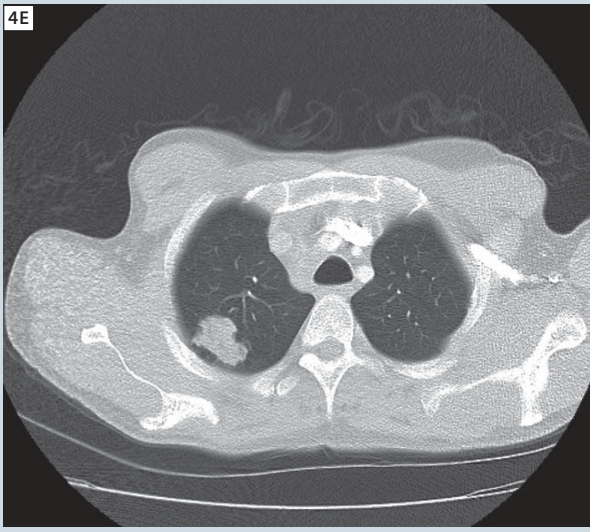

4E CT chest.

4 Gillard JH, Waldman AD, Barker PB. Clinical MR neuroimaging: diffusion, perfusion and spectroscopy. Cambridge University Press, Cambridge, 2004.

5 McRobbie DW, Moore EA, Graves MJ, Prince MR. MRI from picture to proton, 2nd edn. Cambridge University Press, Cambridge, 2007.

6 Meyerand ME, Pipas JM, Mamourian A, Tosteson TD, Dunn JF. Classification of biopsy-confirmed brain tumors using single-voxel MR spectroscopy. AJNR Am J Neuroradiol 1999;20:117–123.

7 Weybright P, Sundgren PC, Maly P, Hassan DG, Nan B, Rohrer S, Junck L. Differentiation between brain tumor recurrence and radiation injury Using MR spectroscopy. AJR 2005;185:1471–1476.

8 Burtscher IM, Skagerberg G, Geijer B, Englund E, Stahlberg F, Holtas S. Proton MR spectroscopy and preoperative diagnostic accuracy: an evaluation of intracranial mass lesions characterized by stereotactic biopsy findings. AJNR Am J Neuroradiol 2000;21:84–93.

Contact
Marc Agzarian BMBS(Hons), FRANZCR
Head of MRI
Division of Medical Imaging
Flinders Medical Centre
Bedford Park, South Australia, 5041
Australia
Phone: +61 8 8204 4405
marc.agzarian@health.sa.gov.au

Angela Walls M.MedSc, B.App.Sc.Med Rad.
Head MRI Radiographer
Division of Medical Imaging
Flinders Medical Centre
Bedford Park, South Australia, 5041
Australia
Phone: +61 8 8204 5750
angela.walls@health.sa.gov.au

Case Series: Presurgical Planning with fMRI/DTI

Jay J. Pillai, M.D.; Domenico Zacà, Ph.D.

Johns Hopkins University, School of Medicine, Neuroradiology Division, Russell H. Morgan Department of Radiology and Radiological Science, Baltimore, MD, USA

Background

Blood Oxygen Level Dependent functional Magnetic Resonance Imaging (BOLD fMRI) is clinically indicated mainly for mapping presurgically motor, sensory and language areas in neurosurgical patients with brain tumors and other potentially resectable lesions (e.g. epilepsy). BOLD fMRI together with Diffusion Tensor Imaging (DTI) determines the location of critical gray matter and white matter areas at risk of being resected during lesion removal and provides also information on language lateralization.

This case series aims to demonstrate how fMRI and DTI can influence the surgical decision making process providing information that would have not been available using only MR structural images. Below the fMRI imaging protocol used at our institution on a Siemens 3T MAGNETOM Trio scanner is reported. Selected parameters of the sequences of interest for this case series were as follows:

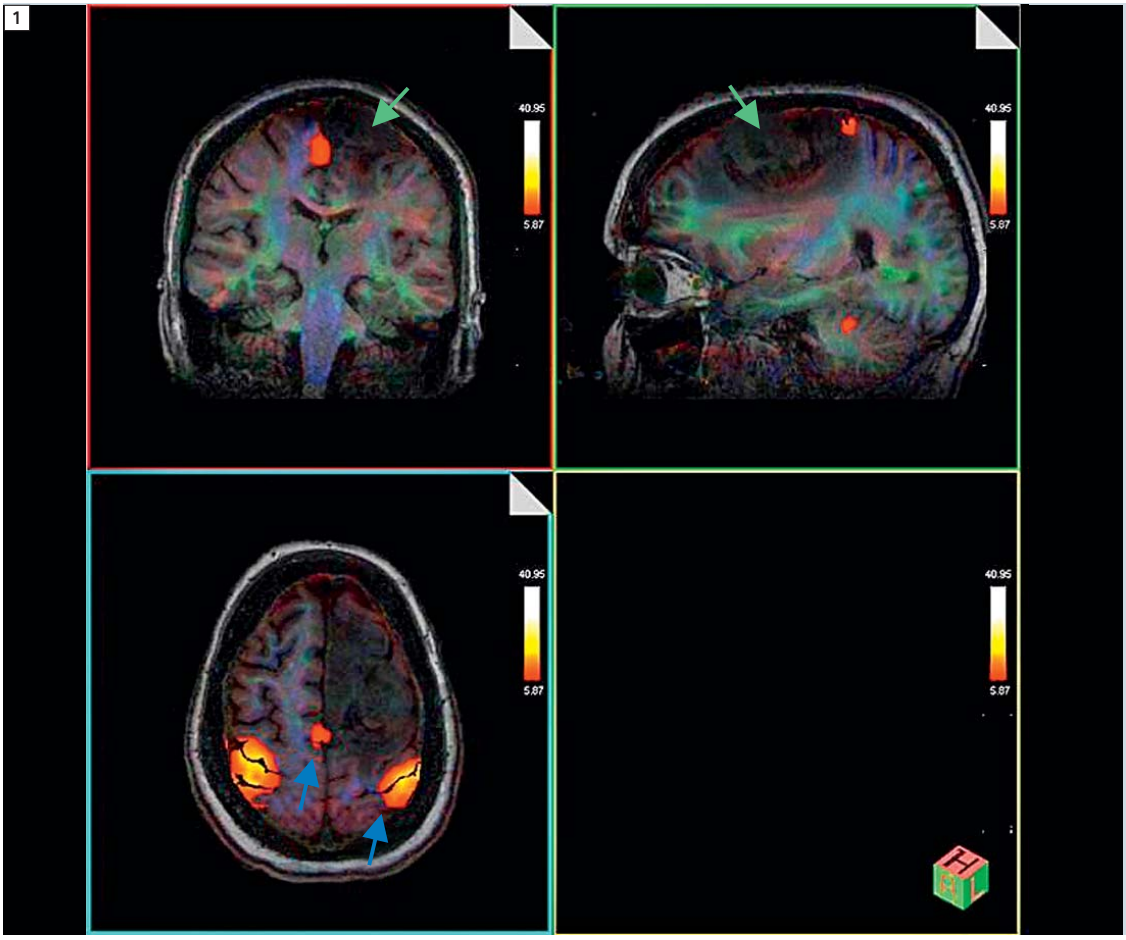

1 Multiplanar view in Neuro3D of fused T1 MPRAGE, bilateral finger tapping activation maps and DTI (FA-weighted) color directional maps. On the axial image two critical foci of activation are visible located posterior medial and lateral to the border of the lesion (blue arrow). On the sagittal and coronal plane infiltration of the cortical spinal tract by the tumor is well depicted.

- **T1-weighted pre-, post-contrast 3D MPRAGE**
  TR/TE/TI: 2300/3.5/900 ms; FA: 9°; voxel size: 1 x 1 x 1 mm³; BW: 240 Hz/pix
- **T2-weighted 3D FLAIR**
  TR/TE/TI: 6000/366/2100 ms; FA: 90°; voxel size: 1 x 1 x 4 mm³; BW: 673 Hz/pix
- **EPI BOLD 2D for functional MRI**
  TR/TE: 2000/30 ms; FA: 90°; voxel size: 3.6 x 3.6 x 4 mm³; BW: 2232 Hz/pix
- **EPI Diffusion Tensor Imaging 2D**
  2 b-values (0-800), 20 directions
  TR/TE: 6600/90 ms; FA: 90°; voxel size: 2.4 x 2.4 x 3 mm³; BW: 1408 Hz/pix

Material and methods

All images shown in this case series were acquired at 3 Tesla (MAGNETOM Trio) using software version *syngo* MR B17. Images were postprocessed using the software version *syngo* MR B17.

BOLD activation maps were calculated based on General Linear Model (GLM) analysis and displayed as thresholded t-statistic maps. DTI data were processed using the diffusion ellipsoid model and the display of the preferred diffusion direction of the voxels was color coded according to the following scheme:

- Red: right – left
- Blue: superior – inferior
- Green: anterior – posterior

The Neuro3D Package was used for multiplanar reconstruction and 3D visualization.

Case 1

This 51-year-old female patient had a diagnosis of a left frontal lobe lesion ten years earlier. After mild episodes of loss of speech follow up MRI examination showed slight increase in tumor size and demonstrated progressive contrast enhancement of this lesion, surgical resection was considered as a viable treatment option. Clinical fMRI/DTI examination was requested primarily for language and motor mapping. Postprocessed DTI, Fractional Anisotropy (FA)-weighted color directional maps and BOLD activation maps were created and fused with structural images by using the Neuro3D Package. Imaging findings show critical motor activation at the posterior margins of the lesion and involvement by the tumor of the corticospinal tract (Fig. 1).
A decision in favor of surgical resection of this lesion was made. The results of brain mapping by fMRI and DTI directed a superior approach as visible on postsurgical coronal T1 contrast-enhanced images (Fig. 2).

Case 2

A 67-year-old female who presented with facial seizures underwent a

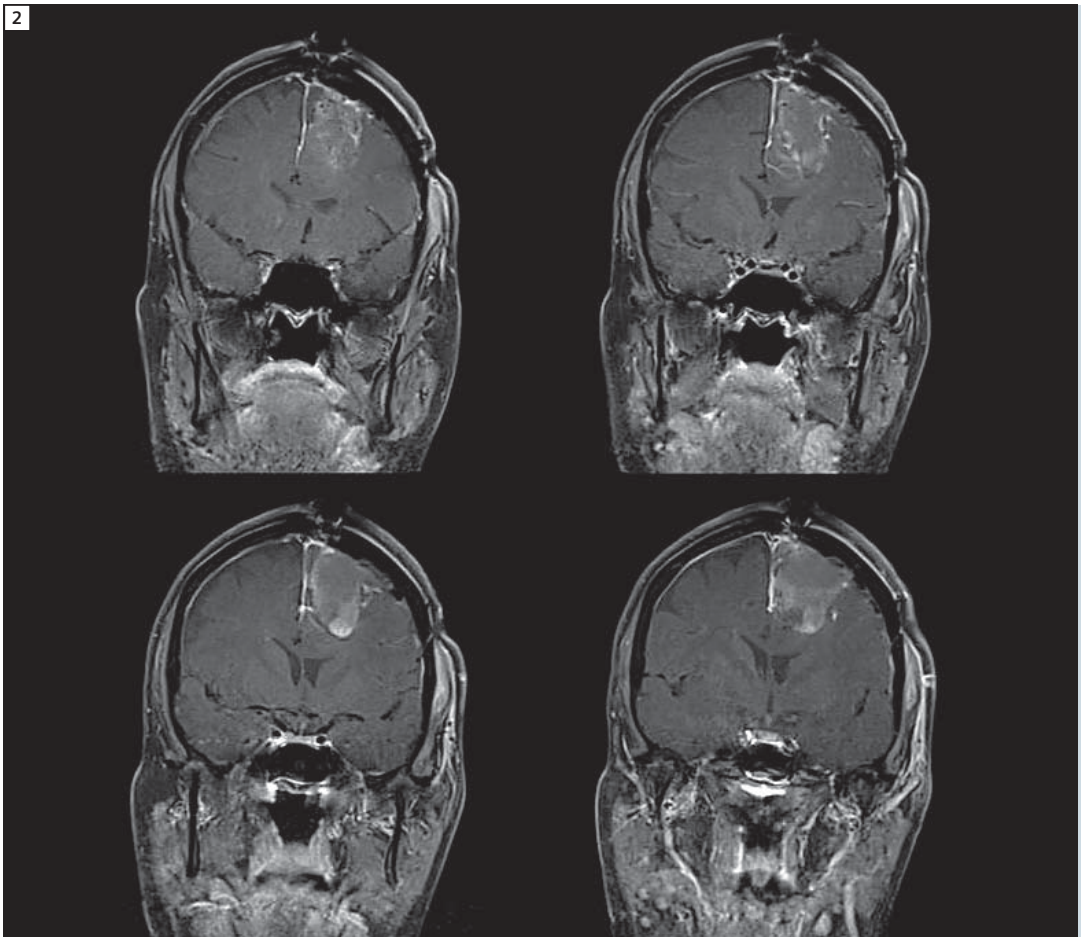

2 Coronal T1 contrast-enhanced images acquired after surgery visualize the surgical approach taken by the neurosurgeon to remove the lesion in order to minimize the risk of postoperative neurological deficits.

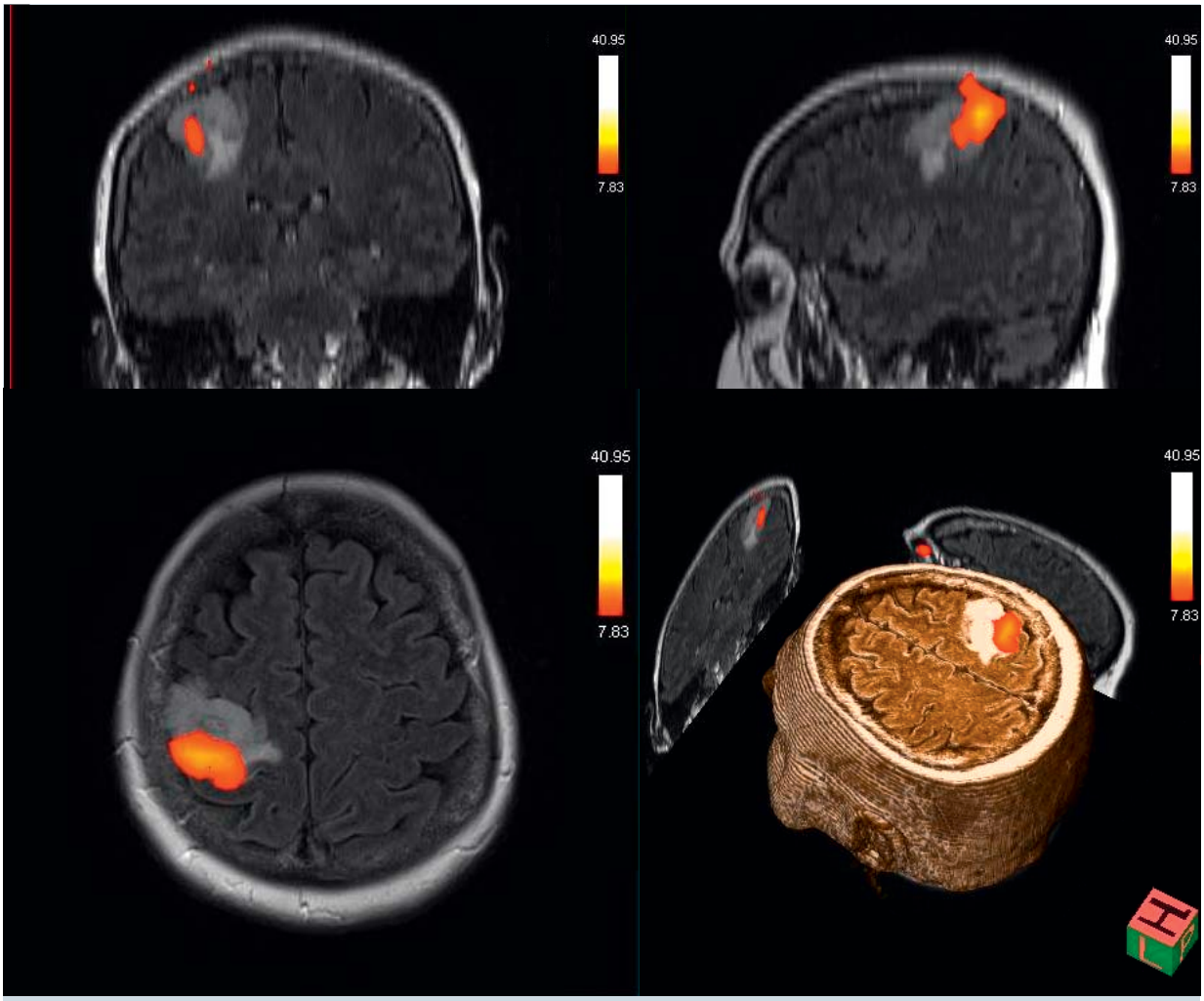

3 Multiplanar reconstruction of left hand activation map fused with T2 FLAIR images localizes the right primary motor cortex that was infiltrated by the mass.

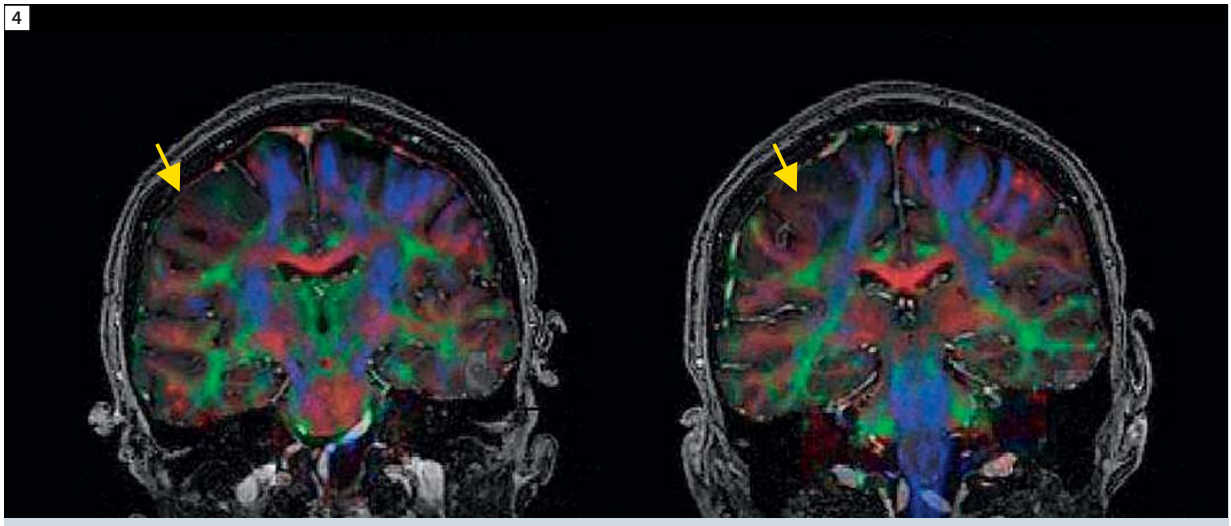

4 Coronal reconstruction of the FA-weighted color directional maps fused with T1 MPRAGE images delineates the infiltration by the tumor of the cortical spinal tract (yellow arrow).

structural MRI scan that revealed a non-enhancing T2 hyperintense right parietal cystic lesion. The neurosurgeon requested a functional MRI and DTI scan for assessment of the tumor surrounding motor function to plan possible surgery.

GLM based activation maps from an alternating hand opening/closing task demonstrated that the right primary motor cortex (PMC) was quite involved by the lesion (Fig. 3). In addition, the reconstructed coronal DTI, FA-weighted, color directional maps demonstrate infiltration by the tumor of the fibers of the corticospinal tract (CST) subserving the face and hand representation areas of the right PMC (Fig. 4).

The surgical decision was to perform awake craniotomy with intraoperative cortical stimulation in order to monitor constantly the left side at risk of a temporary or a permanent neurologic deficit. In the operating room the lesion removal was stopped when the patient experienced weakness on the distal left lower extremity upon stimulation. The surgical resection was therefore subtotal as demonstrated on the post-surgical axial T1 contrast-enhanced images (Fig. 5).

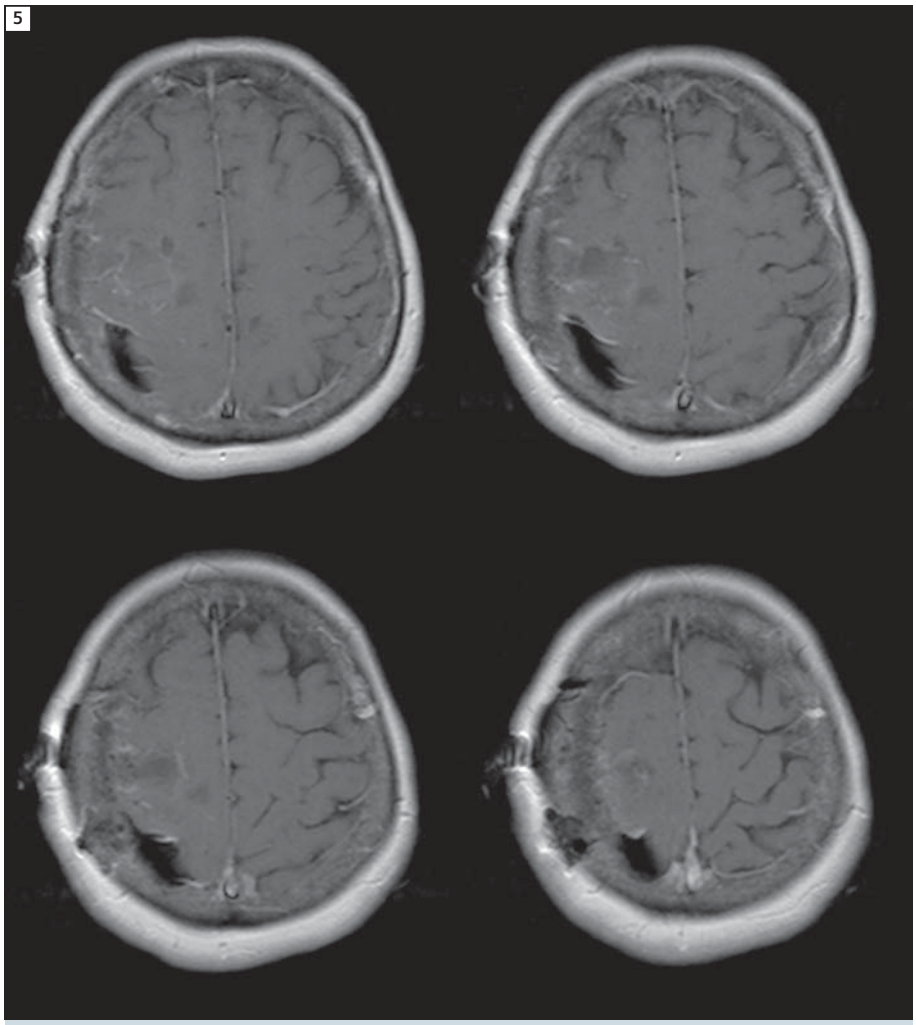

5 Axial post-surgical T1-weighted images demonstrate the surgical trajectory taken for the resection of the lesion.

Conclusion

This short case series shows how fMRI coupled with DTI can assist neurosurgeons in the surgical planning of brain tumor patients who are at risk of developing post-operative neurological deficits. With increasing experience in using and interpreting functional imaging by neuroradiologists and neurosurgeons and with improved standardization in data acquisition and analysis methods, fMRI has the potential to become a routinely used imaging technique for neurosurgical treatment planning.

Acknowledgement

This work was funded in part by a research grant from Siemens Medical Solutions, Inc.

References

1 Medina, L. S., *et al.* Seizure disorders: Functional MR imaging for diagnostic evaluation and surgical treatment – prospective study. Radiology 236, 247-53 (2005).

2 Petrella, J. R., *et al.* Preoperative Functional MR Imaging Localization of Language and Motor Areas: Effect on Therapeutic Decision Making in Patients with Potentially Resectable Brain Tumors. *Radiology* 240, 793-802 (2006).

3 Pillai, J. J. The Evolution of Clinical Functional Imaging during the Past Two Decades and Its Current Impact on Neurosurgical Planning. *AJNR Am J Neuroradiol* 31(2), 219-25 (2010).

Contact
Jay J. Pillai, M.D.
Neuroradiology Division
Russell H. Morgan Department of Radiology and Radiological Science
The Johns Hopkins University School of Medicine & The Johns Hopkins Hospital
600 N. Wolfe Street
Phipps B-100
Baltimore, MD 21287
USA
Phone: +1 410.955.2353
Fax: +1 410.614.1213
jpillai1@jhmi.edu

Neuroimaging as a Clinical Tool in Surgical Planning and Guidance for Pediatric Epilepsy

Binjian Sun, Ph.D.; Robert Flamini, M.D.; Susan Palasis, M.D.; Richard A. Jones, Ph.D.

Children's Healthcare of Atlanta, Department of Radiology, Atlanta, GA, USA

Epilepsy is the fourth most common neurological disorder in all ages. According to the Epilepsy Foundation, 1% of the population is expected to develop epilepsy before 20 years of age. Extra-temporal cortical resection is the most common curative epilepsy surgery in infants* and children, whereas temporal lobectomy is the most common in adults. Children with intractable epilepsy may benefit from early surgical intervention to avoid the potential negative effects of continued seizures and prolonged use of anti-epilepsy drugs on cognitive and psychosocial development and to increase the chances of post-operative neurological reorganization due to the inherent functional plasticity of the pediatric brain. Tellez-Zenteno et al. surveyed 3557 (697 non-lesional, 2860 lesional) temporal and extra-temporal epilepsy data from children for whom structural MRI was used to define the patient as being lesional or non-lesional and who then underwent surgery [1]. The meta-analysis revealed the seizure free post-surgery rate was 45% for non-lesional patients and 81% for lesional patients. This highlights the importance of successfully locating, and characterizing, the epileptogenic zone (EZ), which is defined as the volume of brain tissue responsible for the generation of seizures and whose removal consequently leads to freedom from seizures. It is important to characterize the structural lesion because the spatial relationship of the lesion to the EZ varies between different types of lesions. For most brain

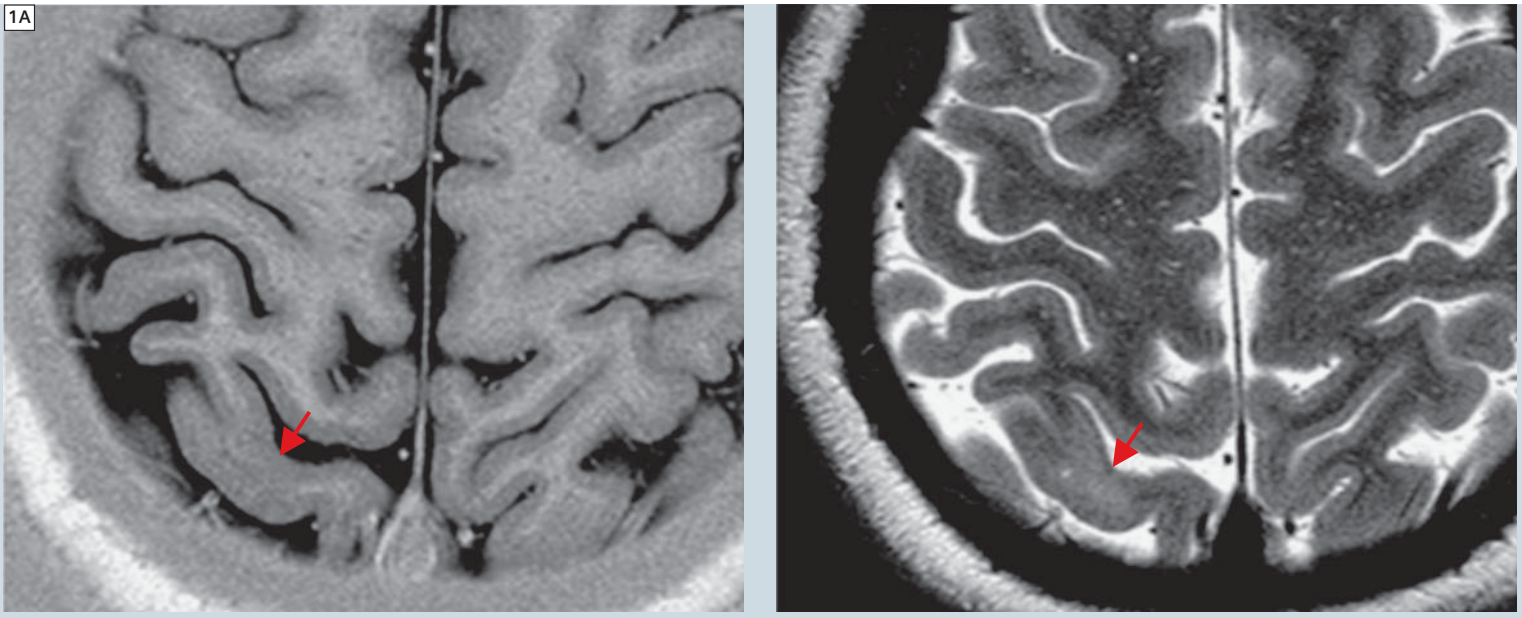

1A Inversion recovery and T2-weighted images acquired with high spatial resolution on a 3T MAGNETOM Trio scanner. A subtle lesion (red arrows) can be seen that is hypo- and hyper-intense on the IR and T2-weighted images respectively.

tumors, removal of the lesion, including the immediate margins of tissue around the lesion, will lead to freedom from seizures in a high percentage of patients. However, in the case of focal cortical dysplasia, removal of the lesion and its margins frequently does not lead to freedom from seizures, implying that the EZ extends beyond the visible lesion in this case. As with any surgery there are potential risks as well as benefits, in particular that the epileptogenic focus may share, or be in close proximity, to eloquent cortex. Thus it is not uncommon for patients to suffer from varying degrees of neurocognitive decline post-surgery. For patients with temporal lobe epilepsy (TLE) the decline is predominately manifested as verbal or visual memory impairment [2–5]. For example, one study showed that TLE patients suffered an average of 11% verbal memory decline following TL resection [4]. Another, more recent, study revealed that although group level comparison shows no significant verbal intellectual loss, roughly 10% of TLE children experienced a significant decline in verbal functioning following TL resection [5]. Hence thorough and meticulous pre-surgical assessments are necessary to address both aspects of the surgical outcome, i.e., post-surgical seizure activity and neurological functioning. Neuroimaging is now routinely prescribed for TLE patients who are potential candidates for temporal lobectomy. The neuroimaging assessment includes video EEG monitoring, structural neuroimaging (MRI), functional cerebral imaging such as fMRI, Single Photon Emission Computed Tomography (SPECT) and Positron Emission Tomography (PET). The results of these evaluations can be used individually, or collectively, to:

1) Localize and characterize the epileptogenic focus and thus help the physician to determine if surgical resection of the extratemporal cortex is appropriate.

2) Identify both the laterality of functions such as language and the location of patient-specific, functionally important, cortical regions and white matter tracts that should, if possible, be spared by surgery.

Localization of epileptogenic focus

The brain lesions associated with pharmacoresistant epilepsy are often subtle and require special expertise for their detection and characterization. In addition, the use of a dedicated epilepsy protocol, rather than a standard brain protocol, has been shown to offer improved lesion detection [6]. Dedicated TL epilepsy protocols include high spatial resolution thin slice, T1 and T2-weighted coronal and axial imaging with the coronal images being acquired in an oblique plane perpendicular to the long axis of the hippocampus when evaluating TLE. It has also been shown that the use of a 3T magnet and phased array coils further improves the sensitivity of lesion detection, when compared to 1.5T results [7]. Figure 1 illustrates two cases where epileptogenic foci were identified on high resolution anatomical MR images. To date, most studies have shown that interictal diffusion imaging is not helpful for lesion localization [8]. Changes in the diffusion tensor have been detected

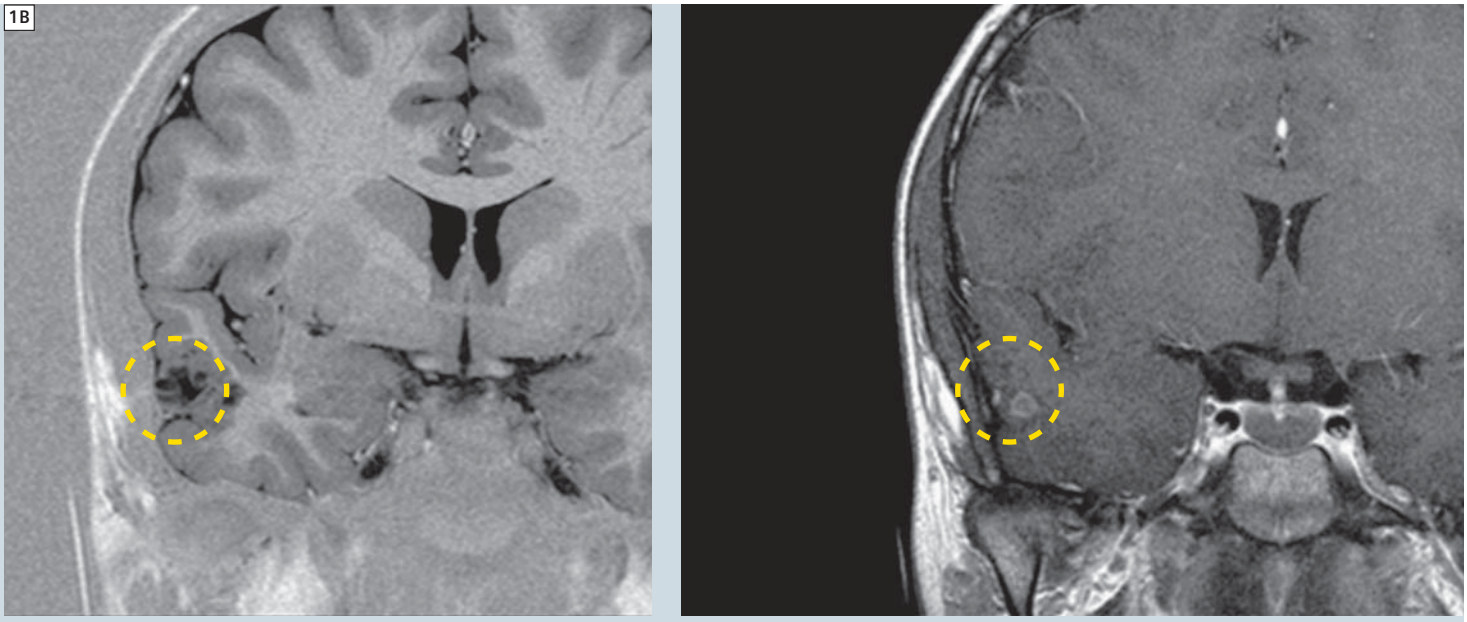

1B Inversion recovery and post-gadolinium T1 images identifying a small cystic lesion (yellow circles) in temporal lobe.

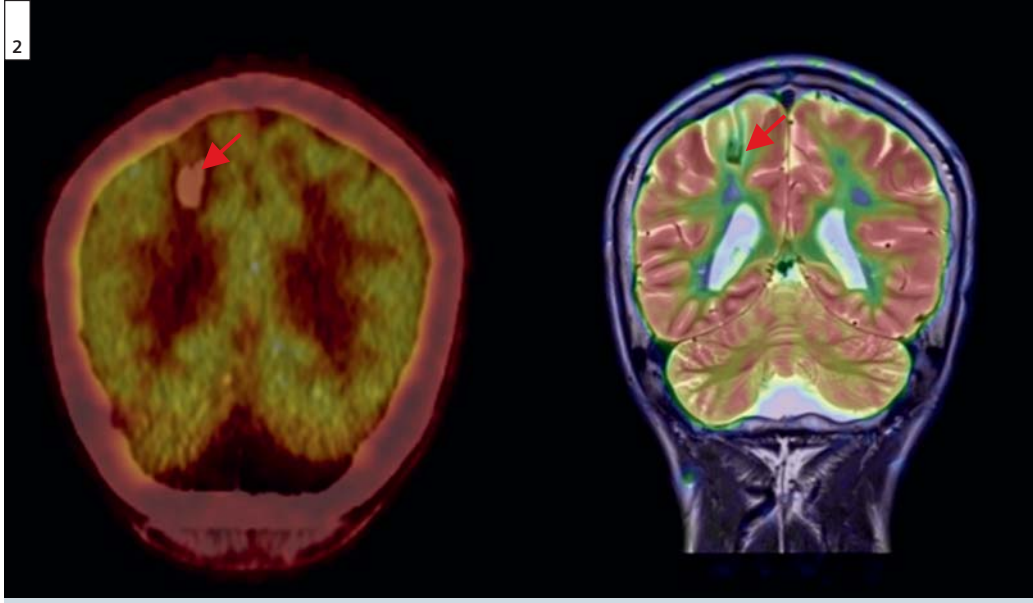

2 Fused PET-CT (left) and PET-MR images of a patient with tuberous sclerosis. The PET images detected regions of hypometabolism in three of the multiple sub-cortical tubers (only one is shown (red arrows)) allowing these to be identified as the possible seizure foci.

but in general do not reach statistical significance even at the group level [9]. This may be, in part, due to partial volume effects from the poor spatial resolution typically used for diffusion studies. The development of higher resolution techniques for diffusion imaging may change this in the future.
In a small portion of our epilepsy surgery population, PET is used to assist the localization of epileptogenic focus. Due to the poor resolution of PET images, CT and/or MRI are also performed on this group of patients. The PET images are then coregistered with CT and MR results in order to allow the anatomical location of areas of poor perfusion to be more accurately identified. Figure 2 shows a case where an epileptogenic lesion was identified on the fused PET-CT and PET-MR images.
Another technique that is used more frequently at our institution for the localization of the EZ is SISCOM (Subtraction Ictal SPECT Co-registered to MRI). This technique combines SPECT studies of a tracer that reflects cerebral perfusion, with the studies being acquired both ictally (during a seizure) and an interictally (between seizures) [10, 11]. Conventionally, side-by-side visual analysis of ictal and interictal SPECT images can be used for lesion identification. However, the interpretation of the images can be quite difficult due to differences in the injected dose, tracer uptake and decay, patient head position, and slice positioning. To address these problems, the SISCOM technique registers the two SPECT scans using a mutual information based registration algorithm (we do an initial crude manual registration in order to avoid problems with local maxima of the registration algorithm) and then normalizes the two SPECT scans prior to computing a difference image that represents a semi-quantitative map of the cerebral blood flow changes occurring during the seizure [10]. Unfortunately, the poor spatial resolution and contrast of the SPECT images complicate the determination of the exact anatomical location of any seizure focus detected on the differential image. For this reason, the differential image is subsequently coregistered to and then represented as a color overlay on a T1-weighted volumetric MR image in order to better localize the lesion. One study showed that the localization of epileptic foci is 88.2% for SISCOM but only 39.2% for side-by-side inspection of SPECT images [11]. Figure 3 shows the SPECT data, the processed difference image and the fused SISCOM images for a patient with TLE.
Using the information from SISCOM and/or video-EEG to further refine the epilepsy protocol can allow an experienced radiologist to detect focal cortical dysplasia in patients who were considered non-lesional on the standard epilepsy protocol [12]. While SISCOM can be a very useful technique, it is rather time and labor intensive as the injection must be performed promptly after the seizure for the technique to work properly. The seizure must also be of sufficient duration and of the type that typically occurs in that patient (video EEG is required to verify this).
For patients scheduled for TL resection, intracranial EEG recordings are performed in some cases in order to provide additional information of the location of the epileptogenic focus, or to better define functional cortex that needs to be spared. If lesions have been identified by structural MRI or an area of abnormal perfusion has been identified on the SISCOM study, the results of these studies are used to guide the grid placement. In our hospital, we used the Stealth station navigation system by Medtronic to guide the electrode grid placement. For the structural images, the procedure is straightforward. For the SISCOM images, the procedure is a little more involved and requires the following steps:

1) Register the differential SPECT image to the anatomical MRI.
2) Color code the differential image.
3) Fuse the color coded SISCOM to the MR image on the navigation system.

After grid placement, the patients are observed using continuous EEG video monitoring in order to detect seizures. Once a seizure is identified, the electrodes showing the strongest activity at the time of the seizure can be localized. In order to identify the spatial location of these electrodes a CT scan of the electrode grid is obtained, preferably performed immediately post-surgery in order to minimize the swelling caused by post-surgical edema. Co-registering of the CT scan to a structural MRI volume is performed using the fusion tool on the MultiModality Workplace (Leonardo). The neurologists and radiologists can then determine the spatial location of the electrodes closest to the source of the seizure activity. Figure 4 illustrates a case of CT grid and MRI co-registration.

Identification of laterality and functional cortex

Traditionally, a neuropsychological evaluation called the Wada test is performed to determine which side of the brain is responsible for certain vital cognitive functions, specifically language and memory. The Wada test consists of a standard neuropsychological assessment performed in conjunction with intracarotid injections of sodium amytal. The drug is injected into one hemisphere at a time inactivating language and/or memory function in that hemisphere in order to evaluate the contralateral hemisphere. The patient is engaged in a series of language and memory related tests during and after the Amytal effect. The results of the test are then used to estimate the potential functional effects of the surgery in language and memory, and help in planning the surgical approach. When localization of function to a particular area of the brain is required electro-cortical stimulation (ECS) was traditionally used. This test requires that electrodes are placed on the surface of the brain and direct stimulation of the electrodes on the exposed brain is then performed to map regionally specific function. As the patient has to interact with the surgeon for this test the actual mapping has to be performed under local, rather than general, anaesthetic.

Recently, fMRI has emerged as a non-invasive alternative method for lateralizing the language and motor networks, and to a lesser degree – memory, in cooperative children with epilepsy [13–15]. Brain mapping with fMRI has also revolutionized the evaluation of patients undergoing epilepsy surgery by providing a non-invasive method for identifying critical brain areas to spare during resection and offering a powerful tool for studying neural plasticity. There are numerous advantages of fMRI over other conventional modes in terms of language mapping: fMRI is non-invasive, does not carry the risk of either the WADA test or ECS, and different paradigms can be utilized to map different cognitive functions. Unlike the WADA test and ECS, fMRI can be readily repeated to confirm findings, and can both lateralize and localize different aspects of language functions. Correlation of fMRI results with those obtained using ECS show good, but not perfect, agreement. For language paradigms, when allowing for up to 10 mm between the activated areas using the two techniques, the sensitivity of fMRI to detect the language areas was between 67 and 100% depending on the paradigm [16]. It should be noted that the intrinsic resolution of fMRI studies is typically in excess of 3 mm and the smoothing used in the post-processing increases this to 5 mm or more.

For the pediatric population, impaired language is the most common adverse consequence of TL surgery. At our institution, language mapping is performed using one or more of three novel fMRI paradigms. The language paradigms were developed in conjunction with the Children's National Medical Center and are designed to target both expressive and receptive language processing. They were specifically developed for the assessment of the BOLD response in the language cortex of children and young adults under clinical conditions. Specifically, the following three tasks are employed, each using a block design:

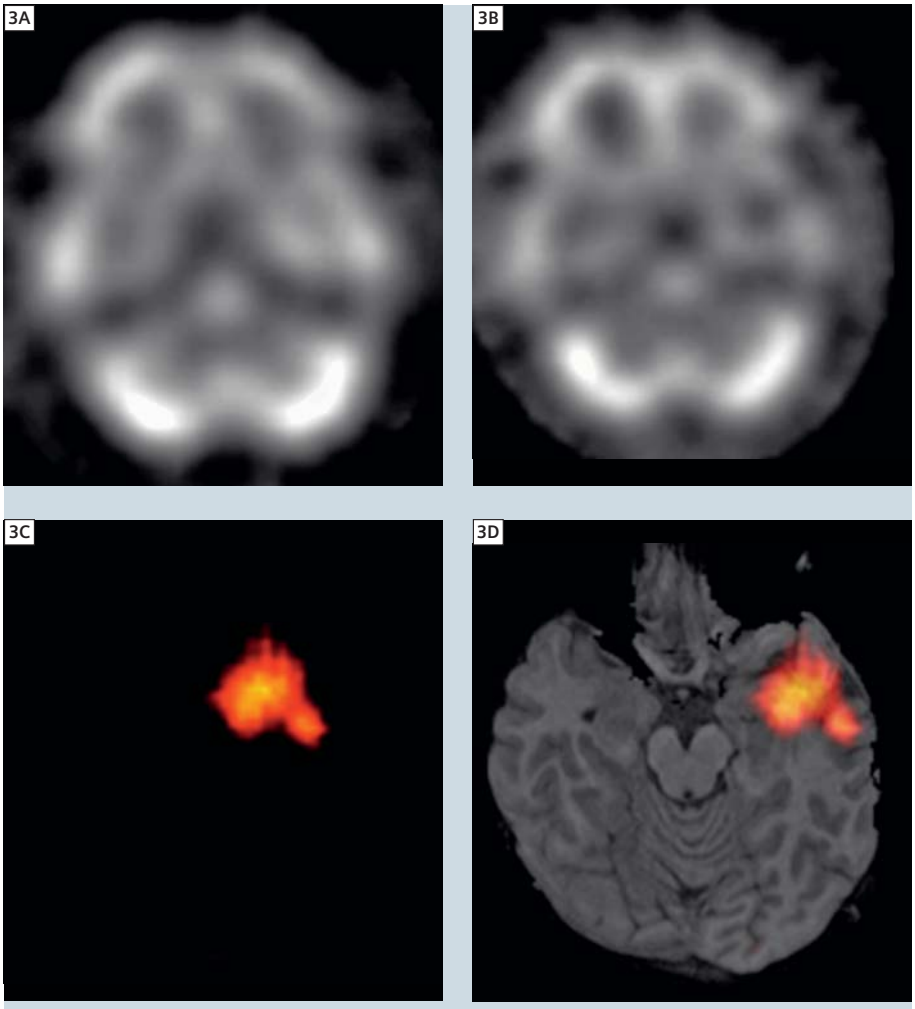

3 SISCOM result for a pediatric patient with TLE (**3A**). Ictal SPECT (**3B**). Interictal SPECT (**3C**). Differential SPECT and (**3D**) SISCOM result.

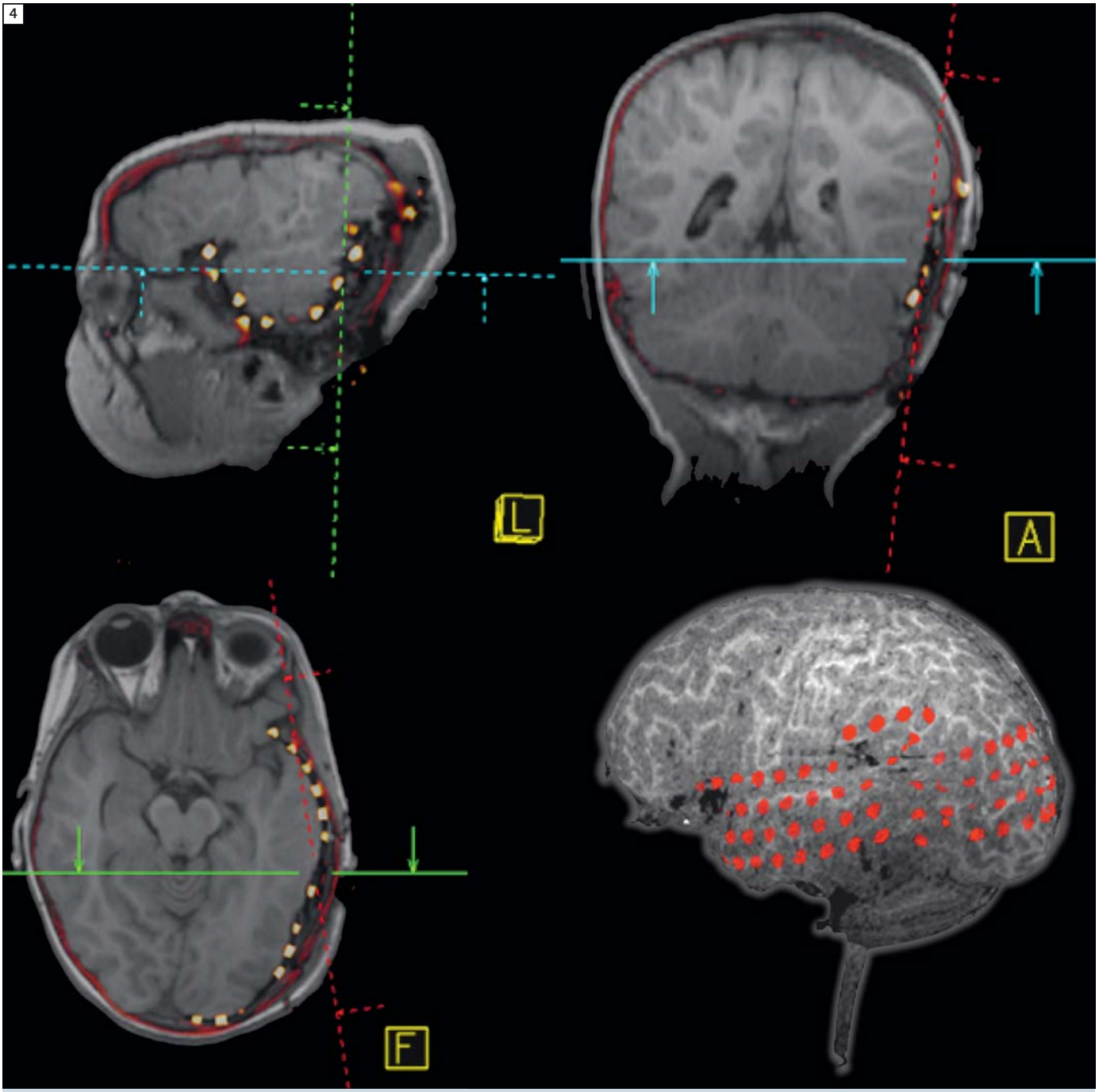

4 This case illustrates CT grid and MRI co-registration. Registration and initial visualization were achieved with 3D task card on a Siemens MultiModality Workplace (Leonardo). The electrodes can be seen as yellow/white area on the fused image due to their high intensity (i.e. high attenuation) on the CT images, areas of bone can be seen in red due to the relatively high attenuation of bone. The 3D representation was generated using in-house software which segments the CT scan to remove the bone and brain tissue and then provides an overview of the position of the grids on the surface of the brain.

5

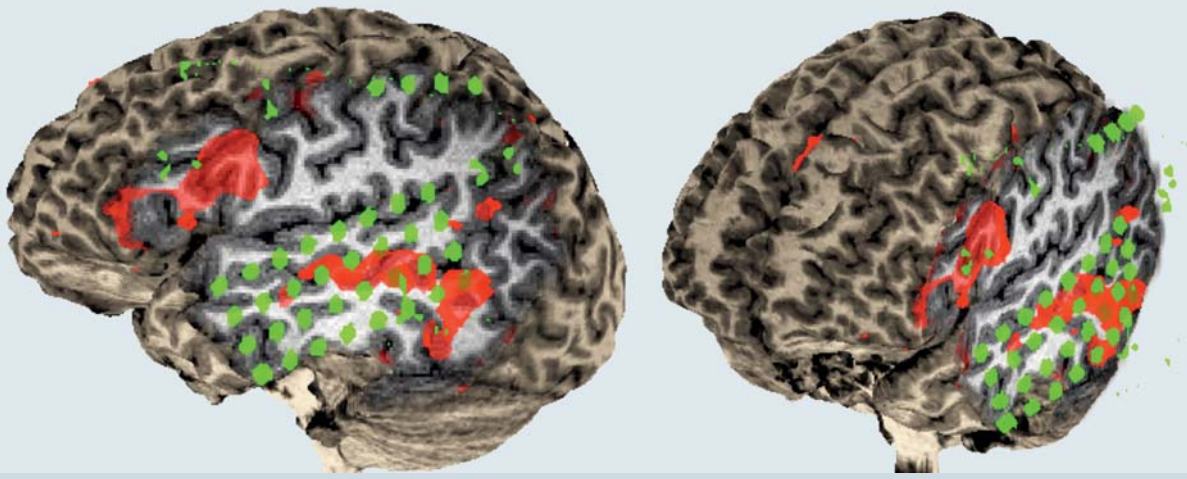

5 A case illustrating CT grid, fMRI (ADDT) activation and MRI co-registration. The CT electrodes are highlighted in green and the fMRI activations are rendered in red.

a) Auditory category decision task (AU CAT): A category is presented followed by a series of words. Participants are instructed to press a button if a word belongs to the specified category;
b) Auditory description decision task (ADDT): A description of an object is presented to the participants. The participants are required to press a button when the description is consistent with the matched object;
c) Listening to stories (Listening): Stories based on Gray Oral Reading Test are presented with pseudorandom inserted beeping sounds. Participants are instructed to press a button when a beep is heard while listening to the story. The participants are told that they will be questioned on the story after the scan in order to try and ensure that the participant pays attention to the story.
The rest condition for all three paradigms consists of reverse speech of the experimental condition with intermittent beeps as cues for button presses. All paradigms comprise five 30 second task blocks and five 30 second control (rest) blocks, resulting in a total duration of five minutes. Participants are instructed to press a single button for correct answers or upon hearing a beep (70% true and 30% false for task condition, matching number of button pushes for the corresponding control condition) during the course of the experiment. The responses are collected and inspected for the purposes of task monitoring and evaluation of response accuracy. The paradigms are also graded for skill and the appropriate version is selected for each participant based on his/her neuropsychological test score. All MRI scans are conducted on a Siemens 3T MAGNETOM Trio scanner equipped with 8-channel receive only head coil. A gradient echo EPI with TR = 3 sec and TE = 36 milliseconds and a nominal spatial resolution of 3.0 mm^3 is used for the fMRI studies. Oblique axial slicing is chosen for the fMRI acquisitions in order to increase coverage and reduce susceptibility effects. Inline fMRI analysis is done within the BOLD task card. Pediatric neuroradiologists and neuropsychologists use these results to determine the laterality of language and to locate the cortical regions implicated in language. The results are communicated to the neurosurgeons so that an optimized surgery plan can be developed. In some cases, the fMRI results along with CT grid and/or SISCOM results are all uploaded to the navigation system and used for realtime surgery guidance. For such purposes, the fMRI data is processed with FSL (www.fmrib.ox.ac.uk/fsl) and the statistical parametric maps are exported in DICOM format, which is required by our navigation system. Briefly, the fMRI data is pre-processed using the standard options and then analyzed using a general linear model, the resulting spatial statistical maps are then projected back to the corresponding anatomical MRIs and fed to the navigation software. Figure 5 shows a case where we simultaneously overlaid a CT grid scan (segmented to exclude brain tissue and bones) and the ADDT fMRI result on the anatomical MRI image. Diffusion tensor imaging (DTI) can also be used to map the major white matter pathways which project into the temporal lobe and this information can be used by the surgeons to try and spare these regions and hence preserve the communication with other regions of the brain. To achieve this goal,

white matter tracts connecting vital cortical regions (as identified by fMRI) are traced on DTI images, and those tracts are then uploaded onto the navigation system for surgical guidance. The DTI data is acquired axially using a 30 directions EPI sequence (b = 1000 sec/mm^2), 5 b = 0 scans, TR/TE = 8900/96 ms, a parallel imaging factor of 2 and a nominal spatial resolution of 2 mm^3. Our radiologists first review the DTI results produced by Neuro3D on the Siemens console and determine if DTI guidance is appropriate. If so whole brain tractography using the FACT algorithm is performed. The relevant fiber tracts are generated using the fMRI results as seed/target points. Binary masks are then created from the fiber tracts (voxels in the path of the tracts are assigned value 1 while others are assigned value 0). The resulting binary images are exported as DICOM images and sent to the navigation system (in a similar manner to the SISCOM and fMRI results) where they can be used to highlight the fiber tracts to be avoided during surgery.

These imaging techniques are now a routine part of the clinical workup for all of the epilepsy patients at our institution. They have greatly improved our ability to detect focal lesions, to minimize the detrimental effects of epilepsy surgery and to provide improved guidance to the neurosurgeon.

References

1 Tellez-Zenteno, J.F., et al., Surgical outcomes in lesional and non-lesional epilepsy: a systematic review and meta-analysis. Epilepsy Res, 2010. 89(2–3): p. 310-8.
2 Binder, J.R., et al., A comparison of two fMRI methods for predicting verbal memory decline after left temporal lobectomy: language lateralization versus hippocampal activation asymmetry. Epilepsia, 2010. 51(4): p. 618-26.
3 Helmstaedter, C. and C.E. Elger, Cognitive consequences of two-thirds anterior temporal lobectomy on verbal memory in 144 patients: a three-month follow-up study. Epilepsia, 1996. 37(2): p. 171-80.
4 Ojemann, G.A. and C.B. Dodrill, Verbal memory deficits after left temporal lobectomy for epilepsy. Mechanism and intraoperative prediction. J. Neurosurg, 1985. 62(1): p. 101-7.
5 Westerveld, M., et al., Temporal lobectomy in children: cognitive outcome. J Neurosurg, 2000. 92(1): p. 24-30.
6 Von Oertzen, J., et al., Standard magnetic resonance imaging is inadequate for patients with refractory focal epilepsy. J Neurol Neurosurg Psychiatry, 2002. 73(6): p. 643-7.
7 Knake, S., et al., 3T phased array MRI improves the presurgical evaluation in focal epilepsies: a prospective study. Neurology, 2005. 65(7): p. 1026-31.
8 Wehner, T., et al., The value of interictal diffusion-weighted imaging in lateralizing temporal lobe epilepsy. Neurology, 2007. 68(2): p. 122-7.
9 Widjaja, E., et al., Subcortical alterations in tissue microstructure adjacent to focal cortical dysplasia: detection at diffusion-tensor MR imaging by using magnetoencephalographic dipole cluster localization. Radiology, 2009. 251(1): p. 206-15.
10 Nehlig, A., et al., Ictal and interictal perfusion variations measured by SISCOM analysis in typical childhood absence seizures. Epileptic Disord, 2004. 6(4): p. 247-53.
11 O'Brien, T.J., et al., Subtraction ictal SPECT co-registered to MRI improves clinical usefulness of SPECT in localizing the surgical seizure focus. Neurology, 1998. 50(2): p. 445-54.
12 Ruggieri, P.M., et al., Neuroimaging of the cortical dysplasias. Neurology, 2004. 62(6 Suppl 3): p. S27-9.
13 Binder, J.R., et al., Determination of language dominance using functional MRI: a comparison with the Wada test. Neurology, 1996. 46(4): p. 978-84.
14 Gaillard, W.D., C.B. Grandin, and B. Xu, Developmental aspects of pediatric fMRI: considerations for image acquisition, analysis, and interpretation. Neuroimage, 2001. 13(2): p. 239-49.
15 Saykin, A.J., et al., Language before and after temporal lobectomy: specificity of acute changes and relation to early risk factors. Epilepsia, 1995. 36(11): p. 1071-7.
16 FitzGerald, D.B., et al., Location of language in the cortex: a comparison between functional MR imaging and electrocortical stimulation. AJNR Am J Neuroradiol, 1997. 18(8): p. 1529-39.

Contact
Richard A. Jones
Department of Radiology
Children's Healthcare of Atlanta
1001 Johnson Ferry Road
Atlanta, GA 30342
USA
Richard.Jones@choa.org

*MR scanning has not been established as safe for imaging fetuses and infants under two years of age. The responsible physician must evaluate the benefit of the MRI examination in comparison to other imaging procedures.

Try them on your system

Trial licenses for most of the applications featured in this issue of MAGNETOM Flash are available free of charge for a period of 90 days: Please contact your local Siemens representative for system requirements and ordering details or visit us online* at **www.siemens.com/discoverMR** for further details, product overviews, image galleries, step-by-step videos, case studies and general requirement information.

1

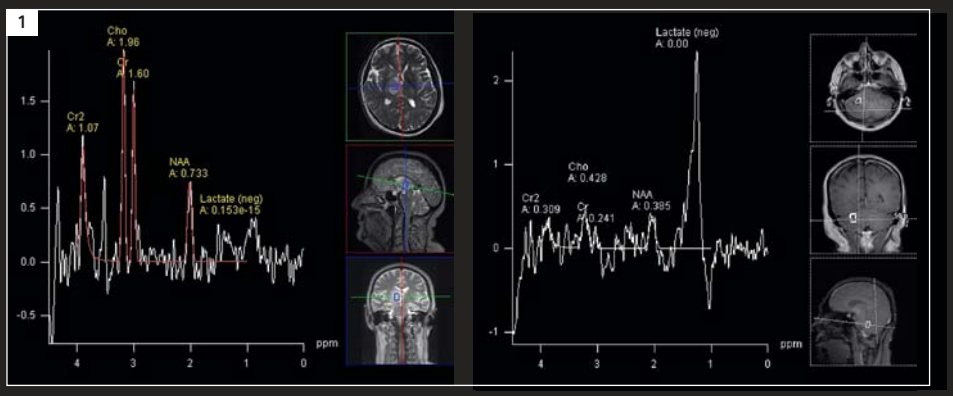

1 Multi-voxel MR Spectroscopy, page 6.

2

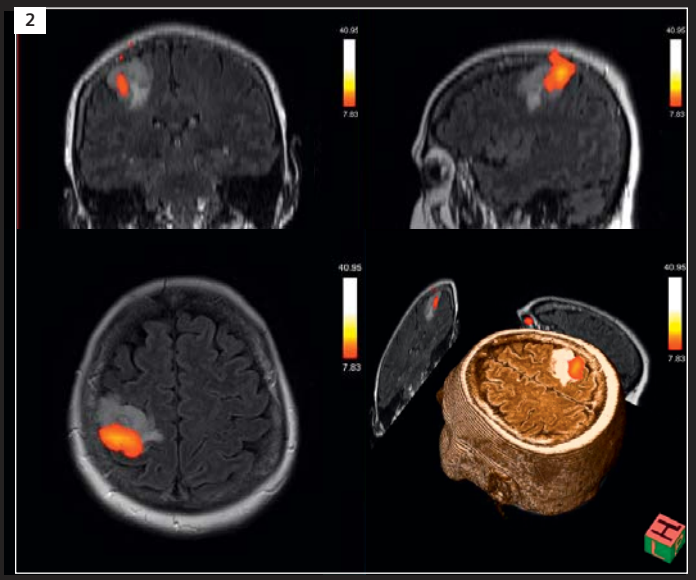

2 Functional MR imaging (*syngo* BOLD) and Diffusion Tensor Imaging (*syngo* DTI), page 14.

3

3 Networked Scanner: Simultaneously work with MAGNETOM Skyra/Aera and *syngo*.via on two screens, page 124.

4

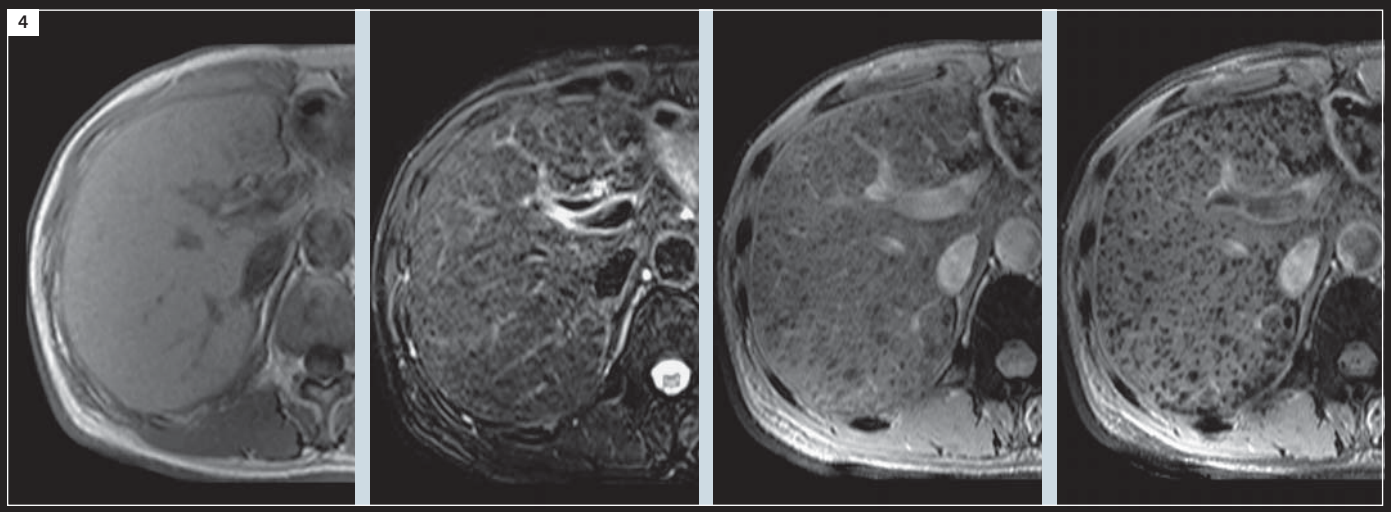

4 Susceptibility-weighted imaging (*syngo* SWI), page 84.

*Direct link for US customers: **www.siemens.com/WebShop**
Direct link for UK customers: **www.siemens.co.uk/mrwebshop**

High-Resolution 3T MR Neurography of the Lumbosacral Plexus

Avneesh Chhabra, M.D.; Aaron Flammang, MBA, BS; John A. Carrino, M.D., M.P.H.

Russell H. Morgan Department of Radiology and Radiological Science, Johns Hopkins Medical Institutions, Baltimore, MD, USA

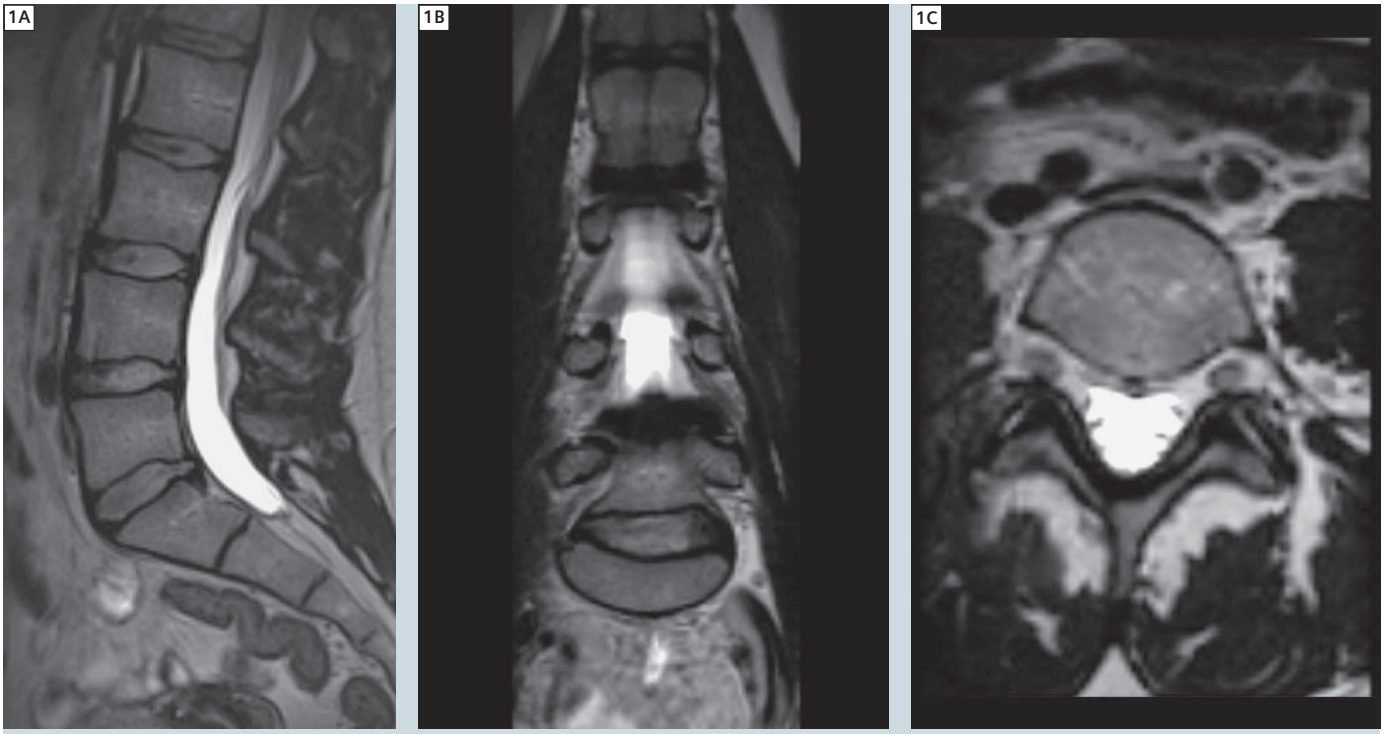

1A–C Lumbosacral Plexus 3T MR Neurography evaluation: Isotropic multiplanar reformats from 3D T2 SPACE **(1A–1C)**.

Abstract

The lumbosacral (LS) plexus is a series of nerve convergences and ramifications that provide motor and sensor innervation to pelvis and lower extremities. LS plexopathy is a serious condition caused by a variety of pathologies. Magnetic Resonance Neurography is an important modality for evaluation of LS plexopathy due to variable clinical presentations and deep location leading to suboptimal accessibility of the plexus to electrodiagnostic studies. This article describes the role of MR Neurography in evaluation of the LS plexus and illustrates the spectrum of pathologies along with their respective imaging findings using 3 Tesla MR Neurography.

Introduction

The lumbosacral (LS) plexus is comprised of an intricate architecture of nerves that supply the pelvis and lower extremity. It can be subject to a variety of pathologies, which may result in LS plexopathy, a clinical syndrome that includes motor and sensory disturbances. The diagnosis of LS plexopathy has traditionally relied on clinical findings and electrodiagnostic study results. However, differentiation of LS plexopathy from spine related abnormality and definition to type, location and extent of pathology often remains a diagnostic challenge due to deep location of the nerves and variable regional muscle innervation [1, 2]. With current high resolution 3 Tesla (T) Magnetic Resonance Neurography (MRN) techniques, diagnostic evaluation of large LS plexus branches, such as sciatic and femoral nerves, as well as smaller segments, such as nerve roots convergences and

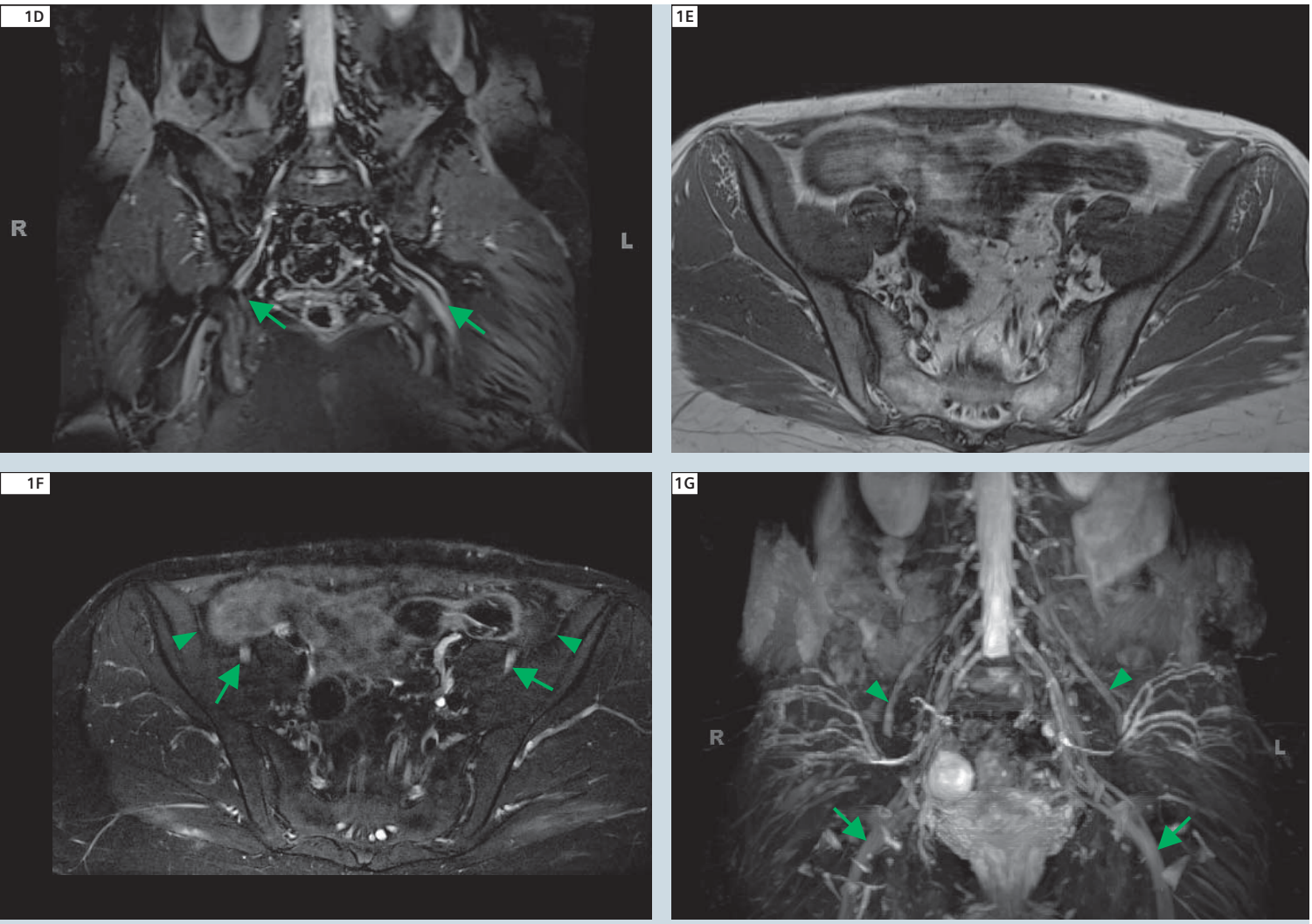

1D–G Coronal reconstructed 3D STIR SPACE **(1D)** showing sciatic nerves (arrows). Axial T1w **(1E)** and T2 SPAIR **(1F)** images showing bilateral femoral nerves (arrows) and lateral femoral cutaneous nerves (arrowheads). MIP coronal 3D STIR SPACE **(1G)** image showing bilateral LS plexus nerve roots, femoral nerves (arrowheads) and sciatic nerves (arrows).

peripheral nerves is feasible, aiding in pre-surgical evaluation and appropriate patient management [3, 4]. This article provides a pertinent discussion of the LS plexus anatomy, current role of MRN in evaluation of plexopathy and describes the respective imaging findings of various pathologies using 3T MR Neurography.

Anatomic considerations

The LS plexus is comprised of lumbar plexus, sacral plexus and the pudendal plexus, with contributions from the ventral rami of lumbar (L1–4 +/– T12), sacral (S1–4 and LS trunk, L4–S1) and the lower sacrococcygeal (S2–4 and C1) nerves, respectively [5]. The plexus is formed lateral to the intervertebral foramina and various branches course through the psoas major muscle. The ventral rami are further split into anterior and posterior divisions. The anterior divisions give rise to the iliohypogastric (L1), ilioinguinal (L1), genitofemoral (L1-L2) and obturator nerves (L2–4). The posterior divisions combine to form the posterior branches [femoral (L2–4) and lateral femoral cutaneous nerves (L2, 3)]. All branches exit lateral to the psoas muscle and course under the inguinal ligament, except the obturator nerve and LS trunk, which exit medial to the psoas muscle. The sacral plexus gives rise to anterior branches, namely the tibial part of the sciatic nerve (L4–S3), pudendal nerve (S1–4) and medial part of the posterior femoral cutaneous nerve (S1–3) and, posterior branches, namely the common peroneal part of the sciatic nerve (L4–S2), superior (L4–S1) and inferior gluteal nerves (L5–S2),

Table 1: S The 3T MR imaging protocol employed in our institution of the evaluation of the lumbosacral plexus.

Sequence	Slice	Field-of-view (cm)	Voxel size (mm^3)	TR/TE (ms)	Turbo factor
Axial T1 TSE	BL	33	0.64	800/12	6
Axial T2 SPAIR	BL	33	1.00	4500/80	17
Coronal PD SPAIR	BL	36-38	0.6	4980/38	7
Coronal T1 TSE	BL	36-38	0.5	550/10	3
3D Coronal STIR SPACE	BL	36-38	1.45	1500/103	61
3D Sagittal T2 SPACE	Lumbar spine	28	1.45	1000/99	69
Coronal 3D VIBE *	BL	36-38	0.58	4.39/2.01	–

Abbreviations are: TSE = Turbo Spin Echo, SPAIR = spectral adiabatic inversion recovery, STIR = short tau inversion recovery, 3D SPACE = three-dimensional Sampling Perfection with Application optimized Contrasts using constantly varying flip angle Evolutions, VIBE = Volume Interpolated Breathhold Exam (* optional), BL = bilateral

lateral part of the posterior femoral cutaneous nerve (S1–3) and the nerve to the piriformis muscle (L5, S2). The above two plexuses connect via the LS trunk to form the LS plexus [2, 5].

Pathologic conditions and indications of MRN

The LS plexus is relatively protected by the axial skeleton and entrapment neuropathy is much less common than brachial plexopathy. It is considered as the counterpart of the brachial plexus in the lower body and is affected by similar types of diseases. The LS plexus may be involved by local processes in the viscinity of the plexus, such as extrinsic compression by space occupying lesions, injury or infiltration by tumor / infectious process – which is an indication for MRN; or in systemic conditions, such as metabolic, autoimmune, vasculitis, ischemic or inflammatory disorders – which are usually diagnosed based on clinical and laboratory findings. MRN may be used in the latter case to confirm lumbar plexitis / plexopathy in clinically confusing presentation and underlying known systemic condition. In addition, a primary or idiopathic form of LS plexopathy may occur, possibly due to altered immunological response and is considered analogous to idiopathic brachial plexopathy [6–8]. The entity has a favorable outcome and spontaneous recovery, whereas its diagnosis is based upon exclusion of other etiologies and sometimes may require confirmation with MRN in case of indeterminate electrodiagnostic results. An important indication of MRN is in patients under consideration for surgery for peripheral nerve lesions (piriformis syndrome/meralgia paresthetica), post abdominal surgery entrapment of ilioinguinal/genitofemoral nerves, or after injury to a large branch (sciatic, femoral, obturator). Finally, MRN is increasingly used for guidance during perineural and intramuscular medication injection.

Clinical findings

LS plexopathy most often presents with asymmetric weakness, pain and/or paresthesias in the lower extremities involving multiple contiguous LS nerve root distributions. Generally, unilateral localization of symptoms indicates a local pathology, whereas bilateral symptoms suggest a systemic process. The clinical picture often varies depending upon the location and degree of plexus involvement. In cases of involvement of the upper nerve roots, patients predominantly present with femoral and obturator nerve symptoms. LS trunk and upper sacral plexus lesions result in foot drop depending on the extent of involvement and weakness of knee flexion or hip abduction. Sensory symptoms may vary based on the individual nerves involved, which may include numbness or

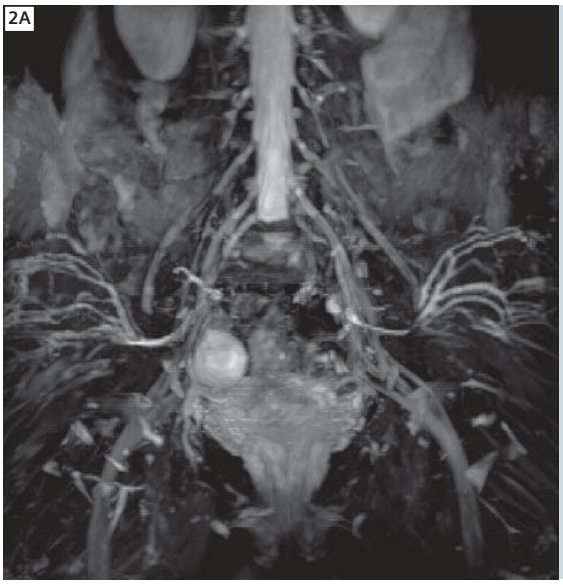

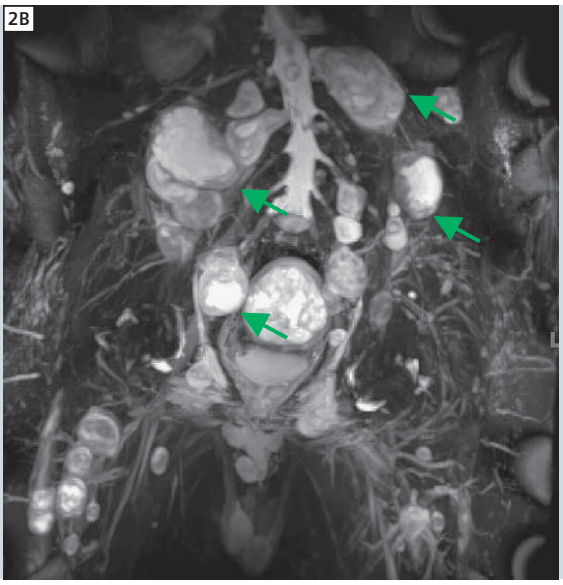

2 Normal vs abnormal LS Plexus. Coronal MIP 3D STIR SPACE images in a normal subject **(2A)** and another subject with schwannomatosis (arrows in **2B**).

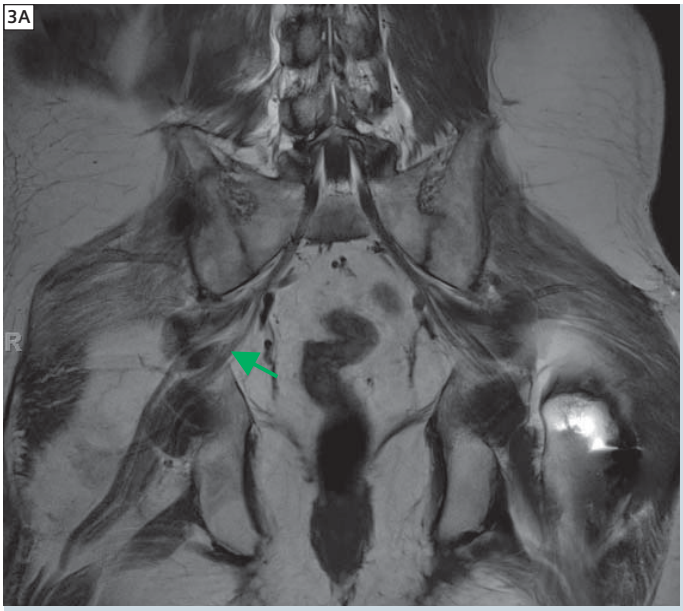

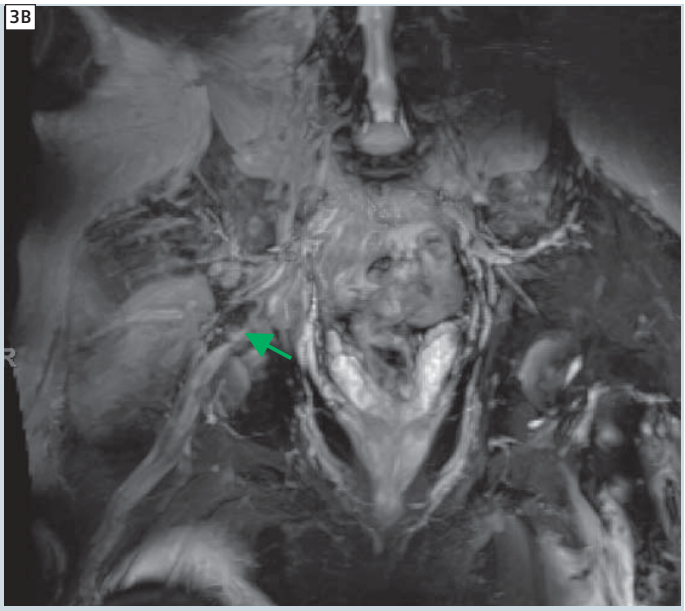

3 Piriformis syndrome – large LS plexus branch nerve abnormality. 33-year-old man with right buttock and pelvic pain, suspected piriformis syndrome. Coronal T1w **(3A)** and coronal MIP 3D STIR SPACE **(3B)** images through the pelvis show split right sciatic nerve by an accessory slip of the right piriformis muscle (arrow). Notice abnormal T2 hyperintensity of the sciatic nerve in keeping with entrapment neuropathy.

dysesthesia in the anterolateral thigh from lateral femoral cutaneous nerve involvement; in the mons and labia majora from genitofemoral nerve involvement and in the lower abdomen and inguinal area, upper medial thigh or pelvis from damage to the ilioinguinal, iliohypogastric, or pudendal nerves, respectively. Rarely, there may be associated bowel and bladder incontinence as well as sexual dysfunction [6–8].

MRN technique and normal appearances

Compared to 1.5T systems 3 Tesla (MAGNETOM Verio and MAGNETOM Trio, Siemens, Erlangen, Germany) imaging is preferred for most MRN examinations by the authors due to high quality scans obtained by these systems due to better signal-to-noise ratio and contrast resolution available in short imaging times. Due to the relatively small nerve structures under interrogation, it is essential to use high resolution imaging with a combination of 2D (dimensional) and 3D isotropic spin echo type imaging for optimal assessment. In the presence of known metal* in the area of imaging, 1.5T imaging is preferred. Table 1 and Fig. 1 show the 3T MRN imaging protocol employed at Johns Hopkins for the evaluation of the LS plexus. For fascicular architecture and subtle signal intensity

changes, high-resolution 2D axial T1w and T2 SPAIR (Spectral Adiabatic Inversion Recovery) images are ideal. Fascicular appearance of nerves is consistently seen with T2 SPAIR images in larger branches, such as femoral nerves and sciatic nerves, as well as in smaller nerves that are affected and enlarged due to neuropathy, such as lateral femoral cutaneous and genitofemoral nerves. 2D imaging is complemented by isotropic 3D images reconstructed in planes perpendicular and longitudinal to the nerves in question. 3D imaging (SPACE – Sampling Perfection with Application optimized Contrasts using constantly varying flip angle Evolutions) allows multiplanar and curved planar reformations. Two types of 3D imaging are performed, focusing in two different locations with two different purposes, 3D STIR SPACE for the LS plexus (from L2-3 level to lesser trochanter of femurs), while T2 SPACE (from L2-S2) is used for the lumbar spine, as spondylosis is a major confounder in the diagnosis of peripheral nerve pathology (Fig. 1). 3D imaging shows the lesions along the long axis of the nerve, course deviations, focal neuroma, nerve gap in cases of injury, etc. for better pre-operative planning and understanding of the referring physicians. Side-side imaging differences of the nerves can also be highlighted on maximum intensity projection (MIP) images. Gadolinium administration is reserved for cases of suspected neoplasm, inflammation, diffuse polyneuropathy, neurocutaneous syndrome, or post-operative complication [9–13]. Additional coronal T1w and STIR/PD SPAIR images aid in detection of lesions along the long axis of the nerves, side-to-side comparison of the nerve morphology and signal intensity (generally symmetrical), as well as for depiction of other incidental findings in relation to hips or spine. SPAIR produces higher SNR and is less prone to pulsation artifacts than STIR imaging, and is also more SAR favorable at 3T imaging [3, 4].

MR Neurography findings of LS plexopathy

MRN assessment of the LS plexus relies on the evaluation of direct morphologic features, such as altered nerve size, abnormal fascicular morphology (disrupted, effaced or enlarged) and focal or diffuse deviations in nerve course. T2 signal intensity (SI) changes (signal alterations approaching the adjacent vascular signal intensity, or asymmetric SI to the other side, given variations due to non-uniform fat saturation); as well as indirect features such as effacement of perineural fat planes due to focal fibrosis/mass lesions (Figs. 2, 3) and regional muscle denervation changes (edema like T2 signal alteration in acute and subacute cases to fatty replacement and atrophy in chronic cases). MRN is useful for detecting the individual segmental nerve abnormalities (enlarged or asymmetrically T2 hyperintense) in cases of plexitis/plexopathy or nerve injury. Similar to brachial plexus imaging, minimal increased nerve T2 signal intensity alone should be perceived with caution, as magic-angle artifact is a well-recognized artifact in LS plexus MR imaging [3, 4]. MRN is also useful in differentiating the plexopathy (nerve abnormality starting distal to the neural foramina, and often involving multiple nerve roots) from lumbar spondylosis (presence of substantial spondylosis, disc herniations, intraspinal mass, and nerve abnormality starting from within and immediately distal to the neural foraminal level in a distribution of the narrowed foramina). It is also worth mentioning that MRN may help exclude LS plexopathy in clinically confusing cases by demonstrating normal symmetrical appearance of bilateral nerve segments. In trauma cases, it is critical to demonstrate whether the injury is merely a stretch injury (merely T2 signal alterations) with nerve continuity; or if there is neuroma formation (focal enlargement of the nerve with effaced fascicular appearance) or nerve root avulsion or nerve discontinuity, which may be indications for surgery (Fig. 4). Peripheral nerve sheath tumors are depicted as focal or fusiform enlargements of the nerves, and may variably demonstrate classic signs, such as the tail, target, fascicular, bag of worms and split-fat signs. Differentiation between benign and malignant peripheral nerve sheath tumors is generally not reliable by imaging, although large size, ill-defined margins, peritumoral edema, significant interval growth and internal heterogeneity,

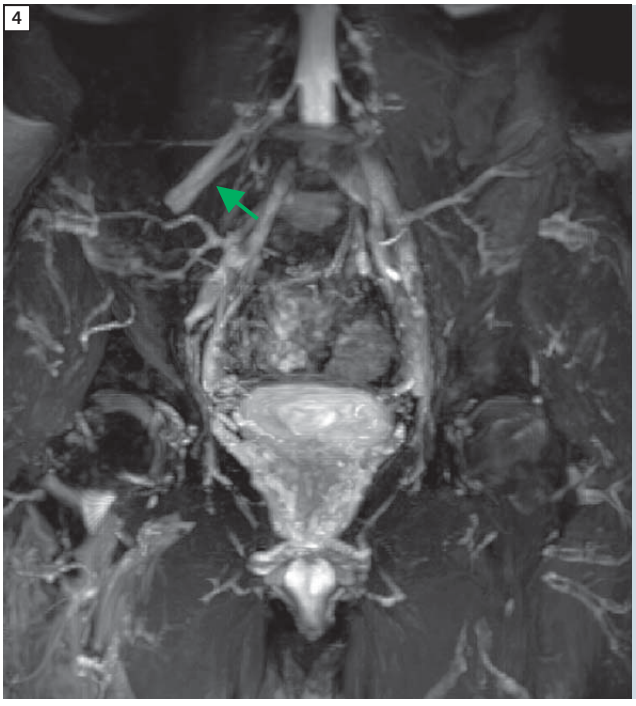

4 Right femoral nerve transection – large LS plexus branch nerve abnormality. 64-year-old man with right leg weakness following recent surgery. Coronal MIP 3D STIR SPACE image through the pelvis shows abrupt termination of the right femoral nerve in keeping with transection (arrow) (Sunderland Grade V injury).

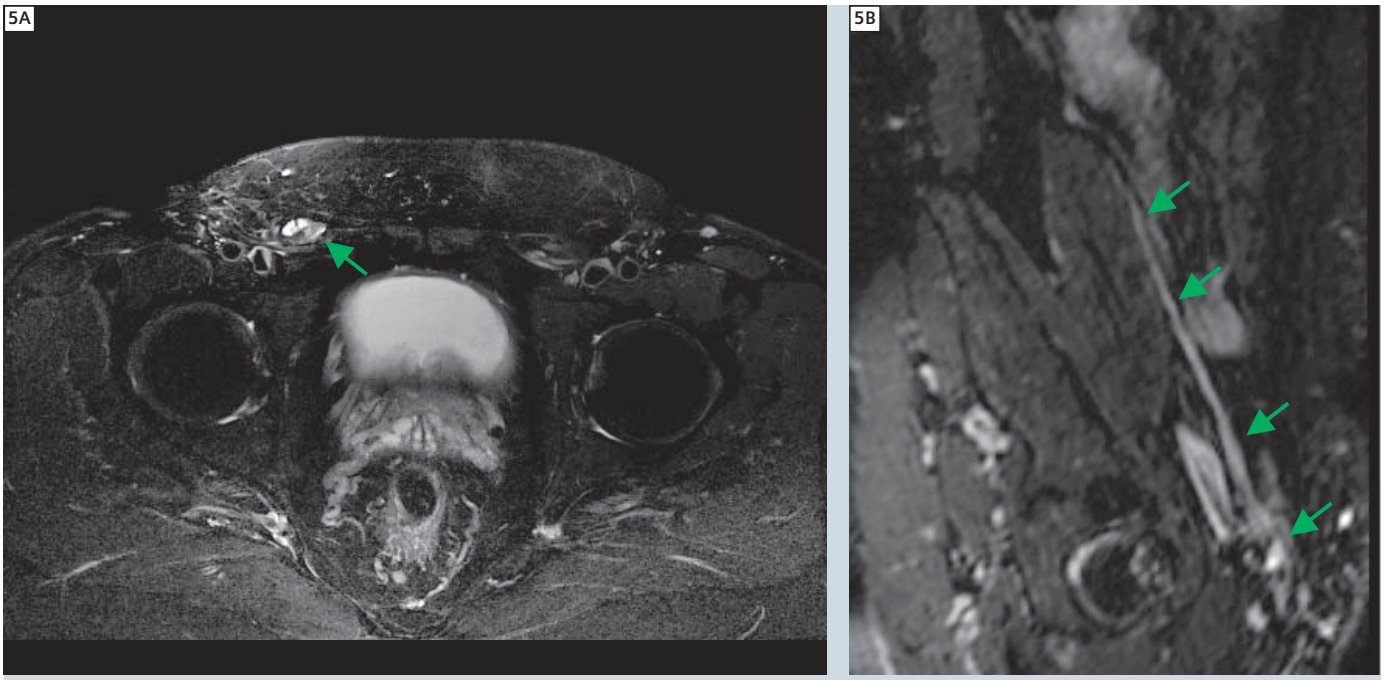

5 Genitofemoral nerve entrapment – small LS plexus branch nerve abnormality. 50-year-old man with right inguinal and scrotal pain, following a prior right inguinal hernia repair. Axial T2 SPAIR **(5A)** and oblique coronal MIP 3D STIR SPACE **(5B)** images through the pelvis show abnormally enlarged and hyperintense right genitofemoral nerve (arrows), with most abnormality at the site of previous hernia repair in keeping with entrapment neuropathy.

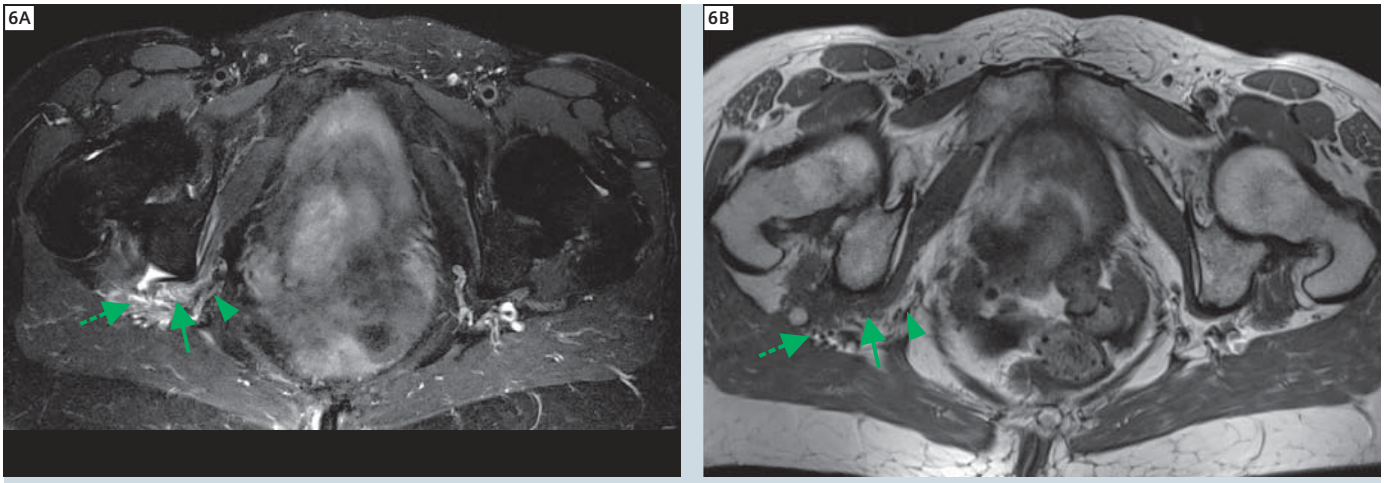

6 Right pudendal and sciatic Neuropathy – small LS plexus branch nerve abnormality. 61-year-old man with right pelvic pain, suspected pudendal neuralgia. Axial T2 SPAIR image through the pelvis shows grade I/II strain of the right obturator internus muscle (large arrow) with mild hyperintensity of the right pudendal nerve (small arrow) and right sciatic nerve (dotted arrows) in keeping with acute neuropathy.

especially in neurofibromas, are suspicious for malignancy. In those cases, a combination of clinical (new onset or increasing pain/ neurological deficit), MRN imaging findings (as above), as well as ^{18}F FDG PET uptake (SUV_{max} >3–4 and increased uptake on delayed imaging) are used to make a clinical decision about percutaneous biopsy/surgical biopsy/ resection. Finally, MRN aids in differentiation of radiation neuropathy (diffuse nerve signal intensity alterations and enhancement in a geographic distribution corresponding to the radiation field) from recurrent mass lesion (focal enhancing lesions) [11–14].

Lumbosacral plexus branch anatomy and pathology

Current high-resolution 3T techniques allow depiction of internal nerve pathology of normal sized large branches, such as sciatic (Fig. 3), obturator, femoral (Fig. 4), various lumbosacral nerve roots as well as enlarged smaller branches,

such as ilioinguinal, genitofemoral (Fig. 5) and pudendal (Figs. 6, 7) nerves. Many of the smaller nerves are sensory nerves, and electrodiagnostic studies are usually not useful for their assessment. Nerve blocks have also been variably used, more so for therapeutic effect rather than for diagnosis of pathology. MRN may detect lesions within (diffuse enlargement proximal to entrapment, neuroma, etc.) or surrounding these nerves (focal fibrosis/mass lesion), thereby impacting patient management. Iatrogenic insults, such as during laparotomy, lymph node dissection, difficult parturition, hernia repair, etc are the leading cause of injury to these fine nerves. MRN may be used to detect focal fibrosis along the course of these nerves and their branches, which may be used to guide neurolysis. Such a procedure may give back patients' necessary sensation or provide pain relief. Finally, MRN may be used to provide guidance for perineural (local anesthetic and steroids) and intramuscular medication (e.g. Botulinium Toxin) injections. It is important to know that an appropriately performed image guided negative block / placebo controlled or graded positive nerve block confers more specificity to the diagnosis rather than a single positive block. Few studies have however, shown the therapeutic value of these blocks [15–22].

Conclusion

In the evaluation of LS plexopathy, 3T MRN provides high quality imaging and is a valuable adjunct to clinical examination and electrodiagnostic tests as it can offer anatomic information and lesion assessment otherwise unattainable by other modalities.

Contact
Avneesh Chhabra, M.D., DNB
Assistant Professor Radiology & orthopedic Surgery
Russell H. Morgan Department of Radiology and Radiological Science
Johns Hopkins Medical Institutions
achhabr6@jhmi.edu

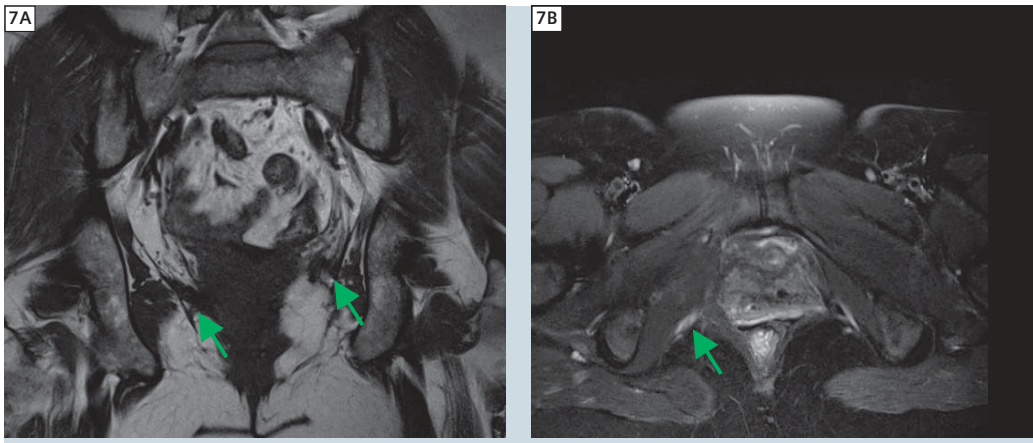

7 Chronic pudendal Neuralgia – small LS plexus branch nerve abnormality. 41-year-old woman with pelvic pain, right > left for many months. Coronal T1w **(7A)** and axial T2 SPAIR **(7B)** images through the pelvis show bilateral pelvic scarring (right > left), along the expected course of the pudendal nerves, causing entrapment (arrows). Notice asymmetrically prominent right pudendal neurovascular bundle (arrow).

*In the US, metal near or in the MR system must be labeled as MR-safe or conditional (with conditions stated).

References

1 Gebarski KS, Gebarski SS, Glazer GM, Samuels BI, Francis IR. The lumbosacral plexus: anatomic-radiologic-pathologic correlation using CT. Radiographics. 1986;6(3):401-25.
2 Petchprapa CN, Rosenberg ZS, Sconfienza LM, Cavalcanti CF, Vieira RL, Zember JS. MR imaging of entrapment neuropathies of the lower extremity. Part 1. The pelvis and hip. Radiographics. 2010;30(4):983-1000.
3 Chhabra A, Lee PP, Bizzell C, Soldatos T. 3 Tesla MR neurography-technique, interpretation, and pitfalls. Skeletal Radiol. 2011 May 6. [Epub ahead of print].
4 Chhabra A, Andreisek G, Soldatos T, Wang KC, Flammang AJ, Belzberg AJ, Carrino JA. MR Neurography: Past, Present, and Future. AJR Am J Roentgenol. 2011 Sep;197(3):583-91.
5 Kirchmair L, Lirk P, Colvin J, Mitterschiffthaler G, Moriggl B. Lumbar plexus and psoas major muscle: not always as expected. Reg Anesth Pain Med. 2008;33(2):109-14.
6 Evans BA, Stevens JC, Dyck PJ. Lumbosacral plexus neuropathy. Neurology. 1981;31(10):1327-30.
7 Sander JE, Sharp FR. Lumbosacral plexus neuritis. Neurology. 1981;31(4):470-3.
8 Hollinger P, Sturzenegger M. Chronic progressive primary lumbosacral plexus neuritis: MRI findings and response to immunoglobulin therapy. J Neurol. 2000;247(2):143-5.
9 Maravilla KR, Bowen BC. Imaging of the peripheral nervous system: evaluation of peripheral neuropathy and plexopathy. AJNR Am J Neuroradiol. 1998;19(6):1011-23.
10 Thawait SK, Chaudhry V, Thawait GK, Wang KC, Belzberg A, Carrino JA, Chhabra A. High-Resolution MR Neurography of Diffuse Peripheral Nerve Lesions. AJNR Am J Neuroradiol. 2010 Nov 24. [Epub ahead of print].
11 Chhabra A, Williams EH, Wang KC, Dellon AL, Carrino JA. MR neurography of neuromas related to nerve injury and entrapment with surgical correlation. AJNR Am J Neuroradiol. 2010 Sep; 31(8):1363-8. Epub 2010 Feb 4.
12 Chhabra A, Soldatos T, Durand D, Carrino JA, McCarthy EF, Belzberg AJ. The role of MRI in the diagnostic evaluation of malignant peripheral nerve sheath tumors. Indian J Cancer. 2011: (in press).
13 Taylor BV, Kimmel DW, Krecke KN, Cascino TL. Magnetic resonance imaging in cancer-related lumbosacral plexopathy. Mayo Clin Proc. 1997;72(9):823-9.
14 Whiteside JL, Barber MD, Walters MD, Falcone T. Anatomy of ilioinguinal and iliohypogastric nerves in relation to trocar placement and low transverse incisions. Am J Obstet Gynecol. 2003;189(6): 1574-8; discussion 8.
15 Klaassen Z, Marshall E, Tubbs RS, Louis RG, Jr., Wartmann CT, Loukas M. Anatomy of the ilioinguinal and iliohypogastric nerves with observations of their spinal nerve contributions. Clin Anat. 2011;24(4):454-61.
16 Hu P, Harmon D, Frizelle H. Ultrasound guidance for ilioinguinal/iliohypogastric nerve block: a pilot study. Ir J Med Sci. 2007;176(2):111-5.
17 Tipton JS. Obturator neuropathy. Curr Rev Musculoskelet Med. 2008;1(3-4):234-7.
18 Beltran LS, Bencardino J, Ghazikhanian V, Beltran J. Entrapment neuropathies III: lower limb. Semin Musculoskelet Radiol. 2010;14(5):501-11.
19 Patijn J, Mekhail N, Hayek S, Lataster A, van Kleef M, Van Zundert J. Meralgia Paresthetica. Pain Pract. 2011;11(3):302-8.
20 Chhabra A, Gustav A, Soldatos T, Wang KC, Belzeberg AJ, Carrino JA. 3T hihg-resolution MR Neurography of sciatic neuropathy. AJR 2011 (in press).

3T MR Imaging of Cartilage using 3D Dual Echo Steady State (DESS)

Rashmi S. Thakkar, M.D.[1]; Aaron J Flammang, MBA-BSRT (R) (MR)[2]; Avneesh Chhabra, M.D.[1]; Abraham Padua, RT (R)[3]; John A. Carrino, M.D., M.P.H.[1]

[1]Johns Hopkins University School of Medicine, Russell H. Morgan Department of Radiology and Radiological Science, Baltimore, MD, USA
[2]Siemens Corporate Research (CAMI), Baltimore, MD, USA
[3]Siemens Healthcare, Malvern, PA, USA

Introduction

Magnetic resonance imaging (MRI), with its excellent soft tissue contrast is currently the best imaging technique available for the assessment of articular cartilage [1]. In the detection of cartilage defects, three-dimensional (3D) MRI is particularly useful because cartilage is a thin sheet wrapped around complex anatomical structure. Isotropic, high resolution voxels enable reformatting of images into more convenient planes for viewing.

An MRI technique specifically for imaging cartilage should be able to accurately assess cartilage thickness and volume, depict morphological changes and show subtleties within the cartilage while minimizing artifactual signal alterations. In addition, it is necessary to evaluate subchondral bone for abnormalities. 3T MR scanners with multichannel dedicated coils allow to obtain image data with high resolution as well as sufficient signal-to-noise ratio (SNR) and contrast-to-noise ratio (CNR) [2]. Conventional spin echo and turbo spin echo sequences (T1, T2, and PD with or without fat suppression) as well as gradient echo techniques (incoherent GRE sequence, such as FLASH and coherent or steady state sequence, such as DESS) have been used for many years in cartilage imaging. Spin echo based approaches have clearly dominated due mostly to efficiency with respect to scan time.

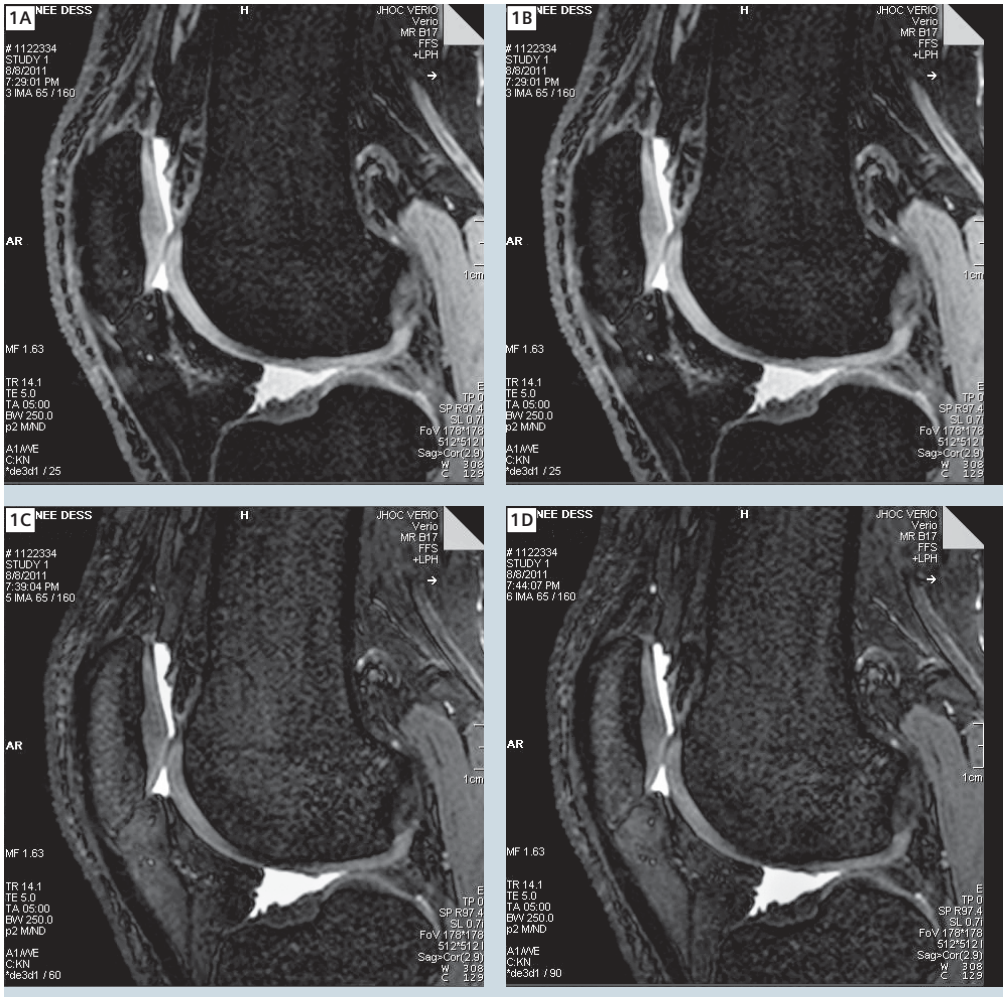

1 Sagittal water selective 3D DESS imaging of the knee (TR/TE 14.1/5 ms) at various flip angles (1A = 25°, 1B = 45°, 1C = 60°, 1D = 90°). With the flip angle of 60° there is highest signal intensity of synovial fluid with highest contrast-to-noise ratio of the cartilage.

In this article, we would like to describe the use of Dual Echo Steady State (DESS) in imaging of the articular cartilage on the Siemens MAGNETOM Verio.

DESS

Dual Echo Steady State (DESS) is a 3D coherent (steady state) GRE sequence. Steady state sequences (FISP, TrueFISP, DESS, PSIF, CISS) have two major characteristics. First, TR is too short for transverse magnetization to decay before the next RF pulse is applied. Second, slice selective (or slab selective) RF pulses are evenly spaced. When phase-coherent RF pulses of the same flip angle are applied with a constant TR that is shorter than the T2 of the tissue, a dynamic equilibrium is achieved between transverse magnetization (TM) and longitudinal magnetization (LM) [3]. Once this equilibrium is reached, two types of signals are produced. The first type is post excitation signal (S+) that consists of free induction decay (FID) arising from the most recent RF pulse. The second signal is an echo reformation that occurs prior to excitation (S–) and results when residual echo is refocused at the time of the subsequent RF pulse [4].
Based on the theory of Bruder et al. [5], the simultaneous acquisition of two separate, steady state, free precession (SSFP) echoes allows the formation of two MR images with clearly different contrasts: S+ = FISP (fast imaging steady precession); and S– = PSIF (reversed FISP). DESS combines these signals into one by applying a sum of squares calculation to both echoes. The PSIF part of the sequence leads to a high T2 contrast, whereas the FISP part provides representative morphological images with a contrast dominated by the T1/T2 ratio. In principle, the different T2 weightings of both echoes (and images), allows the calculation of quantitative T2 maps with a certain functional dependence on T1 based on the chosen flip angle. Hence, the DESS sequence has the potential advantage to combine morphological and functional analysis from the same data set with high

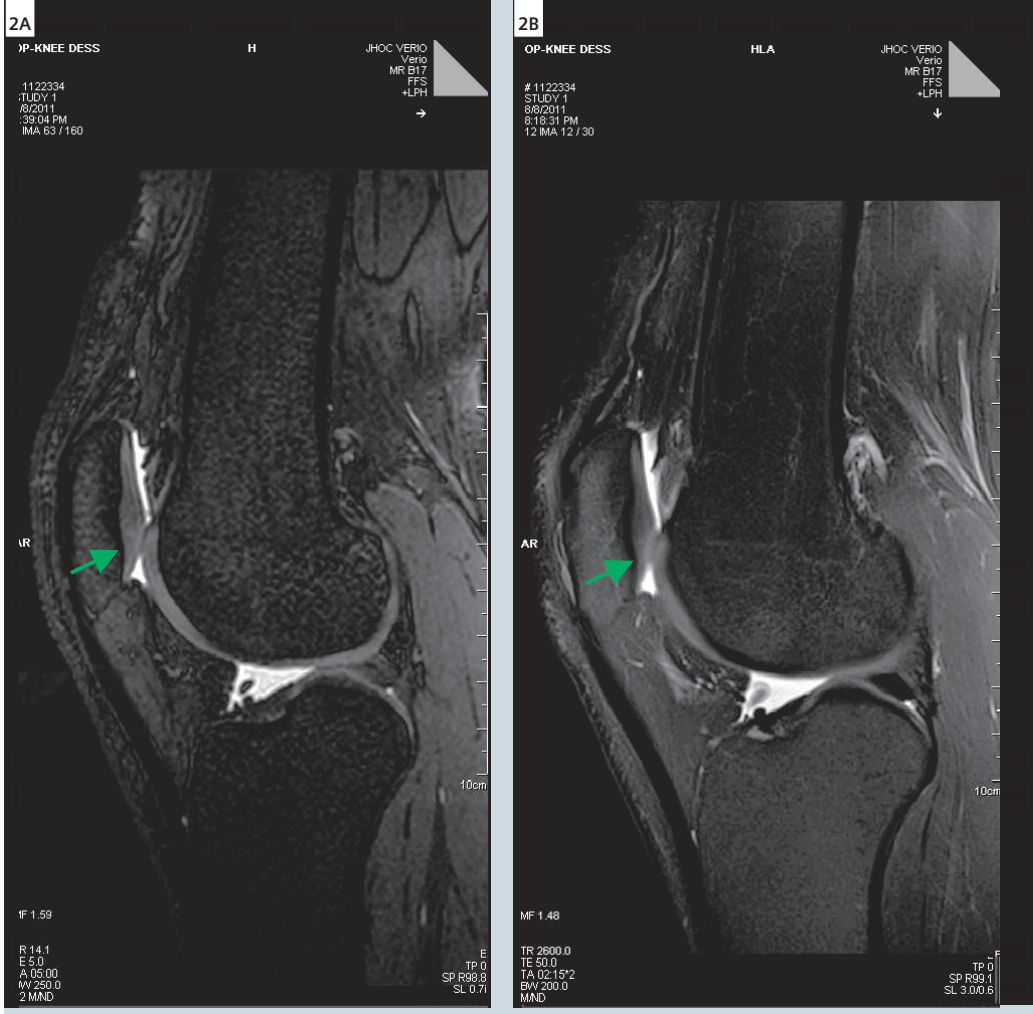

2 Sagittal MRI image of the knee. **(2A)** 3D DESS (TR/TE 14.1/5 ms) at flip angle 60°. **(2B)** 2D proton density with fat saturation (TR/TE 2600/50 ms). PD fat sat **(2B)** shows partial volume averaging of the cartilage of patella and femur, not seen in the 3D DESS sequence **(2A)** due to isotropic imaging. Also note better evaluation of menisci and ligamentum mucosum on the FSPD sequence.

DESS sequence		SNR	CNR (synovial fluid SNR – cartilage SNR)
FA 25°	Cartilage Synovial fluid	30.8 62.9	32.1
FA 45°	Cartilage Synovial fluid	24.38 86.22	61.84
FA 60°	Cartilage Synovial fluid	42.64 198.88	156.24
FA 90°	Cartilage Synovial fluid	25.7 121.22	95.5

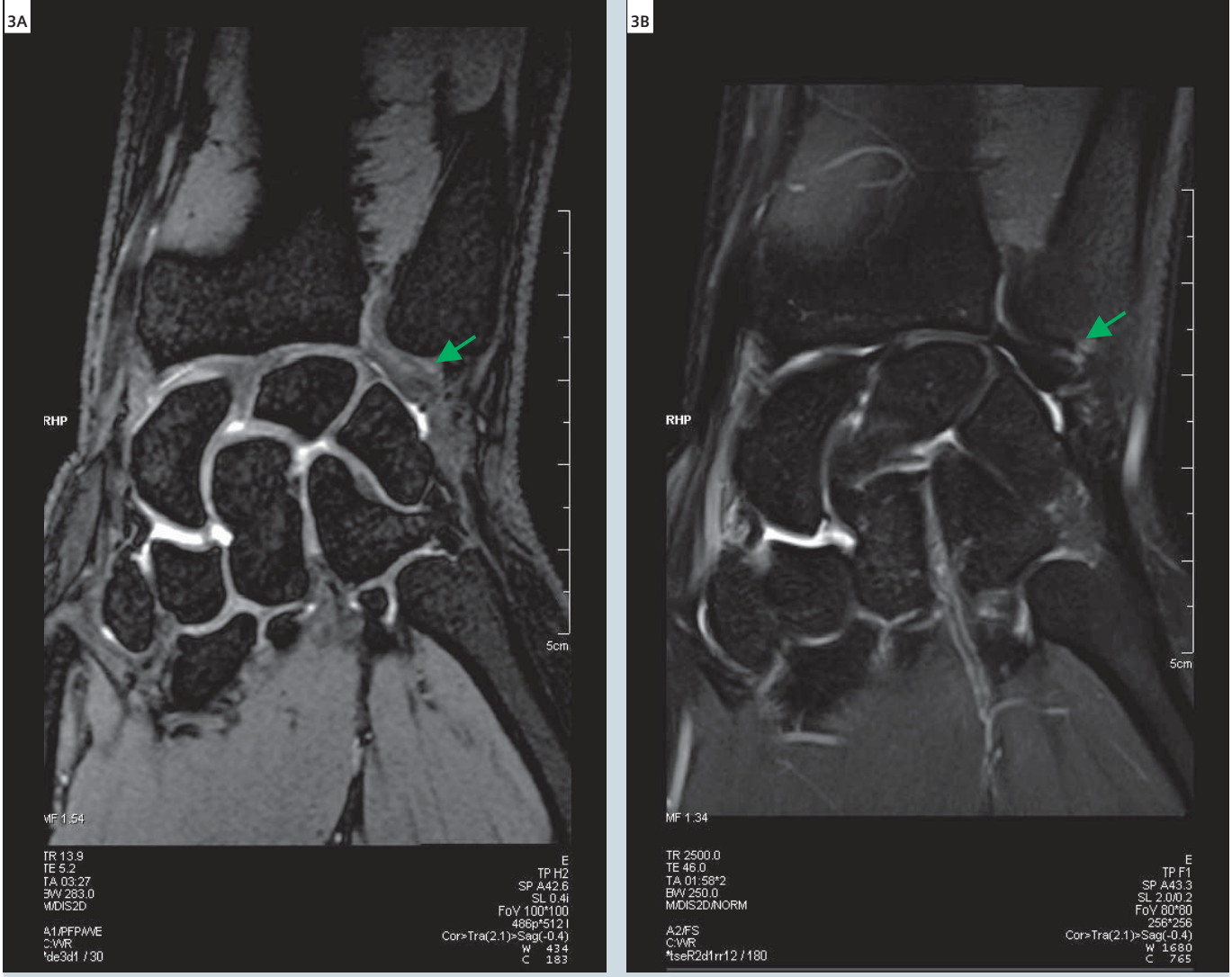

3 Coronal MRI image of the wrist joint. **(3A)** 3D DESS (TR/TE 13.9/5.2 ms) FA 30° and **(3B)** 2D proton density with fat saturation (TR/TE 2500/46 ms). The arrow marks the triangular fibro-cartilage complex of the wrist joint.

resolution in a relatively short imaging time [6]. In DESS, two or more gradient echoes are acquired. Each of these group of echoes are separated by a refocusing pulse and the combined data results in higher T2* weighting, creating high signal in cartilage and synovial fluid [7].

The most important parameter which needs to be kept in mind while acquiring a DESS is the flip angle (FA). According to Hardy et al. [8], the appropriate flip angle for the 3D DESS sequence is 60 degrees. At this point, SNR and cartilage-synovial fluid CNR is highest. In figure 1, we show the knee joint at flip angles of 25, 45, 60 and 90 degrees with the table showing SNR and CNR at various angles. At FA >60°, cartilage-synovial fluid contrast decreased along a curve obtained by the theoretical formula irrespective of TR [9].

Cartilage-synovial fluid contrast is comparable between water excited 3D DESS with a 60° FA and fat suppressed turbo spin echo proton density, which is commonly used for depicting cartilage. With both techniques, signal intensity of cartilage is intermediate and that of synovial fluid is high. Compared to 2D fat suppressed turbo spin echo proton density, slice thickness is typically thinner, suggesting the possibility that 3D DESS is capable of detecting smaller cartilage defects than the 2D technique. Lee et al. [10] have shown that fat suppressed 3D gradient echo sequences are better than 2D fat suppressed proton density sequences for differentiating grade 3 and grade 4 articular cartilage defects.

Water excited or fat suppressed 3D gradient echo imaging is recommended for measuring the exact cartilage thickness without partial volume artifacts, even though the CNR ratio between cartilage and bone marrow is relatively poor [11]. Chemical shift artifact can affect the cartilage-bone interface and fat suppression helps to reduce this. The disadvantages of 3D gradient echo imaging techniques are relatively long scan time, suboptimal contrast of other intra-articular and periarticular structures and metallic susceptibility artifacts. Fat suppressed turbo spin echo proton density is superior for other intra-articular and periarticular structures and is obtained in short imaging time, but it has the previously mentioned disadvantage of partial volume effects (Fig. 2).

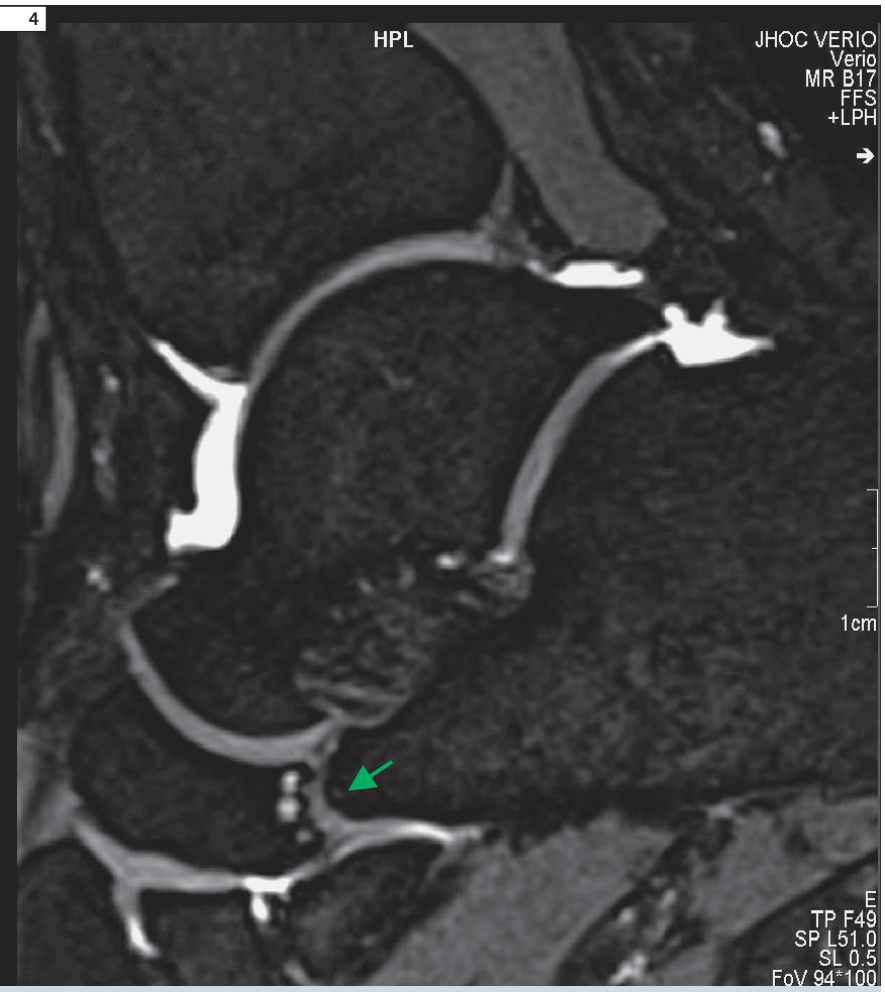

4 Sagittal 3D DESS image of the ankle joint showing the normal articular cartilage. Also note the fibrous calcaneonavicular coalition (arrow).

Clinical implications

3D DESS allows quantitative assessment of cartilage thickness and volume with good accuracy and precision [12]. In comparison with other 3D GRE techniques tested in longitudinal knee osteoarthritis trial, DESS imaging exhibited similar sensitivity to changes in knee cartilage thickness over time [13]. It can be used in other joints such as ankle and wrist; however, there has been no comparative study between DESS and other 3D sequences in imaging of small joints (Figs. 3, 4).

Summary

Cartilage imaging using the 3D DESS technique has many advantages including higher SNR, increased cartilage to fluid contrast and isotropic resolution, which helps to reduce partial volume effects.

Contact
John A. Carrino, M.D., M.P.H.
Associate Professor of Radiology and Orthopaedic Surgery
The Russel H. Morgan Department of Radiology and Radiological Science
Johns Hopkins University School of Medicine
601 North Caroline St. / JHOC 5165
Baltimore, MD
USA
carrino@jhmi.edu

References

1 Gold GE, Chen CA, Koo S, Hargreaves BA, Bangerter NK. Recent advances in MRI of articular cartilage. AJR Am J Roentgenol 2009 Sep;193(3):628-638.
2 Kornaat PR, Reeder SB, Koo S, Brittain JH, Yu H, Andriacchi TP, et al. MR imaging of articular cartilage at 1.5T and 3.0T: comparison of SPGR and SSFP sequences. Osteoarthritis Cartilage 2005 Apr;13(4):338-344.
3 Chavhan GB, Babyn PS, Jankharia BG, Cheng HM, Shroff MM. Steady-State MR Imaging Sequences: Physics, Classification, and Clinical Applications1. Radiographics July-August 2008 July-August 2008;28(4):1147-1160.
4 Gyngell ML. The application of steady-state free precession in rapid 2DFT NMR imaging: FAST and CE-FAST sequences. Magn Reson Imaging 1988 Jul-Aug;6(4):415-419.
5 Bruder H, Fischer H, Graumann R, Deimling M. A new steady-state imaging sequence for simultaneous acquisition of two MR images with clearly different contrasts. Magn Reson Med 1988 May;7(1):35-42.
6 Welsch GH, Scheffler K, Mamisch TC, Hughes T, Millington S, Deimling M, et al. Rapid estimation of cartilage T2 based on double echo at steady state (DESS) with 3 Tesla. Magn Reson Med 2009 Aug;62(2):544-549.
7 Crema MD, Roemer FW, Marra MD, Burstein D, Gold GE, Eckstein F, et al. Articular Cartilage in the Knee: Current MR Imaging Techniques and Applications in Clinical Practice and Research. Radiographics January-February 2011 January-February 2011;31(1):37-61.
8 Hardy PA, Recht MP, Piraino D, Thomasson D. Optimization of a dual echo in the steady state (DESS) free-precession sequence for imaging cartilage. J Magn Reson Imaging 1996 Mar-Apr;6(2):329-335.
9 Moriya S, Miki Y, Yokobayashi T, Ishikawa M. Three-dimensional double-echo steady-state (3D-DESS) magnetic resonance imaging of the knee: contrast optimization by adjusting flip angle. Acta Radiol 2009 Jun;50(5):507-511.
10 Lee SY, Jee WH, Kim SK, Koh IJ, Kim JM. Differentiation between grade 3 and grade 4 articular cartilage defects of the knee: fat-suppressed proton density-weighted versus fat-suppressed three-dimensional gradient-echo MRI. Acta Radiol 2010 May;51(4):455-461.
11 Gold GE, McCauley TR, Gray ML, Disler DG. Special Focus Session. Radiographics 2003 September 01;23(5):1227-1242.
12 Eckstein F, Hudelmaier M, Wirth W, Kiefer B, Jackson R, Yu J, et al. Double echo steady state magnetic resonance imaging of knee articular cartilage at 3 Tesla: a pilot study for the Osteoarthritis Initiative. Ann Rheum Dis 2006 Apr;65(4):433-441.
13 Wirth W, Nevitt M, Hellio Le Graverand MP, Benichou O, Dreher D, Davies RY, et al. Sensitivity to change of cartilage morphometry using coronal FLASH, sagittal DESS, and coronal MPR DESS protocols--comparative data from the Osteoarthritis Initiative (OAI). Osteoarthritis Cartilage 2010 Apr;18(4): 547-554.

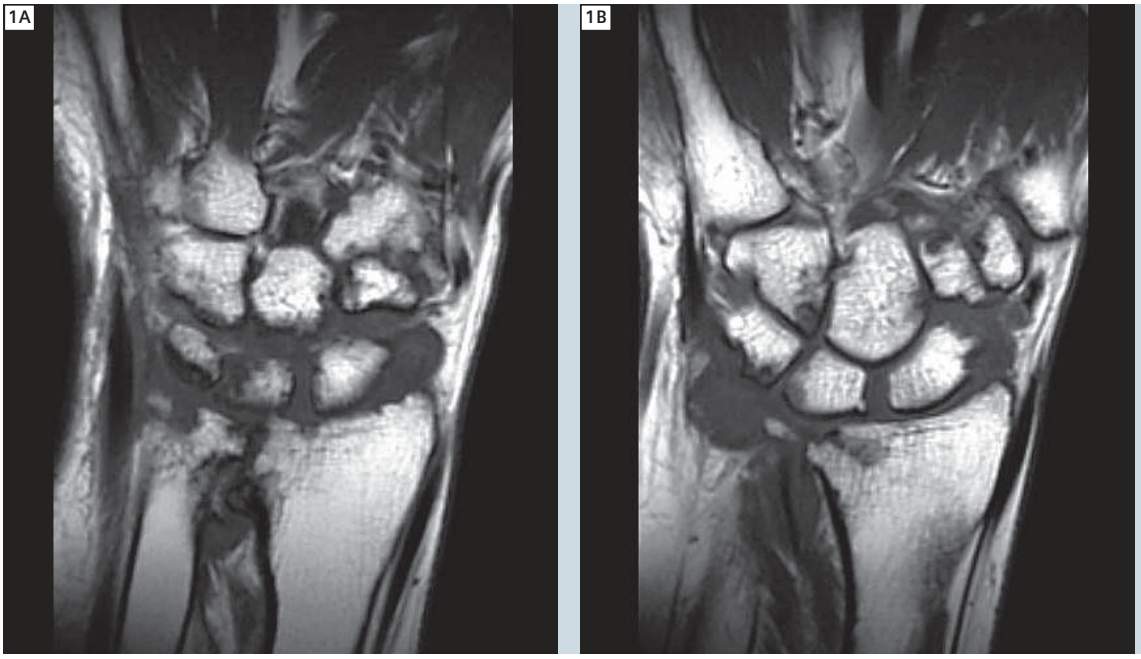

1 Coronal T1w TSE of the wrist in case of advanced rheumatoid arthritis. Multiple erosions of the bones and resulting severe destruction of the joints is shown.

The Importance of MRI of the Wrist in Patients with Rheumatoid Arthritis

Filippo Del Grande, M.D., M.H.E.M.[1]; Aaron J Flammang, MBA BSRT (MR)[2]; Abraham Padua RT (MR)[2]; John A. Carrino, M.D. M.P.H.[1]

[1]Johns Hopkins University School of Medicine, Russell H. Morgan Department of Radiology and Radiological Science, Baltimore, MD, USA
[2]Siemens Medical Solutions, USA

Introduction

Rheumatoid arthritis (RA) is a chronic inflammatory disease affecting the joints, mainly the metacarpo-phalangeal joints (MCP) and the carpal joints.
MR imaging (MRI) is the only imaging modality that can directly detect the early findings of the disease such as bone marrow edema (BME) and synovitis [1]. Moreover MRI can detect tendosynovitis and bone erosions with greater sensitivity than in standard radiography.
The treatments with anti-tumor necrosis factor (TNF) drugs are very expensive and carry potential severe infectious adverse effects. Therefore it is very important to have an early and accurate diagnose of RA which is possible with MRI associated with clinical and laboratory findings. Moreover an early treatment with anti-rheumatic drugs seems to have a better disease outcome at 2 years [2].
We will review the MRI signs of RA such as BME, synovitis/tendosynovitis and bone erosions. The first three manifestation of the disease are included in the rheumatoid arthritis MRI scoring system (RAMRI) of the outcome measurement in Rheumatology clinical trials (OMERACT) [3]. We will not treat cartilage loss that should be treated separately, due to its complexity and the presence of different promising emerging techniques.

MRI in patients with Rheumatoid arthritis

Bone marrow edema is a sign of early manifestation of RA and it shows low signal intensity ill defined areas on T1-weighted sequences and high signal intensity in fluid sensitive sequences such as STIR or T2 fat sat. Several interesting considerations are important regarding BME. First, BME follows the same pattern than bone erosions

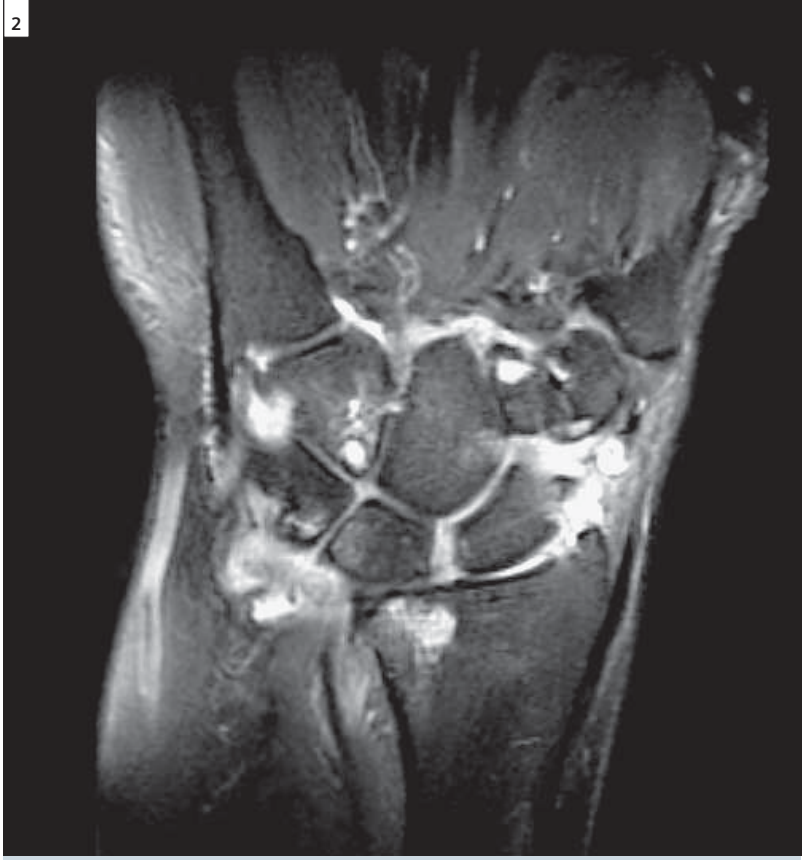

2 Corresponding T1w contrast-media enhanced image to figure 1 is shown. Synovial enhancement as a consequence of acute inflammatory process is present in this case.

suggesting that bone marrow edema is the precursor of bone erosions [4]. Second, BME is the most important prognostic factor for progression of the disease. The authors of one study [5] were able to correctly detect the disease progression in 82% of the cases with a sensitivity of 81% and a specificity of 82% using clinical (hand arthritis, morning stiffness) laboratory (positivity for RF) and imaging criteria (bone marrow edema score in MCP and carpal joints). Another 2-years randomized controlled trial [6] concluded that MRI bone marrow edema is the strongest predictor of progression of the disease in hand, wrist and foot. Third, according to Olech et al. [7] bone marrow edema is the most specific sign (among bone marrow edema, synovitis and bone erosions) for RA. The study [7] showed that BME was 65% sensitive and 82.5% specific for RA and, if the lunatum was not included in the scoring system, the sensitivity decrease to 62.5% but the specificity increase to 87.5%. BME was present in 15% of the control group subjects and, if the lunatum was excluded, in 12.5% of the subjects. Interestingly no one healthy subject presented bone marrow edema in the MCP joint.

Bone erosions represent "the focal loss of cortical and/or underlying trabecular bone" [8] and are better visualized in T1-weighted sequence as interruption of the cortical and trabecular bone. According to the RAMRI criterion bone erosions are defined as follows: "a sharply marginated bone lesion, with correct juxta-articular localization and typical signal characteristics, which is visible in two planes with a cortical break seen in at least one plane" [3]. MRI has a moderate sensitivity (61%) and a good specificity (93%) to detect bone erosions compared to CT as a gold standard whereas standard radiography has a sensitivity of 24% and a specificity of 99% [9]. In order to effectively diagnose bone erosions it is mandatory to run MRI protocols with thin slices (ideally 1 mm), high spatial resolution in two planes according to RAMRI score criteria [10]. Here 3 Tesla MRI could play an important role in the near future, due to its higher signal-to-noise ration (SNR) and the potential to obtain high resolution isotropic 3D sequences.

The starting point of the disease process of RA seems to be the inflammation of the synovium which leads to high cellular inflammatory tissue, the pannus, which in turn is responsible for the cartilage and the bone destruction (bone erosion) [1, 11]. Synovium presents on MRI with low signal intensity on T1-weighted sequences and with high signal intensity on fluid sensitive sequences. Compared to free fluid the intensity signal of synovium is slightly higher on T1-weighted sequences and slightly lower on T2 fat set sequences.

Contrast-enhanced MRI is mandatory in RA patients in order to detect and quantify the inflammation synovium enhancement following the RAMRIS score whereas detection and quantification of BME and bone erosion don't need the administration of Gadolinium. One interesting study of Agarwal et al. [12] used diffusion tensor imaging (DTI) in order to test an alternative method to evaluate the inflammation of the synovium in 18 patients and 6 volunteers. The principle of DTI is based on the isotropic or anisotropic movement of water molecules. The molecules are moving isotropic if they can move freely in all direction like in fluid whereas they are moving anisotropic if they are limited in the movement due to other components like in tissues. The degree and direction of diffusion can be described in a scale value from 0 to 1 [8]. In patients with RA the water molecules present a restricted motion due to the fractional anisotropy of the inflammatory fluid (effusion). According to the study these

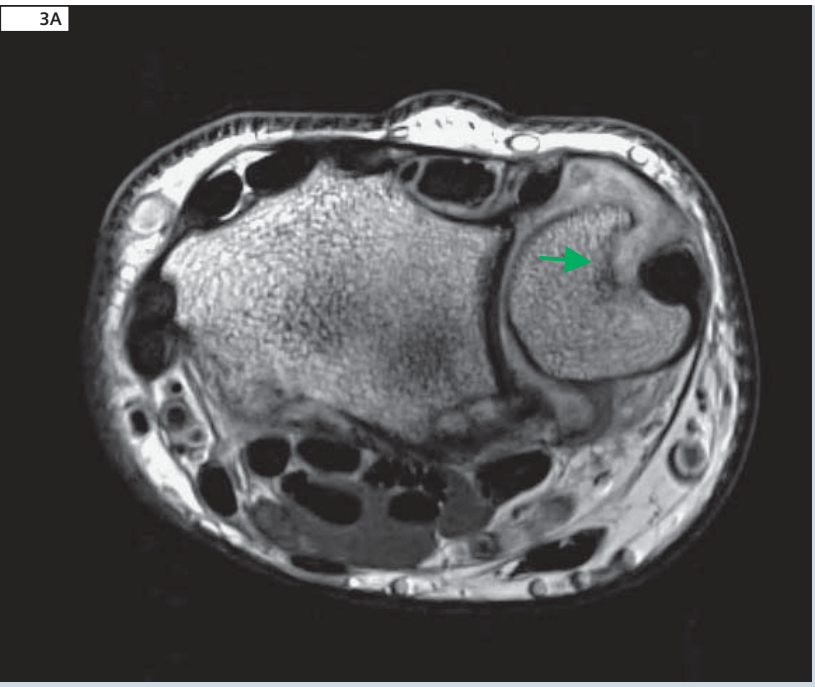

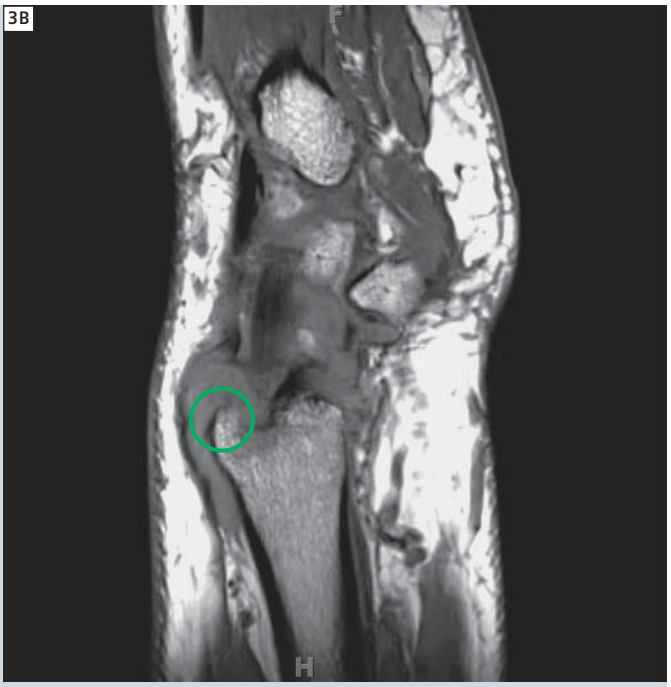

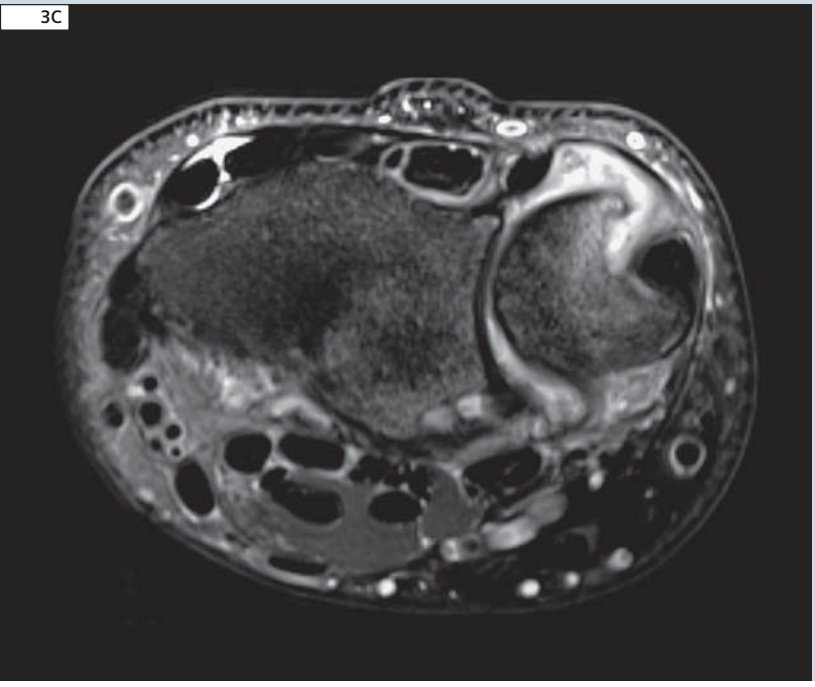

3 Synovial reaction and early signs of bone errosion of the ulnar styloid processus. **3C**: Corresponding T2w image with fat saturation showing oedema within the bone and fluid collection as well as thickening of the synovia.

values are significantly altered in patients with RA compared to healthy individuals. DTI is by no doubt an interesting and promising technique to study the synovial inflammation with the great advantage of the absence of contrast media and the risks that are connected such as nephrogenic systemic fibrosis [13], acute adverse reactions and other, less important but common adverse events, such as extravasations. Moreover, according to the study, DTI has a similar sensitivity in detection synovial inflammation compared to conventional T1-weighted fast SE fat sat sequences. According to one recent study [14] even flexor tendosynovitis, that can be detected with MRI or sonography, has a strong predictive value for RA. The study analyzed 99 patients with unspecific arthritis or suspected RA and negative standard X-rays. Moreover by adding RF or anti-cyclic citrullinated peptides (anti-CCP) the predictor was stronger with a sensitivity of 83% and a specificity of 63% [14].

Conclusion

MRI is an imaging modality that can detect RA in the early stadium. This information is mandatory to start appropriate therapies that are very expensive and that carry potential severe adverse reactions. Due to its higher SNR and the potential increase in spatial resolution, 3 Tesla MRI will probably play an important role to improve the detection of bone erosions and to implement new technique in the near future without the need of gadolinium administration.

Contact
Filippo Del Grande, M.D., M.H.E.M.
Research Fellow
Johns Hopkins Hospital
Musculoskeletal Radiology
Russell H. Morgan Department of
Radiology and Radiological Science
600 N. Wolfe Street
Phipps B-100
Baltimore, MD 21287
USA
Fdelgra1@jhmi.edu

John A. Carrino, M.D., M.P.H.
Associate Professor of Radiology and
Orthopaedic Surgery
Johns Hopkins University School of
Medicine
Section Chief, Musculoskeletal Radiology
Russell H. Morgan Department of
Radiology and Radiological Science
600 N. Wolfe Street
Phipps B-100
Baltimore, MD 21287
USA
carrino@jhmi.edu

References

1 Kosta PE, Voulgari PV, Zikou AK, Drosos AA, Argyropoulou MI. The usefulness of magnetic resonance imaging of the hand and wrist in very early rheumatoid arthritis. Arthritis Res Ther 2011 Jun 9;13(3):R84.
2 Lard LR, Visser H, Speyer I, vander Horst-Bruinsma IE, Zwinderman AH, Breedveld FC, et al. Early versus delayed treatment in patients with recent-onset rheumatoid arthritis: comparison of two cohorts who received different treatment strategies. Am J Med 2001 Oct 15;111(6):446-451.
3 Ostergaard M, Edmonds J, McQueen F, Peterfy C, Lassere M, Ejbjerg B, et al. An introduction to the EULAR-OMERACT rheumatoid arthritis MRI reference image atlas. Ann Rheum Dis 2005 Feb;64 Suppl 1:i3-7.
4 Peterfy CG, Countryman P, Gabriele A, Shaw T, Anisfeld A, Tsuji W, et al. Magnetic resonance imaging in rheumatoid arthritis clinical trials: emerging patterns based on recent experience. J Rheumatol 2011 Sep;38(9):2023-2030.
5 Duer-Jensen A, Horslev-Petersen K, Hetland ML, Bak L, Ejbjerg BJ, Hansen MS, et al. Bone edema on magnetic resonance imaging is an independent predictor of rheumatoid arthritis development in patients with early undifferentiated arthritis. Arthritis Rheum 2011 Aug;63(8):2192-2202.
6 Hetland ML, Ejbjerg B, Horslev-Petersen K, Jacobsen S, Vestergaard A, Jurik AG, et al. MRI bone oedema is the strongest predictor of subsequent radiographic progression in early rheumatoid arthritis. Results from a 2-year randomised controlled trial (CIMESTRA). Ann Rheum Dis 2009 Mar;68(3):384-390.
7 Olech E, Crues JV,3rd, Yocum DE, Merrill JT. Bone marrow edema is the most specific finding for rheumatoid arthritis (RA) on noncontrast magnetic resonance imaging of the hands and wrists: a comparison of patients with RA and healthy controls. J Rheumatol 2010 Feb;37(2):265-274.
8 Borrero CG, Mountz JM, Mountz JD. Emerging MRI methods in rheumatoid arthritis. Nat Rev Rheumatol 2011 Feb;7(2):85-95.
9 Dohn UM, Ejbjerg BJ, Hasselquist M, Narvestad E, Moller J, Thomsen HS, et al. Detection of bone erosions in rheumatoid arthritis wrist joints with magnetic resonance imaging, computed tomography and radiography. Arthritis Res Ther 2008;10(1):R25.
10 Drape JL. MRI in rheumatoid arthritis: a dual emergency. J Radiol 2008 May;89(5 Pt 1):543-545.
11 Cyteval C. MR imaging of the hands in rheumatoid arthritis. J Radiol 2010 Jan;91(1 Pt 2):111-119.
12 Agarwal V, Kumar M, Singh JK, Rathore RK, Misra R, Gupta RK. Diffusion tensor anisotropy magnetic resonance imaging: a new tool to assess synovial inflammation. Rheumatology (Oxford) 2009 Apr;48(4):378-382.
13 Jalandhara N, Arora R, Batuman V. Nephrogenic systemic fibrosis and gadolinium-containing radiological contrast agents: an update. Clin Pharmacol Ther 2011 Jun;89(6):920-923.
14 Eshed I, Feist E, Althoff CE, Hamm B, Konen E, Burmester GR, et al. Tenosynovitis of the flexor tendons of the hand detected by MRI: an early indicator of rheumatoid arthritis. Rheumatology (Oxford) 2009 Aug;48(8):887-891.

Listen – Discuss – Share

8th MAGNETOM World Summit

May 31 – June 3, 2012, Paris, France

Join us for the 8th MAGNETOM World Summit, where you will discover new techniques and methods to maximize the use of your MAGNETOM system. Through information and best-practice sharing, you will walk away with fresh ideas and invaluable tools that will help you to improve efficiencies and keep you on the edge of new trends in MRI.

In addition to the interesting and challenging program, the 8th MAGNETOM World Summit offers you important networking opportunities with your colleagues and peers. We look forward to seeing you in Paris, France.

So get ready and register now for an informative and interactive event at

www.simens.com/magnetom-world

Configuration and Use of the MR Knee Dot Engine

Kai Reiter (RT); Sebastian Auer (RT)

Radiology Herne, Herne, Germany

1

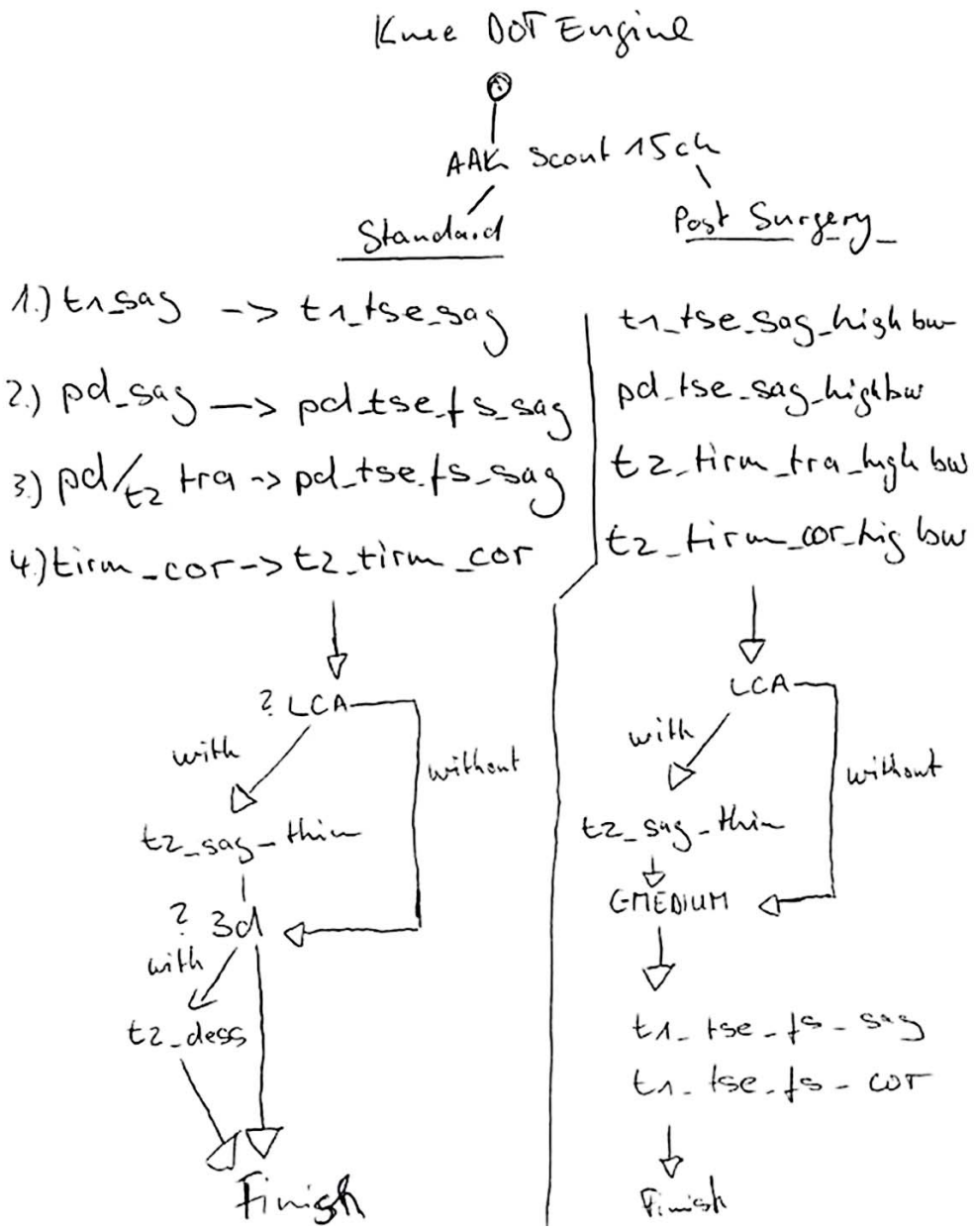

We are a radiological joint practice in the heart of the Ruhr district of Germany. At our various magnetic resonance scanners, we perform on every unit between 30–45 MR Imaging (MRI) examinations each day. As a result of the high throughput, we are always interested in 'Workflow Optimization'. We have, among other things, determined standardized examination protocols. Our MR Knee Dot Engine now goes a step further. Thanks to Dot, the Day Optimizing Throughput Engine and the integrated AutoAlign Knee function, an MR knee examination can now be performed examination-independent with consistent image quality using only a few mouse clicks. Global configurations of the Exam Task Card can also be set automatically with Dot.

Using the AutoAlign Knee function, we have optimized the sequences in such a way that the Technologist at the console only has to check whether enough slices cover the knee. There is no need to re-angle.

In a so-called guidance, helpful tips and figures with tilting can be added to each protocol. Furthermore, the most important protocol parameters can be summarized on an individual parameter card to ensure that beginners are not confused by the number of possible modifications that can be made to the parameters, thus allowing them to concentrate on the most important parameters. Thanks to Dot, our MR beginners are instructed on our 3T MAGNETOM Skyra. Here are a few helpful tips that also apply to other Dot protocols:

First you should think about how the usual clinical questions can be processed with the fewest standardized measuring programs possible:

- Which protocols are required?
- With which sequences?
- In which versions?
- With which possible optional additional sequences?

Sometimes a rough planning sketch (Fig. 1) helps to clarify the required version and possible additional options and how those can be implemented with the given means of a Dot Engine (strategies, decisions).

In our practice, there are basically two main versions for the knee MRI:

a) Standard knee imaging for an initial finding without contrast agent:
pd tse fs sag, pd tse fs tra, t1 tse sag, t2 tirm cor. It might be helpful to do a thin slice t2 tse sag to show the anterior cruciate ligament or a 3d t2 DESS to image the cartilage.

b) Post-operative imaging with contrast agent:
By default, these protocols are scanned with a high bandwidth as these patients have often been provided with metal implants*.
pd tse fs sag, pd tse fs tra, t1 tse sag, t2 tirm cor. It might be helpful to do a thin slice t2 tse sag, post contrast agent t1 tse fs cor and t1 tse fs sag to show the anterior cruciate ligament.

The schematic sequence that we have thus standardized, including the branching/options specified therein, can be displayed completely using a single Dot Engine.

Implementation

The best way of implementing a Dot Engine is according to the following procedure:

1. Configuration of the Dot Engine basic structure (strategies, options)
2. Assignment of the protocols
3. Adjustment of the workflow properties (copy references, settings, ...)
4. Verification and fine tuning (AutoAlign, Generic view, ...)

*The MRI restrictions (if any) of the metal implant must be considered prior to patient undergoing MRI exam.

1. Configuration

- Go to the examination explorer and enter a new examination.
- Use the right mouse button in the “Exam Properties” and select the corresponding “Body Part” (KNEE). You now have the option to determine the laterality. We have stored “Both” as default in our institute (Fig. 2).

Thanks to these few steps, the examiner no longer needs to make these decisions when selecting the patient. The device detects the coil position and will release the “Autocenter” function with the previous patient selection.

Now the foundation of the Dot Engine is determined:

- Press the right mouse button under “Insert” to select “Dot Engine Step” (Fig. 3).
- Now select the “Ortho Patient View” and go to “Edit Configuration”.
- Here, under “Set-up”, the previously determined strategies and the “Clinical decision points” for the additional Ligamentum cruciatum anterius (LCA) sequence are entered (Fig. 3).

TIP: To add strategy names and clinical decision point names select the + icon in the corresponding area of the patient view setup page and type desired name. Secondly, the scout is entered into the exam explorer beneath the ortho patient view independent of a strategy branch. We always scan an AutoAlign Scout. In doing so, a 3D volume is acquired and multiplanar reconstructions (MPRs) are calculated in all 3 planes. Thanks to the AutoAlign Knee algorithms, the sequence is angled using landmarks. The Technologist only needs to check whether there are sufficient slices covering the knee and respond accordingly.

2

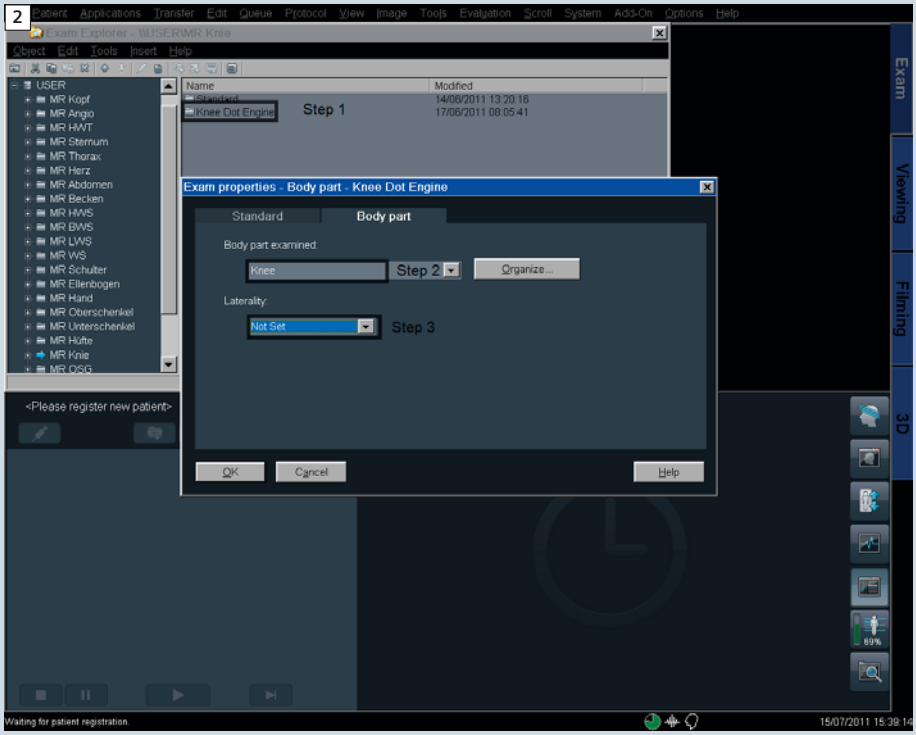

3

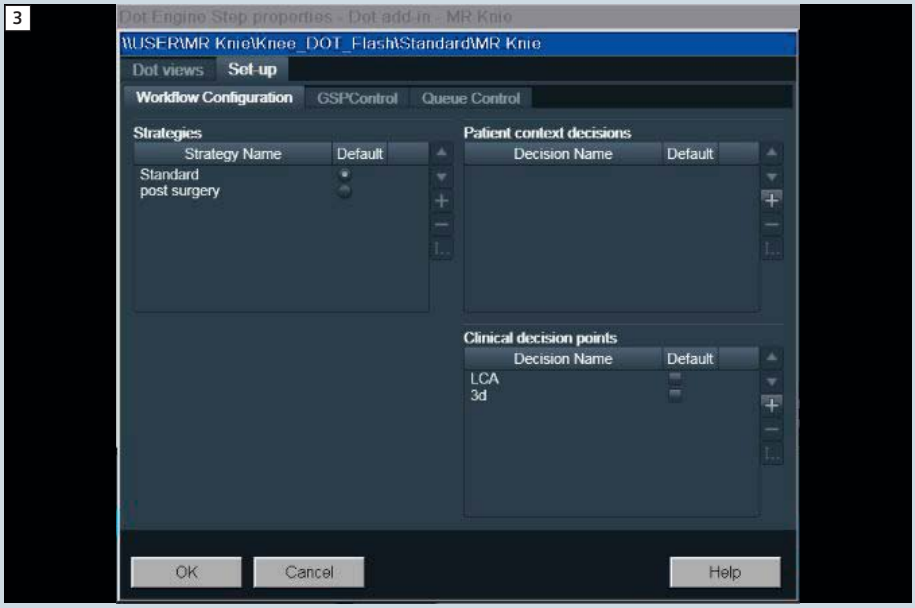

2. Protocol assignment

The remaining sequences must now be entered as follows:

- In the context menu under the right mouse button, select “Insert”.
- Select “Strategy Branch”, enter the sequence weighting name, e.g. t1 sag and confirm.
- Double-click to open the sequence weighting name.
  The previously entered strategies “Standard” and “Post surgery” are displayed.

In both strategy folders, each of the respective sequence sequences must now be entered, e.g. with “Standard” a normal t1_tse_sag and with “Post surgery”, a t1_tse_sag_high_bw (Fig. 4). Repeat this maneuver until all sequences have been assigned to the respective strategy branches and strategies.
In the next step, the LCA sequence is saved as “Clinical decision points”.

- In the context menu under the right mouse button, select “Insert” and “Decision Step”.
- Select the decision “LCA” and “Confirm decision before start” (Fig. 5) and confirm with ok.
- Double-click on the LCA branch and add additional LCA sequences (t2_tse_sag_thin) in the branch “with LCA”.

4

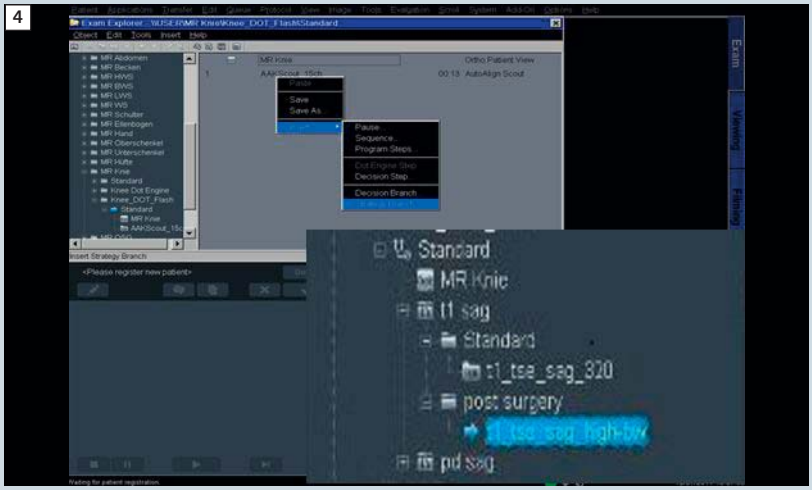

5

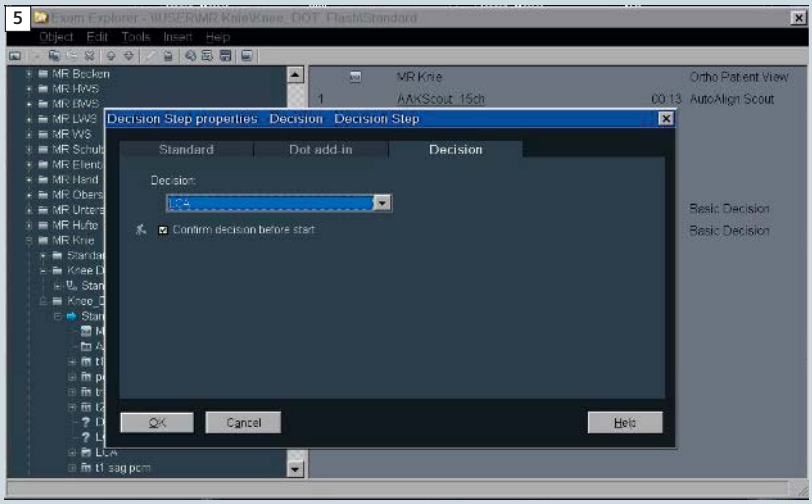

For the next option or decision, insert the 3D sequence and inline MPR which will be saved as a “Clinical decision points”.

- Use the right mouse button to insert “Decision Step”. Select the decision “3D” and “Confirm decision before start” and confirm with ok.
- Double-click on the “3D” decision branch and add additional 3D sequences (t2_dess) in the branch “with 3d”. After the t2_DESS sequence is inserted, use the right mouse button and go to the sequence properties, Dot add-in and from the drop down menu choose “MPR Assignment” and confirm with ok (Fig. 6).

Now an additional “Decision step” is entered that is used to select the “MPR Planning” (Fig. 7). This has the advantage that the respective postprocessing MPRs can be planned before the 3D sequence is scanned and automatically carried out following the measurement. Postprocessing the 3D sequences can no longer be forgotten.

TIP: To insert MPR Planning:

1. Insert “mpr planning” name in the ortho patient view properties > setup within the clinical decision area.
2. Right mouse button: Insert a decision step within the “with 3D” decision branch.
3. Select the Dot add-in tab and change the drop down menu item from basic decision to MPR Planning.
4. Finally select “edit configuration” icon then the set-up tab. Here the inline MPR views wanted can be configured for orientation, FOV, slices etc.
5. Click ok to confirm changes.

The last two sequences for the strategy post-contrast t1 sag pcm and t1 cor pcm will each be entered in their respective “Strategy Branches”.

In doing so, the “Standard Strategy” remains empty as the examination is completed after the 3D branch.

6

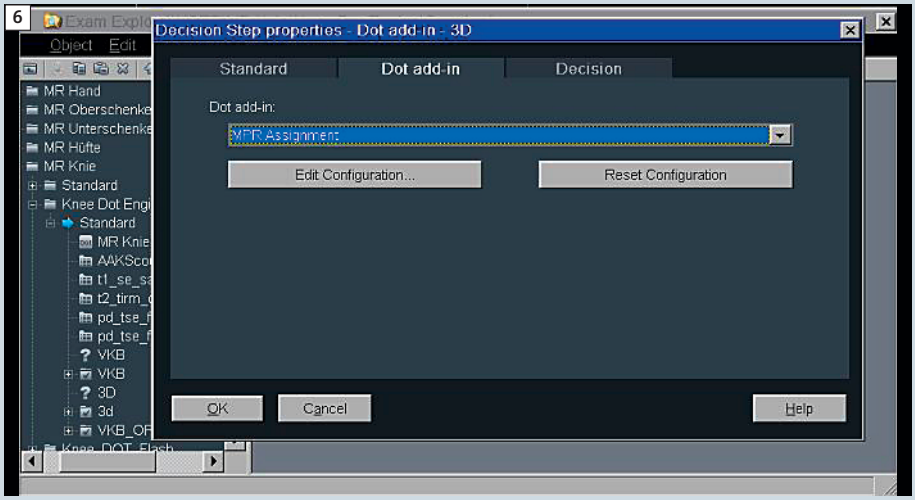

7

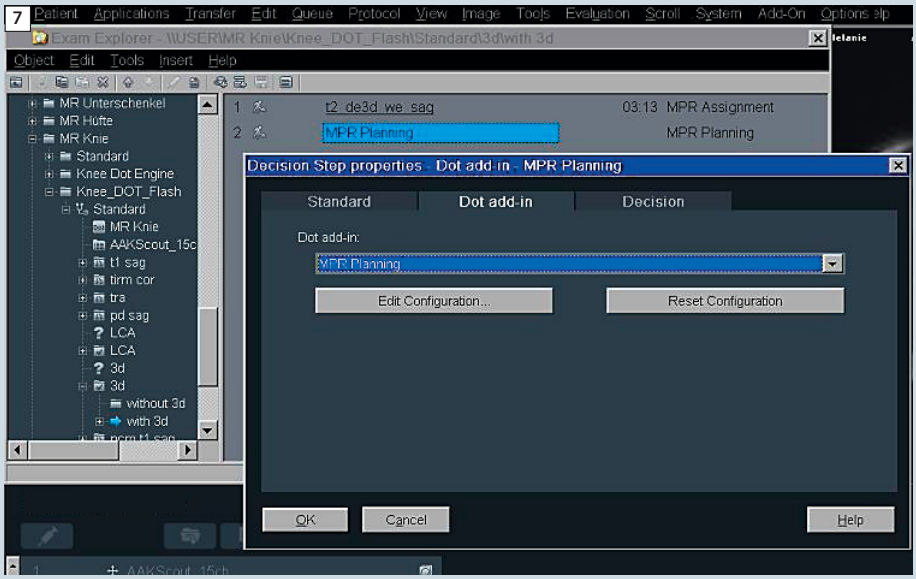

3. Adjusting the workflow properties

The number of slices, the resolution, the field-of-view (FOV) as well as all other parameters are set here and the copy references are assigned. You have to switch to Simulator Mode and determine the copy references for the "Standard" and for the "Post Surgery" strategy (Fig. 8).

4. Verification and fine tuning

The Dot-Engine works best when you use the AutoAlign settings. The following settings exist:

1. Knee Standard: sagittal plane and coronal level
2. Knee Meniscus: coronal and sagittal plane at the height of the joint gap
3. Knee Patella routine: transversal
4. Knee Patella cartilage: transversal angled to the patella
5. Knee Femur cartilage: transversal angled to the femur
6. Knee ACL: angled for the front cruciate ligament
7. Knee PCL: angled for the rear cruciate ligament

Open the sequence and in "Routine" card, select the respective algorithm for the sequence under "AutoAlign". We use the "Knee Standard" setting for the sagittal plane and coronal sequence and the "Knee Patella routine" for the transversal patella sequence.
The "Knee ACL" algorithm is stored for the ACL sequence.
AutoAlign detects the laterality of the examined knee and suggests the appropriate tilting.
Guidance information is stored in the opened protocol under "Set-up".
Select the sequence and, under "Set-up", set the guidance protocol instructions and instruction figures to show how the angulation is carried out. On the configuration card "Parameters", we have determined that only the following parameters should be displayed:
Slices, Thickness, FOV readout, FOV phase, TR and Concatenations (Fig. 9).

8

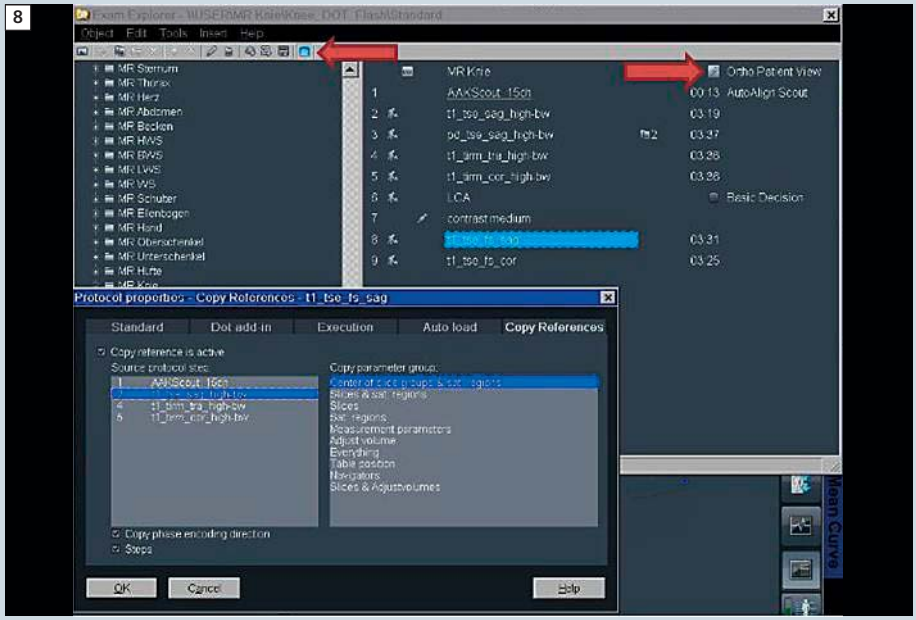

9

When applying the MR Knee Dot Engine this is what happens (Fig. 10):
The sequence has been successfully angled in the system thanks to AutoAlign.
The parameter card is clearly laid out and easy to use.

Contact
Kai Reiter (Ltd.MR-MTRA)
Radiologie Herne
Hospitalstr. 19
44649 Herne
Germany
Phone: +49 (0) 23 25 -98 65 234
Fax: +49 (0) 23 25 -63 79 7298
reiter@radiologieherne.de

10

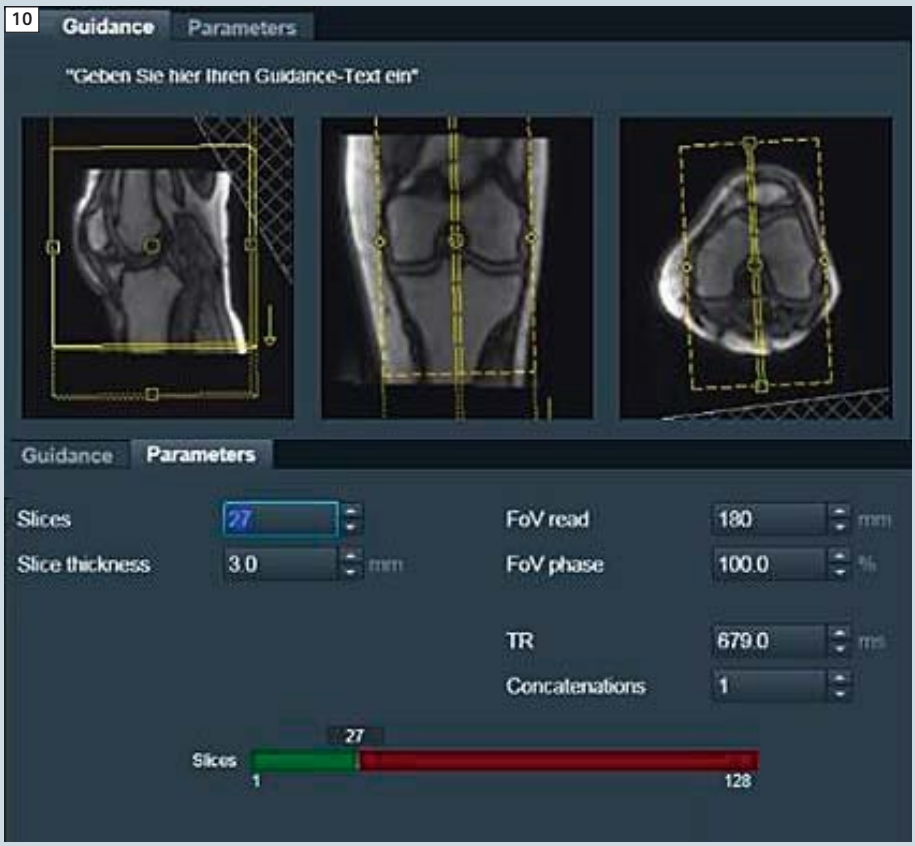

What's your favorite Dot Feature?

"In some pathologies, we need to obtain inter-examination reproducibility and to be able to carry out examinations swiftly. In the area of knee pathology in particular, Dot and its AutoAlign function have enabled us to position slices automatically without the need for user intervention."

Alexandre Fuchs, MD
Radiologist
Imagerie Médicale Sainte Marie, Osny, France

"One of the major benefits of Dot is that it provides us with a relatively easy way to perform slice positioning through a library of images, which guide the user to specific anatomical points by means of landmarks."

Romain Olliac, Technologist
Service de Radiologie Polyvalente Diagnostique et Interventionnelle Hôpital Pitié-Salpêtrière, Paris, France

What's your favorite Dot Feature?

Dot (Day optimizing throughput) is the most comprehensive MRI workflow solution, and it helps take the complexity out of MRI. Dot has now established itself in the field and our customers have told us what they like best about Dot:

"Within our environment, we just could not provide a cardiac MRI service without the Cardiac Dot Engine."

Dr. Russell Bull, MRCP, FRCR
Consultant Radiologist
Royal Bournemouth Hospital, Bournemouth, UK

"The Dot Decisions functionality in Abdomen Dot has enabled us to schematize and simplify these protocols. With Dot, we can now ensure our examinations are far more reproducible and of excellent quality."

Arnaud Lambert
Technologist
Imagerie Médicale Saint Marie, Osny, France

"Cardiac Dot (Engine) allows us to obtain automatic positioning of the main slices necessary to evaluate cardiac function with a high degree of reproducibility."

Professor Philippe Cluzel, MD, PhD
Service de Radiologie Polyvalente Diagnostique et Interventionnelle Hôpital Pitié-Salpêtrière, Paris, France

"AutoAlign is helpful especially for colleagues who rarely perform knee examinations because the slices are positioned automatically, which saves a lot of time. Furthermore, our knee examinations have become reproducible."

Linda Willeke
Technologist
St. Franziskus Hospital, Münster, Germany

Experience a Dot workflow yourself and hear from more customers at

www.siemens.com/Dot

Dot is now available for 3T MAGNETOM Skyra and MAGNETOM Verio and for 1.5T MAGNETOM Aera and MAGNETOM Avanto.

Visit our site optimized for tablets and smartphones

Simplifying the Workflow of Long Bone Imaging for Short Bore Systems

Russell Grossen, RT(R) (MR)

Uptime Service Center, Cary, NC, USA

Introduction

Imaging of long bones on the 1.5T MAGNETOM Espree and MAGNETOM ESSENZA systems can be challenging at times for technologists. This article will provide tips that will make long bone imaging easier to acquire.

Workflow for sagittal and coronal imaging

First we will go through the workflow of scanning a lower leg on the MAGNETOM Espree. This exam can be done by placing the Body Matrix Coil lengthwise covering the lower leg. Position the patient so that the landmark is in the center of the middle of the lower leg and acquire a separate axial, sagittal, and coronal localizer to visualize the lower leg, as seen in figure 1.

1

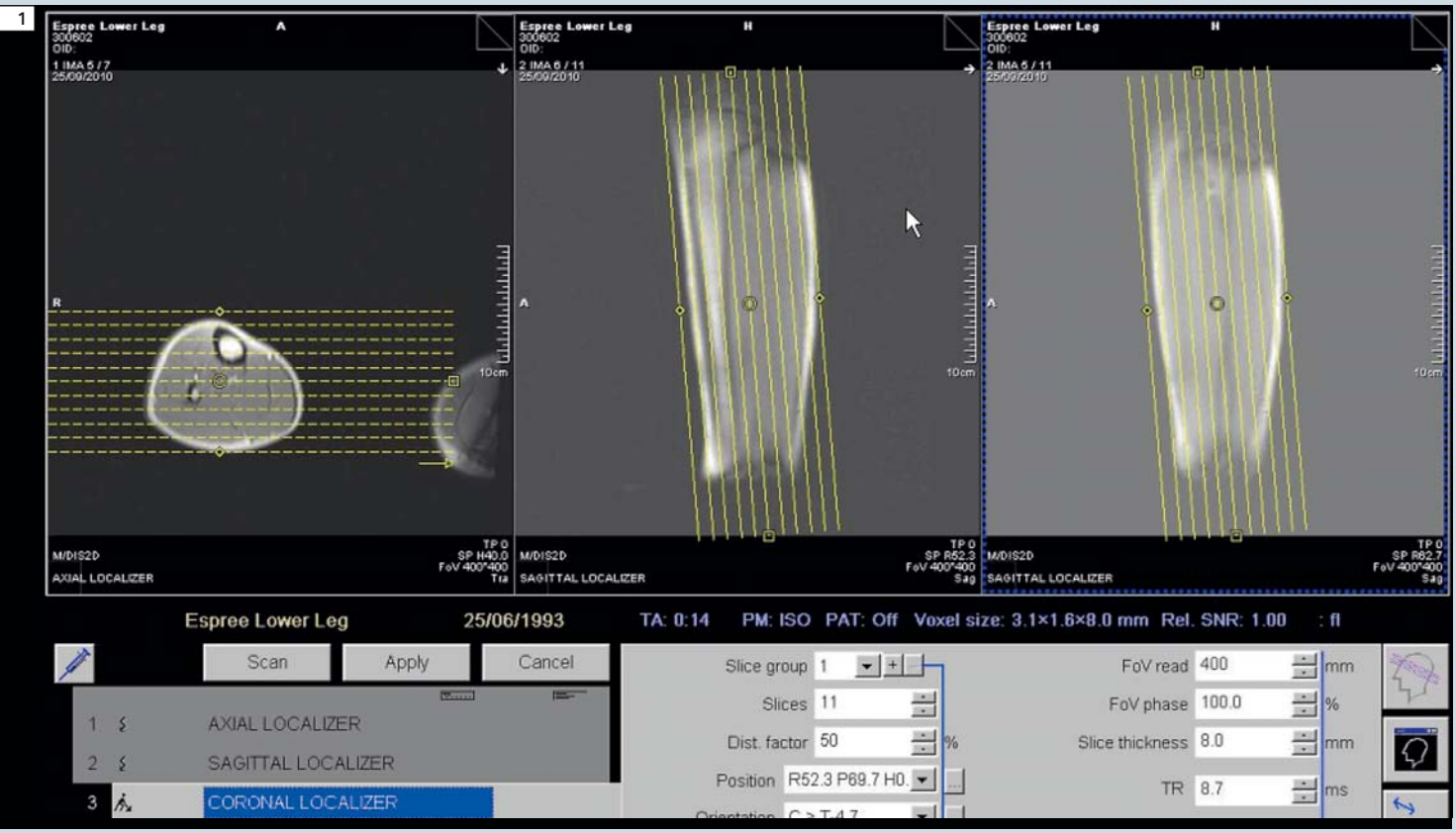

- Once the localizers are complete, the overlap for sagittal and coronal composed images needs to be determined. To view the overlap value, press Ctrl + 9 on the keyboard, which will open the overlap window. In Figure 2 we can see an overlap of 50 mm. This value can be adjusted, but it is not recommended to go below 50 mm.

2

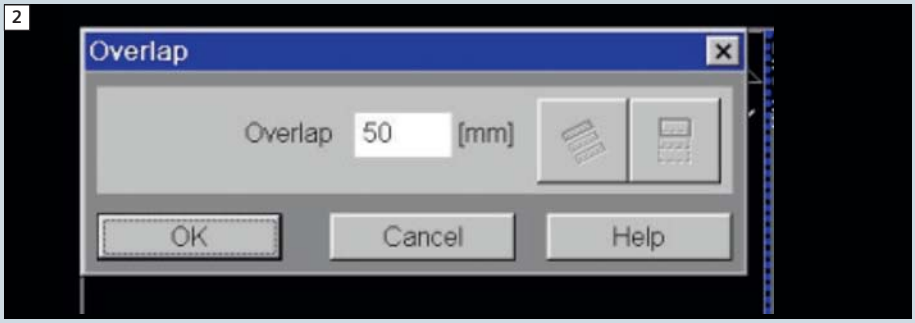

- Next, we will bring over a T1-weighted sagittal sequence with a field-of-view (FOV) of 220 mm. This is positioned on the upper half of the lower leg.

- After the slices are positioned appropriately, select the Scan button which will apply and run the T1-weighted sagittal sequence and also appends the same T1w sagittal in the open status, as seen in figure 3.

3

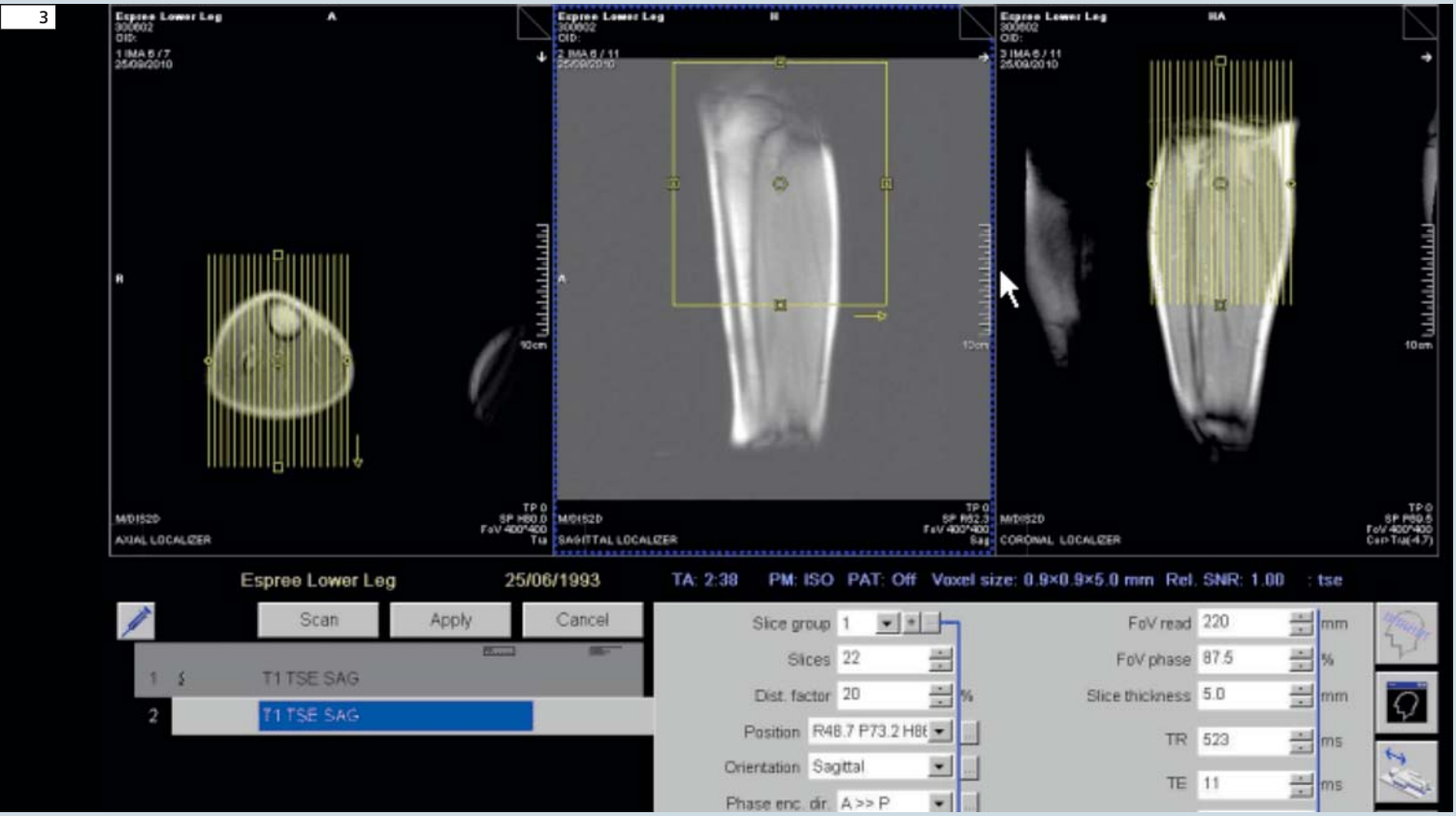

- Press Ctrl + 7 to shift the FOV and slice group to cover the lower half of the lower leg and then select **Apply**.

- Finally, we will use Composing to combine both of the T1w sagittal series into a single dataset in the Patient Browser. Once both of the T1 sagittals are finished reconstructing, select both series in the Patient Browser and select **Applications > Composing** from the main menu. Choose the MR Adaptive Composer option and then select **Patient > Save All As** to save all of the images to the Patient Browser.

4

5

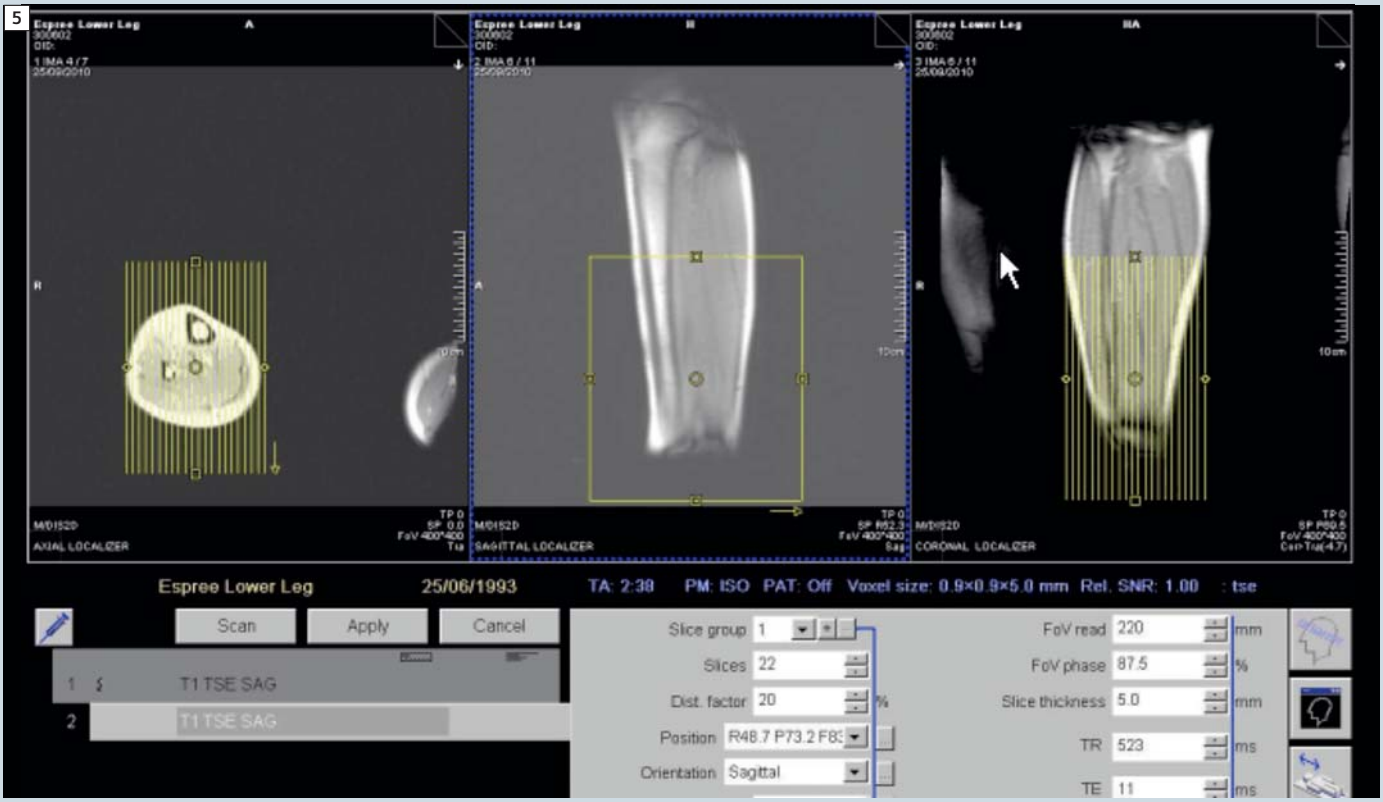

- The composed T1w sagittal series can now be used as a localizer for the rest of the study. Drag and drop the composed T1w sagittal series from the Patient Browser into one of the three positioning segments (GSP) in the Exam Task Card to use for further positioning. Repeat the steps above to acquire additional sagittal or coronal series, as demonstrated in figure 7.

6

7A

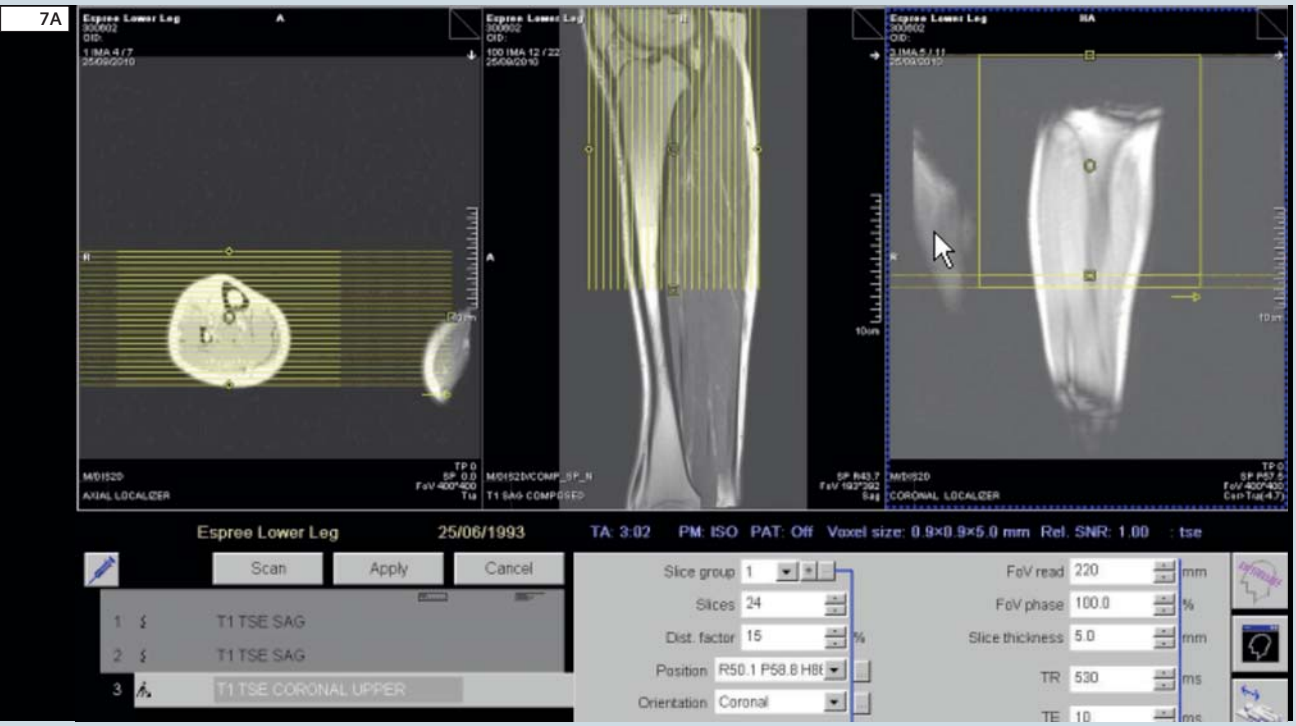
Espree Lower Leg
25/06/1993
TA: 3:02
PM: ISO
PAT: Off
Voxel size: 0.9×0.9×5.0 mm
Rel. SNR: 1.00
: tse
Scan
Apply
Cancel
1 T1 TSE SAG
2 T1 TSE SAG
3 T1 TSE CORONAL UPPER
Slice group 1
Slices 24
Dist. factor 15 %
Position R50.1 P58.8 H8
Orientation Coronal
FoV read 220 mm
FoV phase 100.0 %
Slice thickness 5.0 mm
TR 530 ms
TE 10 ms

7B

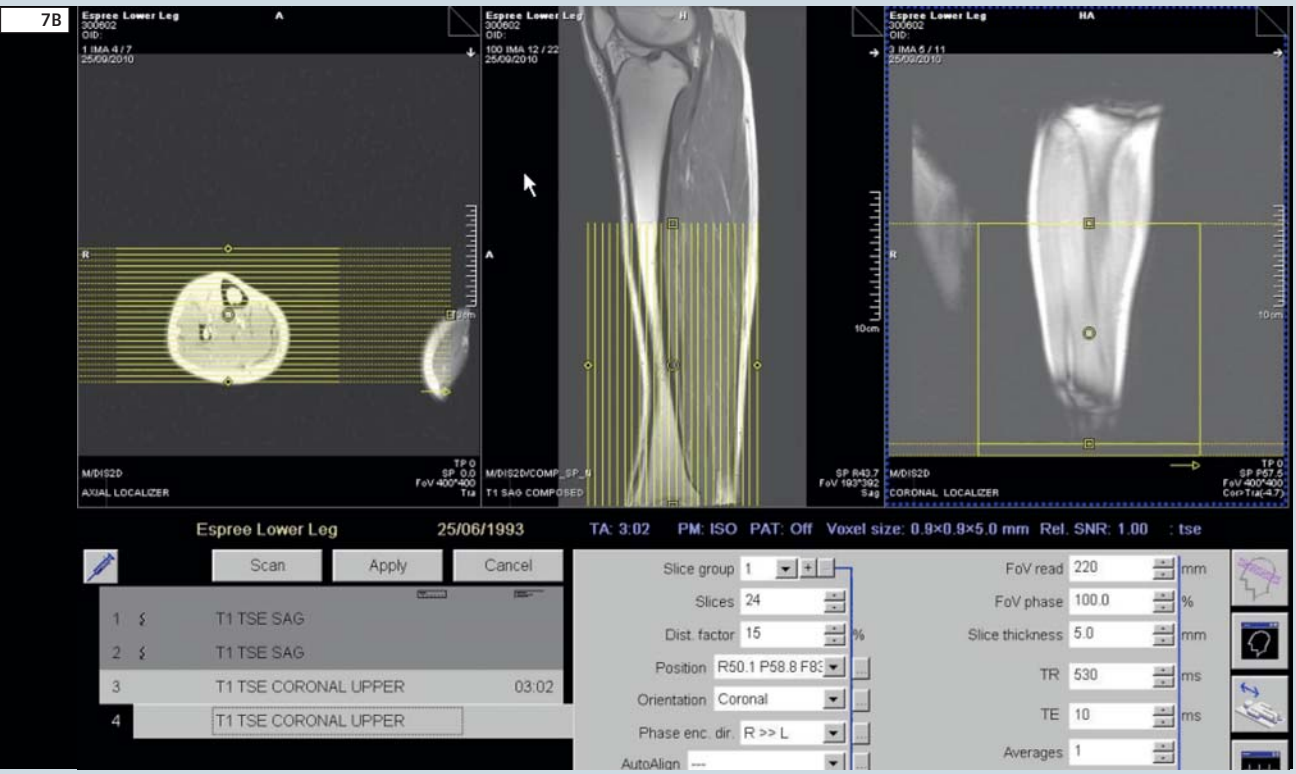
Espree Lower Leg
25/06/1993
TA: 3:02
PM: ISO
PAT: Off
Voxel size: 0.9×0.9×5.0 mm
Rel. SNR: 1.00
: tse
Scan
Apply
Cancel
1 T1 TSE SAG
2 T1 TSE SAG
3 T1 TSE CORONAL UPPER 03:02
4 T1 TSE CORONAL UPPER
Slice group 1
Slices 24
Dist. factor 15 %
Position R50.1 P58.8 F8
Orientation Coronal
Phase enc. dir. R >> L
AutoAlign ---
FoV read 220 mm
FoV phase 100.0 %
Slice thickness 5.0 mm
TR 530 ms
TE 10 ms
Averages 1

Workflow for axial imaging

- Load the composed coronal and sagittal composed images and the axial images from the localizer into the three graphical segments in the Exam Task Card. Position the axial slices on the upper portion on the lower leg, then select the **Scan** button which will apply the T1w axial sequence and also appends the same T1w axial in the open status, as seen in figure 8.

8

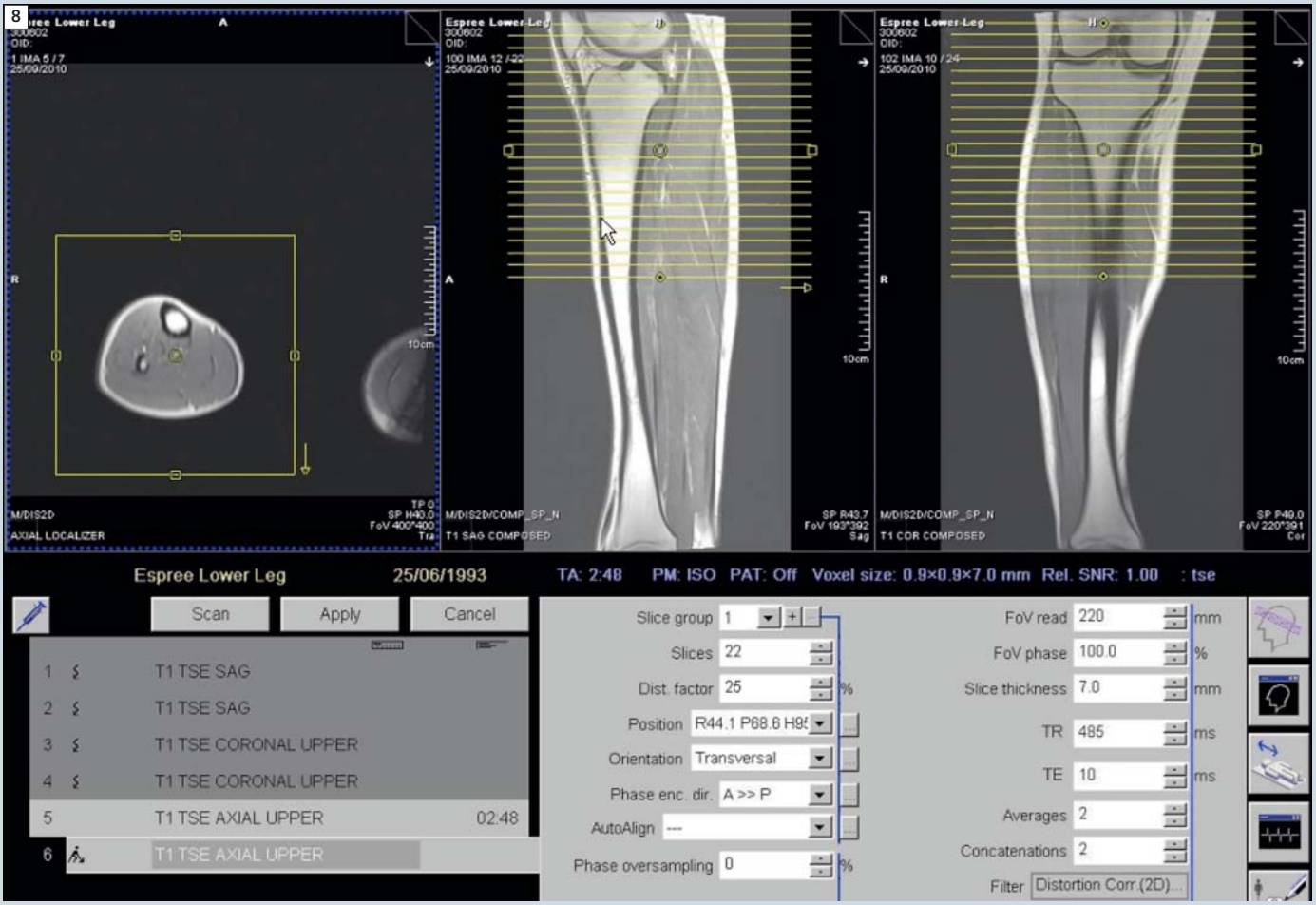

- Press Ctrl + 3 to shift the axial slice group inferiorly to cover the lower half of the lower leg and then select **Apply**.

Conclusion

The workflow for long bone imaging can be simplified and easily reproduced by using short-cut tools available on *syngo* based MAGNETOM systems: The Scan button in the exam queue along with the keyboard shortcuts Ctrl + 7 (FOV-) and Ctrl + 3 (Stack-) and the Composing software make long bone imaging a routine exam on short bore systems.

9

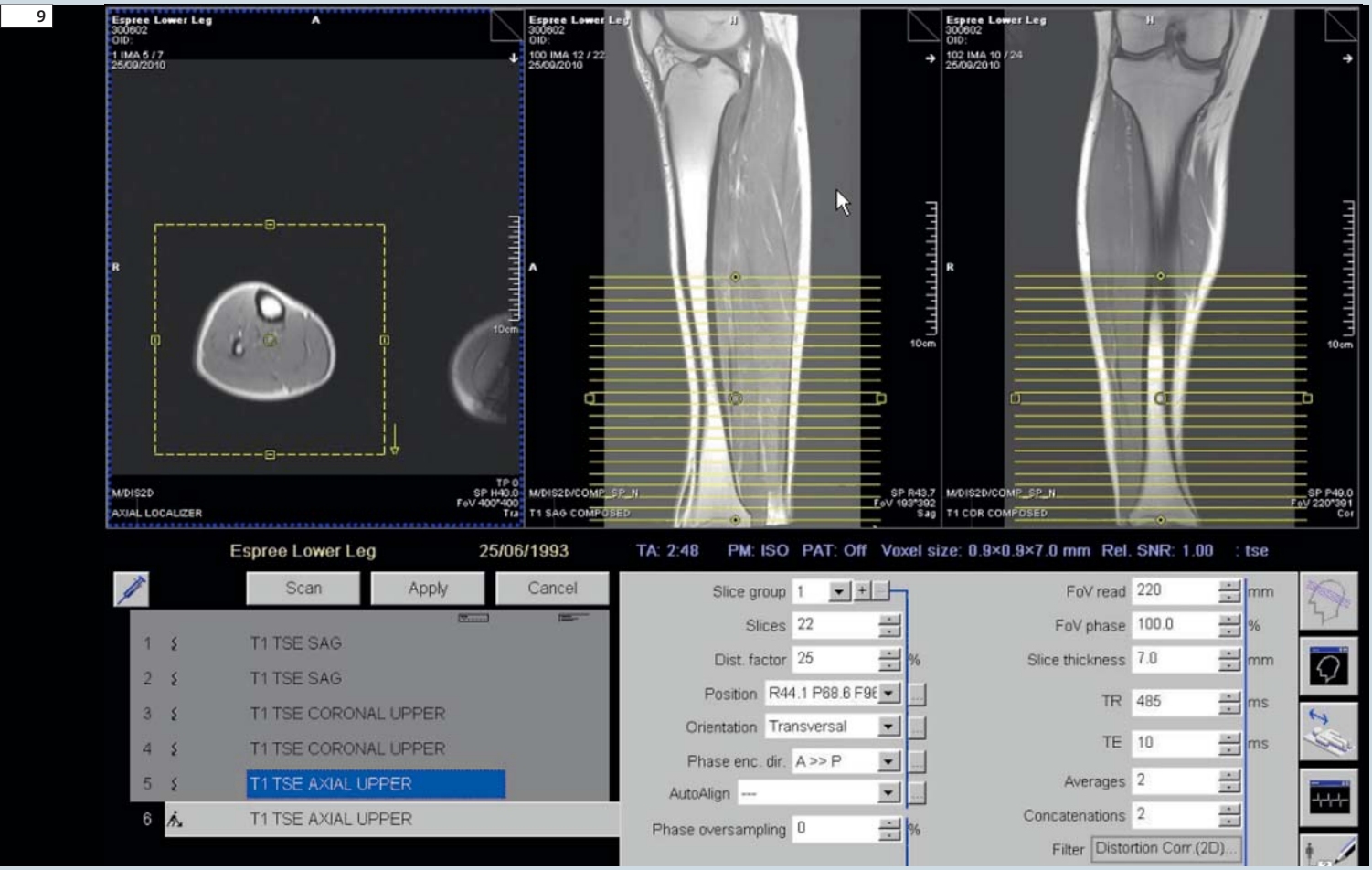

Keyboard shortcuts

Stack –	**Ctrl + 3**
Stack +	**Ctrl + 4**
Gap Filling –	**Ctrl + 5**
Gap Filling +	**Ctrl + 6**
FoV –	**Ctrl + 7**
FoV +	**Ctrl + 8**
Overlap ...	**Ctrl + 9**

Contact
Russell Grossen
MR Support Specialist
Siemens Medical Solutions USA, Inc.
RSC Applications
209 Gregson Drive
Cary, NC 27511-6495
USA
Phone: +1 (919) 319-2824
russell.grossen@siemens.com

1

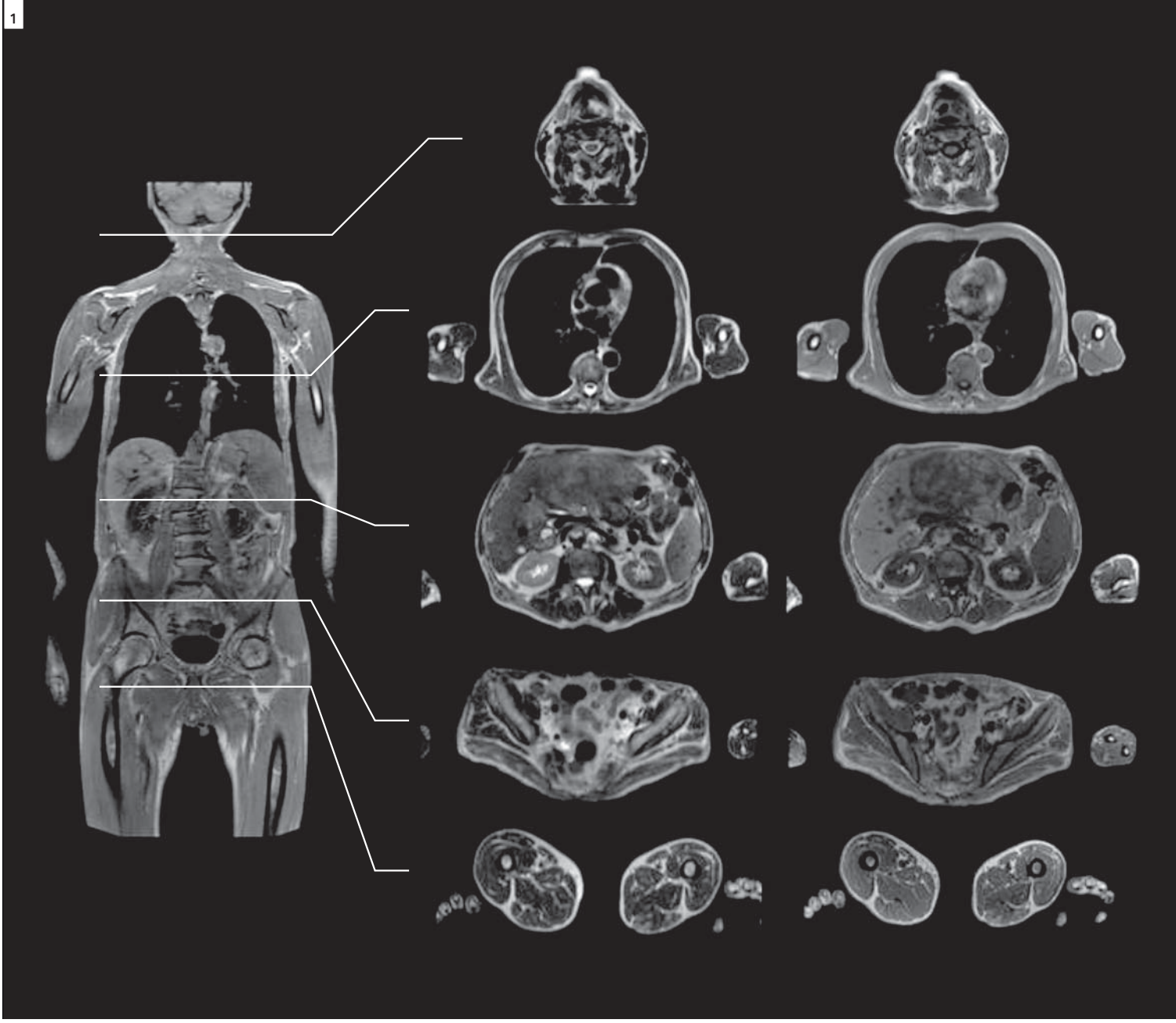

From Local Imaging to Understanding the Extent of Diseases. Clinical Need and Technical Advances in Multi-Region MRI

M. Lichy[1], B. Kiefer[1], M. Ganten[2], H.-P. Schlemmer[2]

[1]*Siemens AG, Healtcare Sector, Erlangen, Germany*
[2]*German Cancer Research Center Heidelberg, Department of Radiology, Germany*

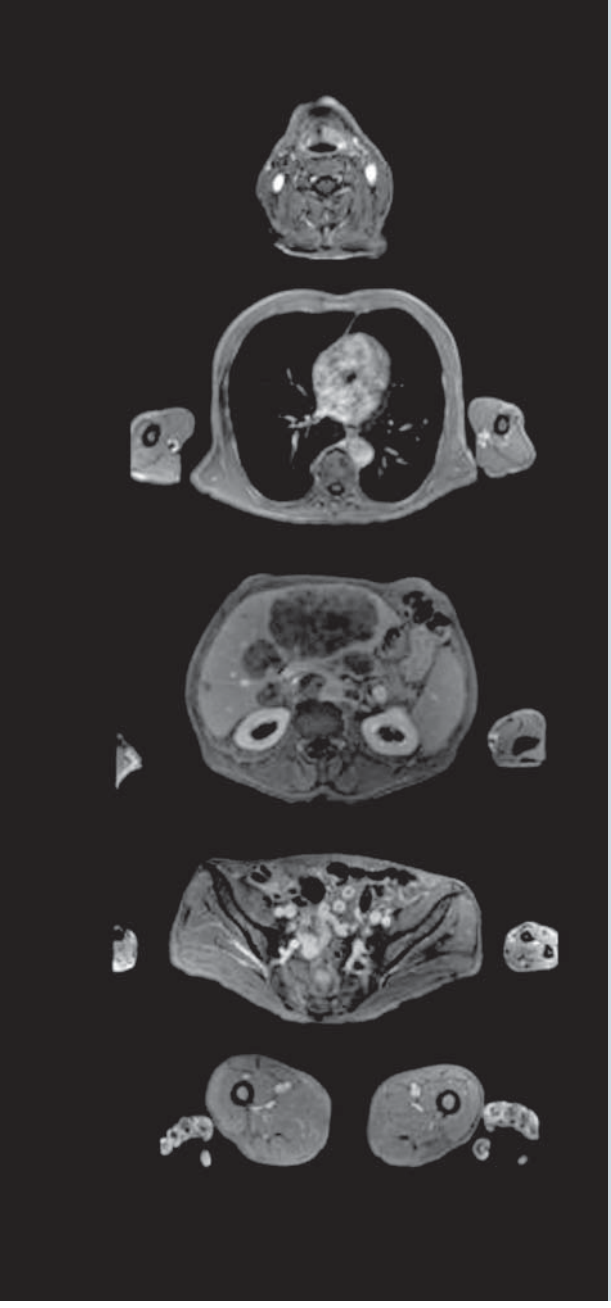

1 This is a typical example of the capabilities of MRI to provide whole-body or multi-station information for therapy assessment with the aid of efficient MR sequence techniques even in patients with advanced stage of disease. The images were acquired at 1.5 Tesla (MAGNETOM Avanto). The basic sequences are shown: coronal T1w 3D VIBE, transversal T2w HASTE, T1w 2D FLASH (pre- and post-contrast). This patient was scanned as a follow-up evaluation of systemic therapy in case of a malign melanoma. In 2009, the first manifestation of this cancer was diagnosed (digit 3 right foot). In 2010, a distant inguinal lymph node metastases was resected and the patient received local radiotherapy. After resection of a transition metastases of the right upper limb, CT scan showed suspicious lymph nodes. In addition, this patient underwent surgery because of a meningeoma of the frontal falx and the olfactoriuous nerve. Extensive metastastic spread within the liver and paraortal lymph node stages is evident as well as suspicious findings for bone filiae including diffuse contrast-enhancement of the bone marrow of the pelvis and both femura which can be interpreted as diffuse bone marrow involvement. However, based on previous scans (not shown), stable disease could be concluded.

Hardware innovation such as the introduction of multi-receiver channel whole-body scanners at 1.5 and 3 Tesla, combined with image acquisition acceleration techniques (parallel imaging), have made multi-region up to whole-body magnetic resonance imaging (MRI) possible [1]. The capability of MRI to offer best soft-tissue contrast as well as the ongoing improved understanding of systemic aspects of diseases has resulted in a wide demand for the imaging of these systemic aspects with MRI, especially for oncological examination and for vascular diseases. The capability to assess all relevant information for diagnoses, therapy planning and therapy control within one exam (e.g. TNM staging in case of rectal cancer; whole assessment of the vessel tree from the abdominal aorta to the pedal arteries in case of peripheral vessel disease) is not only appealing for clinicians and patients from a clinical / practical point-of-view; but because multi-region MRI can potentially replace multiple exams which cover only dedicated aspects, then time and money saving benefits are also evident.

Multi-region MRI in clinical routine

More flexible protocols of multiplanar multi-region MR exams have been developed by several working groups to reduce total imaging time and improve robustness of MR scans (e.g. HASTE technique for T2-weighted contrast; navigator based techniques instead of respiratory belt for motion freezing MRI). In addition, to improve diagnostic accuracy and to focus on disease relevant findings, three-dimensional imaging techniques (dynamic contrast-enhanced scans for detection of liver metastases; T2w TSE sequences for advanced pelvic tumors [2], T1w VIBE technique for detection of lung nodules) can easily be integrated within such a diagnostic work-up. So far, whole-body MRI has shown advantages for the detection of

distant metastatic disease, especially from tumors frequently spreading to the liver or brain [3, 4]. It is especially useful as a radiation-free alternative for the surveillance of tumor patients with a positive prognosis and the need for multiple follow-up exams. Furthermore, it has been introduced as a whole-body bone marrow screening application. Within this context, high accuracy for the detection of skeletal metastases and staging of hematologic diseases, such as multiple myeloma or lymphoma, is given.

But even with the given evidence and the known advantages of whole-body / multi-region MRI, its clinical broad application is often limited. Longer examination times and complex scan planning compared to other imaging modalities are perhaps the main limiting factors in daily routine. The need to reduce the complexity of such multi-region / whole-body MR scans has resulted in the development of continuously moving table MR imaging techniques. With less interaction required, a significant reduction of imaging time has been demonstrated – without reducing image quality. This imaging technique has already proven its clinical potential [5 – 8] not only for large field-of-view MR angiography but also for efficient multi-region scanning for tumor staging, and has consequently found its way into daily practice as a reliable and efficient imaging technique.

Hybrid imaging techniques

Within the last decade, however, MRI has also been challenged especially for oncological applications by the advent of a hybrid imaging technology: The combination of PET/CT (PET = positron emission tomography; CT = computed tomography) allows not only the assessment of morphological changes but offers also insight into metabolism and specific aspects of biology. For example, PET/CT with ^{18}F-FDG allows the detection of an increase of glucose consumption, a common feature of tumor tissue. On the other hand, magnetic resonance can be used to understand functional aspects and impairment of tissue: For example, vessel density and permeability can be derived from T1w dynamic contrast-enhanced scans. The further advantages of diffusion-weighted imaging (DWI), which can provide information about cell density, and its application as a whole-body imaging technique, have offered new opportunities in managing oncologic diseases [9 – 11]. The exact role of morphologic (continuously moving table) MR, functional MRI (DWI) and PET(/CT) in patient care is subject of ongoing debate. Beyond that, the combination of MR and PET in one integrated, simultaneous whole-body imaging modality has now become clinical reality – with so far unseen possibilities in managing systemic aspects of diseases [12, 13].

Conclusion

Multi-region / whole-body MRI represents a comprehensive diagnostic tool that signals a clear improvement not only in diagnoses but also in therapy planning and follow-up in a wide range of applications, especially in oncological, but also vascular, diseases. In recent years further technology developments such as the continuously moving MR imaging techniques and improvements in scanner user interfaces and reading software have assisted the technologists and clinicians in efficient and accurate multi-region / whole-body MR scanning.

Contact
Professor Heinz-Peter Schlemmer, M.D., Ph.D.
German Cancer Research Center
Radiology (E010)
Im Neuenheimer Feld 280
69120 Heidelberg
Germany
Phone: +49 6221 42 2563
h.schlemmer@dkfz-heidelberg.de

References

1 Schlemmer HP et al.: Fast whole-body assessment of metastatic disease using a novel magnetic resonance imaging system: initial experiences. Invest Radiol. 2005 Feb;40(2):64-71.
2 Lichy MP et al.: Magnetic resonance imaging of the body trunk using a single-slab, 3-dimensional, T2-weighted turbo-spin-echo sequence with high sampling efficiency (SPACE) for high spatial resolution imaging: initial clinical experiences. Invest Radiol. 2005 Dec;40(12):754-60.
3 Schmidt GP et al.: Whole-body MRI at 1.5 T and 3 T compared with FDG-PET-CT for the detection of tumour recurrence in patients with colorectal cancer. Eur Radiol. 2009 Jun;19(6):1366-78. Epub 2009 Feb 4.
4 Schmidt GP et al.: Comprehensive imaging of tumor recurrence in breast cancer patients using whole-body MRI at 1.5 and 3 T compared to FDG-PET-CT. Eur J Radiol. 2008 Jan;65(1):47-58. Epub 2007 Dec 20.
5 Bley TA et al.: Sliding multislice MRI for abdominal staging of rectal gastrointestinal stromal tumours. In Vivo. 2007 Sep-Oct;21(5):891-4.
6 Sommer G et al.: Sliding multislice MRI for abdominal staging of patients with pelvic malignancies: a pilot study. J Magn Reson Imaging. 2008 Mar;27(3):666-72.
7 Koziel Ket al.: Peripheral MRA with continuous table movement: Imaging speed and robustness compared to a conventional stepping table technique. Eur J Radiol. 2011 Feb 3.
8 Haneder S et al.: Magnetic resonance angiography (MRA) of the calf station at 3.0 T: intraindividual comparison of non-enhanced ECG-gated flow-dependent MRA, continuous table movement MRA and time-resolved MRA. Eur Radiol. 2011 Jul;21(7):1452-61. Epub 2011 Jan 28.
9 Lichy MP et al.: Tumor detection by diffusion-weighted MRI and ADC-mapping--initial clinical experiences in comparison to PET-CT. Invest Radiol. 2007 Sep;42(9):605-13.
10 Padhani AR, Koh DM. Diffusion MR imaging for monitoring of treatment response. Magn Reson Imaging Clin N Am. 2011 Feb;19(1):181-209. Review.
11 Horger M et al.: Whole-body diffusion-weighted MRI with apparent diffusion coefficient mapping for early response monitoring in multiple myeloma: preliminary results. AJR Am J Roentgenol. 2011 Jun;196(6):W790-5.
12 Judenhofer MS et al.: Simultaneous PET-MRI: a new approach for functional and morphological imaging. Nat Med. 2008 Apr;14(4):459-65. Epub 2008 Mar 23.
13 von Schulthess GK, Schlemmer HP. A look ahead: PET/MR versus PET/CT. Eur J Nucl Med Mol Imaging. 2009 Mar;36 Suppl 1:S3-9.

Relevant clinical information at your fingertips

From technology to clinical applications, you will find all the latest news on Siemens MR at

www.siemens.com/magnetom-world

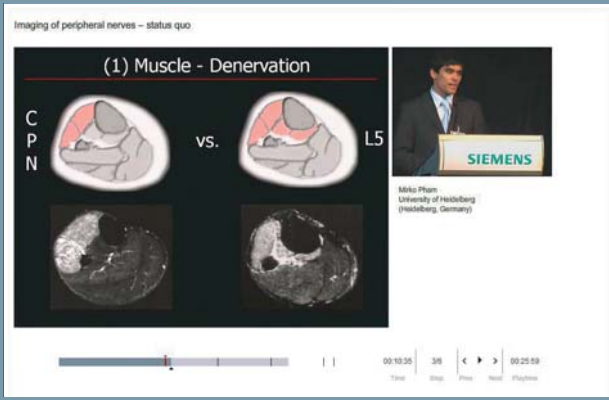

Don't miss the talks of international experts on Magnetic Resonance Imaging.

Go to
Education > e-trainings & Presentations

The centerpiece of the MAGNETOM World Internet platform consists of our users' clinical results. Here you will find case reports and clinical methods.

Go to
Clinical Corner > Case Studies

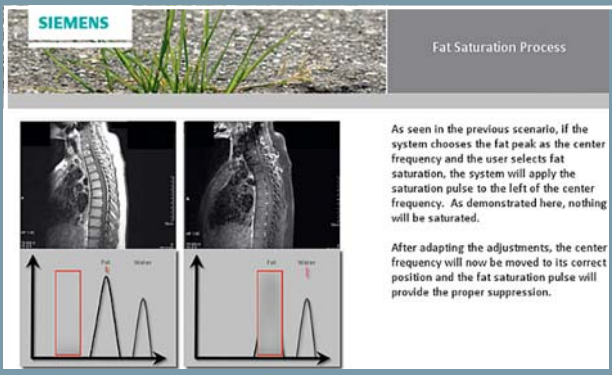

Just a mouse click away you will find application videos and useful tips allowing you to optimize your daily MR examinations.

Go to
Clinical Corner > Application Tips

For the whole range of clinical MR information visit us at

www.siemens.com/magnetom-world

Multi-Station Examinations in Pediatric MRI

Markus Lentschig, M.D.

ZEMODI, Zentrum für moderne Diagnostik, Bremen, Germany

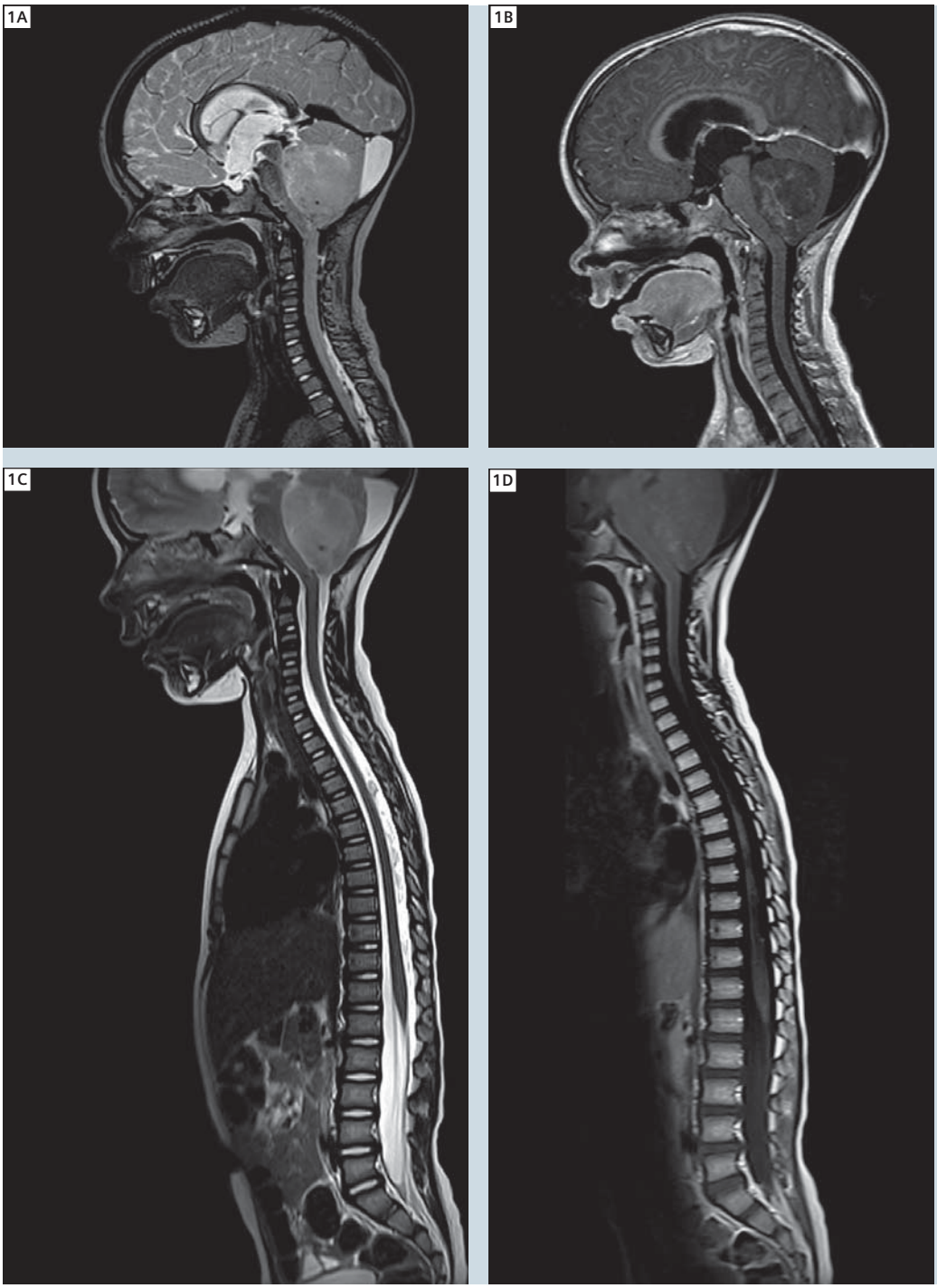

1 Images of a staging MRI of a 3-year-old boy with proven medulloblastoma are shown. In addition to detailed information about the primary tumor, evaluation of the whole central nervous system is required.
(1A) 3D T2w SPACE
(1B) 3D T1w ce MPRAGE
(1C) 2D T2w TSE and corresponding T1w TSE ce
(1D) for evaluation of the myelon. Images acquired with 1.5T MAGNETOM Avanto.

Background

Recent years have seen an increasing demand for pediatric MR examinations, independently of other developments in imaging technology that benefit children* / adolescents, such as the significant reduction of radiation dosage in CT scans, or the evolution of ultrasound including CEUS (contrast-enhanced ultrasound). It is, of course, also true that the increase in numbers of pediatric MRI scans has not been in line with the overall growth of MR referrals for all departments, because indications of pediatric MRI, as well as planning, conducting and reading of these exams differ significantly from adult MRI. Sedation is frequently required, especially in very young children, whilst the wide, 24/7 availability of ultrasound and its high diagnostic performance are other limiting factors when it comes to determining why and when MRI is to be used to image diseases in children.

However, ultrasound also has its limitations. Firstly, the results of ultrasound exams depend on the skills of the radiologist / pediatrician: A high variance is often seen in clinical reality when it comes to quantification of findings especially for follow-up exams performed by different physicians. Secondly, they offer only a partial insight into the body; and important structures like the central nervous system or bones are only partially evaluable, or not at all, (depending on age) with this method. Of course, inter-observer variability and quality assurance are familiar topics to us radiologists; but by scanning large volumes in high detail, CT and MRI have clear advantages when it comes to reliable and repeatable results. The documentation of MRI/CT is also different to ultrasound: It allows a much more comprehensive analysis also for questions which arise retrospectively after the exam was conducted.

Combining these advantages and adding the diagnostic performance (including the capability to derive functional parameters) for most indications and lack of any radiation, it is clear why MRI nowadays plays such an important role in pediatric imaging, especially when imaging is required to trigger therapy decisions with severe consequences to the child. There has been much written about protocols, indications and the techniques to be used. This issue of the MAGNETOM Flash also contains an extensive overview of whole-body MRI in children. In contrast to the broad range of indications in imaging adults, pediatric imaging with MRI aims very often to be more systemic and perhaps as a consequence of MRI creating special conditions, especially for young children, multi-stage examinations are frequently performed. This case series presents some examples from our daily routine to

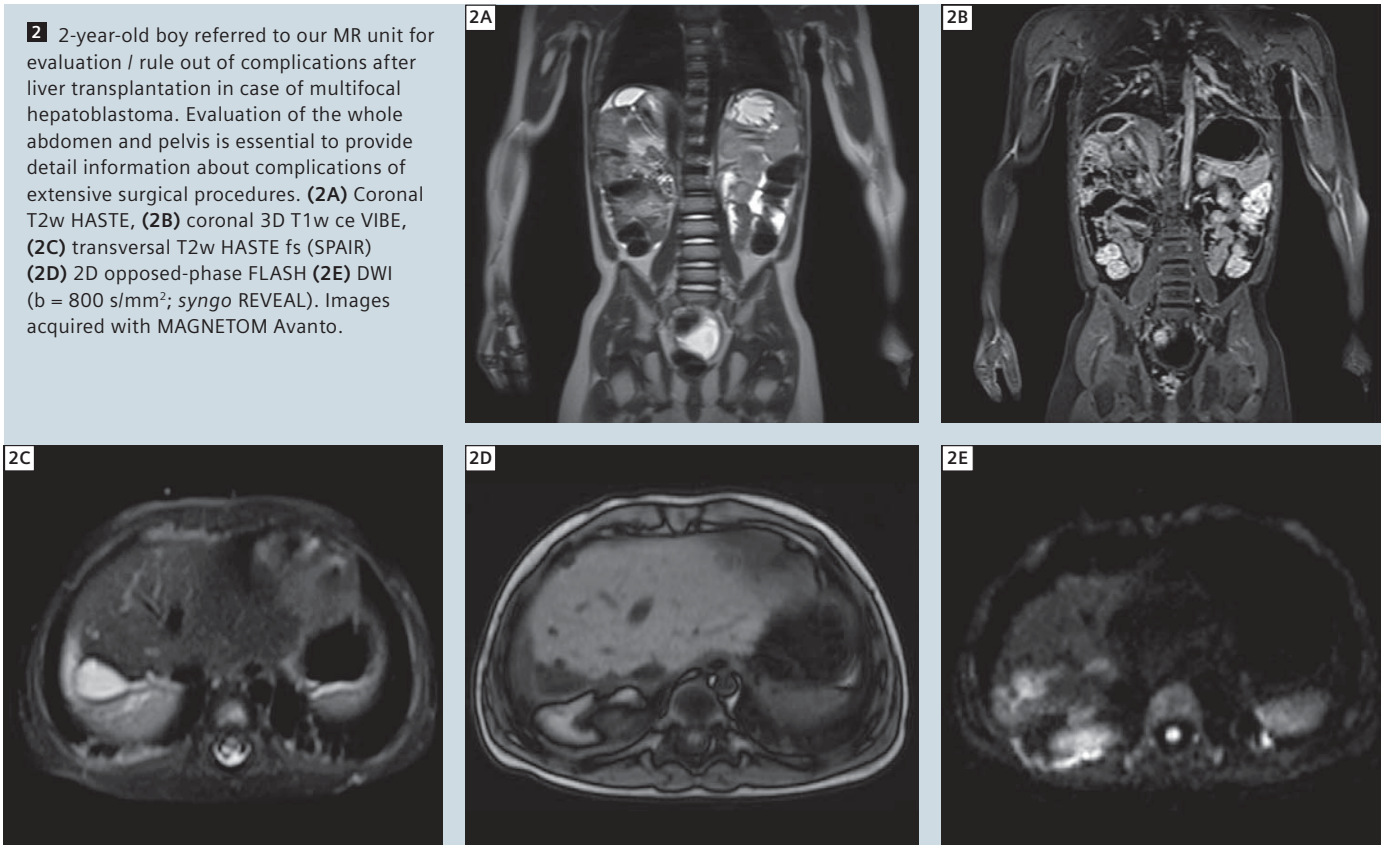

2 2-year-old boy referred to our MR unit for evaluation / rule out of complications after liver transplantation in case of multifocal hepatoblastoma. Evaluation of the whole abdomen and pelvis is essential to provide detail information about complications of extensive surgical procedures. **(2A)** Coronal T2w HASTE, **(2B)** coronal 3D T1w ce VIBE, **(2C)** transversal T2w HASTE fs (SPAIR) **(2D)** 2D opposed-phase FLASH **(2E)** DWI (b = 800 s/mm²; *syngo* REVEAL). Images acquired with MAGNETOM Avanto.

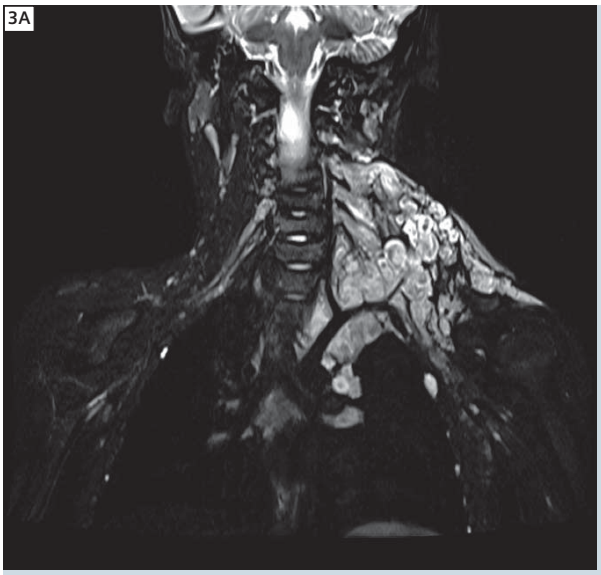

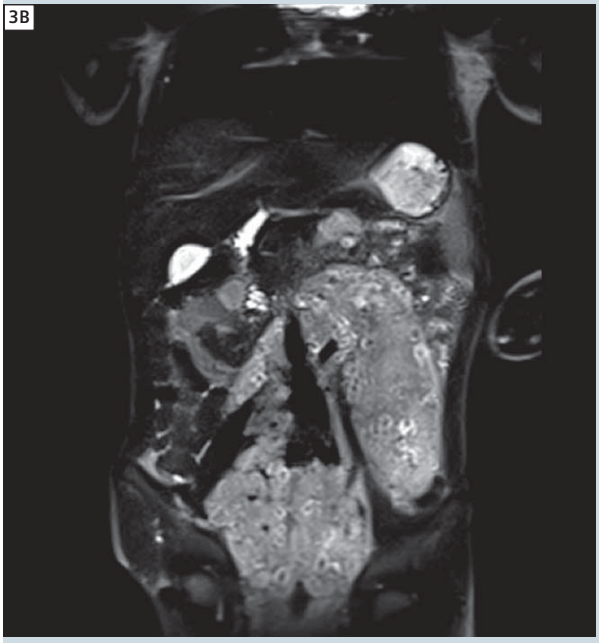

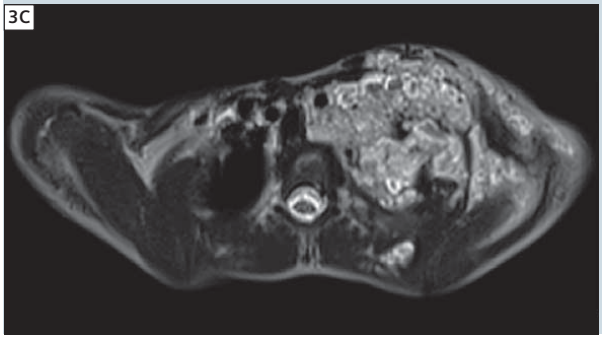

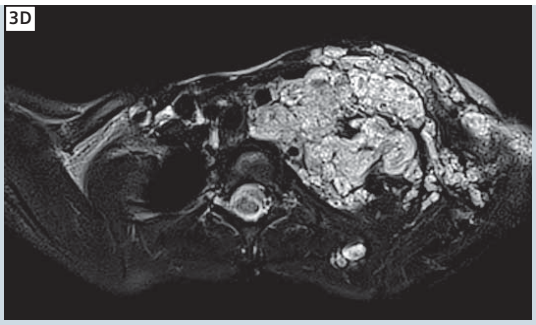

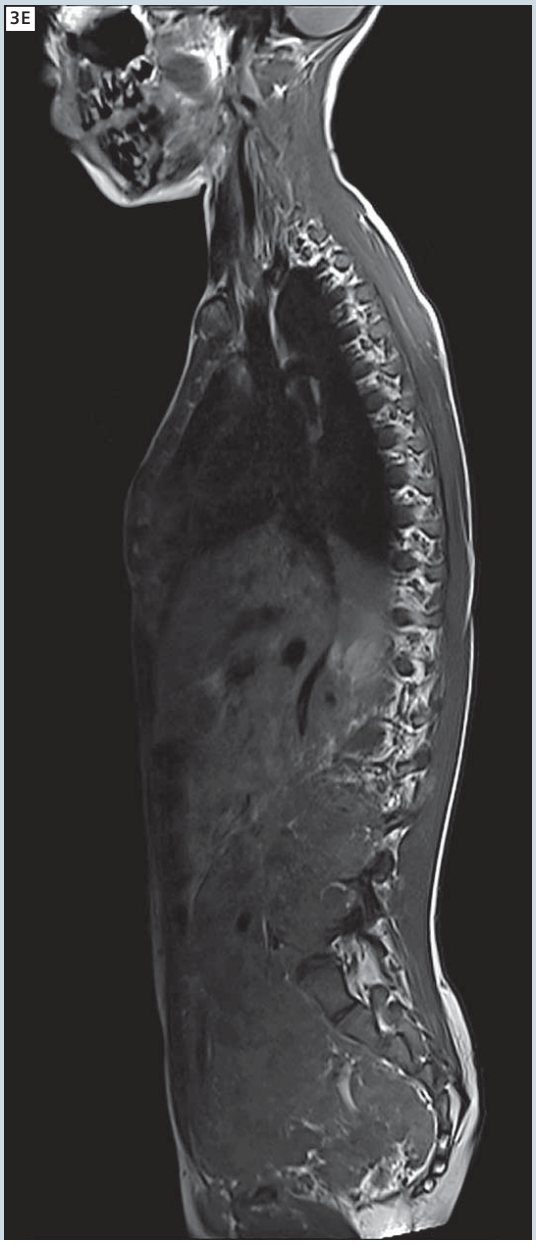

3 Detection of a malignant transformation of neurofibromas are challenging. MRI with its superior soft-tissue contrast is therefore often used as the method of choice for follow-up of patients with Recklingshausen's disease. Here we show the MRI exam of a 9-year-old boy with extensive involvement especially of the left cervical, but also the huge growth of neurofibromas in the abdomen / retroperitoneum. Additional value of ^{18}F-FDG PET in the detection of malignancy is reported (not shown in this case) and may certainly be one of the future applications of MR/PET for this indication. **(3A)** Coronal T2w STIR of the cervical plexus and **(3B)** T2w HASTE of the abdomen / retroperitoneum, **(3C)** transversal T2w HASTE and **(3D)** T2w TSE with motion correction (*syngo* BLADE) of the left cervical tumor bulk, **(3E)** sagittal T1w ce without fs for evaluation of the abdominal manifestations. The images were acquired with 1.5T MAGNETOM Espree.

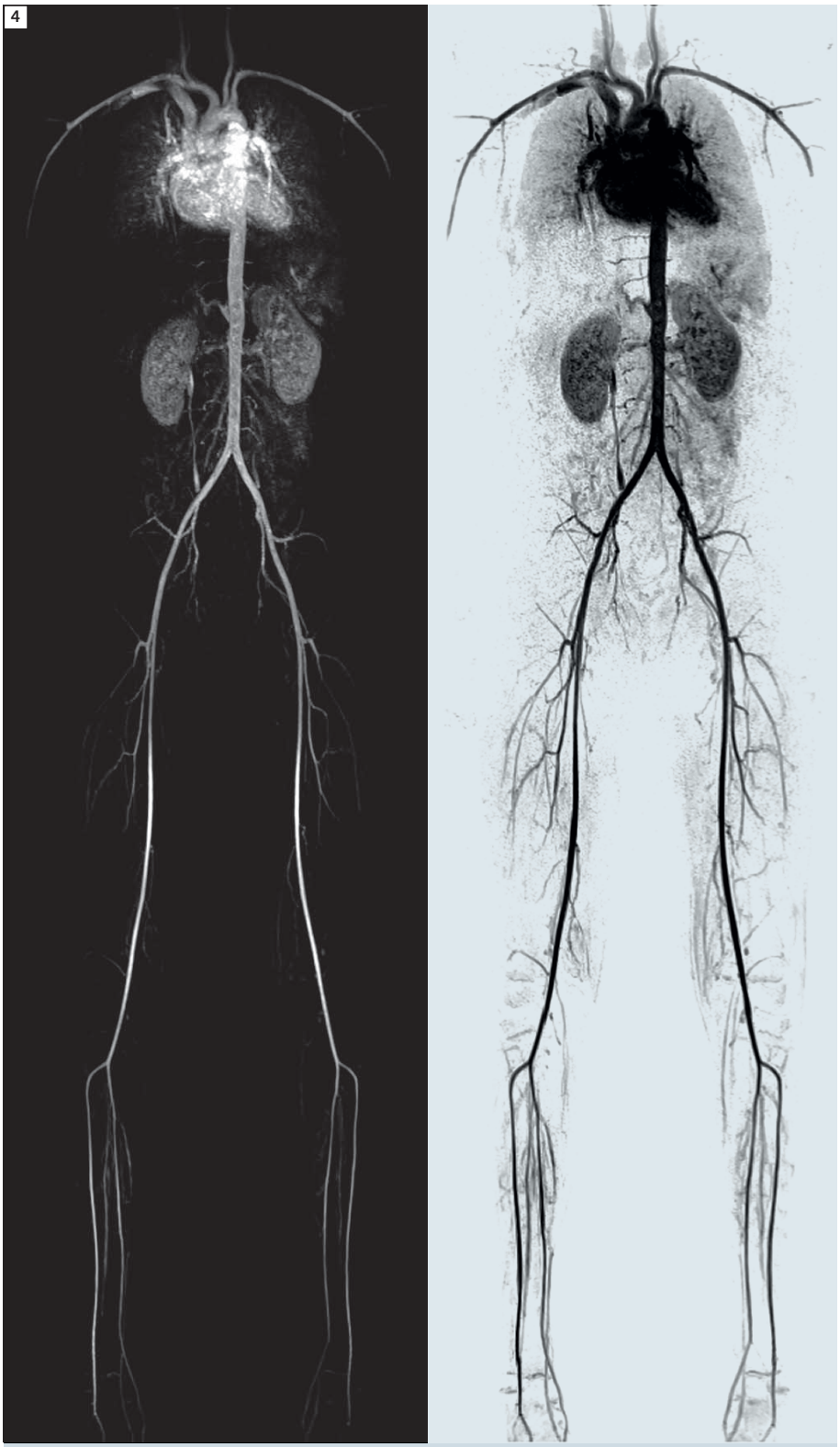

4 Evaluation of the main arteries throughout the whole body trunk and lower extremities where there is suspicion of panarteriitis nodosa. Maximum intensity projections (MIP) and inverted image derived from a ce 3D FLASH, acquired as continuously moving table MRI (*syngo* TimCT) are shown. Images acquired with 1.5T MAGNETOM Avanto.

demonstrate the quality of today's routine pediatric MR examinations and how today's scanner technology can assist in the assessment of systemic aspects of disease.

*MR scanning has not been established as safe for imaging fetuses and infants under two years of age. The responsible physician must evaluate the benefit of the MRI examination in comparison to other imaging procedures.

Contact
Markus G. Lentschig, M.D.
ZEMODI
Zentrum für moderne Diagnostik
MRT und MR/PET
Schwachhauser Heerstr. 63a
D-28211 Bremen
Germany
Phone +49 421 69641-600
Fax +49 421 69641-649
www.zemodi.de

Pediatric Whole-Body MR Imaging Status Quo and Practical Aspects in Daily Routine

Jürgen Schäfer, Ilias Tsiflikas, Claus D. Claussen, Ulrich Kramer

University Hospital of Tübingen, Department of Radiology, Tübingen, Germany

Introduction

Up until the start of the last decade, whole-body magnetic resonance imaging could not be performed in one single examination due to the technical constraints associated with the equipment e.g., field-of-view (FOV), number of coils, and number of high-frequency channels were all subject to limitations. In addition, it was extremely time-consuming to transfer both patients and coils to perform a multi-stage/whole-body MRI examination (WB-MRI). It was only when MR systems were enhanced by means of coil elements that offer flexible switching and multiple receiver channels, as well as automatic table movement (Tim – Total imaging matrix; introduced in 2003) that whole-body examinations with high spatial resolution became clinically feasible. Furthermore, the use of high-density coils is

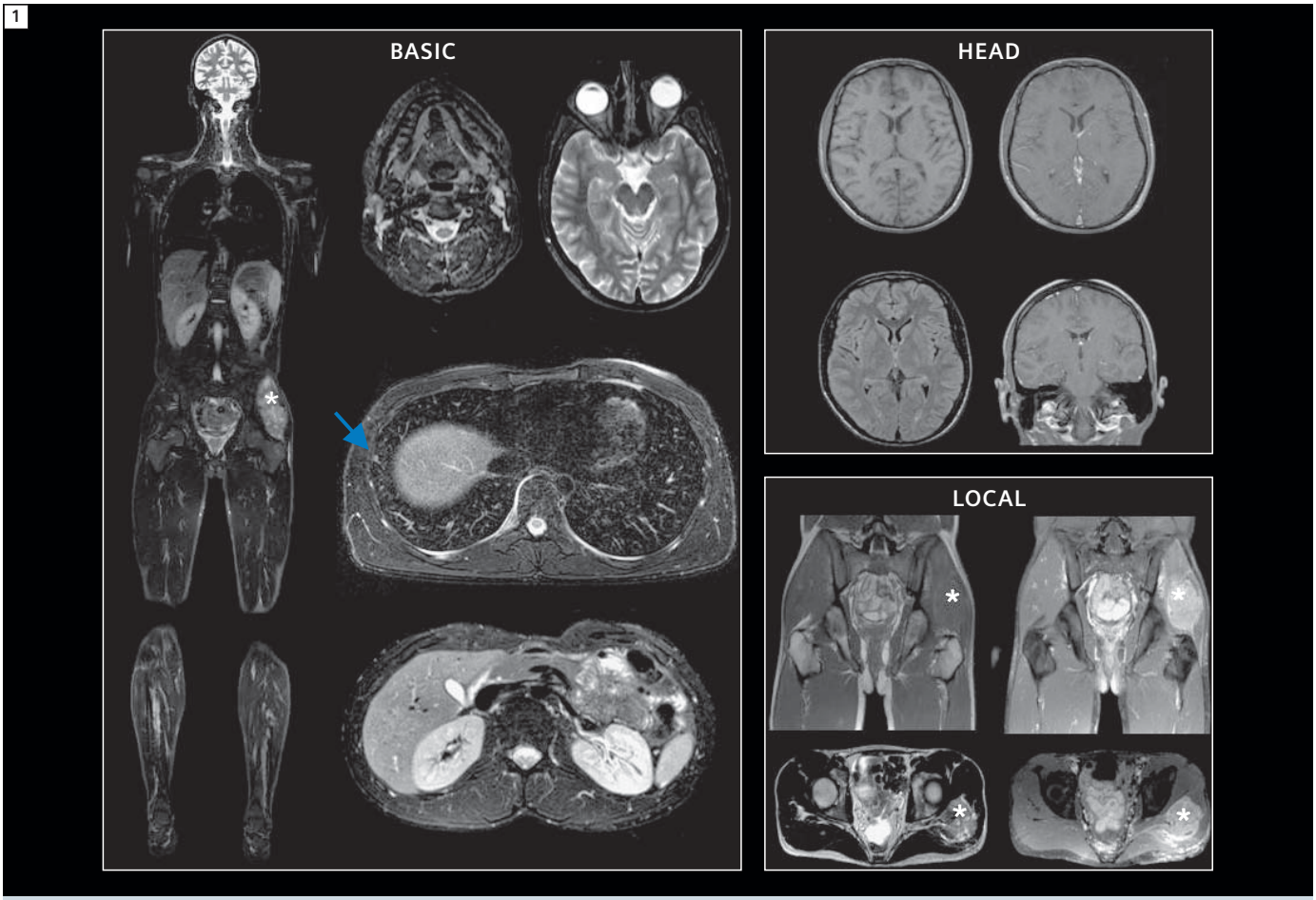

1 Sequence protocol for staging solid pediatric tumors. 17-year-old male, clearcell sarcoma in the gluteal region (asterisk) and pulmonary metastasis (arrow). Left side: basic module (coronal TIRM whole-body, transversal TIRM head and neck, T2w TSE fat sat with PACE and ECG triggering thorax, T2w TSE fat sat with PACE). Upper right side: head module. Lower right side: local staging.

absolutely essential if parallel imaging techniques are to be used effectively, because they play a key role in allowing MRI to be performed within a clinically-efficient time frame, without compromising the resolution, etc. [1]. The use of this MR technology is now widespread and it serves as the basis for developing fully-integrated MR/PET systems (molecular MRI) that are suitable for clinical applications [2].

WB-MRI marks a paradigm shift in MR imaging, because examinations no longer have to be purely organ-focused and can be used to carry out illness-related evaluations instead. As far as children* are concerned, systematic diagnosis without using ionizing radiation is of paramount importance. At the same time, fewer multiple and sequentially performed partial-body examinations are required. The benefits of combining diagnostic information for treatment-related decisions into a single examination are clear. However, within the field of pediatric radiology in particular, it is essential to take into account that many examinations require sedation.

A range of main indications have emerged for WB-MRI in pediatric centers:

- Assessment of multifocality in the case of bone marrow processes
- Rheumatic diseases, including fever syndromes
- Diagnosis of the spread of solid tumors

There are, however, several questions surrounding the use of WB-MRI, which relate to the following issues:

- Examination protocols and strategies
- Findings evaluation and reading
- Indications and diagnostic accuracy

This review aims to summarize the current state of this method in everyday clinical applications. It also covers practice-related aspects which are of significance when WB-MRI is used in a pediatric context. In this respect, we are able to draw on our own experience of having carried out over 600 whole-body examinations on children* and young patients, which also clearly demonstrates the clinical relevance of this method in everyday clinical routine.

* MR scanning has not been established as safe for imaging fetuses and infants under two years of age. The responsible physician must evaluate the benefit of the MRI examination in comparison to other imaging procedures.

Technical requirements, examination protocols, and strategies

The current systems support the planning and implementation of a whole-body examination in diverse ways; for example, table movement, coil selection, and calibration for parallel imaging are fully automatic. The whole-body images that are often required to demonstrate findings are also generated automatically by the scanner and variations in signal intensity, which are in part due to multiple-channel coils are optimally compensated.

Patients are examined in a supine position with their arms resting by their sides. Consequently, the arms can also be included in the scan and assessed easily. In our experience, it takes approximately 3 minutes to put the coils in place for a WB-MRI, although the specific needs of the child must be taken into account. Experience to date shows that using a large number of surface coils only rarely causes claustrophobia, even among children. Nevertheless, our experience shows that the administration of a sedative/endotracheal anesthesia should be factored in when planning a whole-body MRI for a child up to the age of seven. This decision depends both on the examination time and, therefore, on the clinical question, as well as the local conditions for preparing a child appropriately for an MRI examination. Essentially, preparing a child for a whole-body scan is no different from what is required for a partial body scan. However, an effort should be made to keep the scan time as short as possible, particularly in the case of non-sedated patients. In general, this necessitates thorough protocol planning prior to the start of the examination, with modifications being implemented during the actual scan where necessary.

Table 1 provides an overview of the MRI protocols used at our institution. Even though no standardized examination protocol has yet been established for pediatric WB-MRI, STIR (Short Tau Inversion Recovery) sequence acquisition is now commonplace and has proven to offer the sensitivity for practically all medical issues [3–10]. Therefore, a coronal STIR sequence is normally used as search sequence at the beginning of the examination. What we refer to as the basic module (Fig. 1) is then supplemented by transverse STIR/T2-weighted imaging with fat saturation in the head/neck area and trunk of the body. At the same time, the use of a respiratory trigger in the abdomen as well as a respiratory and cardiac trigger in the thorax achieves excellent image quality, which enables assessment of the internal organs, including the lungs (Fig. 2). As an alternative or in addition, the BLADE technique can be used to further reduce both motion and flow artifacts [10]. Diffusion-weighted imaging (DWI) is not included in the table shown. As clinical experience involving this technology grows, the proposed examination protocols will undoubtedly undergo significant modifications.

Further sequences are determined by indication and disease (for example, bone and bone-marrow vs. whole-body staging for solid tumors) and by the clinical context (initial examination vs. follow-up). To facilitate visualization of the spinal column processes, a sagittal plane is advantageous [7], combining STIR and T1-weighted native sequences helps to distinguish marrow infiltrates from reactive changes or red bone marrow [3, 7, 10]. Small osteoblastic metastases can also be detected more reliably using T1-weighted sequences [12]. Some working groups have proposed the additional administration of contrast agents for bone marrow pathologies within the context of WB-MRI [3, 13].

Particularly in the context of initial diagnosis of soft tissue tumors or tumor-like pathologies in children, it is our policy to run additional native sequences in both the cranial and abdominal areas (Table 1) based on the experience of other working groups [14], although this approach has not even been adopted in recent studies [6, 15]. In our view, T1-weighted fat-saturated sequences are also required

Table 1:
1.5T WB-MRI protocols used at the University of Tübingen for pediatric patients

Module	Region	Sequence	Slice thickness [mm] **
Basic module	WB	coronal STIR TSE	3.0 – 5.0
	Head/Neck	transversal STIR TSE	4.0
	Thorax	transversal T2 TSE fs*	4.0
	Abdomen and Pelvis	transversal T2 TSE fs*	4.0
Extensions	WB	coronal T1w TSE	3.0 – 5.0
	Brain	transversal FLAIR	4.0
	Brain	transversal T1w-SE	4.0
	Abdomen and Pelvis	transversaT1w 2D GRE	4.0
Extensions after CM application	WB	coronal T1w TSE fs	3.0 – 5.0
	Brain	transversal / coronal T1w-SE	4.0
	Neck, Thorax Abdomen and Pelvis	transversal T1w 2D GRE fs	4.0

*Triggering: Thorax (breath and ECG), Abdomen (breath).
**Adaption of resolution to size /age required.
***Measurement times are given for 5 stations. When imaging infants and small children this can be reduced to 2 to 3 stations.
fs (fat saturation) technique is used depending on region-of-interest.

after administering contrast agents (Table 1) if the WB-MRI is to provide a definitive diagnosis of tumors beyond the scope of medical studies and the available reference standard (e.g. Positron Emission Tomography, PET). Further indications for administering contrast agents are when neoplastic syndromes can be discounted and in the case of fever syndromes or rheumatic joint diseases when the synovia need to be analyzed.
A distinction needs to be made between the proposed protocols referred to above and dedicated regional organ protocols similar to those used for partial body measurements. For example, in the case of solid tumors, these are based on guidelines or national and international study protocols produced by various specialist medical associations and practitioners. This means that it is either necessary to extend the scan time accordingly or to omit certain aspects from the WB-MRI protocol (e.g. no additional abdominal and cranial imaging in the case of osteogenic sarcoma).
Whole-body angiography in pediatric applications is only rarely performed (e.g. in vascular malformations and aneurysms).
The aforementioned whole-body DWI could, in the future, make a significant contribution to differentiating tissue and the effects of treatment. If further steps can be taken to bolster diagnostic accuracy, this method may allow significant streamlining of the WB-MRI protocols described [16, 17].

Findings

In contrast to organ-focused scans, WB-MRI generates large numbers of images. In scenarios that also involve the acquisition of T1-weighted images before and after administering contrast agents and dedicated examinations of the central nervous system (CNS) or diffusion-weighted images of the body, approximately 1,000 images constitute the norm, even in the case of pediatric whole-body examinations. Using optimized software (which, for example, automatically displays a complete series for a particular region or organ system and all the sequences associated with a lesion) can considerably reduce the time required for image analysis. Particularly in view of the multiple follow-ups involved, software solutions are becoming increasingly important [19]. In addition to the number of images, which demands a high level of attention, up until now there has

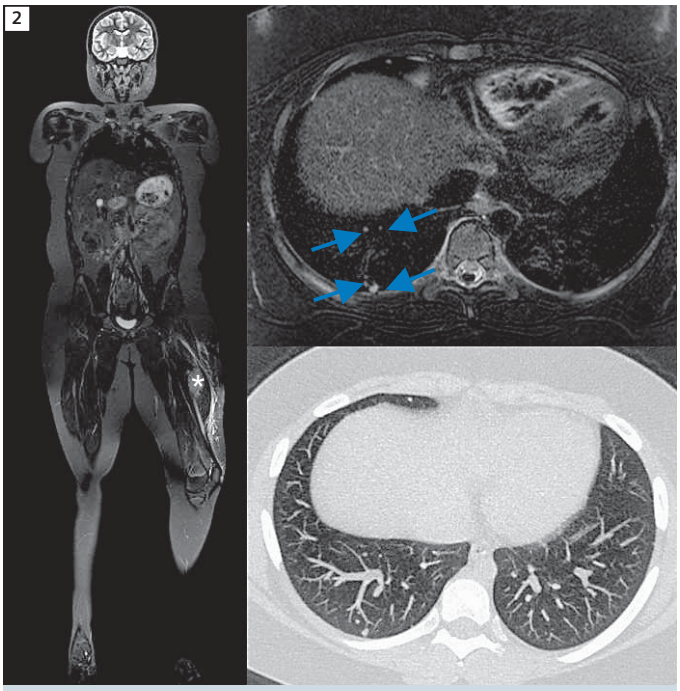

2 10-year-old girl with sarcoma. WB-MRI was performed for staging. Filiae are demonstared at the left leg (asterisk) and multiple small lung metastases (arrows) are seen and proven by biopsy; comparison to CT is shown. Left: TIRM WB coronal. Upper right: T2w TSE with PACE and ECG triggering, lower right: CT Thin MIP.

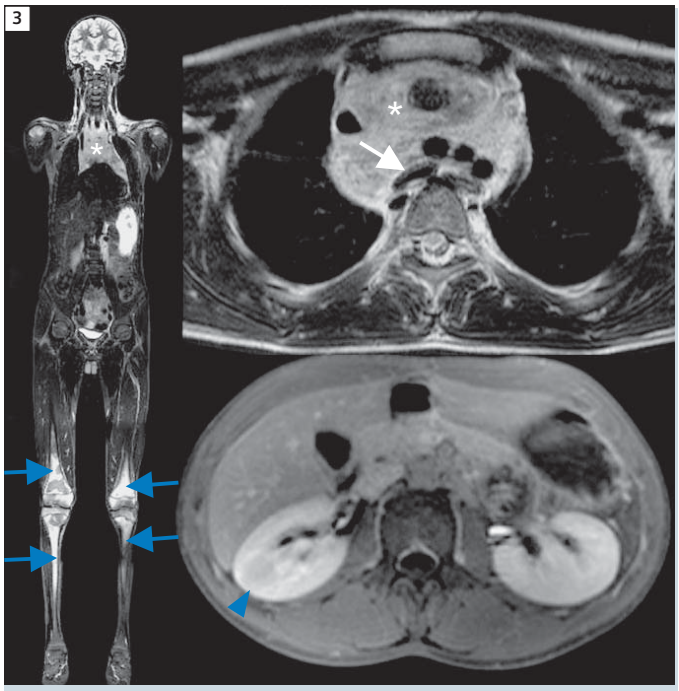

3 Oncologic whole-body MRI in a 15-year-old boy suffering from Non-Hodgkin-Lymphoma. **(3A–C)** The comprehensive staging depicts all tumor sites in the mediastinum (asterisk), in bones (arrows) as well as in the kidney (arrow head). **(3B)** The severe compression of the trachea is well demonstrated (open arrow).

been a risk of clinical oversights in terms of findings which are not immediately obvious, particularly during screening examinations. Given that, in contrast to scintigraphic methods, both normal findings and pathological changes can display the same signal intensity in STIR sequences, small foci, e.g. in the vicinity of a hyperintense bowel, are easily overlooked. In principle, other sequences, such as T1 both before and after administering contrast agents, and particularly DWI are useful for effectively detecting pathological findings.

Diseases, indications, and related questions to be answered by WB-MRI

Since WB-MRI was introduced for pediatric applications, several studies have been published which compare the method against various reference standards (conventional imaging, functional imaging, clinical parameters) by focusing on small patient groups that are frequently heterogeneous and studying different techniques and medical issues [3–5, 7–11, 14, 16, 21–23]. Various problems have been identified concerning the widespread use of WB-MRI in pediatrics, particularly with regard to treatment planning and follow-up. These problems are linked to the issue of evidence-based medicine involving large populations. Nevertheless, clear indications can be derived from the available studies for a range of malignant and non-malignant diseases in children that eliminate the need for additional imaging completely, or at least help to reduce it. In this respect, bone scintigraphy is particularly worthy of mention. We shall now move on to a discussion of the key diseases, indications and medical issues that have been investigated to date using WB-MRI, along with details of possible diagnostic algorithms.

Unifocal vs. multifocal

For all diseases where using a unifocal, rather than a multifocal approach has consequences for the type of treatment, WB-MRI for pediatric applications has an extremely important role to play. A typical example of this would be Langerhans' cell histiocytosis (LCH). Based on the guidelines of the AWMF (Arbeitsgemeinschaft der medizinischen Fachgesellschaften e.V. – association of the scientific medical societies in Germany) covering the fields of pediatric oncology and hematology (current version dated 01/2008), the primary form of image-based diagnosis would comprise the following: X-ray of thorax, radiographic skeletal survey and any supplementary skeletal scintigraphy that may be required, along with a CT of the thorax and a cranial MRI examination [20]. Multifocal analysis has major consequences both with regard to treatment and follow-ups (e.g. local treatment or even a *wait and see* strategy as opposed to systematic treatment with steroids and Vinblastine). A series of studies on a variety of diseases has revealed that WB-MRI is superior to X-ray-based methods or skeletal scintigraphy for the

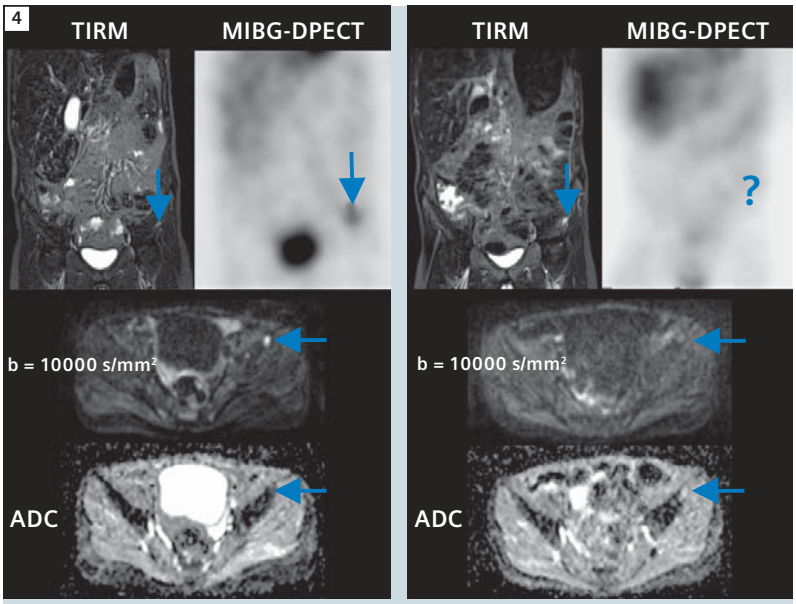

4 10-year-old girl with neuroblastoma, stage IV. Follow-up of a medullar metastases is shown (arrow). Comparison between DWI and MIBG Scintigraphy is provided. Left: pre-therapy; right: after therapy. Corresponding to therapy response an increase of the ADC can be seen.

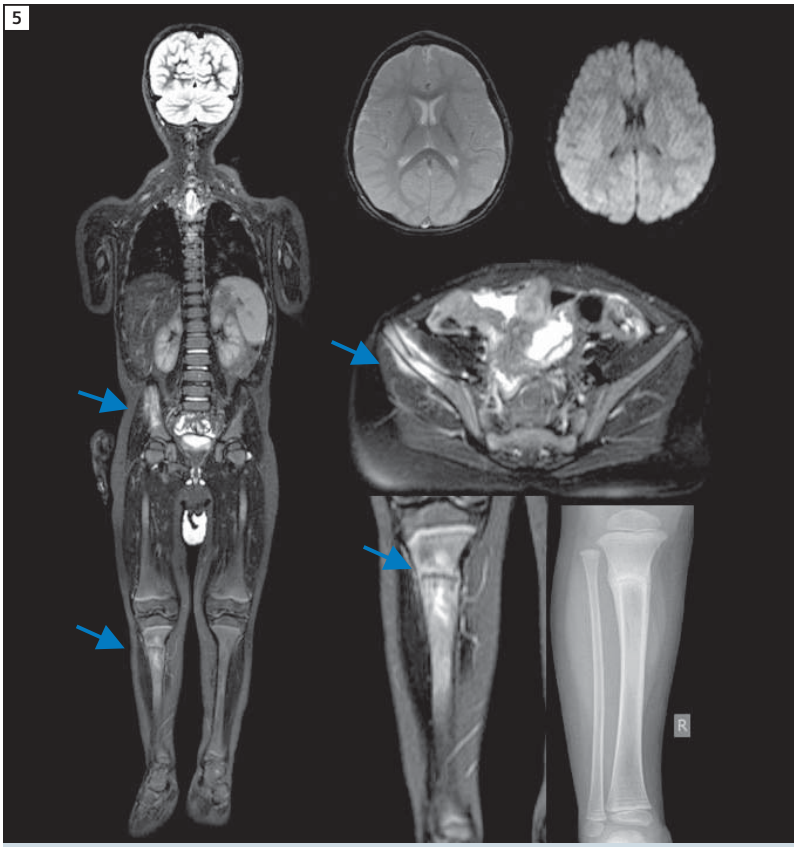

5 Screening in case of battered child, 3-year-old boy. WB-MRI shows fractures of the right Tibia and right pelivs. No intracranial injury is seen. X-ray performed after WB-MRI shows abvious repair and scleroses of the fracture.

purpose of assessing bone marrow infiltration [4, 7, 12, 21, 22]. The reduced sensitivity of scintigraphy is easily explained, particularly in the context of LCH (where this sensitivity problem has been documented in a small number of cases), as it is linked to the primary attack on the bone marrow and the rapid bone deterioration that sometimes occurs subsequently [9, 22]. The inferiority of X-ray examination is also evident [10, 22]. Another reason for using WB-MRI is that it is possible to detect extraskeletal manifestations, including attacks on the CNS [22].

In clinical terms and in terms of imaging, there can sometimes be an overlap between LCH and chronic recurrent multifocal osteomyelitis (CRMO). CRMO is characterized by non-bacterial inflammation with very heterogeneous processes. However, it is the typically multifocal nature of CRMO with occasional symmetric metaphyseal lesions which distinguishes CRMO and other conditions from bacterial osteomyelitis (Fig. 6). Investigations carried out at our clinic revealed that, in the case of CRMO, there was no significant correlation between the extent of skeletal lesions detected by WB-MRI and clinical parameters. However, they produced clear evidence that X-ray examinations (18%) are less sensitive than MRI in the case of this disease [13]. In our view, WB-MRI is the method of choice for CRMO, because it detects not only symptomatic but also inapparent manifestations, for example in a high-sensitivity examination of the spinal column.

Status in the case of rheumatic diseases

WB-MRI performed on adults allows to detect significantly more asymptomatic regions with arthritis or enthesitis than clinical examinations or tests [23]. The latter sometimes have a significant impact on treatment (for example, when using TNF-alpha inhibitors) and thus on the outcome [23, 24]. According to one study, 73% of patients examined with psoriatic arthritis underwent changes to their treatment [23]. Extraskeletal findings also play a significant role in cases of rheu-

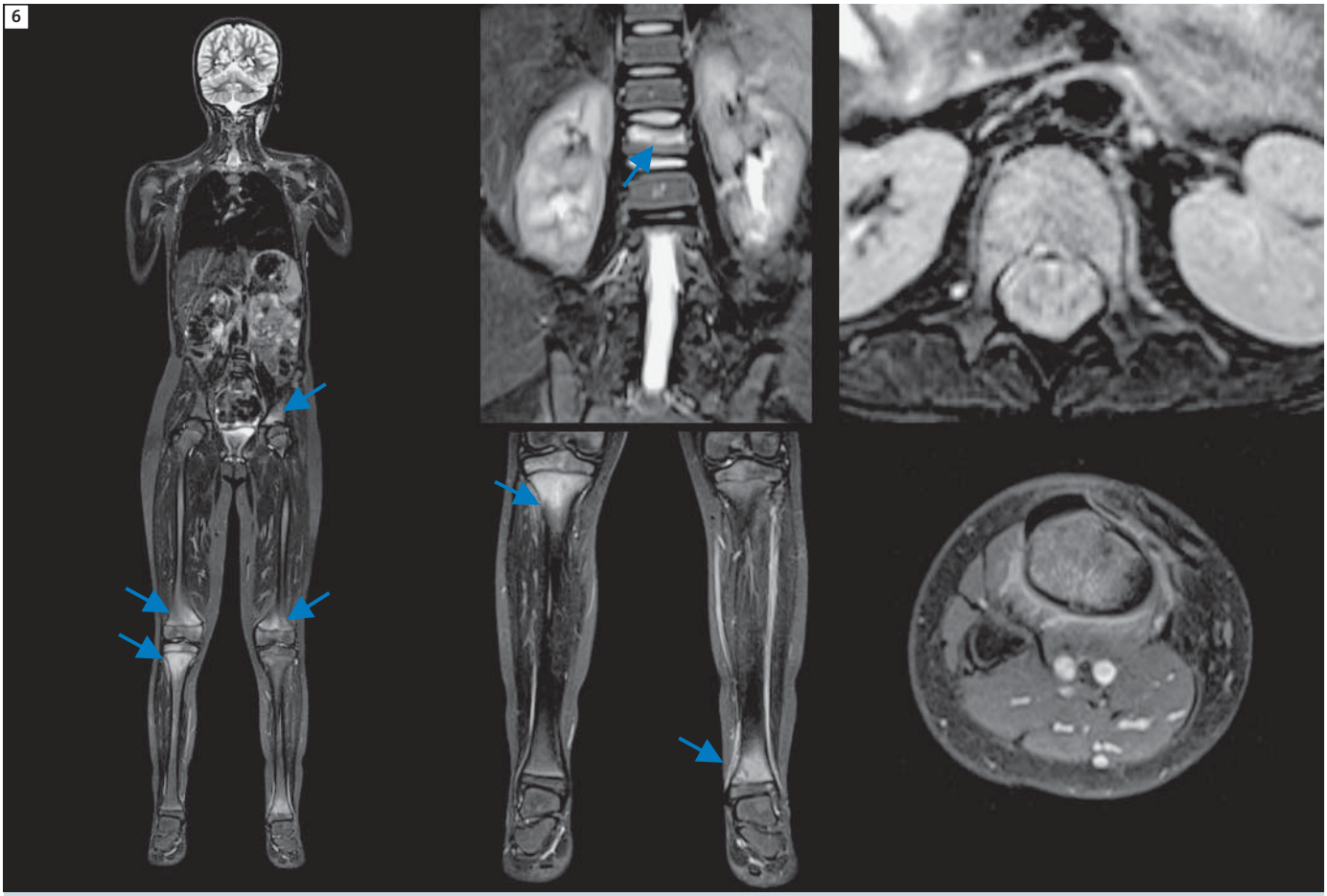

6 WB-MRI in case of chronic non-bacterial osteomyelitis (CNO) (7-year old girl). Multiple partially symmetric findings, some with periostal reaction are shown (arrows). Clinically occult lesion within the spine.

matic and autoinflammatory diseases as well as vasculitides, such as (dermato) myositis, scelroderma/morphea and sarcoidosis [25]. In such cases, we believe that a clear indication for using WB-MRI is either when there are conflicting clinical and laboratory findings, or if multifocality is not detectable clinically or by using sonography (for example, on the cervical vertebrae), which then necessitates changes to treatment (Fig. 8).

WB-MRI in the case of fever syndromes, unclear inflammation constellations and search for the focus of infection

Both immunocompetent and non-immunocompetent patients fall into this heterogeneous indication group. A vague increase in individual or multiple inflammation markers is common to all patients. Reasons for this may include: a systemic disease, an undetected focus or a hitherto unknown/recurrent malignant occurrence. Up until now, thorax X-rays, abdominal sonography and sometimes sonography of pleura, joints, and lymph nodes have been recommended as the definitive imaging methods [26]. Reports concerning the use of WB-MRI in pediatric applications are scarce, yet it has been described as groundbreaking specifically where there is skeletal involvement. With regard to the newly-available MR/PET technology, reference is made to the results obtained from what we believe to be the largest study focusing on PET(/CT), which involved 32 patients with FUO (fever of unknown origin)/increased inflammatory parameters. In this context, the PET/CT technology resulted in a definitive diagnosis for 2 out of 3 children [28]. In light of this data, WB-MRI still represents a highly personalized diagnostic decision, but it should (given the relevant clinic and impact on treatment) clearly be taken into account when making diagnostic considerations.

Screening for systemic diseases

WB-MRI has already been used for asymptomatic patients to ensure both a better definition of diseases and improved assessment of the scale of systemic conditions [29]. However, the clinical benefit is still open to debate and practical aspects such as screening intervals remain unresolved. Nevertheless, data relating to pediatric patients is available for specific diseases

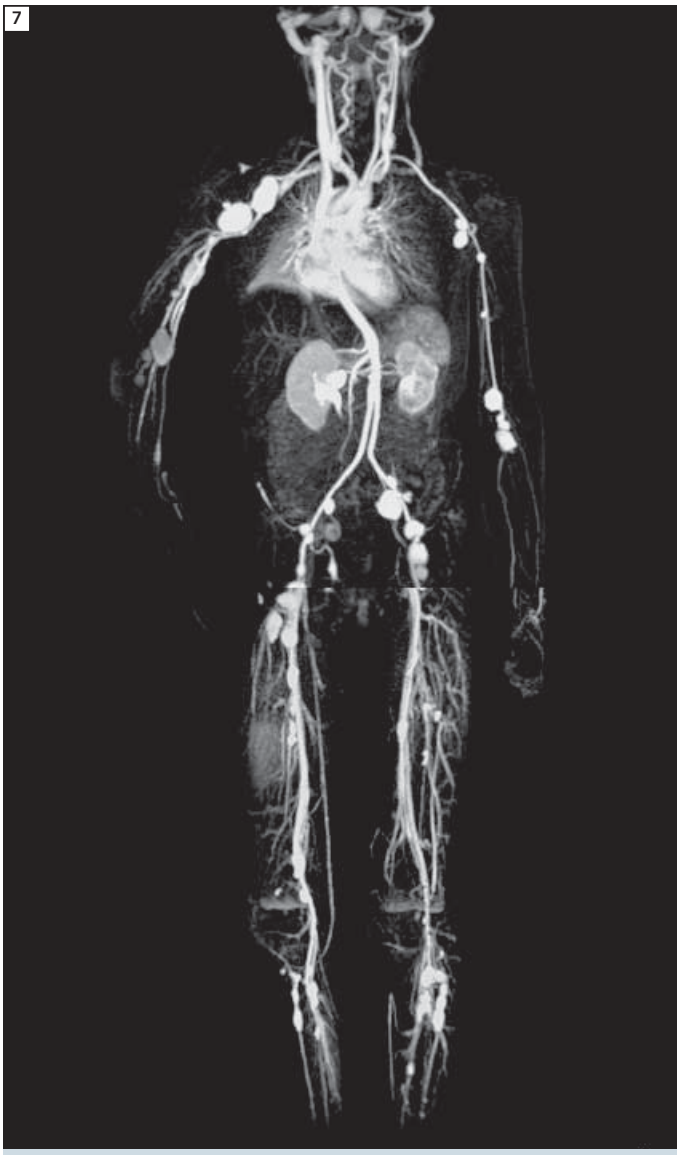

7 WB-MRA in case of a vessel-syndrome with mutliple aneurysms (3-year-old girl).

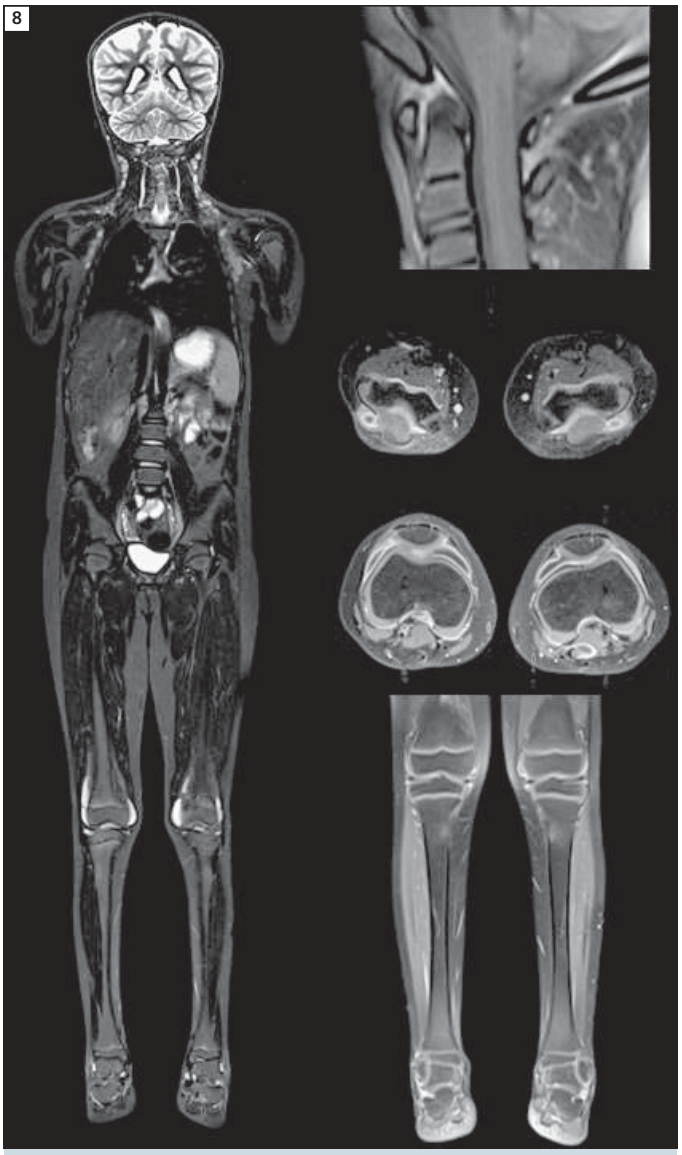

8 JIA (5-year-old girl) synovialitis of the large joint including the atlantoaxial joint.

or syndromes and certain patterns of disease progression. Neurofibromatosis-1 (NF-1) is one example of the progression of malignant tumors. In young patients with NF-1 who had already developed a malignant peripheral nerve sheath tumor, the tumor burden associated with neurofibroma appeared significantly larger on the WB-MRI scan than for those patients where there was no detectable malignant tumor [30]. However, this distinction could not be detected in clinical examinations and so patients with a high tumor burden require close follow-up care. Differentiating between fibromas and malignant nerve tumors by means of morphology is only possible to a limited degree and in this context, the sensitivity of conventional MRI is generally lower than that of FDG PET/CT [31, 32].

WB-MRI allows effective screening for the detection of asymptomatic osteonecrosis. For patients who have received high-dose chemotherapy in combination with steroids, MRI detects considerably more instances of avascular necrosis. In particular, the ability to demonstrate the extent of the condition and where it is localized is crucial when making treatment-related decisions [3] (Fig. 8). Hereditary vascular malformations are also a suitable indication for determining how relevant a particular treatment is (Fig. 7). In addition to showing the spread of the disease, the technology makes it

possible to differentiate between hemangiomas and also between lymphatic and venous malformations.

Child abuse

In cases of child abuse cranial MRI is the most sensitive method for assessing hemorrhages, ischemic and axonal damage [33]. However, MRI is often used following a cranial CT scan in cases of acute impaired consciousness. Therefore, in our view it would be sensible to perform a whole-body scan afterwards as part of the same examination (Fig. 5). Indeed, a report comprising 4 cases has revealed that MRI offers a higher level of sensitivity than X-ray imaging when used for musculoskeletal injuries [34]. Nevertheless, X-ray scans are necessary e.g. to evaluate the age of fractures where multiple trauma has been sustained [33].

Staging and spread of malignant tumors

Unfortunately, the number of published studies and the number of pediatric patients included within these are limited. Furthermore, the entities and medical issues evaluated are often heterogeneous [4–9, 15, 30, 35]. Despite this, it is still possible to assert that WB-MRI generally produces a higher level of diagnostic accuracy for various organ systems compared to other whole-body imaging techniques, such as scintigraphy, CT, and PET/CT. The question as to when and for which entities WB-MRI should be used exclusively in the context of primary staging, or when it fulfils a supplementary role, cannot be fully answered on the strength of present studies. In our view, and in accordance with the available literature, an indication for using WB-MRI is when the diagnostic algorithm suggests skeletal scintigraphy: osseous Ewing's sarcoma, osteosarcoma as well as suspected soft tissue sarcoma. Using an adapted methodology, e.g. as proposed in Table 1, soft tissue findings can be accurately diagnosed [6]. A supplementary CT of the thorax, as prescribed by the relevant guidelines, remains an essential part of the clinical routine even when WB-MRI is used during initial staging, although MRI of the lungs is now capable of producing extremely meaningful and reliable diagnostic information [36].

As far as the application of WB-MRI is concerned, neuroblastoma (among other conditions) occupies a special position among malignant tumors. Firstly, whole-body imaging is not generally indicated when the disease is clearly in the early stages or for early-stage nephroblastoma and hepatoblastoma; secondly, receptor scintigraphy involving metaiodobenzylguanidine (MIBG) has always been carried out up until now, although this only provides information about tumor spread if the findings are positive. In our view, and in the opinion of other authors [37], WB-MRI for neuroblastomas should be the preferred choice in two scenarios, in particular: 1) when there are extensive local primary findings in the context of a preoperative assessment of the regional (e.g. thoracoabdominal or spinal) spread and 2) when metastasis is suspected following a negative MIBG scintigram and/or a positive bone marrow biopsy (Fig. 4). The introduction of a new staging system by the International Neuroblastoma Risk Group (INRG) means that the assessment of multicompartment extension using MRI has a major role to play. Furthermore, WB-MRI appears to offer a higher level of sensitivity than MIBG scintigraphy when used for bone and bone marrow findings.

As far as lymphoma staging is concerned, it has been clear for a long time that MRI is capable of identifying more affected regions than conventional imaging (CT, scintigraphy) [5] (Fig. 3). A recent study demonstrates an almost identical level of sensitivity for nodal manifestations (99%) and only a marginally lower level of sensitivity for extranodal manifestations (91%) compared with FDG PET/CT [15]. However, in the case of nodal manifestations and assuming a threshold value of 1 cm, a purely morphological assessment results in the stage being under- or overestimated in individual cases. This limitation could be overcome by applying diffusion-weighted imaging [38, 39]. A study involving 40 patients has illustrated the superiority of FGD PET over MRI for both early and late treatment responses [40]. It is not yet clear whether MR methods such as DWI are capable of taking over this role, although initial results suggest that diffusion-weighted MRI is comparable with PET. Specifically in connection with the MR/PET technology that is now available, this opens up new horizons in terms of diagnosis and treatment monitoring.

As far as we are aware, no studies have been published regarding the use of WB-MRI for the restaging of malignant tumors in children. However, in our experience, significant inferences can be made using WB-MRI findings. Suspected recurrent tumors or metastasis involving symptoms such as pain, fever, and neurological abnormalities or other abnormalities detected in the lab can be swiftly ruled out or confirmed. Examination protocols can be adapted according to the suspected diagnosis, so that the full potential of MRI specificity can be utilized. Naturally, this also applies to renewed post-treatment monitoring, for which alternative regimes need to be validated (Fig. 1).

Organ-focused diagnostic accuracy of WB-MRI

Several studies on adults and children have demonstrated that, irrespective of the methodology selected, WB-MRI offers a significantly higher level of sensitivity than skeletal scintigraphy when used for malignant bone- and bone marrow lesions [4, 7, 12, 21, 22]. Compared to PET/CT, classifying the data is more difficult. In this respect, benchmark setting has an important role to play. Furthermore, it has been sufficiently well established that PET reveals considerable differences between specific tumor entities and the associated grading with regard to hypermetabolism, meaning that there are likely to be differences between the diagnostic accuracy of the two methods.

In general, MRI is to be viewed as the imaging method of choice for assessing brain metastases, rather than using CT

and FDG PET/CT [41]. It has also been demonstrated that, in the case of liver metastases also, WB-MRI offers a comparable or higher level of sensitivity than CT and PET/CT when used with adults [42]. As far as we are aware, no data has been published on the pediatric use of WB-MRI within this particular context. The ability to detect lung metastases depends not only on the technology used but also the size of the foci. In general, a threshold size of 3 to 5 mm at 1.5T can be assumed, with the likelihood of detection increasing with the size of the foci [43, 44]. In the case of those patients where lung metastases have consequences for treatment, the primary approach of our institute is to perform a CT scan after the WB-MRI. However, the use of CT for follow-ups is decreasing.

Studies on adults have revealed that conventional WB-MRI offers lower levels of sensitivity and specificity when assessing lymphogenic metastasis of carcinoma than FDG PET/CT [42]. Nevertheless, in the field of pediatric oncology, it should be noted that lymph node metastasis may mean something quite different from what it signifies when dealing with carcinoma in adults. Consequently, lymph node involvement in neuroblastoma is not, per se, automatically associated with a worse prognosis [45] and, in the case of osteogenic sarcoma, lymph node metastases are, per se, to be regarded as rare [46]. In this context, we also wish to draw attention to staging based on lymph node sampling in the case of nephroblastoma [47].

References

1 Schlemmer HP, Schäfer J, Pfannenberg C, et al. Fast whole-body assessment of metastatic disease using a novel magnetic resonance imaging system: initial experiences. Invest Radiol 2005; 40:64-71.

2 Pichler BJ, Kolb A, Nagele T, Schlemmer HP. PET/MRI: paving the way for the next generation of clinical multimodality imaging applications. J Nucl Med 2010; 51:333-336.

3 Beer M, Stenzel M, Girschick H, Schlegel PG, Darge K. Ganzkörper-MRT bei Kindern mit Verdacht auf Osteonekrose nach intensiver Chemotherapie: Erste Ergebnisse. Fortschr Röntgenstr 2008; 180:238-245.

4 Daldrup-Link HE, Franzius C, Link TM, et al. Whole-body MR imaging for detection of bone metastases in children and young adults: comparison with skeletal scintigraphy and FDG PET. AJR Am J Roentgenol 2001; 177:229-236.

5 Kellenberger CJ, Miller SF, Khan M, Gilday DL, Weitzman S, Babyn PS. Initial experience with FSE STIR whole-body MR imaging for staging lymphoma in children. Eur Radiol 2004; 14:1829-1841.

6 Krohmer S, Sorge I, Krausse A, et al. Whole-body MRI for primary evaluation of malignant disease in children. Eur J Radiol 2010; 74(1):256-261.

7 Kumar J, Seith A, Kumar A, et al. Whole-body MR imaging with the use of parallel imaging for detection of skeletal metastases in pediatric patients with small-cell neoplasms: comparison with skeletal scintigraphy and FDG PET/CT. Pediatr Radiol 2008; 38:953-962.

8 Mazumdar A, Siegel MJ, Narra V, Luchtman-Jones L. Whole-body fast inversion recovery MR imaging of small cell neoplasms in pediatric patients: a pilot study. AJR Am J Roentgenol 2002; 179:1261-1266.

9 Mentzel HJ, Kentouche K, Sauner D, et al. Comparison of whole-body STIR-MRI and 99mTc-methylene-diphosphonate scintigraphy in children with suspected multifocal bone lesions. Eur Radiol 2004; 14:2297-2302.

10 Steinborn M, Wortler K, Nathrath M, Schoniger M, Hahn H, Rummeny EJ. Ganzkörper-MRT bei Langerhans-Zell-Histiozytose im Kindes- und Jugendalter zur Beurteilung des Skelettsystems. Fortschr Röntgenstr 2008; 180:646-653.

11 Alibek S, Adamietz B, Cavallaro A, et al. Contrast-enhanced T1-weighted fluid-attenuated inversion-recovery BLADE magnetic resonance imaging of the brain: an alternative to spin-echo technique for detection of brain lesions in the unsedated pediatric patient? Acad Radiol 2008; 15:986-995.

12 Ketelsen D, Rothke M, Aschoff P, et al. Nachweis ossarer Metastasen des Prostatakarzinoms – Vergleich der Leistungsfahigkeit der Ganzkörper-MRT und der Skelettszintigrafie. Fortschr Röntgenstr 2008; 180:746-752.

13 Fritz J, Tzaribatchev N, Claussen CD, Carrino JA, Horger MS. Chronic recurrent multifocal osteomyelitis: comparison of whole-body MR imaging with radiography and correlation with clinical and laboratory data. Radiology 2009; 252:842-851.

14 Ley S, Ley-Zaporozhan J, Schenk JP. Whole-body MRI in the pediatric patient. Eur J Radiol 2009; 70:442-451.

15 Punwani S, Taylor SA, Bainbridge A, et al. Pediatric and Adolescent Lymphoma: Comparison of Whole-Body STIR Half-Fourier RARE MR Imaging with an Enhanced PET/CT Reference for Initial Staging. Radiology 2010; 255:182-190.

16 Lichy MP, Aschoff P, Plathow C, et al. Tumor detection by diffusion-weighted MRI and ADC-mapping--initial clinical experiences in comparison to PET-CT. Invest Radiol 2007; 42:605-613.

17 Bohlscheid A, Nuss D, Lieser S, Busch HP. Tumorsuche mittels kernspintomografischer Diffusionsbildgebung--Erste Erfahrungen. Fortschr Röntgenstr 2008; 180:302-309.

18 Shabshin N, Schweitzer ME, Morrison WB, Carrino JA, Keller MS, Grissom LE. High-signal T2 changes of the bone marrow of the foot and ankle in children: red marrow or traumatic changes? Pediatr Radiol 2006; 36:670-676.

19 Muller-Horvat C, Plathow C, Ludescher B, et al. Befunderstellung bei der Ganzkörperbildgebung mittels einer workflowoptimierten Befundungssoftware--Erste Erfahrungen einer Multireader-Analyse. Fortschr Röntgenstr 2007; 179:721-727.

20 www.awmf-online.de/. (German language)

21 Ohlmann-Knafo S, Kirschbaum M, Fenzl G, Pickuth D. Diagnostischer Stellenwert der Ganzkörper-MRT und der Skelettszintigrafie in der ossären Metastasendetektion bei Mammakarzinompatientinnen – eine prospektive Doppelblindstudie an zwei Klinikzentren. Fortschr Röntgenstr 2009; 181:255-263.

22 Goo HW, Yang DH, Ra YS, et al. Whole-body MRI of Langerhans cell histiocytosis: comparison with radiography and bone scintigraphy. Pediatr Radiol 2006; 36:1019-1031.

23 Weckbach S, Schewe S, Michaely HJ, Steffinger D, Reiser MF, Glaser C. Whole-body MR imaging in psoriatic arthritis: Additional value for therapeutic decision making. Eur J Radiol. 2009 Jul 23. [Epub ahead of print].

24 Appel H, Hermann KG, Althoff CE, Rudwaleit M, Sieper J. Whole-body magnetic resonance imaging evaluation of widespread inflammatory lesions in a patient with ankylosing spondylitis before and after 1 year of treatment with infliximab. J Rheumatol 2007; 34:2497-2498.

Summary

WB-MRI enables the effects of diseases on the organ systems of children and young people to be fully detected without exposure to radiation. At our clinic, WB-MRI not merely represents the ideal supplement to established methods. Rather, it forms an integral part of diagnosis because of the extensive diagnostic information that it provides and the way it reduces the need for further forms of imaging. It makes it possible to diagnose the spread of diseases in soft tissue/organs during an examination, thereby allowing risk stratification to take place before embarking on treatment. Hodgkin's lymphoma constitutes an exception here, as the findings to date have revealed that PET (PET/CT) is a superior form of technology for this disease, both during initial staging and treatment monitoring.

Contact
Professor Jürgen Schäfer, M.D.
University Hospital of Tübingen
Department of Radiology
Hoppe-Seyler-Str. 3
72076 Tübingen
Germany
juergen.schaefer@med.uni-tuebingen.de

25 Tzaribachev N, Well C, Schedel J, Horger M. Whole-body MRI: a helpful diagnostic tool for juvenile dermatomyositis case report and review of the literature. Rheumatol Int. 2009 Oct;29(12):1511-4.
26 Wirth S, Böhles H, Creuzig P, et al. Leitlinien Kinder- und Jugendmedizin der DGKJ. Elsevier 2009; H3 3-15.
27 Rozmanic V, Banac S, Miletic D, Manestar K, Kamber S, Paparic S. Role of magnetic resonance imaging and scintigraphy in the diagnosis and follow-up of osteomyelitis in cat-scratch disease. J Paediatr Child Health 2007; 43:568-570.
28 Jasper N, Dabritz J, Frosch M, Loeffler M, Weckesser M, Foell D. Diagnostic value of [(18) F]-FDG PET/CT in children with fever of unknown origin or unexplained signs of inflammation. Eur J Nucl Med Mol Imaging. 2010 Jan;37(1):136-45.; 37.
29 Hegenscheid K, Kuhn JP, Volzke H, Biffar R, Hosten N, Puls R. Whole-body magnetic resonance imaging of healthy volunteers: pilot study results from the population-based SHIP study. Fortschr Röntgenstr 2009; 181:748-759.
30 Mautner VF, Asuagbor FA, Dombi E, et al. Assessment of benign tumor burden by whole-body MRI in patients with neurofibromatosis 1. Neuro Oncol 2008; 10:593-598.
31 Matsumine A, Kusuzaki K, Nakamura T, et al. Differentiation between neurofibromas and malignant peripheral nerve sheath tumors in neurofibromatosis 1 evaluated by MRI. J Cancer Res Clin Oncol 2009; 135:891-900.
32 Ferner RE, Golding JF, Smith M, et al. [18F]2-fluoro-2-deoxy-D-glucose positron emission tomography (FDG PET) as a diagnostic tool for neurofibromatosis 1 (NF1) associated malignant peripheral nerve sheath tumours (MPNSTs): a long-term clinical study. Ann Oncol 2008; 19:390-394.
33 Erfurt C, Hahn G, Roesner D, Schmidt U. Kinderradiologische Diagnostik bei Verdacht auf Kindesmisshandlung. Radiologe 2009; 49: 934-941.
34 Eltermann T, Beer M, H. G. Diagnostic imaging of child abuse. Pediatrics 2009; 123:1430-1435.
35 Goo HW, Choi SH, Ghim T, Moon HN, Seo JJ. Whole-body MRI of paediatric malignant tumours: comparison with conventional oncological imaging methods. Pediatr Radiol 2005; 35:766-773.
36 Ley-Zaporozhan J, Ley S, Sommerburg O, Komm N, Muller FM, Schenk JP. Clinical application of MRI in children for the assessment of pulmonary diseases. Fortschr Röntgenstr 2009; 181:419-432.
37 Goo HW. Whole-body MRI of neuroblastoma. Eur J Radiol. 2009; Sep 23. [Epub ahead of print].
38 Kwee TC, Quarles van Ufford HM, Beek FJ, et al. Whole-Body MRI, Including Diffusion-Weighted Imaging, for the Initial Staging of Malignant Lymphoma: Comparison to Computed Tomography. Invest Radiol. 2009; Oct;44(10):683-690.
39 Holzapfel K, Duetsch S, Fauser C, Eiber M, Rummeny EJ, Gaa J. Value of diffusion-weighted MR imaging in the differentiation between benign and malignant cervical lymph nodes. Eur J Radiol 2009; 72:381-387.
40 Furth C, Steffen IG, Amthauer H, et al. Early and late therapy response assessment with [18F]fluorodeoxyglucose positron emission tomography in pediatric Hodgkin's lymphoma: analysis of a prospective multicenter trial. J Clin Oncol 2009; 27:4385-4391.
41 Kitajima K, Nakamoto Y, Okizuka H, et al. Accuracy of whole-body FDG-PET/CT for detecting brain metastases from non-central nervous system tumors. Ann Nucl Med 2008; 22:595-602.
42 Schmidt GP, Baur-Melnyk A, Herzog P, et al. High-resolution whole-body magnetic resonance image tumor staging with the use of parallel imaging versus dual-modality positron emission tomography-computed tomography: experience on a 32-channel system. Invest Radiol 2005; 40:743-753.
43 Biederer J, Schoene A, Freitag S, Reuter M, Heller M. Simulated pulmonary nodules implanted in a dedicated porcine chest phantom: sensitivity of MR imaging for detection. Radiology 2003; 227:475-483.
44 Koyama H, Ohno Y, Kono A, et al. Quantitative and qualitative assessment of non-contrast-enhanced pulmonary MR imaging for management of pulmonary nodules in 161 subjects. Eur Radiol 2008; 18:2120-2131.
45 Evans AE, D'Angio GJ, Sather HN, et al. A comparison of four staging systems for localized and regional neuroblastoma: a report from the Childrens Cancer Study Group. J Clin Oncol 1990; 8:678-688.
46 Harris MB, Gieser P, Goorin AM, et al. Treatment of metastatic osteosarcoma at diagnosis: a Pediatric Oncology Group Study. J Clin Oncol 1998; 16:3641-3648.
47 Fuchs J, Kienecker K, Furtwangler R, et al. Surgical aspects in the treatment of patients with unilateral wilms tumor: a report from the SIOP 93-01/German Society of Pediatric Oncology and Hematology. Ann Surg 2009; 249:666-671.

Simultaneous MR/PET – Clinical Reality?

Nina Schwenzer; Christina Pfannenberg; Holger Schmidt; Bernd Pichler; Claus D. Claussen

University of Tübingen, Department of Diagnostic and Interventional Radiology and Department of Preclinical Imaging and Radiopharmacy, Tübingen, Germany

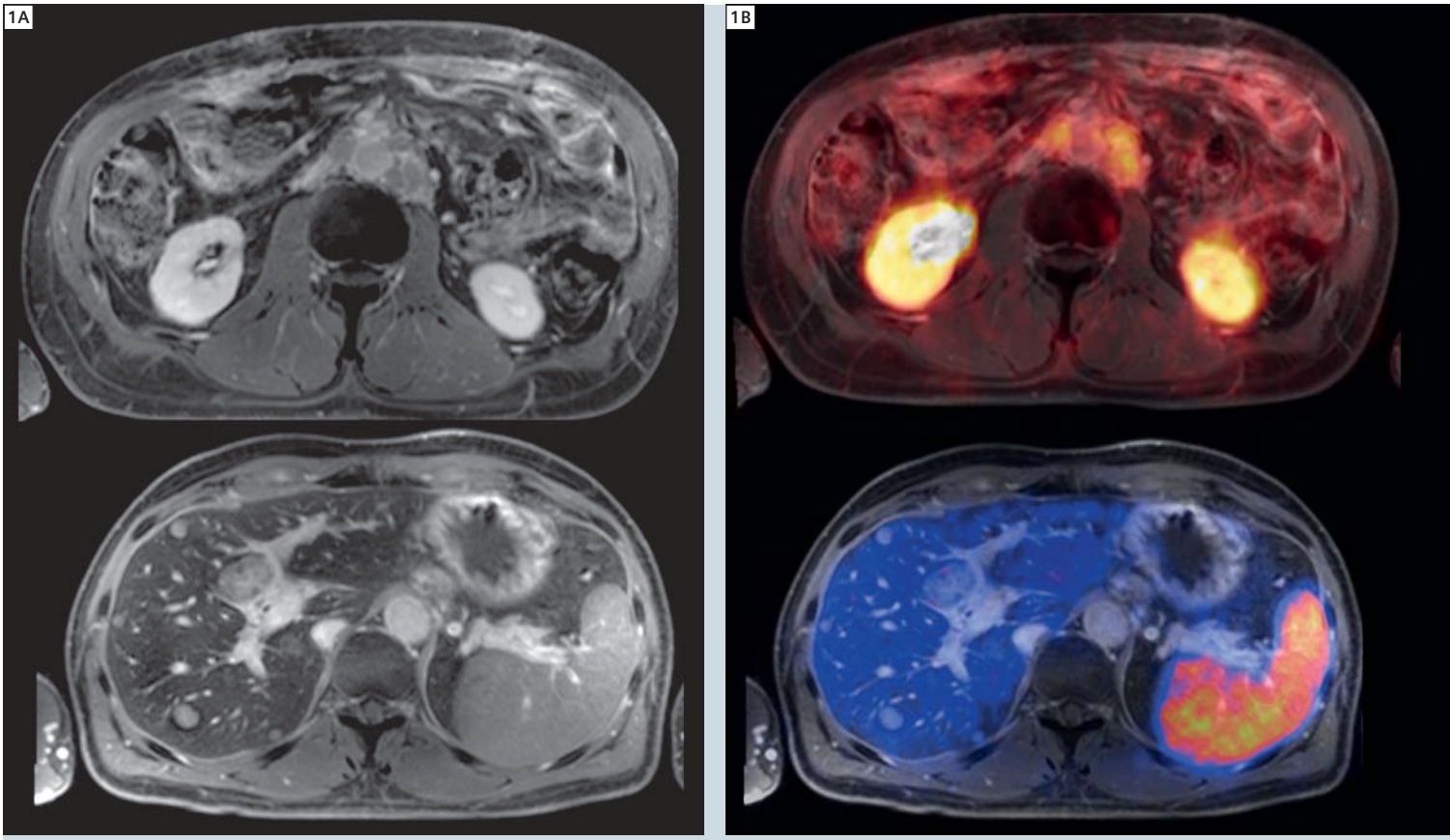

1A–B **1A**: Contrast-enhanced T1w 2D FLASH with fat saturation showing extensive retroperitoneal and hepatic tumor spread of the NET with partially necrotic areas. Corresponding DOTATATE PET in figure **1B**, acquired during simultaneous MR/PET, shows only slightly increased uptake/receptor upregulation of the retroperitoneal metastases and no focality within the liver.

Background

Much has already been written about the technology, the basic ideas as well as the potential clinical needs behind the combining of MR and PET. As with all new imaging methodologies, there is debate as to how much this technology is really needed (similarly, for example, with the availability of PET/CT) and the discussion regarding MR/PET in particular concerns the level of integration and, even more fundamentally, the question whether the simultaneity of MRI and PET acquisition is really required.

It should be pointed out that now that the MR/PET technology is available in the Biograph mMR, real simultaneous imaging with different methodologies is possible in a clinical setting for the first time – a clear paradigm shift in how we acquire information about patients and their diseases. The combining of functional information derived by MR and the possibility to influence PET information and vice versa is stimulating researchers worldwide and hopefully this will also clearly impact on how we provide biomarkers for therapy decisions throughout the continuum of patient care. But also from a purely clinical and very practical perspective, simultaneity

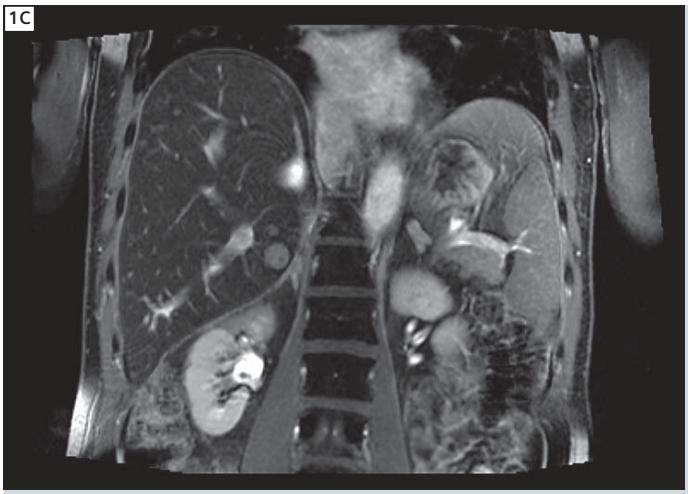

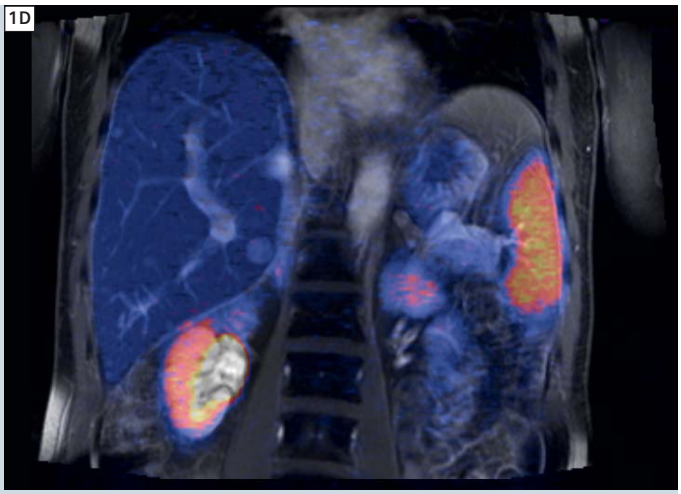

1C–D Corresponding coronal MR/PET.

of acquisition promises definite advantages over sequential acquisition – independently of how this sequential approach is organized (main concepts: a) different scanners and combination of results with software only, b) different scanners in different rooms with patient transport solution, or c) different scanners in the same room with patient transport solution). More detail about concepts and technology of MR/PET can also be found in the research supplement of the MAGNETOM Flash issue 3/2010 and in the MAGNETOM Flash issue 1/2011.

Impact of MRI on mMR imaging protocols

MRI has one main disadvantage when combining MR and PET in addition to not providing quantitative information about tissue density (a fact which has to be taken into account for attenuation correction of PET data): Data acquisition speed is limited compared, for example, to today's CT. MR imaging speed can of course be improved to some extent by increasing the strength of the B_0 field; by using different sequence techniques; by applying parallel imaging; and through its combinations (e.g. T2w 3D acquisition is only feasible within clinical routine as a turbo-spin-echo technique by the combination of variable flip angle evolutions with long echo trains and parallel imaging; *syngo* SPACE). In addition, the need for multiple contrasts and the capability to derive functional parameters like perfusion (T2* dynamics), cellularity (diffusion-weighted imaging, *syngo* REVEAL), microvessel density and permeability (T1w DCE; *syngo* VIBE or *syngo* TWIST for acquiring 4D data sets, *syngo* Tissue 4D for pharmaceutical modelling) are resulting in complex and relatively long examination times. For example, a comprehensive brain scan for tumor resection planning with MRI involves not only morphology scans (multiplanar T1w and T2w contrast including contrast media application) but possibly also fiber tracking and functional MRI to evaluate, for example, the tumor's involvement of essential areas like the motor cortex. An MRI exam that provides the required information can easily exceed half an hour and complex whole-body scans with MRI can easily take one hour.

Furthermore, these scans also generate a huge volume of imaging data. A standard whole-body MRI protocol in our clinical daily practice comprises 1,000 to 1,500 images; and this amount is increased dramatically by adding information from DWI, T1w DCE, etc. To provide another example of the level of complexity of these multimodal MRI approaches: A state-of-the-art prostate MRI exam aimed at local tumor staging / detection includes not only multiplanar / 3D high-resolution T2w TSE images but also T1w DCE, 3D MR spectroscopy, and DWI (including ADC calculations). Leaving aside the necessary post-processing, more than 2,000 images are acquired and have to be taken into account for diagnoses. But what does this mean to the simultaneously acquired PET data, and how is this influenced by such a relatively time-consuming and complex MRI exam?

In today's sequential PET/CT routine, PET can be regarded as a stand-alone imaging acquisition. CT (independent if only as a native low-dose or multi-phase contrast-enhanced scan) is acquired completely independently from the PET. Consequently, long PET measurement times are not desirable. Furthermore, the relatively small dimensions of the PET beds in a larger number of PET/CT scanners and physiological processes like filling of the bladder, bowel movement and uncomfortable patient fixation require the shortest possible PET scan times, in overall terms and per bed, especially also to limit the time-difference between the "snap-shot" CT (a whole-body scan with the latest CT generation can be done in less than 10 seconds at sub-millimetre resolutions) and the corresponding metabolic / PET information. As a further consequence of the time-constraints on PET measurements, dynamic

and late PET scans can be considered as wishful thinking and are not yet part of clinical routine, despite the promising results reported over recent years. This also applies to some degree to gated PET acquisition. Another problem is the relatively small number of patients included in these reports which makes it difficult to apply these techniques in daily patient care on a larger scale and thereby make economies of scale. But how do the relatively long MRI examination times, the need for complex functional information and the simultaneous acquisition of MR and PET data fit together? How will MR influence the PET acquisition and vice versa?

- The used PET detector for simultaneous MR/PET is characterized by a large field-of-view (in fact the largest available for clinical routine) which allows us to cover large areas if not the whole organ (brain, liver) in one go. Furthermore, the high sensitivity allows for fast PET scans per bed and in total. However, the relatively long MR imaging time and the high sensitivity of the detector results in an 'oversampling' of PET data, allowing gated PET scans (e.g. by adding information of the diaphragm movements derived from the simultaneous acquired MRI) or even longer dynamic PET acquisition when focusing on one organ. And whilst such an exam will take longer than a standard PET/CT, such a patient would have to undergo an MRI anyhow, and a dynamic PET scan would not really be possible in clinical routine for a PET/CT scanner aiming for a high patient through-put.
- PET information can be used to reduce the required amount of MR information; in fact, MR and PET point out different aspects of biology and so far it is more a question of diagnostic power of an individual biomarker and their combination that will determine the content of future MR/PET protocols. The 3D in-phase / opposed phase T1w sequence for attenuation correction will replace its counterparts in the MR protocol only in rare cases. Also, thanks to the 3D VIBE with Dixon technique, this is nowadays a simple one breathhold scan and does not really extend the overall scan time. Nevertheless, information derived from this MR sequence is of a diagnostic nature as it is for any low-dose attenuation CT scan for PET/CT.
- Of course, simultaneous MR/PET does offer multiple chances to improve PET performance, for example by adding information about perfusion information to dynamic PET data, or by allow for motion or volume correction. It is evident that these techniques are especially appealing for very specific PET tracers (e.g. for dementia evaluation) or for obtaining dedicated biological information for therapy adoption, for example the presence and adoption to hypoxic stress of tumor tissue.

Clinical examples
Study design and equipment

At a given point in time, all patients examined with the Biograph mMR are included in clinical studies. In the first phase, imaging capabilities of the system are evaluated to derive important information for advanced imaging protocols. We also want to compare the clinical performance of MR/PET with PET/CT for existing PET/CT indications. Because of the convincing results of the first phase of the clinical testing and after

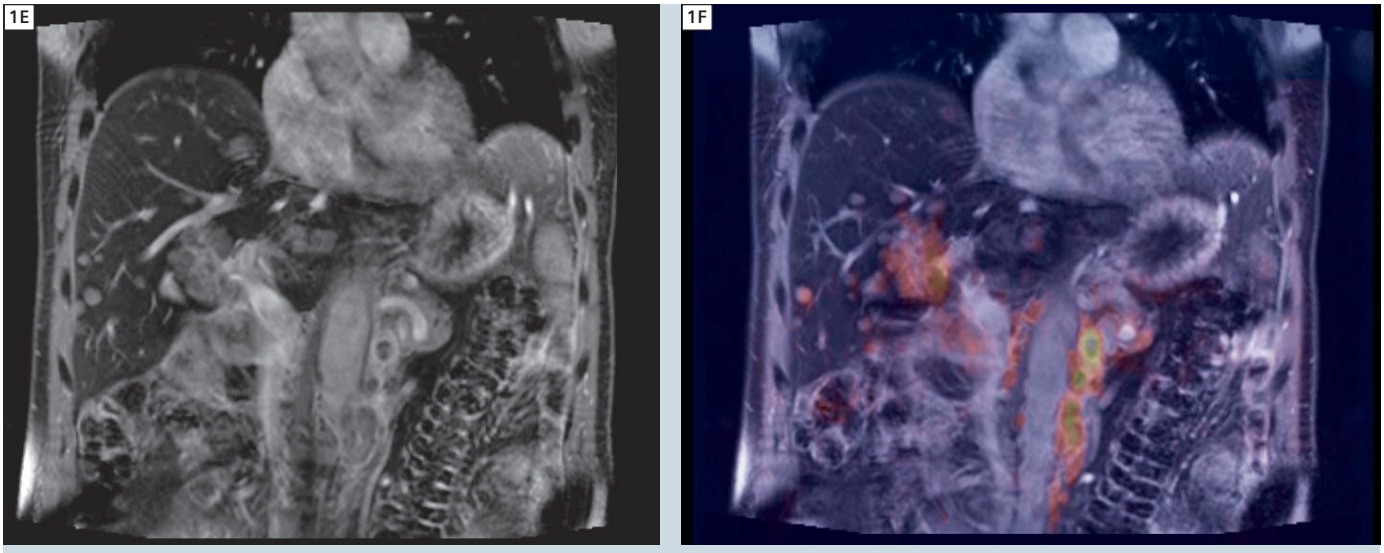

1E–F **1E** (MR only) and **1F** (b=800 s/mm^2 overlaid) show the extensive retroperitoneal tumor spread. In contrast to PET, DWI demonstrates areas with restricted diffusion as an expression of high cellularity which is not directly linked to the receptor expression but more to cell density. Not shown in this case are the quantitative ADC maps which are used to separate T2-shine through effects from real restriction of diffusion. These effects can both contribute to the signal in the original b-value images.

receiving the CE-label for the Biograph mMR, we expanded our IRB approval for the use of our system for imaging children* and now regularly use contrast-media for, for example, dynamic liver evaluations.

All patients have an indication for PET/CT and are scanned at the PET/CT and at the mMR. We apply body-weight adjusted PET tracers according to our clinical PET/CT protocols; the second scan is performed with the residual activity. Most of our patients received the PET/CT scan first. However, for some indications we now change this order. The installation of the Biograph mMR at our institution was the second world-wide, and the BrainPET prototype the first, used for advanced neuro-research and basic / methodology evaluation of the MR/PET technology. This scanner is placed in our radiopharmaceutical laboratories, which can produce all common radiopharamaceuticals in clinical imaging and research. The Biograph mMR is placed in a different building, but short delivery ways allow us to apply ^{11}C labelled tracers and other tracers than FDG within the framework of clinical pilot studies.

*MR scanning has not been established as safe for imaging fetuses and infants under two years of age. The responsible physician must evaluate the benefit of the MRI examination in comparison to other imaging procedures.

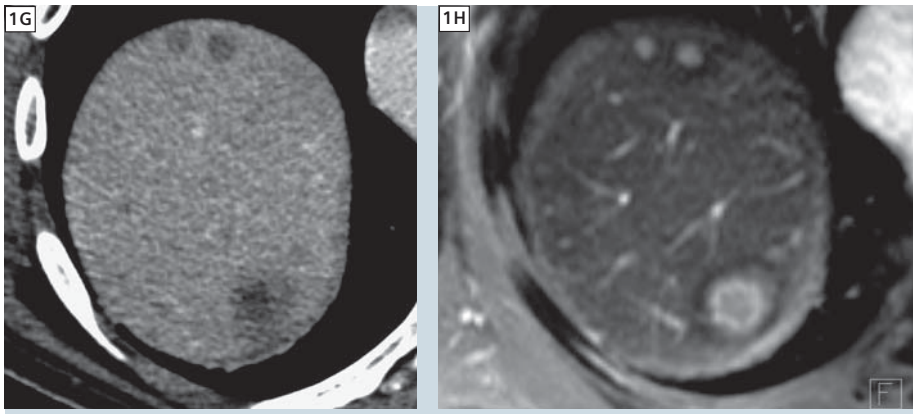

1G–H **1G**: Contrast-enhanced CT scan (late phase) and corresponding MRI in **1H** (contrast-enhanced late phase) show the superior soft contrast of MRI which enables detailed information about regional differences within the metastases.

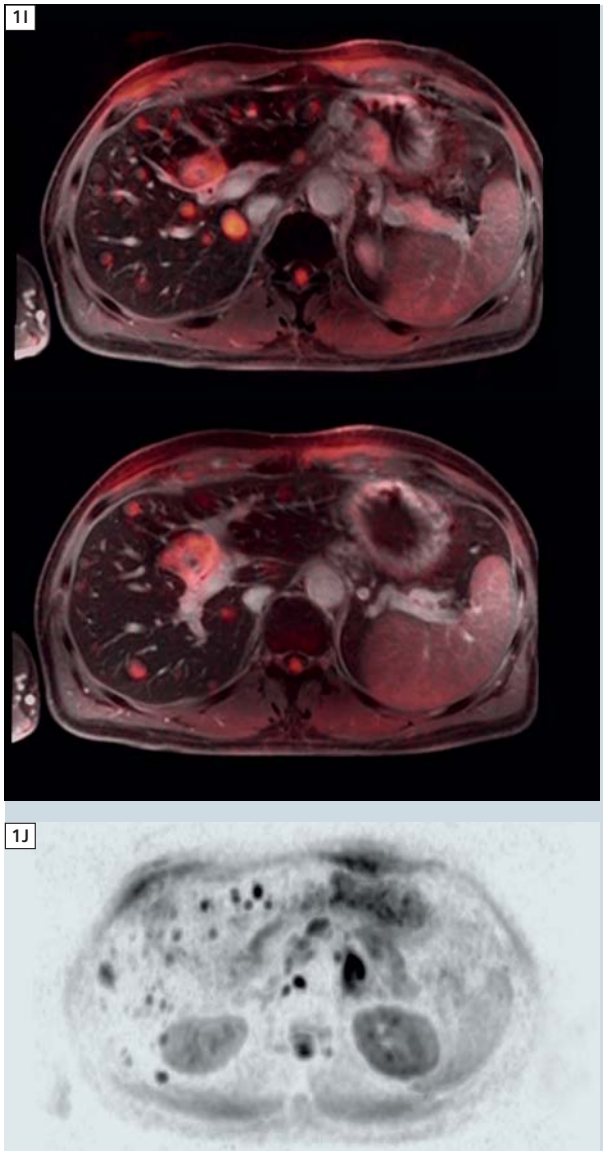

1I–J **1I** (DWI superimposed on contrast-enhanced T1w ce FLASH) and **1J** (thick-slice MIP of original b-value images) show the potential of DWI to provide detailed information about the total tumor load. Nevertheless, simply based on the original b-value images, a differentiation between tumor and reactive tissue, e.g. after surgery, as seen in the ventral abdominal wall, can be challenging. There is an additional finding of increased fat content of the liver.

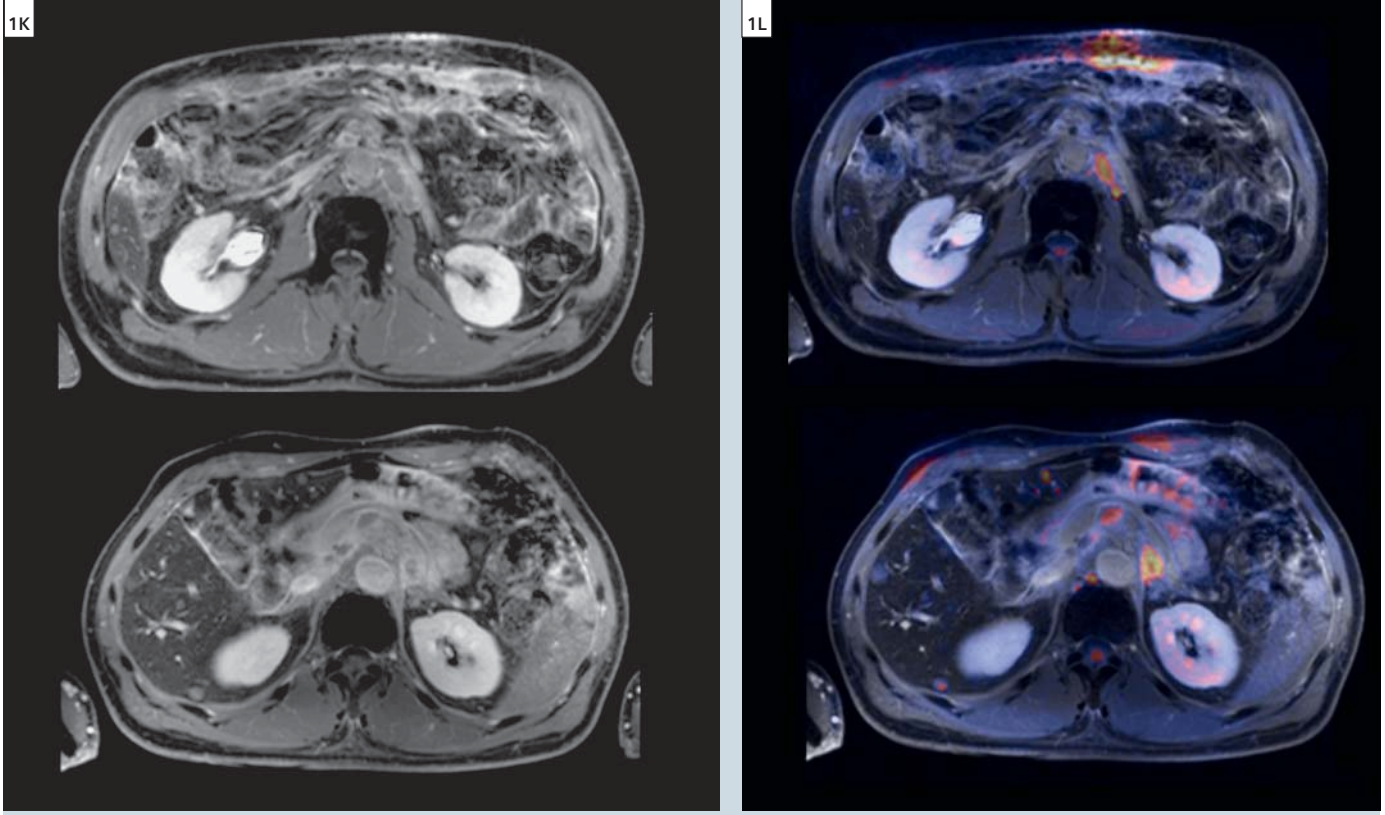

1K–L T1w contrast-enhanced MRI demonstrating extensive spread and involvement of paraortic lymph nodes stages with necrosis. In addition, diffuse enhancement of the peritoneum can be seen **(1K)**. Overlayed high b-value images do show however different aspects of metastases than T1w scan **(1L)**. Compare with figure 1B for evaluation of receptor status of the metastases.

MR/PET imaging protocols

We are now still in the evaluationary phase for different MR/PET protocols depending on clinical indications and patients' capabilities. In general, we try to focus more on clinically relevant combinations than to rigidly adhere to our imaging protocols. This approach can best be compared to the modules for whole-body MRI proposed by several working groups, which take into account clinical patterns of disease as well as the diagnostic power of MRI sequences, e.g. dynamic liver scans for colorectal cancers, coronal whole-body TIRM in case of high probability of bone metastases and FLAIR and post-contrast scans of the brain in case of lung cancer, etc., are added to a basic protocol. Our MR/PET protocols aim first at acquiring a comprehensive overview that is more comparable to conventional PET/CT and comprises basic MR sequences including the sequence for attenuation correction and then add a focused scan. Here we limit the scan range to smaller areas of interest and perform the specific MR protocols that also allow us to acquire dynamic PET data.
In the following case reports we describe two typical cases from our patient cohort. Both patients were scanned first with the PET/CT and then with the Biograph mMR.

Case 1
Evaluation of metastatic spread in case of a neuroendocrine tumor (NET)

This exam had to answer three important questions: First, what is the total tumor load; second, can this NET be treated by an internal radiotherapy; and finally, are there any complications that would cause an adoption of the therapy (e.g. recommendation of supportive actions in case of congestion of the biliary tract, obstruction of the urinary tract etc.). As one of the few clinical available 'therapeutics', ^{68}Ga DOTATATE was used in this patient. Over-expression of Somatostatine receptors of NET are a common finding. DOATATE has similar characteristics to DOTATOC and is used for imaging NETs. If labelled with ^{68}Ga, DOTATOC as well as the applied DOTATAE can be used as a tracer specific PET tracer to provide not only information about degree of receptor expression but also an evaluate the effectiveness of potential systemic ^{90}Y labelled DOTATOC/DOTATATE application for internal radiotherapy. However, as is the case for other tumors, metabolism and in this case receptor expression may vary not only between patients but also between different metastases of the same tumor within one individual. In addition, a common organ for metastastic spread of NET is the liver, but small filiae can easily be missed even when showing higher DOTATOC uptake because of the high background activity of liver tissue. Furthermore, since limited disease would potentially allow a more radical and curative approach e.g. atypical resection of liver metastases, a precise detection of filiae is essential for therapy assessment. It has been shown that MRI (using arterial phase of dynamic liver scans and / or diffusion weighted imaging) is the most accurate imaging method for an accurate evaluation of liver metastases of a NET. But DWI in particular also has

the potential to provide fast assessment of the total tumor load. By quantifying diffusion restriction it has already proved itself as an early therapy response biomarker for other tumor entities.

The images shown are from a 47-year-old male patient. With a weight of 82 kg and body height of 195 cm (BMI 21.56 kg/m^2), 167 mBq of ^{68}Ga DOTATATE was injected. After an uptake time of 20 min, a PET/CT was acquired including contrast-enhanced diagnostic CT scans and 78 min after tracer injection, the MR/PET examination was started (due to low residual activity, time per bed was 8 min, 3 beds were measured). PET/CT and MR/PET showed both multiple hepatic, coelical and retroperitoneal filiae of the known NET with only slightly increased receptor expression, most evident for the ceolical / retroperitoneal metastases. As expected, MRI could visualize more hepatic filiae and also allow for a more sensitive evaluation of diffuse reactions of the great omentum due to both advanced tumor spread and to the surgical approach before the patient was sent to our department. For the hepatic filiae, only discrete uptake could be seen in some larger metastases. However, this is not visible within the normal range of standard uptake values as used for images with overlaid PET; clear focal uptake is not seen and multiple metastases show no increased uptake compared to the liver background. As expected, the diagnostic performance of the PET/CT is inferior to MRI (MR/PET) but the information derived from MRI and DWI also show different aspects of tumor biology than PET; DWI reveals areas with higher cellularity that are not necessarily linked to a higher level of receptor expression.

Alongside the clinically comprehensive information derived from a combined MR/PET, this case shows clearly the high image quality achievable in challenging cases in the abdomen where MRI at 3T not only has the advantage of a high SNR but must also take into account potential negative effects. We do not apply to this patient the motion-freezing techniques which we also evaluate at our institution in a clinical setting. Motion-freezing and correction will unquestionably have an impact on diagnostic accuracy, especially for brain and liver MR/PET exams. However, in this clinical example no change of therapy would be evident: The extent of disease and the missing clear increase of uptake of the liver metastases compared to the residual normal liver parenchyma and the massive tumor load negates any further surgical approach.

Case 2
Evaluation of lung cancer

Lung cancer is perhaps the most evident indication for a PET/CT scan. MRI has not played a role in the diagnostic work-up so far, although the diagnostic accuracy of MRI has improved dramatically over recent years. The potential to detect small lung nodules is size-dependent but especially for the therapeutic relevant lesions with diameters >4 mm is comparable to state-of-the-art helical CT techniques. By adopting MR sequence techniques, lung MRI at 3T is clinical reality. Furthermore, MRI can add important information about, for example, infiltration of the chest wall, or provide detailed knowledge about vessel impairment which can be used for a detailed

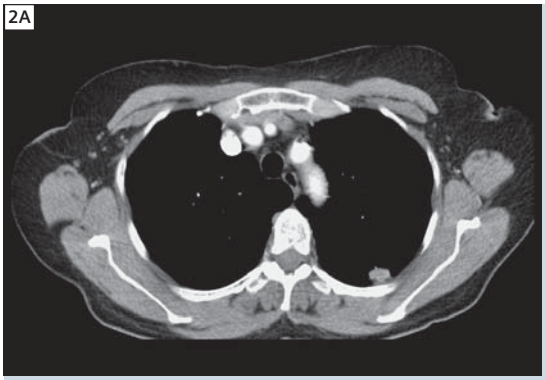

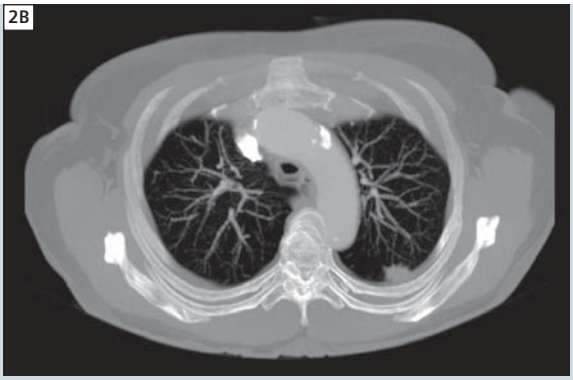

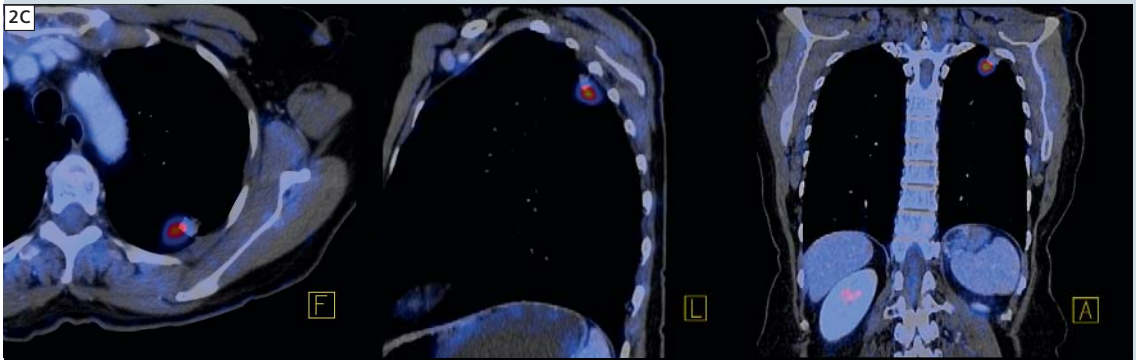

2A–C Contrast-enhanced CT scan (**2A** soft-tissue window and **2B** lung window) demonstrates the left apical lung nodule. As expected clear focal FDG uptake can be seen, however, fused on the contrast-enhanced diagnostic CT scan, a mismatch between PET (which is acquired during free breathing) and the cancer is seen in **2C**. However, fused on the native attenuation correction CT, this mismatch is as expected less evident (not shown).

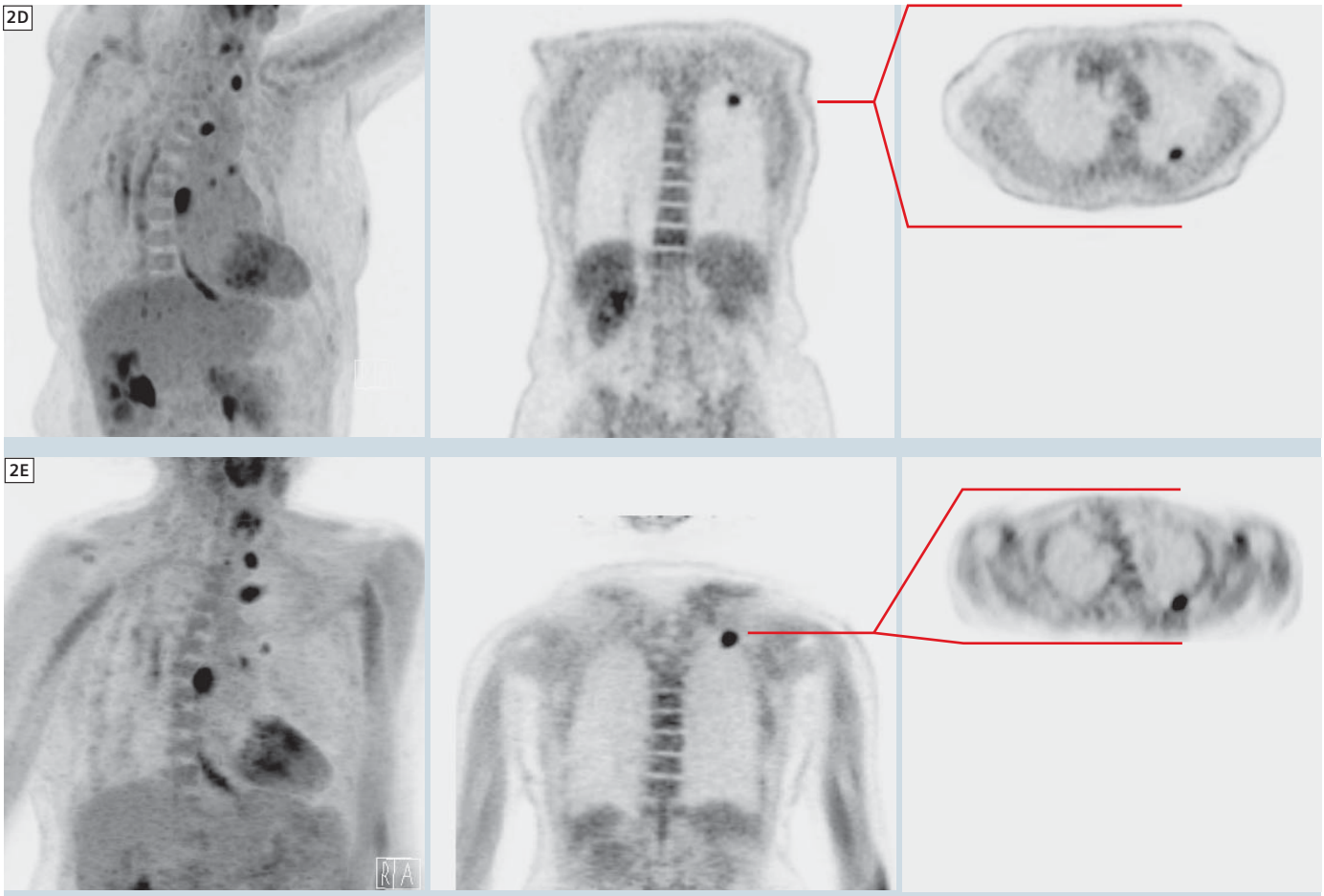

2D–E **2D** shows MIP and MPR of the PET derived from the PET/CT scan. Corresponding PET derived from the MR/PET in **2E**. Note that the MR/PET scan had to utilize the residual activity of the first acquired PET/CT. Note also that for MR/PET the arms can be positioned more comfortably without negative impact on image quality even if positioned outside the MRI's FOV. Findings details are given in the text.

surgical therapy assessment. In addition, MRI can provide functional parameters such as:

- cellularity by DWI,
- 3D motion patterns of the lesions by dynamic MRI (TrueFISP techniques, in development are sequences with radial k-space sampling schemes in combination with compressed sensing; evaluation of motion is feasible with CT, too, especially in an elderly patient undergoing radiotherapy this is a clinically realistic setting. However, especially for young female patients, additional radiation should be avoided)
- perfusion (again, radiation is a topic for CT scans when applied to young patients but also information derived especially by T1w DCE scans does differ from CT acquired perfusion data. DCE MRI was successfully applied to differentiate benign versus malignant lung lesions).

Especially in the evaluation of lung lesions of unknown origin in younger patients, MRI has to be considered as a clear alternative to conventional CT exams.

In this case, a 70-year-old female (weight 60 kg, height 165 cm, BMI 22,04 kg/m^2) – after injection of 381 mBq ^{18}F-FDG and an uptake time of 55 min – underwent a PET/CT, including multi-phase contrast-enhanced CT scans, for staging of a suspected lung cancer. The patient was than referred to our MR/PET unit. Simultaneous MR/PET was started 122 min after injection of FDG; PET acquisition time per bed was adapted to 6 min to compensate for the low residual tracer activity (2 bed positions were acquired which covered the whole thorax as well as the cervical region).

PET/CT and MR/PET showed both the left apical lung cancer neighbouring the pleura but without clear evidence of an affection of the thorax wall; also no signs of a pleural infiltration are seen. In addition, two small hiliar lymph nodes are present as well as paraoesphagel lymphnodes which were all rated as metastases because of their high and

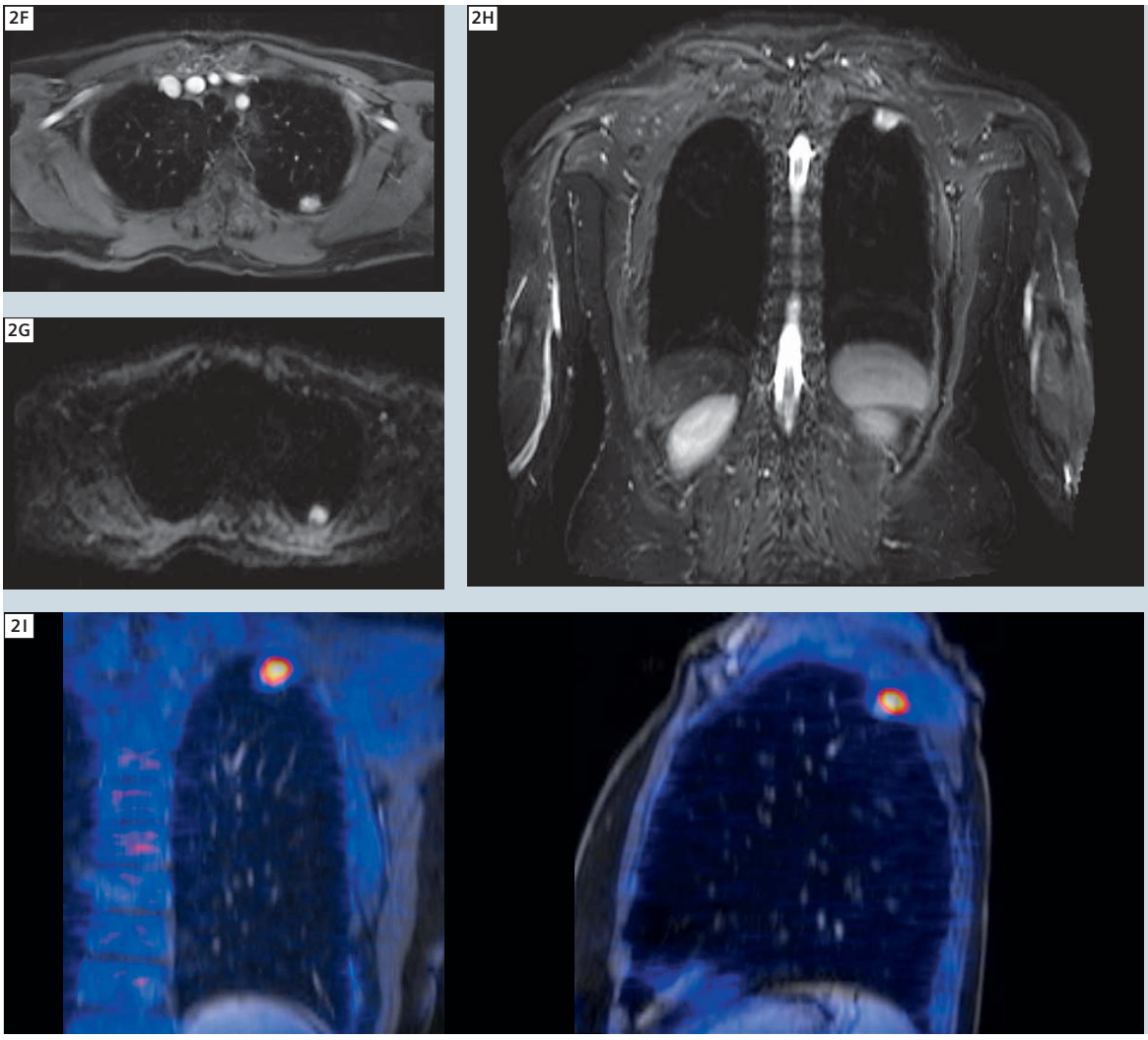

2F–I Transversal arterial phase T1w 3D VIBE scan is shown in **2F**. **2G** shows corresponding original b = 400 s/mm² DWI measurement. In **2H** coronal T2w STIR reveals the contact of the lesion to the very apical border of the pleura. Figure **2I** demonstrates focal uptake of the lesion also with the MR/PET examination. PET information is displayed with the simultaneously acquired contrast-enhanced 3D VIBE which demonstrates the high perfusion of the lesion.

focal FDG uptake. Both PET data sets also show a focal uptake within the oesophagus which has to be considered as a potential second malignoma. Both exams also demonstrate an increased but non-focal uptake of the lower oesophagus as often seen in case of recurrent inflammation which would also increase the possibility of a malignancy.

Another finding which corresponded to nodular formation in morphology was a small focal FDG uptake within the thyroid gland. Southern Germany is considered as an iodine-deficient area and therefore findings within the thyroid gland are common, however, a focal uptake within the gland can be linked also to thyroid cancer and a further evaluation of this finding is required, too.

Attenuation correction of PET data derived from the MR/PET examination is based on a segmentation approach. A direct comparison between of PET/CT and MR/PET is challenging in a clinical setting; different bio-distribution when measuring at different time-points is perhaps the main factor, but the problems associated with the measurement itself as well as different reconstructions of the PET images, etc., are also potential factors influencing the comparability of the two scans. With a SUVmax / SUVavg of 8.1 / 4.1 for the PET/CT and 8.8 / 4.3 for the MR/PET for the primary lung cancer lesion, a good correlation between the two scans is evident. However, it also shows that quantification of PET data is dependent on various factors which have to be taken into account, together with the error level that is deemed to be clinically acceptable, and these issues require an increased awareness especially from us clinicians.

This case clearly demonstrates that simultaneous MR/PET is clinically feasible at high quality and diagnostic accuracy, even where PET/CT would otherwise be considered as standard. MR/PET is a also a clear alternative for evaluation of lung lesions where radiation exposure is relevant, especially in young female patients. This clinical example comprises only basic MR techniques, but

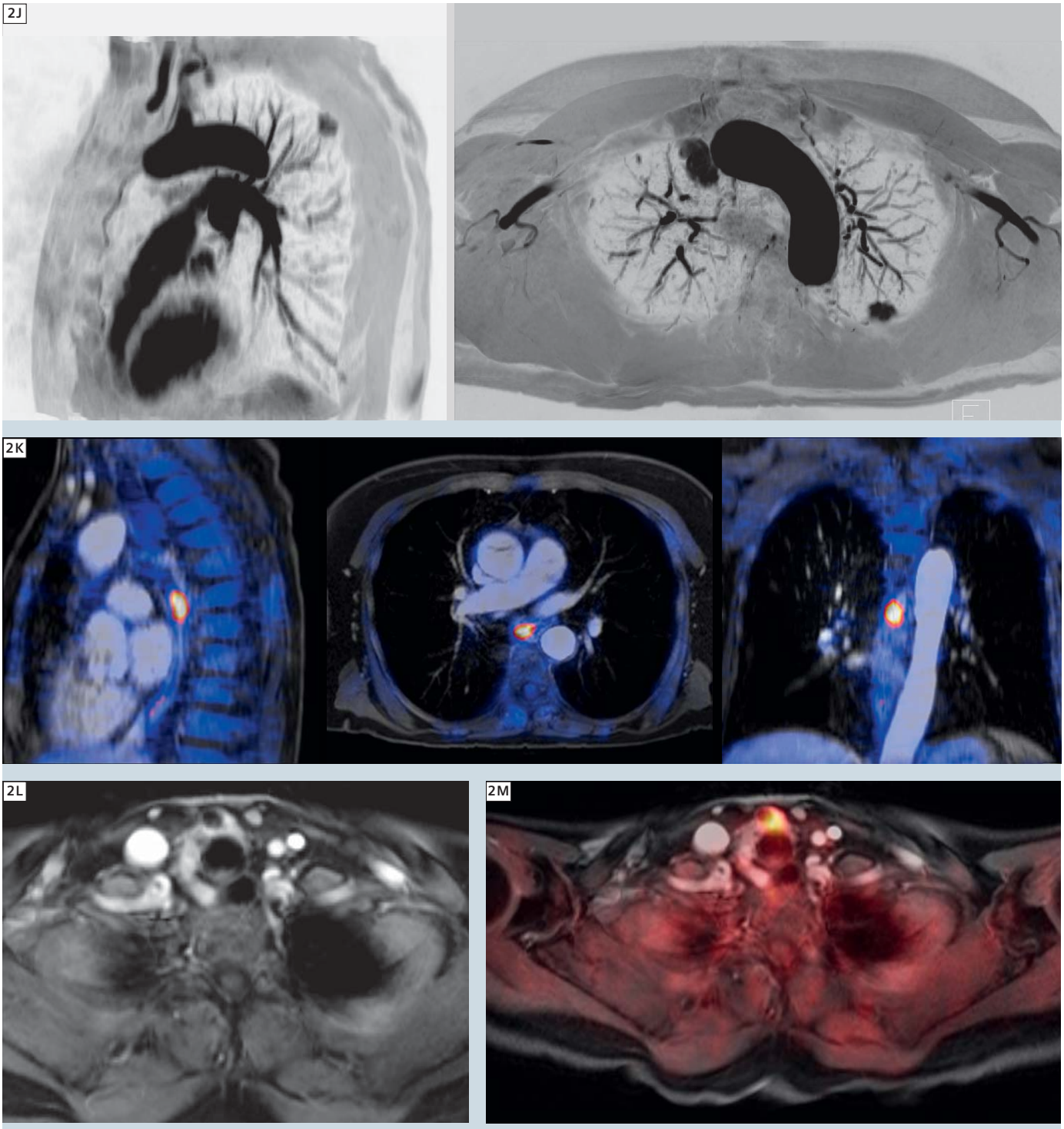

2J–M **2J** shows the relative relationship to the lung vessels. Images are thick-slice MPR and based on arterial phase 3D VIBE MR acquisition. In **2K** a multiplanar reconstruction based on the same MR sequence is shown, superimposed on the PET data and visualizing the focal uptake within the oesophagus of unknown origin. **2L** shows nodular changes within the thyroid gland and **2M**) superimposed with the PET the focal appearance of the increased FDG uptake in this area.

MRI can already deliver variable functional parameters. In this particular case, motion-freezing or correction would have been favourable but not clinically essential. However, especially for follow-up of small lung lesions, it has to be considered as an integral part of simultaneous MR/PET examinations.

Conclusion

As shown by the two cases in our ongoing clinical evaluation study, simultaneous MR/PET has already proven its potential to deliver outstanding image quality and offer all the advantages of MRI and PET in one examination. It is also evident that simultaneous MR/PET is about much more than just adding a radiation-free imaging modality to PET and that we have only begun to understand the clinical benefits of molecular MR. There is no doubt that it has huge potential to advance imaging in patient care and to provide detailed biomarkers for a vast range of diseases and therapies.

References

1 Thorwarth D, Henke G, Müller AC, Reimold M, Beyer T, Boss A, Kolb A, Pichler B, Pfannenberg C. Simultaneous 68Ga-DOTATOC-PET/MRI for IMRT treatment planning for meningioma: first experience. Int J Radiat Oncol Biol Phys. 2011 Sep 1 ;81(1):277-83. Epub 2011 Feb 6.

2 Werner MK, Brechtel K, Beyer T, Dittmann H, Pfannenberg C, Kupferschläger J. PET/CT for the assessment and quantification of (90)Y biodistribution after selective internal radiotherapy (SIRT) of liver metastases. Eur J Nucl Med Mol Imaging. 2010 Feb;37(2):407-8. Epub 2009 Dec 9.

3 Gehler B, Paulsen F, Oksüz MO, Hauser TK, Eschmann SM, Bares R, Pfannenberg C, Bamberg M, Bartenstein P, Belka C, Ganswindt U. [68Ga]-DOTATOC-PET/CT for meningioma IMRT treatment planning. Radiat Oncol. 2009 Nov 18;4:56.

4 Plathow C, Staab A, Schmaehl A, Aschoff P, Zuna I, Pfannenberg C, Peter SH, Eschmann S, Klopp M. Computed tomography, positron emission tomography, positron emission tomography/computed tomography, and magnetic resonance imaging for staging of limited pleural mesothelioma: initial results. Invest Radiol. 2008 Oct;43(10):737-44.

5 Plathow C, Aschoff P, Lichy MP, Eschmann S, Hehr T, Brink I, Claussen CD, Pfannenberg C, Schlemmer HP. Positron emission tomography/computed tomography and whole-body magnetic resonance imaging in staging of advanced nonsmall cell lung cancer-initial results. Invest Radiol. 2008 May;43(5):290-7.

6 Lichy MP, Aschoff P, Plathow C, Stemmer A, Horger W, Mueller-Horvat C, Steidle G, Horger M, Schafer J, Eschmann SM, Kiefer B, Claussen CD, Pfannenberg C, Schlemmer HP. Tumor detection by diffusion-weighted MRI and ADC-mapping--initial clinical experiences in comparison to PET-CT. Invest Radiol. 2007 Sep;42(9):605-13.

7 Judenhofer MS, Wehrl HF, Newport DF, Catana C, Siegel SB, Becker M, Thielscher A, Kneilling M, Lichy MP, Eichner M, Klingel K, Reischl G, Widmaier S, Röcken M, Nutt RE, Machulla HJ, Uludag K, Cherry SR, Claussen CD, Pichler BJ. Simultaneous PET-MRI: a new approach for functional and morphological imaging. Nat Med. 2008 Apr; 14(4) :459-65. Epub 2008 Mar 23.

8 Schraml C, Schwenzer NF, Martirosian P, Bitzer M, Lauer U, Claussen CD, Horger M. Diffusion-weighted MRI of advanced hepatocellular carcinoma during sorafenib treatment: initial results. AJR Am J Roentgenol. 2009 Oct;193(4):W301-7.

9 Boss A, Stegger L, Bisdas S, Kolb A, Schwenzer N, Pfister M, Claussen CD, Pichler BJ, Pfannenberg C. Feasibility of simultaneous PET/MR imaging in the head and upper neck area. Eur Radiol. 2011 Jul;21(7):1439-46. Epub 2011 Feb 10.

10 Pichler BJ, Kolb A, Nägele T, Schlemmer HP. PET/MRI: paving the way for the next generation of clinical multimodality imaging applications. J Nucl Med. 2010 Mar;51(3):333-6. Epub 2010 Feb 11.

11 von Schulthess GK, Schlemmer HP. A look ahead: PET/MR versus PET/CT. Eur J Nucl Med Mol Imaging. 2009 Mar;36 Suppl 1:S3-9.

12 Schlemmer HP, Pichler BJ, Schmand M, Burbar Z, Michel C, Ladebeck R, Jattke K, Townsend D, Nahmias C, Jacob PK, Heiss WD, Claussen CD. Simultaneous MR/PET imaging of the human brain: feasibility study.Radiology. 2008 Sep;248(3):1028-35.

13 Catana C, van der Kouwe A, Benner T, Michel CJ, Hamm M, Fenchel M, Fischl B, Rosen B, Schmand M, Sorensen AG. Toward implementing an MRI-based PET attenuation-correction method for neurologic studies on the MR-PET brain prototype. J Nucl Med. 2010 Sep;51(9):1431-8.

14 Wehrl HF, Judenhofer MS, Thielscher A, Martirosian P, Schick F, Pichler BJ. Assessment of MR compatibility of a PET insert developed for simultaneous multiparametric PET/MR imaging on an animal system operating at 7 T. Magn Reson Med. 2011 Jan;65(1):269-79.

15 Guérin B, Cho S, Chun SY, Zhu X, Alpert NM, El Fakhri G, Reese T, Catana C. Nonrigid PET motion compensation in the lower abdomen using simultaneous tagged-MRI and PET imaging. Med Phys. 2011 Jun;38(6):3025-38.

16 Catana C, Benner T, van der Kouwe A, Byars L, Hamm M, Chonde DB, Michel CJ, El Fakhri G, Schmand M, Sorensen AG. MRI-assisted PET motion correction for neurologic studies in an integrated MR-PET scanner. J Nucl Med. 2011 Jan;52(1):154-61.

17 Eiber M, Martinez-Möller A, Souvatzoglou M, Holzapfel K, Pickhard A, Löffelbein D, Santi I, Rummeny EJ, Ziegler S, Schwaiger M, Nekolla SG, Beer AJ. Value of a Dixon-based MR/PET attenuation correction sequence for the localization and evaluation of PET-positive lesions. Eur J Nucl Med Mol Imaging. 2011 Sep;38(9):1691-701. Epub 2011 Jun 18.

18 Delso G, Martinez-Möller A, Bundschuh RA, Ladebeck R, Candidus Y, Faul D, Ziegler SI. Evaluation of the attenuation properties of MR equipment for its use in a whole-body PET/MR scanner. Phys Med Biol. 2010 Aug 7;55(15):4361-74. Epub 2010 Jul 20.

Contact
Assoc. Professor Nina Schwenzer, M.D.
University of Tübingen
Department of Diagnostic and Interventional Radiology
Hoppe-Seyler-Straße 3
72076 Tübingen
Germany
nina.schwenzer@med.uni-tuebingen.de

Abdominal Susceptibility-Weighted Imaging: A New Application for Liver Disease

Yongming Dai, Ph.D.[1]; Mengsu Zeng, M.D.[2, 3]; E. Mark Haacke, Ph.D.[4]; Jiani Hu, Ph.D.[4]; Renate Jerecic, Ph.D.[5]

[1]Siemens Healthcare China, MR Collaborations NE Asia, Shanghai, China
[2]Department of Radiology, Zhongshan Hospital, Fudan University, Shanghai, China
[3]Department of Medical Imaging, Shanghai Medical School, Fudan University, Shanghai, China
[4]Department of Radiology, Wayne State University, Detroit, Michigan, USA
[5]Siemens Healthcare, MR Marketing, Erlangen, Germany

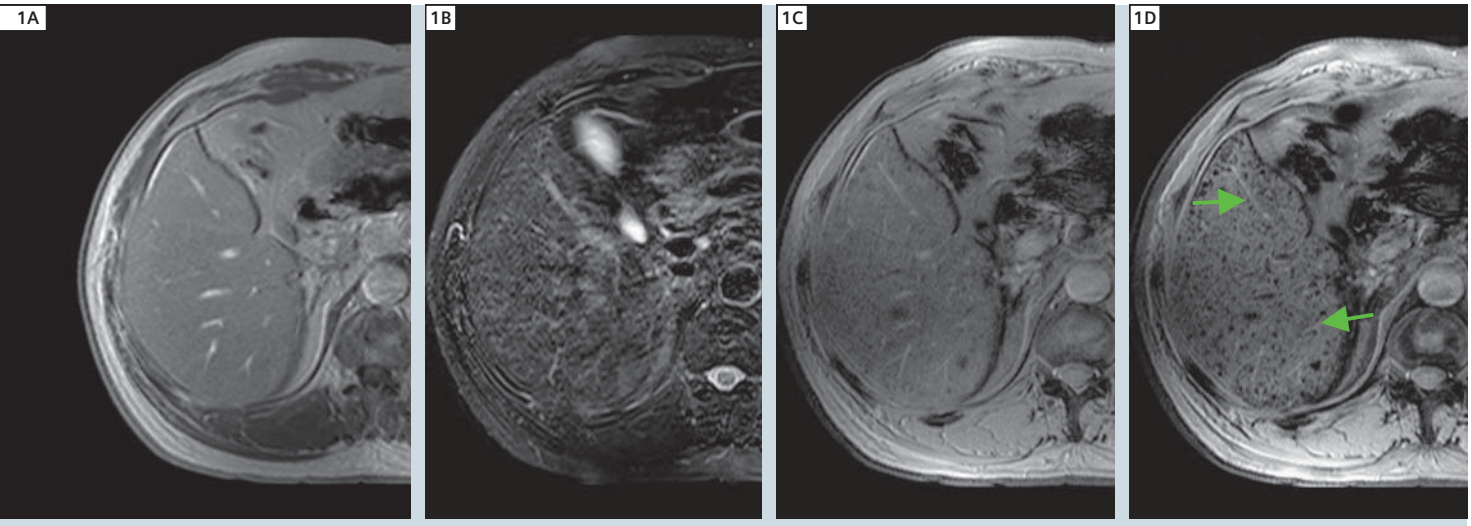

1 A 55-year-old man with cirrhosis caused by hepatitis B. **(1A)** Transversal T1-weighted imaging (flip angle 70°, TR/TE 140/2.46 ms) failed to demonstrate low-signal-intensity nodules. **(1B)** T2-weighted imaging (flip angle 122°, TR/TE 3700/84 ms) was affected in its ability to detect nodules because of the low contrast in the liver **(1C)** Transversal T2*-weighted imaging (flip angle 20°, TR/TE 150/10 ms) and **(1D)** transversal SWI (flip angle 20°, TR/TE 150/10 ms) showed innumerable low-signal-intensity nodules and only SWI showed nodules with diameter less than 2.5 mm, based on the signal void (white arrows). *Images courtesy of Zhongshan Hospital.*

Susceptibility-Weighted Imaging (SWI) is a new means to enhance MR imaging contrast by taking advantage of phase information induced by local susceptibility changes between tissues and veins [1]. In many studies [2], SWI has been proven to be of great value in the evaluation of various neurologic disorders, including traumatic brain injury (TBI), coagulopathic or other hemorrhagic disorders, vascular malformations, cerebral infarction, neoplasms, and neurodegenerative disorders associated with intracranial calcification or iron deposition. However, the rest of the body also offers a myriad of possibilities for SWI such as imaging vessel walls [3], imaging nerves, imaging calcium and imaging iron deposition in the heart and liver [4]. Imaging the brain with SWI has been a challenge because the amount of iron there (except for microbleeds) is quite small and requires very long echo times to image (especially for imaging the oxygen saturation in vessels and ferritin). Imaging iron in the liver, however, lies at the opposite end of the spectrum especially for imaging cirrhosis or hemachromatosis where iron concentrations can exceed 1 mg / gm tissue. The advantage of using the phase information, especially in the cases of high iron deposition, is that even for very short echoes

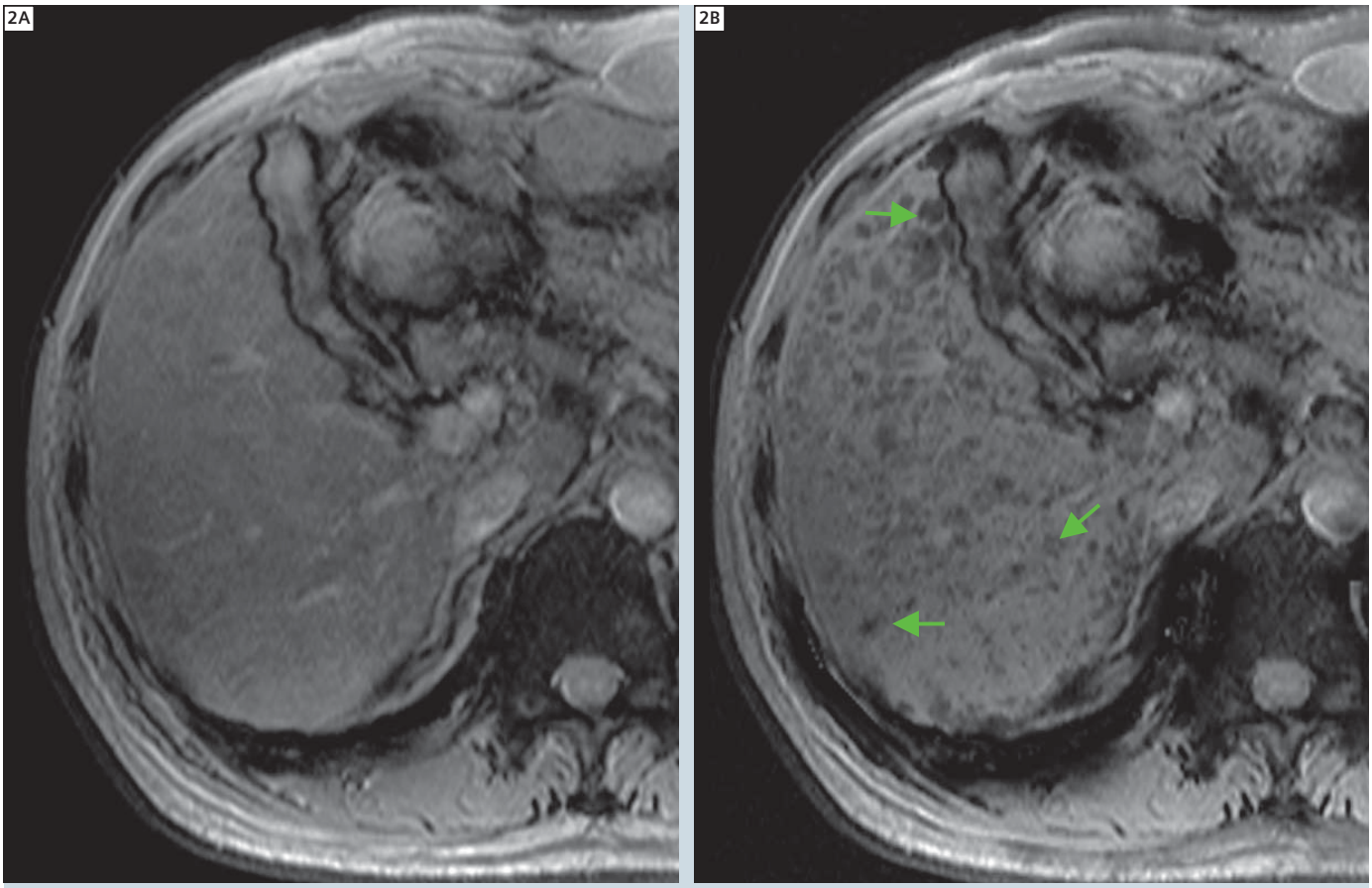

2 A 51-year-old man with HCC in cirrhotic liver (secondary to hepatitis B). **(2A)** transversal T2*-weighted imaging (flip angle 20°, TR/TE 150/10 ms) shows few nodules; **(2B)** transversal SWI (flip angle 20°, TR/TE 150/10 ms) shows innumerable low-signal-intensity nodules (arrows). *Images courtesy of Zhongshan Hospital.*

(at least where signal remains) phase information can play a role in monitoring not only the presence of iron but the amount of iron present as well [5]. In this case, the challenge is imaging the tissue with short enough echo times so as not to lose all signal in a liver affected with high iron overload. The purpose of this article is to introduce the reader to a practical version of SWI in the liver using a 2D breathhold multi-echo gradient echo scan.

In hepatitis, iron deposition (siderosis) often occurs within reticuloendothelial cells, as ferritin is mobilized from damaged hepatocytes [6–8]. However, in the cirrhotic liver, iron accumulates within regenerative or dysplastic nodules referred to as "siderotic nodules" (SN). Some findings suggest increased iron deposition may be a biomarker for the degree of underlying chronic liver disease [9–11].

Siderotic nodules can be detected with variable sensitivity using ultrasound, CT, T1-weighted gradient echo (GRE), T2-weighted fast spin echo, and T2*-weighted GRE MRI [10, 12–17]. To date, using T2* with long echoes (TE > 9 ms, at 1.5T) and low flip angles (< 45°) has been the method of choice at 1.5T. Our approach has been to use 2D breathhold SWI with short echoes to assess SN at the more challenging field strength of 3T. Imaging at 3T is tougher in this case because the susceptibility effect is proportional to the product of echo time and field strength [18]. Imaging a fixed amount of iron at 1.5T with an echo time of 20 ms before losing signal would require an echo time of 10 ms at 3T. This limits the resolution that is possible. As will be seen here, the current system limits do not prevent rapid high resolution imaging of the liver with SWI to image siderotic nodules.

A standard 12-channel body matrix coil was used for imaging on a Siemens 3T MAGNETOM Verio system. Imaging included pre-contrast transversal T1-weighted 2D GRE (flip angle 70°, TR/TE 140/2.46 ms), transversal T2-weighted fat-suppressed 2D turbo spin echo (TSE, flip angle 122°, TR/TE 3700/84 ms, echo train length (ETL) 9), transversal T2*-weighted 2D GRE (flip angle 20°, TR/TE 150/10 ms) and transversal abdominal 2D SWI (flip angle 20°, TR/TE 150/10 ms). For all sequences, the following parameters were used: Field-of-view (FOV)

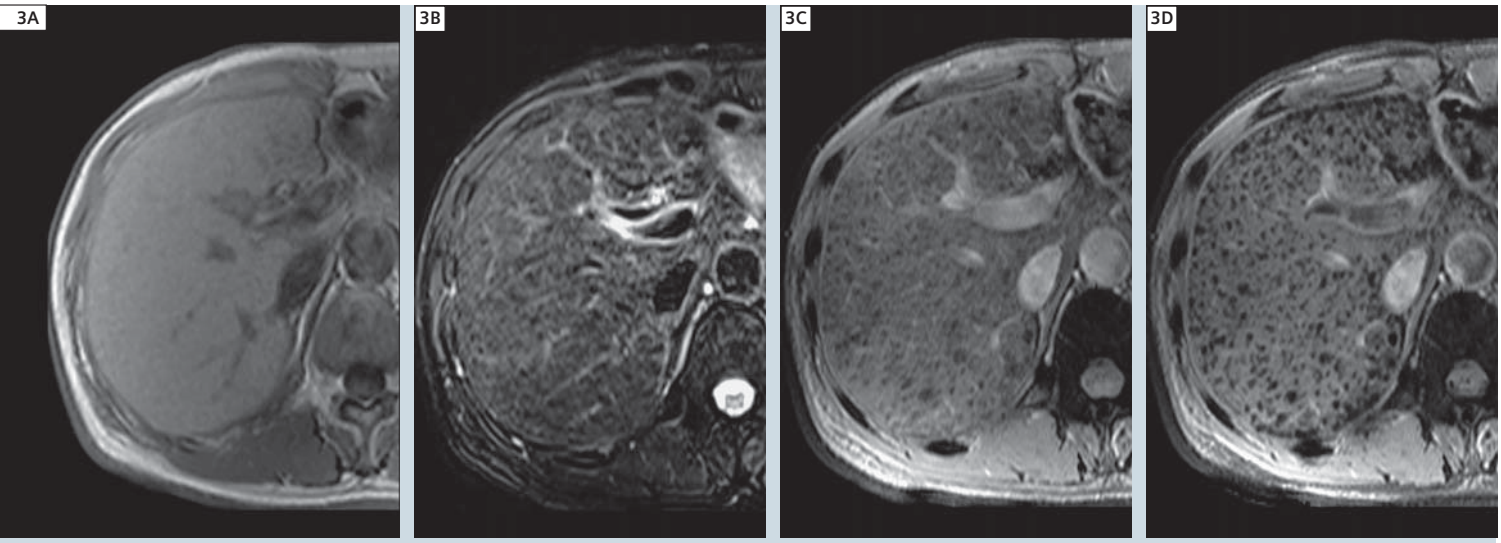

3 A 50-year-old man with cirrhosis caused by hepatitis C. **(3A)** Transversal T1-weighted imaging (flip angle 70°, TR/TE 140/2.46 ms) and **(3B)** T2-weighted imaging (flip angle 122°, TR/TE 3700/84 ms) fail to demonstrate low-signal-intensity nodules with good conspicuity. (3C) Transversal T2*-weighted imaging (flip angle 20°, TR/TE 150/10 ms) demonstrated low-signal -intensity nodules and **(3D)** transversal SWI (flip angle 20°, TR/TE 150/10 ms) showed innumerable low-signal-intensity nodules with the best conspicuity. *Images courtesy of Zhongshan Hospital*.

380 × 285 mm²; matrix 320–384 × 250; 30 slices, slice thickness 5 mm with a gap of 1 mm. Two to three 15–20 seconds breathhold acquisitions were acquired to cover the liver.

Our new multi-echo, multi-slice 2D GRE sequence with SWI reconstruction** was used for abdominal SWI. A complete scan consisted of a concatenation of 3 adjacent 10-slice transversal acquisitions each taking 16 seconds, an easy breathhold period. In total, 30 slices could be acquired in less than 1 minute: 20 seconds for 3 breathholds (6 seconds/per), 3 breathhold instructions (3 seconds/per) and 2 breaks (5 seconds/per) between every two breathholds.

We evaluated 40 patients who had cirrhosis from a variety of causes including hepatitis B (n = 28), hepatitis B and C (n = 3), and hepatitis B surface antigen carriers (n = 9). To compare the number of small nodules, a single representative slice was chosen from the 30-slice T2*-weighted GRE dataset which was, by consensus, felt to subjectively contain the most SN. Conventional T1, T2, T2* were analyzed along with SWI. The "siderotic" nodules (SN) were counted, and their sizes measured by both readers, in consensus, using a ruler tool on the workstation (*syngo* MultiModality Workplace, MMWP, Siemens Healthcare). SN conspicuity was graded on each sequence based on the ratio of SN signal intensity to background parenchyma. Normal controls and cirrhotic patients were analyzed the same way.

In general, SWI detected far more SN than the other methods. The total number of SN detected by SWI was greater by factors of 14.8, 4.6, and 1.5 compared to conventional T1, T2 and T2* methods, respectively (Fig. 1). In 10 of the 40 patients, the number of SN detected by SWI was more than two times that of T2*-weighted imaging, and in a single case, nearly 5 times greater, (Fig. 2). SN could not be detected by T1-weighted imaging in 10 patients. Also, SWI detected smaller SN (less than 2.5 mm in diameter according to the signal void) more frequently than T2*-weighted imaging. Lesion conspicuity was least with T1-weighted imaging and greatest with SWI (Fig. 3). More practically for radiologic purposes, SWI had superior contrast (i.e., lesions appeared more hypointense to background hepatic parenchyma) and better visibility than other methods.

A TE of 10 ms at 1.5T has been shown to be 80% sensitive for the detection of SN, though using a longer TE (15 to 20 ms at 1.5T) may increase sensitivity [19, 12]. If we assume SWI to be the gold standard for the detection of SN, the sensitivity of T2*-weighted MRI for lesions greater than 2.5 mm in diameter was 85% in this study, which is similar to the sensitivity of 80% achieved by Krinsky et al. with a TE of ≥9 ms at 1.5T using whole-explant livers as the gold standard [19].

Several factors account for the improved detection of SN with SWI compared to other sequences. Since SWI uses processed phase information to enhance susceptibility effects in the image, it can better detect changes in susceptibility compared to T2*-weighted images. Theoretical investigations have indicated that a highly paramagnetic object measuring less than a quarter of a voxel can have a dramatic appearance within a single voxel, due to the "amplified signal cancellation" [20].

Improved detection of SN has several possible clinical implications and avenues for future research. Improved detection of iron may allow nodules not definitively siderotic on T2*-weighted images to be classified as siderotic, reducing the need for biopsy. Excessive hepatic iron content is an accepted risk factor for developing hepato-cellular carcinoma (HCC). Both low and high grade siderotic dysplastic nodules (DN) have been considered pre-malignant lesions, but a relationship has not been established [11]. A poor response to interferon therapy has been correlated with increased hepatic iron content [21, 22], and the MRI grade of SN has been shown to significantly correlate with degree of peri-portal inflammatory activity in cirrhotic patients [9]. Distribution of iron within a nodule has implications for the detection of HCC; a pattern of decreased hepatic iron uptake within a portion of an otherwise iron-accumulating nodule ("nodule within a nodule" sign) has been shown to be highly predictive of HCC [23–25]. Additionally, regions of parenchymal iron sparing raise suspicion of HCC when detected in the background of diffuse iron deposition [26]. Therefore, improved detection of SN may also provide insight into the relationship between disease activity, progression, malignancy, and therapeutic response.

In conclusion, the use of breathhold 2D SWI in the liver should open a new door in the study of cirrhosis of the liver and in the future to the study and quantification of iron in hemachromatosis.

*This information about this product is preliminary. The product is under development and not commercially available in the U.S., and its future availablility cannot be ensured.

**WIP – Work in progress. This technology is under development and is not available for sale in the U.S.

References

1 E.M. Haacke, S. Mittal, Z. Wu, J. Neelavalli and Y.-C.N. Cheng, AJNR 30:19–30, January 2009.

2 S. Mittal, Z. Wu, J. Neelavalli and E.M. Haacke, AJNR 30:232–252, February 2009.

3 Qi yang, et al, Imaging the vessel wall in major peripheral arteries using susceptibility-weighted imaging, JMRI Volume 30(2): 357–365(2009).

4 Yongming Dai, et al, Improving Detection of Siderotic Nodules in Cirrhotic Liver With a Multi-Breath-Hold Susceptibility-Weighted Imaging Technique, JMRI 34:318–325(2011).

5 E.M. Haacke, J. Tang, J. Neelavalli, and Y.C.N. Cheng, Susceptibility Mapping as a Means to Visualize Veins and Quantify Oxygen Saturation, JMRI 32:663–676 (2010).

6 Prieto J, Barry M, Sherlock S. Serum ferritin in patients with iron overload and with acute and chronic liver diseases. Gastroenterology 1975;68(3):525–33.

7 Adams PC. Iron overload in viral and alcoholic liver disease. J Hepatol 1998;28:19–20.

8 Ludwig J, Hashimoto E, Porayko MK, et al. Hemosiderosis in cirrhosis: a study of 447 native livers. Gastroenterology 1997;112(3):882–8.

9 Kim MJ, Mitchell DG, Ito K, Kim JH, Pasqualin D, Rubin R. Hepatic iron deposition on magnetic resonance imaging: correlation with inflammatory activity. J. Comput. Assist. Tomogr. 2002;26(6):988–993.

10 Jingbo Zhang, Glenn A. Krinsky. Iron containing nodules of cirrhosis. NMR Biomed. 2004;17(7):459–464.

11 Krinsky GA, Zivin SB, Thorner KM, Lee VS, Theise ND, Weinreb JC. Low-grade siderotic dysplastic nodules: determination of premalignant lesions on the basis of vasculature phenotype. Acad. Radiol. 2002;9(3):336–341.

12 Siegelman ES, Mitchell DG, Semelka RC. Abdominal iron deposition: metabolism, MR findings, and clinical importance. Radiology 1996;199(1):13–22.

13 Murakami T, Nakamura H, Kuroda C, et al. Case report. Siderotic nodules in hepatic cirrhosis disappearing after biliary hemorrhage: MR imaging. J. Comput. Assist. Tomogr. 1991;15(6):1039–1041.

14 Murakami T, Nakamura H, Hori S, et al. CT and MRI of siderotic regenerative nodules in hepatic cirrhosis. J. Comput. Assist. Tomogr. 1992; 16:578–582.

15 Itai Y, Ohnishi S, Ohtomo K, et al. Regenerating nodules of liver cirrhosis: MR imaging. Radiology 1987;165(2):419–423.

16 Ohtomo K, Itai Y, Ohtomo Y, Shiga J, Lio M. Regenerative nodules of liver cirrhosis: MR imaging with pathologic correlation. Am. J. Radiol. 1990;154(3):505–507.

17 Murakami T, Kuroda C, Marukawa T, et al. Regenerating nodules in hepatic cirrhosis: MR findings with pathologic correlation. Am. J. Radiol. 1990;155(6):1227–1231.

18 E.M. Haacke et al, Establishing a Baseline Phase Behavior in Magnetic Resonance Imaging to Determine Normal vs. Abnormal Iron Content in the Brain. JMRI 26:256–264 (2007).

19 Krinsky GA, Lee VS, Nguyen MT, et al. Siderotic nodules in the cirrhotic liver at MR imaging with explant correlation: no increased frequency of dysplastic nodules and hepatocellular carcinoma. Radiology 2001;218(1):47–53.

20 Cheng YC, Haacke EM. Predicting BOLD signal changes as a function of blood volume fraction and resolution. NMR Biomed. 2001;14(7–8):468–77.

21 Van Thiel DH, Friedlander L, Fagiuoli S, Wright HI, Irish W, Gavaler JS. Response to interferon alpha therapy is influenced by the iron content of the liver. J. Hepatol. 1994; 20(3):410–415.

22 Barton AL, Banner BF, Cable EE, Bonkovsky HL. Distribution of iron in the liver predicts the response of chronic hepatitis C infection to interferon therapy. Am. J. Clin. Pathol. 1995;103(4): 419–424.

23 Terada T, Kadoya M, Nakanuma Y, Matsui O. Iron accumulating adenomatous hyperplastic nodule with malignant foci in the cirrhotic liver: histopathologic, quantitative iron, and magnetic resonance imaging in vitro studies. Cancer 1990;65(9): 1994–2000.

24 Mitchell DG, Rubin R, Siegelman ES, Burk DL, Rifkin MD. Hepatocellular carcinoma within siderotic regenerative nodules: the "nodule-within-nodule" sign on MR images. Radiology 1991;178(1):101–103.

25 Sadek AG, Mitchell DG, Siegelman ES, Outwater EK, Matteucci T, Hann HW. Early hepatocellular carcinoma that develops within macroregenerative nodules: growth rate depicted at serial MR imaging. Radiology 1995;195(3):753–756.

26 Pomerantz S, Siegelman ES. MR imaging of iron depositional disease. Magn. Reson. Imag. Clin. N. Am. 2002;10(1):105–120, vi.

Contact
Yongming Dai
Siemens Healthcare China
MR Collaboration NE Asia
No. 278, Zhouzhu Road
SIMZ, Pudong New Area
Shanghai, 201318
P.R.China
yongming.dai@siemens.com

Dixon Sequence: Liver MRI and *syngo*.via Layouts

Jean-Paul Abécassis, M.D.; Denis Parienté, M.D.

Imagerie Paris Centre, Paris, France

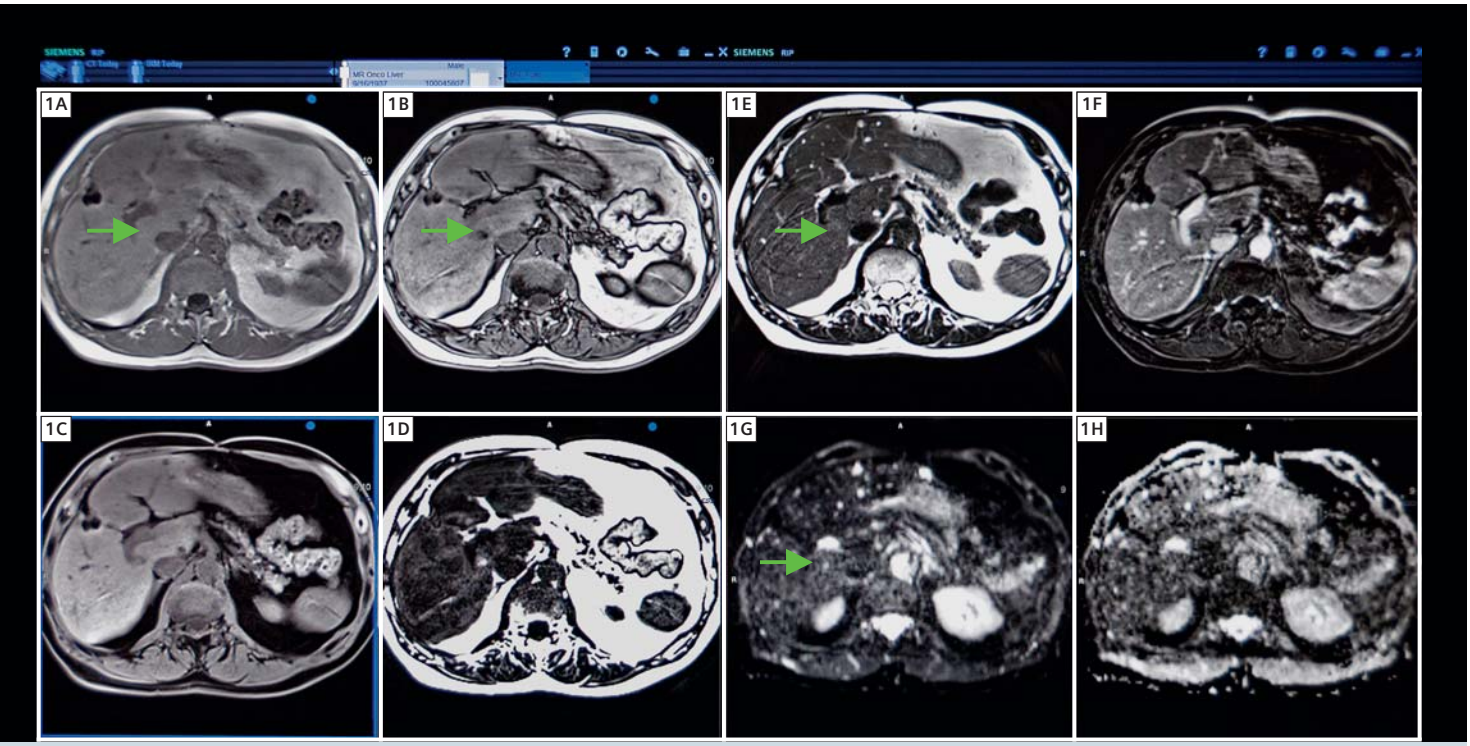

1 MRI of the liver in a 67-year-old patient, treated for hemochromatosis, operated 3 years ago for hepatocarcinoma. In phase T1 **(1A)**, T2 **(1E)** and DWI **(1G)** show simple cysts and scarring from surgery; opposed phase T1 **(1B)** and water T1 **(1C)** show unspecific hypointense signal internally to the right branch of the portal vein (arrow); fat T1 **(1D)** show the abnormality as a hyperintense signal compatible with lipid rich hepatocarcinoma, confirmed by the VIBE sequence **(1F)**.

Purpose

The purpose of this article in to illustrate the benefit of the Dixon T1 sequence in liver MRI and to emphasize the specific layouts that have been adapted from factory supplied *syngo*.via layouts to display its results.

Introduction

The Dixon sequence allows separation of fat and water in spin echo T1 images. Previous to the development of this sequence, application of a dephasing gradient resulted in two images, one with fat and water in phase (standard T1) and one with fat and water dephased (opposed phase image). Recent technical developments have widened the field of utilisation, with breathhold acquisition and by generating, from a 3 point acquisition a water-only image and a fat-only image.
A variety of liver lesions ranging from benign to malignant may contain fat. The most common benign liver lesions containing fat are hepatocellular adenoma, focal steatosis, lipoma, and pseudo-lipoma of the Glisson capsule. Examples of malignant tumors include hepatocellular carcinoma and liposarcoma. Identification of fat within a liver lesion can be critical in characterization of a lesion.

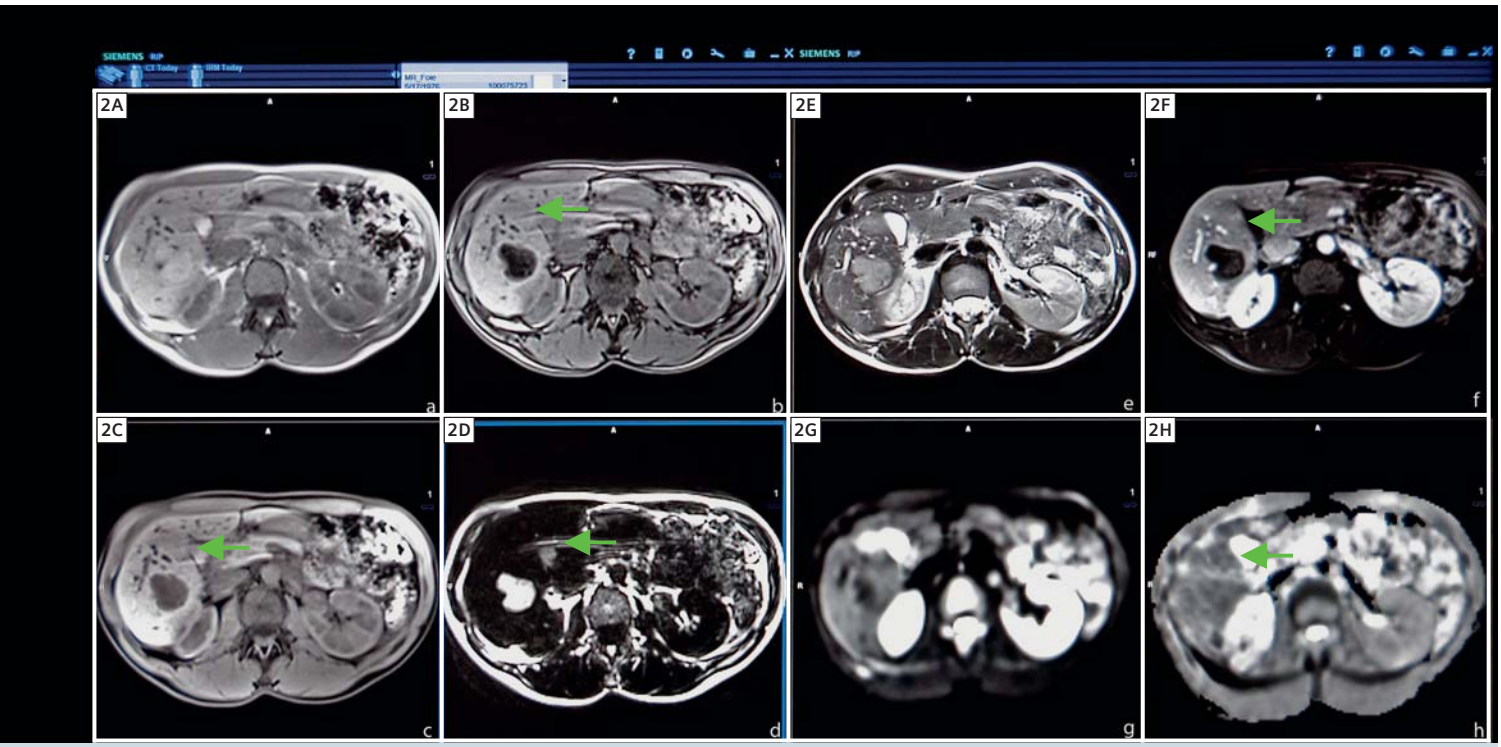

2 MRI of the liver in a 35-year-old woman, referred for multiple incidental lesions at ultrasound, with a history of 15 years of oral contraception: T1 **(1A)** displays an isointense 3 cm lesion in the right lobe of the liver; T2 **(2E)**, VIBE **(2F)** and DWI **(2G)** are unspecific, but the fat-only T1 image shows bright signal typical of hepatocellular adenoma **(2H)**.

Sequence details

Images have been acquired using a 1.5T MAGNETOM Aera, with the following parameters: field-of-view 380 mm², TR 6.77 ms, TE 2.38 ms, slice thickness 3 mm, breathhold acquisition time 21 s, results in 4 T1w images at each slice level: in phase image (standard T1), opposed phase image, water-only image (fat suppressed T1), fat-only image. An axial Dixon T1 sequence is part of our routine abdominal protocol, and also includes an axial T2 BLADE, axial diffusion-weighted imaging (DWI) sequence with 3 b-values (100, 400, 800) and axial T1 post contrast VIBE dynamic sequence at 0, 30s, 60s and 180s.

Conclusion

T1 Dixon images are an essential part of liver examinations, allowing immediate recognition of intra-tumoral macroscopic fat or intracellular lipid using a specific 4D *syngo*.via layout.

syngo.via Layouts

In order to diagnose the cases in this study, we used the onco-liver workflow* and its 'dynamic' layout. In the dual monitor version of this layout, each screen is divided into 4 windows, synchronised for zooming and navigation but not for windowing. The left screen displays the 4 Dixon images (in phase, opposed phase, water-image, fat-image). The windows of the right screen are assigned to T2 BLADE, VIBE, DWI and the ADC map. An important aspect to understand when working with *syngo*.via is that the layouts not only arrange images in a certain order, but they also assign certain functions to the image segments. In this case, with the 'dynamic' layout, the VIBE and DWI segments are 4D windows, allowing to scroll through space (up and down) and through time (left to right) from one b-value to another (diffusion) or from one injection time to another (contrast images).

Another example for how we have adapted *syngo*.via layouts is in our prostate MR workflow.

In imaging the prostate, there are roughly 2 different indications: either the patient has a known cancer and we need to assess the extent of the lesion, or the patient is suspected of having cancer but prior biopsies are negative and the question is "is there a target lesion for a new set of biopsies?" To assess the extension, we have adapted a layout, with axial, coronal and sagittal T2, diffusion and ADC map, T1, to assess post biopsy hemorrhage and axial T2 of the pelvis to look for adenopathies (Fig. 3).

3

3 *syngo*.via layout to read prostate examinations.

In this last example we have taken a standard taskflow and adapted it in order to visualize the VIBE sequence in all 3D planes. This layout has proved to be very useful to quickly assess the vessels (Fig. 4).
The ability to structure our own workflows and layouts in *syngo*.via has helped us to improve the diagnostic process in our practice. As with any software, the more we use it, the more possibilities we discover, and the more efficient we become.

Contact
Denis Parienté, M.D.
Imagerie Paris Centre
102 Avenue Denfert-Rochereau
75014 Paris
France
Phone +33 (0)1 43 35 55 20
denisparіente@gmail.com

*This feature is work in progress and is not commercially available in the US.

4

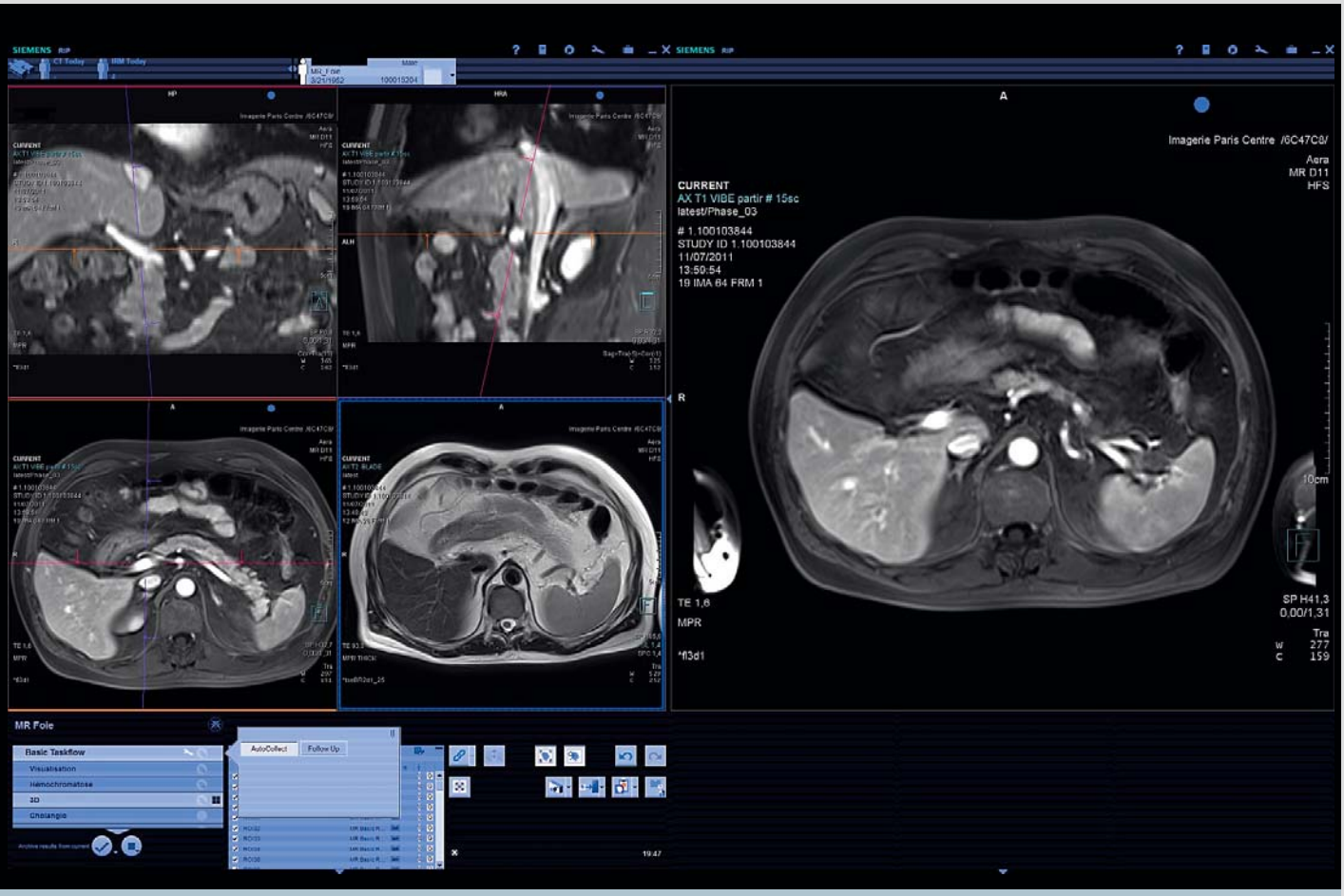

4 *syngo*.via layout to visualize the VIBE sequence in all 3D planes.

CMR Imaging of Profound Macrovascular Obstruction

Anurag Sahu, M.D., FACC[1]; Gary McNeal, BS[2]

[1]*Emory University Hospital, Atlanta, GA, USA*
[2]*Siemens Healthcare, MR RD Cardiac Collaboration, Hoffman Estates, IL, USA*

Introduction

Cardiac cine imaging of the myocardium may be used to assess wall motion abnormalities, wall thinning, the presence of tumor and thrombus, and morphological variants in a wide variety of cardiac syndromes and conditions. Dynamic first-pass myocardial perfusion imaging may be used to assess the myocardium for reversible ischemia, irreversible ischemia, microvascular and macrovascular obstruction. Delayed myocardial enhancement imaging may be used to assess myocardial viability in the setting of chronic and acute infarct, as well as a host of other non-ischemic cardiomyopathies. In this case report, all three techniques were used to collectively assess for myocardial viability in a patient presenting with chest pain.

Patient history

42-year-old male with a history of diabetes mellitus presented to an outside hospital with complaints of chest pain. He was found to have ST elevation in the anterior leads and received thrombolytic therapy. His ST segment elevation did not resolve and chest pain resolution did not occur for a period of 24 hours. Four days later he was transferred to our institution for consideration of bypass surgery versus interventional therapy for obstructive coronary artery disease. Echocardiography illustrated severely depressed LV function with akinetic anterior wall. Cardiac MRI was requested for assessment of LV function, myocardial viability, and to evaluate for possible left ventricular thrombus.

Methods

All imaging was performed on a 1.5T Siemens MAGNETOM Avanto, software version *syngo* MR B17, using a 6-channel anterior body array coil and the 6-channel spine array coil. Initial pre-contrast cardiac cine imaging of the myocardium was performed in short axis and long axis views with a segmented TrueFISP pulse sequence (Fig. 1): TR 38.8 ms, TE 1.2 ms, flip angle (FA) 66°, field-of-view (FOV) 317 x 350 mm, matrix 174 x 192, slice thickness (SL) 7 mm, 1 average, 14 segments, bandwidth (BW) 930 Hz/pix, GRAPPA x2, retrospective gating, normalized, medium smoothing filter, scan time 6–7 s/slice. There was akinetic wall motion in the territory of the left anterior descending coronary artery (LAD).

Dynamic first-pass myocardial perfusion imaging was performed in 3 short axis views (base, mid, apex) with an SR TurboFLASH pulse sequence (Fig. 2): TR 225 ms, TE 1.2 ms, FA 12°, Mag Prep Non-sel SR Perf, TI 120 ms, FOV 300 x 360 mm, matrix 120 x 192, Slice 8 mm, 1 average, 86 segments, BW 521 Hz/pix, GRAPPA x2, diastolic gating, normalized, medium smoothing filter, scan time 60 heartbeats. Single dose (0.1 mmol/kg) Multihance contrast agent was bolus

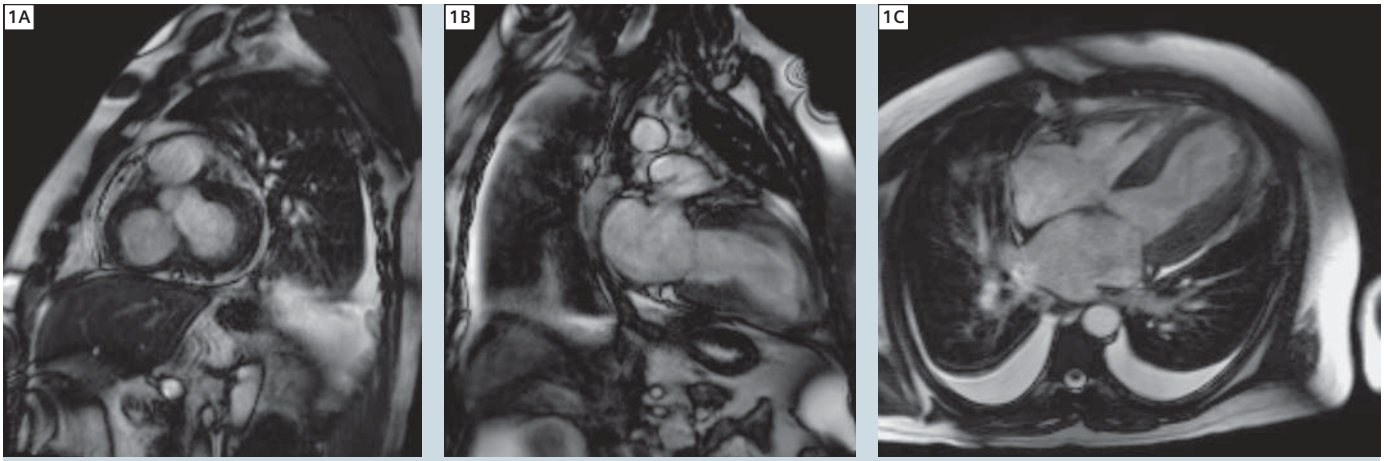

1 Segmented TrueFISP cine **(1A)**, short axis, **(1B)** 2-chamber-view, **(1C)** 4-chamber-view.

injected during first-pass scan at 3 ml/sec, flushed by 20 ml normal saline at 3 ml/sec. Patient was instructed to hold the breath for as long as possible, then breathe slow and shallow for remainder of scan. There was transmural hypo-intense signal in the LAD territory.

Post-contrast cardiac cine imaging of the myocardium was performed in multiple short axis and long axis views with a Real-time TrueFISP pulse sequence (Fig. 3): TR 117.3 ms, TE 1.0 ms, FA 59°, FOV 360 x 360 mm, matrix 121 x 160, slice 8 mm, 1 average, 51 segments, BW 1488 Hz/pix, TGRAPPA x3, normalized, medium smoothing filter, scan time 3 s/slice. There was akinetic wall motion and transmural hypo-intense signal in the LAD territory.

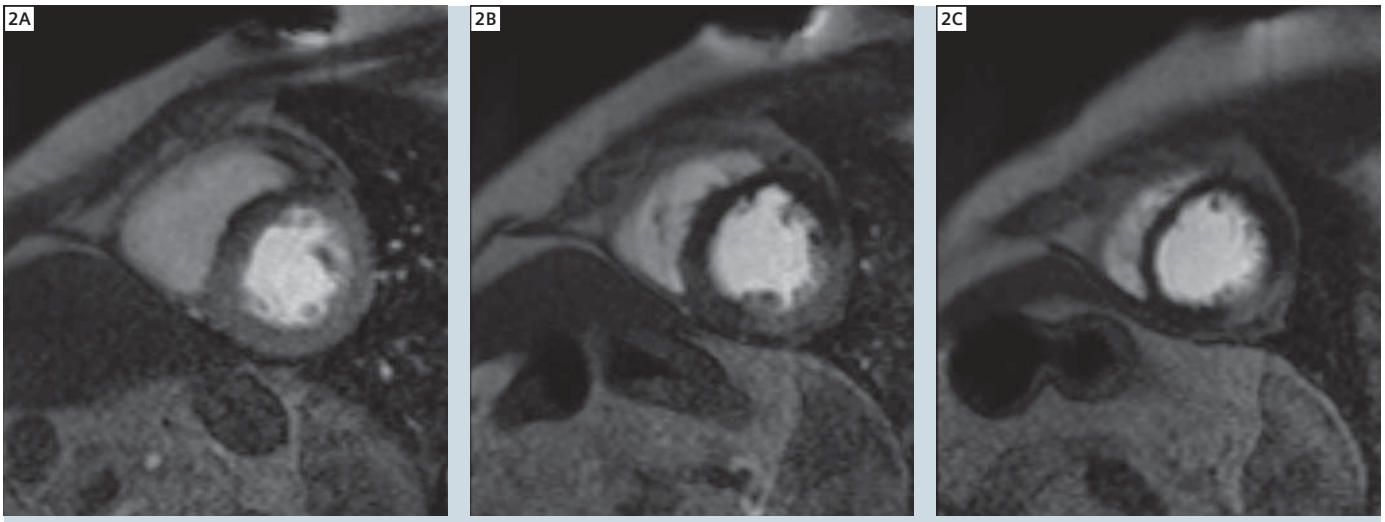

2 SR TurboFLASH first-pass perfusion: **(2A)** base, **(2B)** mid, **(2C)** apex.

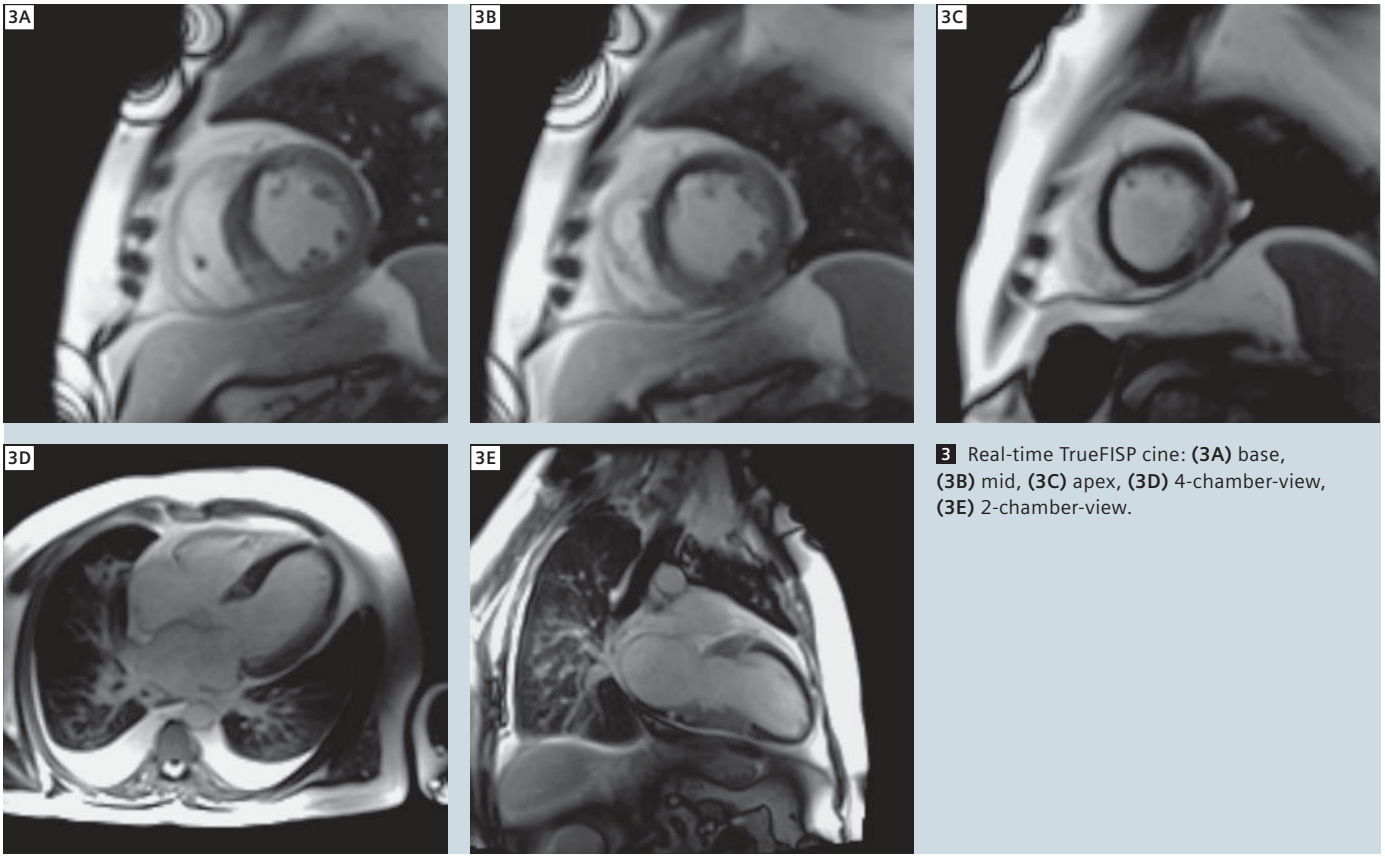

3 Real-time TrueFISP cine: **(3A)** base, **(3B)** mid, **(3C)** apex, **(3D)** 4-chamber-view, **(3E)** 2-chamber-view.

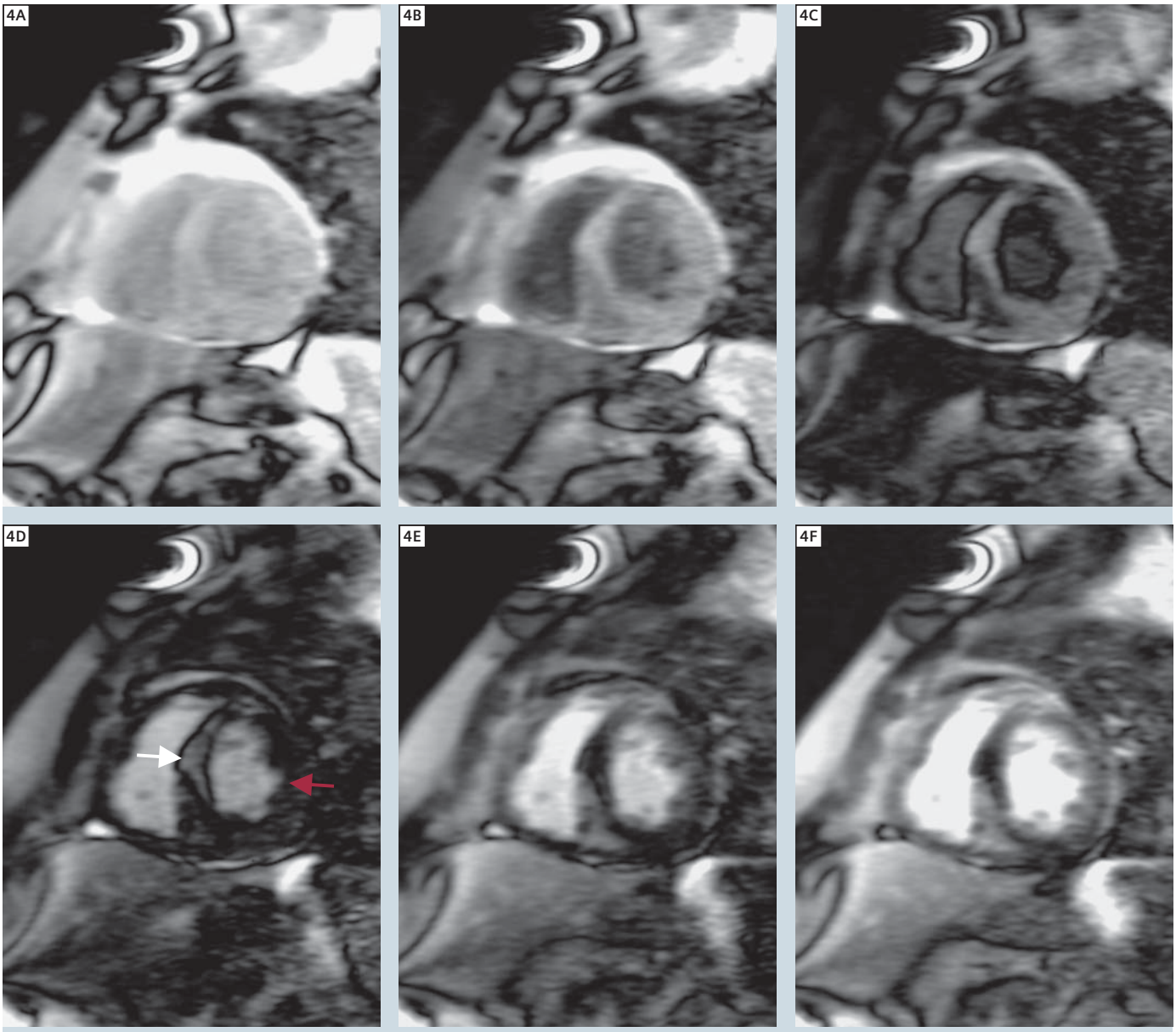

4 TI scout **(4A)** 95 ms, **(4B)** 130 ms, **(4C)** 167 ms, **(4D)** 202 ms, **(4E)** 240 ms, **(4F)** 275 ms.

TI Scout imaging was performed at a mid-ventricular level 8 minutes post-contrast using an IR TrueFISP pulse sequence (Fig. 4): TR 36.0 ms, TE 1.1 ms, FA 50°, Mag Prep TI Scout, FOV 262 x 350 mm, matrix 72 x 192, slice 7 mm, 1 average, 14 segments, BW 965 Hz/pix, normalized, medium smoothing filter, scan time 8-9 s/slice. Initially we were confused by the appearance of the septal wall. At TI 202 ms (Fig. 4D, white arrow) the antero-septal segment.demonstrates mid-grey signal intensity with surrounding dark-rim artifact which mimicks the characteristic appearance of normal myocardium at a slightly short TI time. In the next frame at TI 240 ms (Fig. 4E) the antero-septal segment.demonstrates well-nulled signal intensity with no surrounding dark-rim artifact which mimicks the typical appearance of normal myocardium at the optimal TI time. We mistakenly considered the antero-septal segment to represent normal myocardium, and we subsequently performed delayed enhancement imaging at TI 240 ms. In retrospect, the antero-septal segment actually represents abnormal myocardium whereas the lateral segment (Fig. 4D, yellow arrow) actually represents normal myocardium. As the lateral segment nulls optimally at TI 202 ms, we should have used that TI for optimal delayed enhancement imaging.

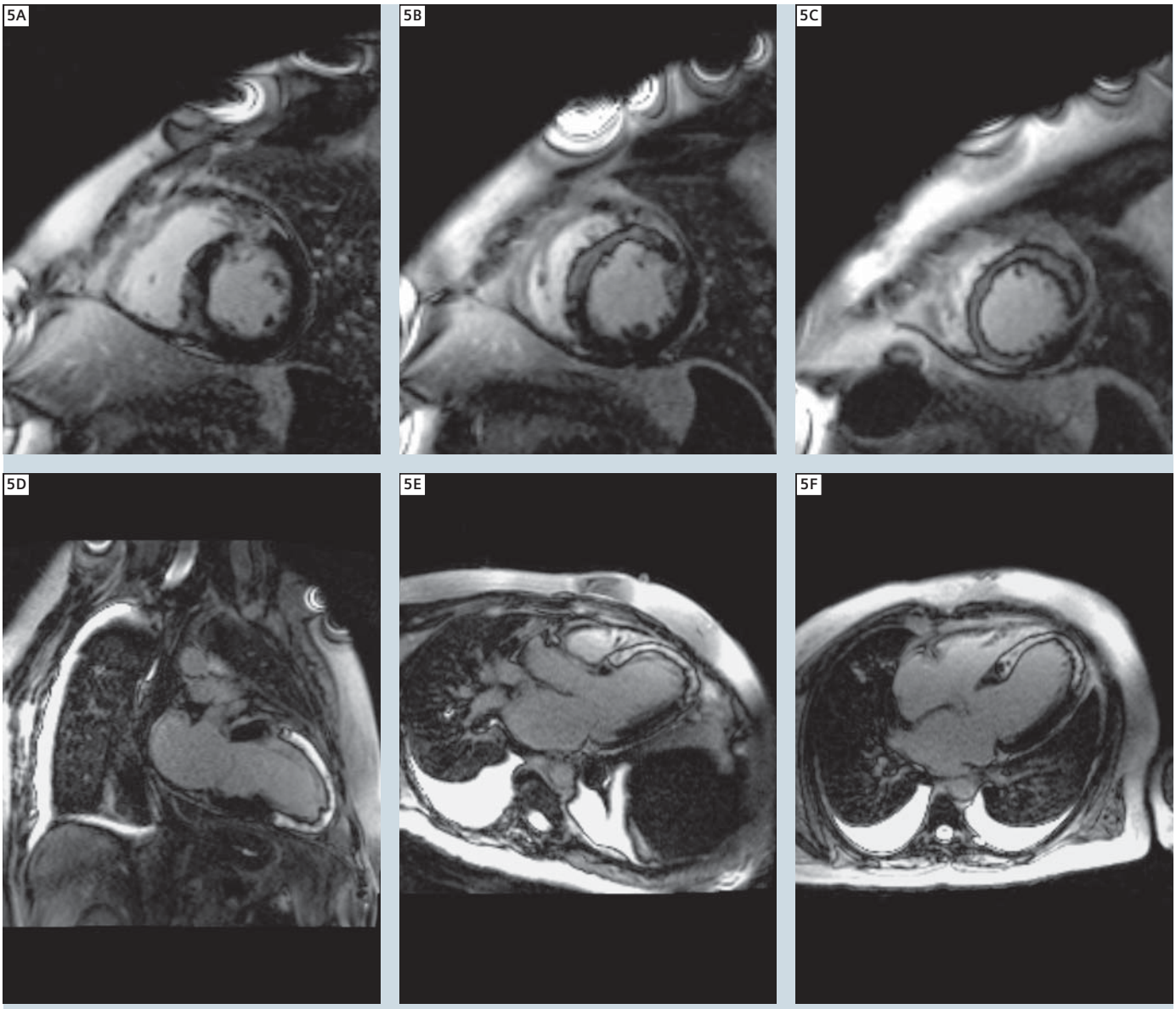

5 SS IR TrueFISP delayed enhancement TI 240 ms, MAGNITUDE images **(5A)** base, **(5B)** mid, **(5C)** apex, **(5D)** 2-chamber-view, **(5E)** 3-chamber-view, **(5F)** 4-chamber-view.

Delayed enhancement imaging was initially performed in multiple short axis and long axis views 9 minutes post-contrast using a single-shot IR TrueFISP pulse sequence (Fig. 5): TR 713 ms, TE 1.1 ms, FA 50°, Mag Prep Non-sel IR, TI 240 ms, FOV 350 x 350 mm, matrix 144 x 192, slice 8 mm, 1 average, 121 segments, BW 1184 Hz/pix, GRAPPA x2, normalized, medium smoothing filter, scan time 2 heartbeats/slice. In these MAGNITUDE images the viable myocardium appears to be well-nulled with no dark rim artifact at TI time of 240 ms, and there appears what was initially thought to be hyper-enhancement pattern in the LAD territory with an unusual dark rim artifact around the lesion. However, we subsequently determined that this bright signal in these MAGNITUDE images likely represents significant macrovascular obstruction (very long tissue T1) rather than myocardial scar (very short tissue T1).

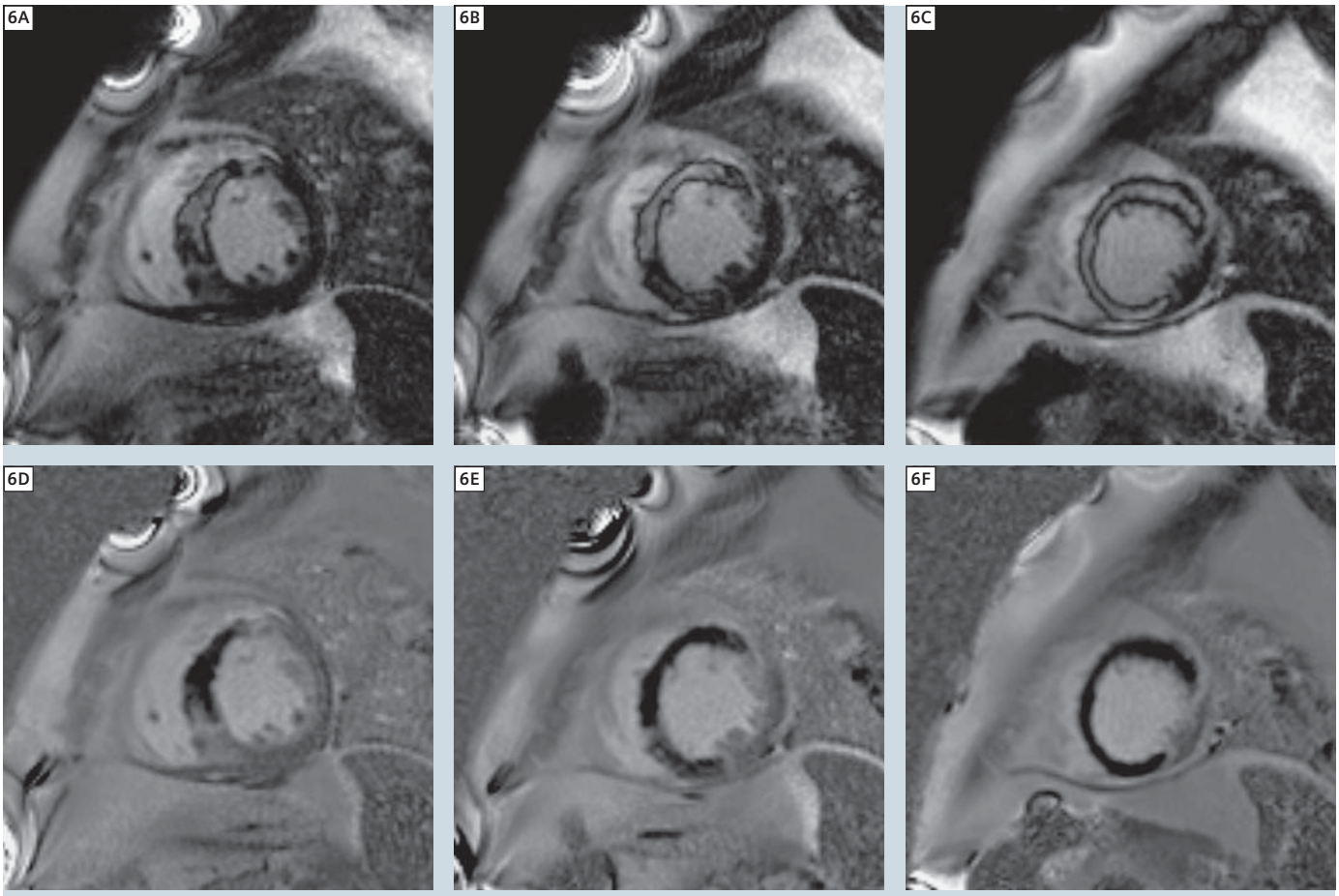

6 SS IR TrueFISP delayed enhancement TI 270 ms, MAGNITUDE images: **(6A)** base, **(6B)** mid, **(6C)** apex; PSIR images: **(6D)** base, **(6E)** mid, **(6F)** apex.

Delayed enhancement imaging was repeated in multiple short axis views 12 minutes post-contrast using a single-shot IR TrueFISP pulse sequence (Fig. 6): TR 800 ms, TE 1.1 ms, FA 40°, Mag Prep Non-sel IR, TI 270 ms, FOV 360 x 360 mm, matrix 144 x 192, slice 8 mm, 1 average, 180 segments, BW 1532 Hz/pix, GRAPPA x2, normalized, medium smoothing filter, scan time 2 heartbeats/slice. In the MAGNITUDE images there appears what was initially thought to be hyper-enhancement pattern in the LAD territory with an unusual dark rim artifact around the lesion, but otherwise good nulling in the normal myocardium. However, in the PSIR images the normal myocardium in the lateral and infero-lateral segments was intentionally windowed to a mid-grey level in order to demonstrate the much darker signal intensity in the LAD territory. The darker the signal intensity in a PSIR image, the longer its tissue T1 value. These PSIR images clearly demonstrate that the abnormal myocardium in the LAD territory has a much longer tissue T1 value than the normal myocardium elsewhere, thus suggesting no uptake of gadolinium in the LAD territory.

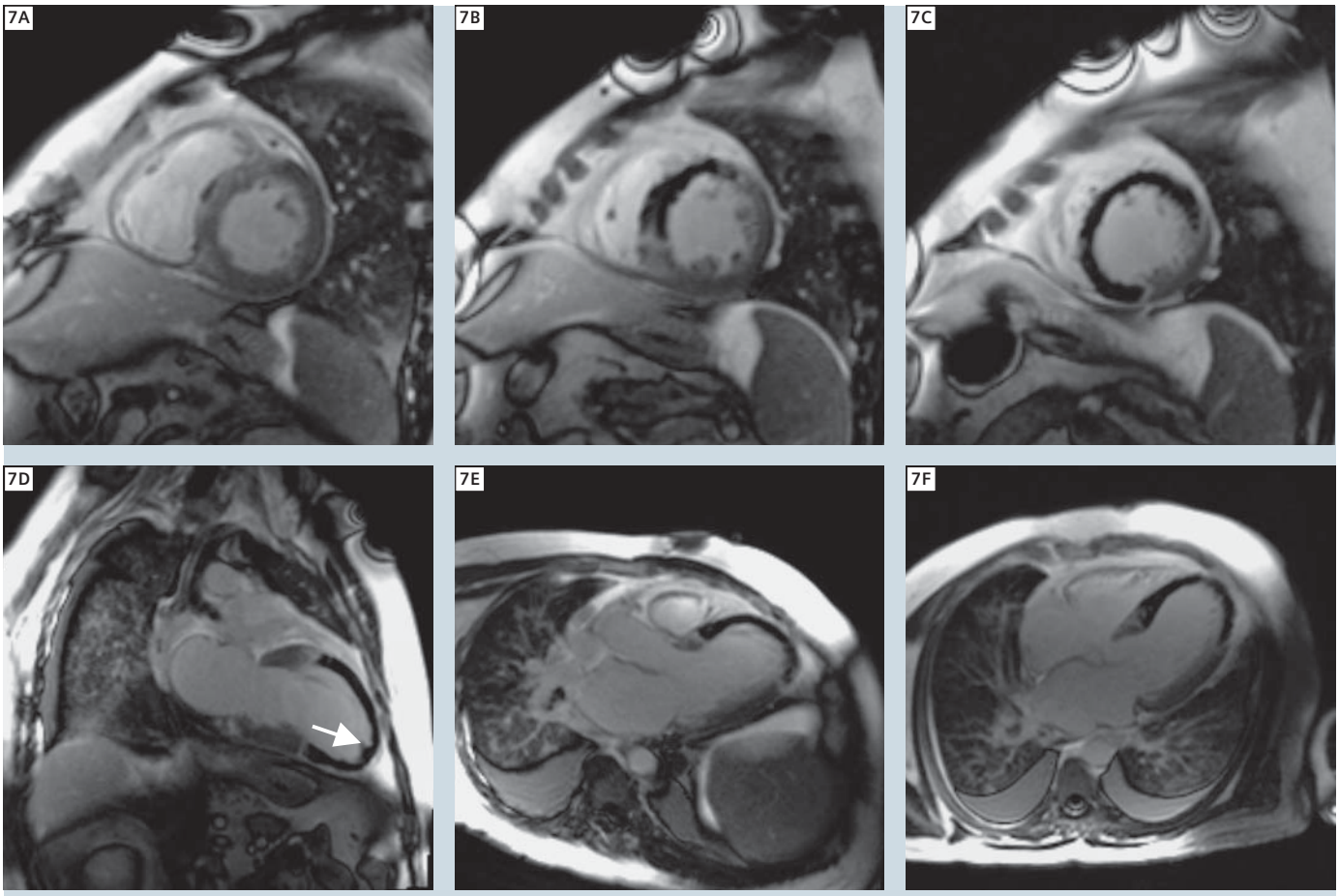

7 SS IR TrueFISP delayed enhancement TI 600 ms, MAGNITUDE images: **(7A)** base, **(7B)** mid, **(7C)** apex, **(7D)** 2-chamber-view, **(7E)** 3-chamber-view, **(7F)** 4-chamber-view.

Delayed enhancement imaging was repeated in multiple short axis and long axis views 13 minutes post-contrast using a single-shot IR TrueFISP pulse sequence (Fig. 7): TR 754 ms, TE 1.1 ms, FA 50°, Mag Prep Non-sel IR, TI 600 ms, FOV 350 x 350 mm, matrix 144 x 192, slice 8 mm, 1 average, 121 segments, BW 1184 Hz/pix, GRAPPA x2, normalized, medium smoothing filter, scan time 2 heartbeats/slice. In these MAGNITUDE images there is mid-grey signal intensity in the viable myocardium, with complete signal nulling at TI 600 ms in the LAD territory. This long TI technique is normally performed when evaluating intracavity thrombus, which appears extremely hypo-intense because it is completely avascular (white arrow). Fortunately, this technique further verified the long tissue TI of myocardium in the LAD territory likely due to macrovascular obstruction.

To corroborate the findings of non-viable myocardium in the LAD territory a Positron Emission Tomography (PET) viability study was also obtained after the CMR study (Fig. 8). Baseline resting perfusion imaging with Rubidium-82 in the Vertical Long Axis (VLA) view demonstrated absent perfusion of the entire apex, mid to apical anterior wall, and apical inferior wall. Myocardial glucose metabolism imaging with ^{18}F-fluoro-deoxyglucose (FDG) in the VLA view demonstrated absent metabolism in the same territory.

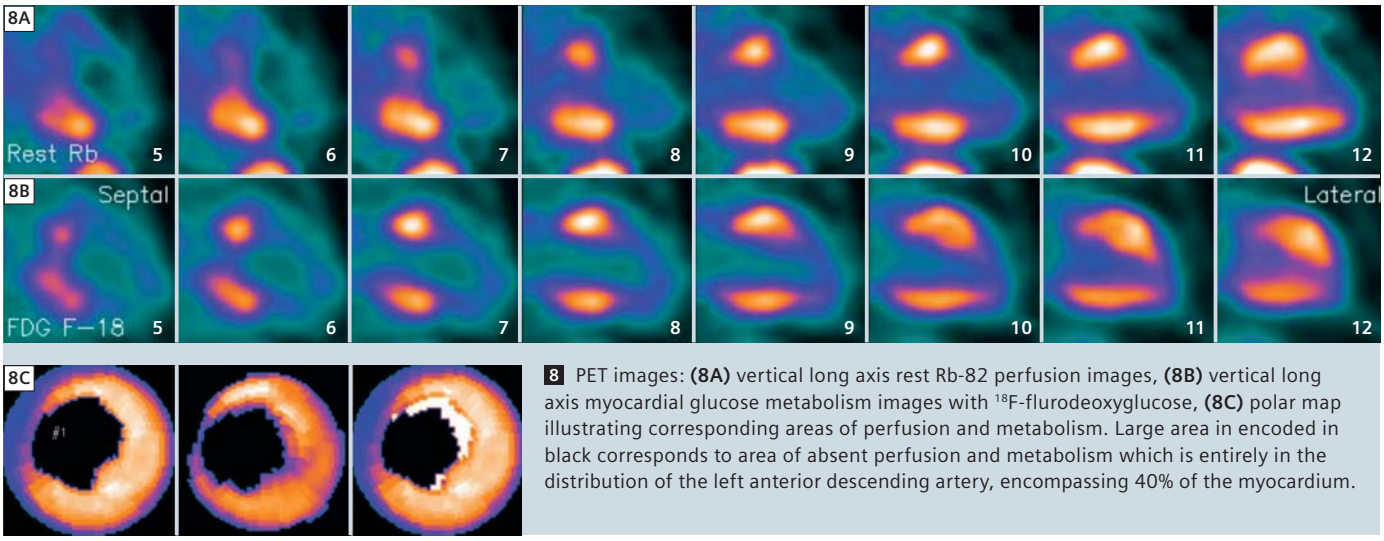

8 PET images: **(8A)** vertical long axis rest Rb-82 perfusion images, **(8B)** vertical long axis myocardial glucose metabolism images with ^{18}F-flurodeoxyglucose, **(8C)** polar map illustrating corresponding areas of perfusion and metabolism. Large area in encoded in black corresponds to area of absent perfusion and metabolism which is entirely in the distribution of the left anterior descending artery, encompassing 40% of the myocardium.

The PET study was acquired using a Siemens Biograph-40 PET/CT scanner comprised of a lutetium oxyorthosilicate (LSO) block detector ring of 162 mm FOV operating in 3D mode. Images were reconstructed dynamically (one 80-second frame, five 20-second frames, one 270-second frame) to generate time-activity curves for the left ventricular myocardium and the left ventricular cavity at a mid-ventricular level. Only frames with a greater than 2:1 average count ratio between the left ventricle and left ventricular cavity were used to generate the final static reconstruction. Diagnostic images with prompt gamma compensation (128 x 128 matrix) were reconstructed using ordered-subsets expectation maximization (OSEM) algorithm (4 iterations, 16 subsets) with a Gaussian post-filter of 7 mm.

Discussion

Initial cine imaging demonstrated akinetic wall motion in the territory of the left anterior descending artery (LAD), suggestive of either ischemia or infarct (Fig. 1). We then performed resting first-pass perfusion imaging which demonstrated an absence of contrast uptake, also suggestive of either ischemia or infarct in the LAD territory (Fig. 2). Post-contrast real time cine imaging demonstrated the same pattern of akinetic wall motion as the pre-contrast cine imaging, and also demonstrated the same absence of contrast update as the first-pass perfusion imaging (Fig. 3).

Delayed myocardial enhancement imaging was performed to evaluate for myocardial viability. The TI scout demonstrated optimal myocardial nulling at 240 ms (Fig. 4). Our initial viability images acquired at TI 240 ms demonstrated bright transmural signal in the same distribution as the dark signal appeared in the first-pass perfusion images (Fig. 5). However, the extent and morphology of the bright transmural signal was unusual, and a dark rim artifact surrounding the transmural bright signal was confounding. A bright rim artifact is typically indicative of the TI time being slightly too short for maximal nulling of viable myocardium, and thus it is not typically associated with a region of ischemia or infarct. Furthermore, in this case, the viable myocardium appears to be well-nulled with no dark rim artifact at TI time of 240 ms. We speculate that the dark rim artifact surrounding the abnormal myocardium in the LAD territory may be from fat/fluid interface cancellation, similar to that seen surrounding the pleural effusion in figures 5E, F. In retrospect, T2-weighted imaging would have been helpful to elucidate this.

To evaluate for incomplete myocardial nulling, the viability scan was repeated with a slightly longer TI of 270 ms (Fig. 6). The MAGNITUDE images again demonstrated good nulling of the normal myocardial tissue, with transmural bright signal and dark rim artifact in the LAD territory. The PSIR images demonstrated profoundly hypo-intense signal in the LAD territory with no dark rim artifact, and the viable myocardium demonstrated mid-grey signal intensity. This PSIR pattern would not be consistent with transmural scar tissue. In PSIR images, the darker the signal intensity the longer the tissue's T1 value. The observed PSIR pattern indicated that the T1 value of the abnormal tissue in the LAD territory was significantly longer than the T1 value of the remaining viable myocardium. This would be consistent with complete lack of perfusion of the entire LAD territory, likely from macrovascular obstruction.

In order to evaluate for thrombus, the viability scan was repeated with a much longer TI of 600 ms (Fig. 7). In addition to demonstrating thrombus (Fig. 7D, white arrow), the MAGNITUDE images demonstrated mid-grey signal intensity in the viable myocardium, with complete signal nulling in the LAD territory. The fact that normal myocardium nulled at TI <300 ms but the abnormal myocardium nulled at TI 600 ms confirmed that the T1 value of the abnormal myocardium was much longer than that of the normal myocardium. This could only occur if the LAD territory was completely deprived of perfusion due to extensive

macrovascular obstruction. These findings are consistent with a large myocardial infarction in the LAD territory with no evidence of viability.

Infarct scar tissue would typically be responsible for delayed hyper-enhancement signal, but no scar was identified in this patient. As predicted by the dotted lines in figure 9, MAGNITUDE images acquired at an intermediate TI 270 ms (Figs. 6A–C) demonstrated nulling of the normal viable myocardium with relatively higher signal in the obstructed myocardium. As predicted by the solid lines in figure 9, PSIR images acquired at an intermediate TI 270 ms (Figs. 6D–F) demonstrated relatively higher signal in the normal viable myocardium than the obstructed myocardium. As predicted by the solid lines in figure 9, MAGNITUDE images acquired at a long TI 600 ms (Fig. 7) demonstrated nulling of the obstructed myocardium with relatively higher signal in the normal viable myocardium.

This study illustrates findings that can be seen in macrovascular obstruction, specifically the transmural hyper-enhancement accompanied by a dark rim artifact. This finding was initially confusing because it is more commonly seen in normal myocardium which is incompletely nulled. Therefore, a PET viability study was also obtained to corroborate the CMR findings (Fig. 8). Baseline resting perfusion imaging with Rubidium-82 in the vertical long axis (VLA) view demonstrated absent perfusion of the entire apex, mid to apical anterior wall, and apical inferior wall. Myocardial glucose metabolism imaging with ^{18}F-fluorodeoxyglucose (FDG) in the VLA view demonstrated absent metabolism in the same territory. PET is considered a highly sensitive tool to detect viability. These findings are consistent with a large myocardial infarction in the LAD territory with no evidence of viability.

Clinical outcome

Non-reperfusion of the culprit vessel in STEMI portends a poor outcome. In cases where reperfusion occurs with optimal lytic therapy, death rates are reduced to 7% compared to 13% in patients treated with medical therapy alone [1–2]. In-hospital death rates can be even more substantially reduced with primary percutaneous intervention in ST-elevation myocardial infarction (STEMI) patients. The prognosis though, for any patient, varies markedly based upon each individual clinical and epidemiologic markers. In this case, the presence of diabetes mellitus, anterior wall infarction, and depressed LV function places him at substantially higher risk for cardiac morbidity and mortality. Because of this reason, an assessment of myocardial viability was deemed as a crucial element in his long term management. Unfortunately, in this case the anterior wall was non-viable and profound macrovascular obstruction was noted. Thus the patient was not referred for coronary artery bypass grafting or percutaneous intervention. Aggressive medical therapy for heart failure was initiated and the patient was referred to the heart failure service for long-term management. Because of the non-recoverability in function in the anterior wall and an LVEF of less than 35%, the patient was considered for ICD therapy. However, since early implantation of an ICD (within one month post-infarct) has not been shown to decrease mortality in high risk patients with recent myocardial infarction [3], decision was made to not implant ICD and send the patient home with a life-vest. We plan to implant an ICD at a later date if the patient's EF remains lower than 35%, which is highly likely given the large size of the non-viable lesion.

9

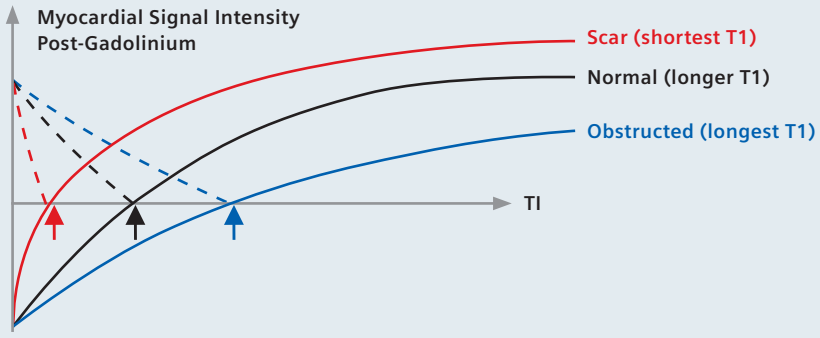

9 Signal intensity curves for three types of myocardial tissues with different T1 values. Dotted lines show the signal trajectories for MAGNITUDE images, whereas solid lines show the signal trajectories for PSIR images. **(9A)** Infarct scar tissue (red curve) would typically have the shortest T1 value and thus the shortest TI null point on MAGNITUDE images (red arrowhead). **(9B)** Normal viable myocardium (black curve) would typically have a longer T1 value and thus an intermediate TI null point on MAGNITUDE images (black arrowhead). **(9C)** Myocardial tissue which receives absolutely no perfusion due to either microvascular or macrovascular obstruction typically demonstrates the longest T1 values (blue curve) with correspondingly longer TI null points (blue arrowhead).

Acknowledgements

The authors would like to thank Dr. Edwin Wu, Northwestern University, Chicago, for his review of the manuscript and his insights regarding the appearance of macrovascular obstruction.

References

1 N Engl J Med 1993; 329:673.
2 Lancet 1999; 354:716.
3 N Engl J Med 2004; 351:2481-8.

Contact
Anurag Sahu, M.D.
Assistant Professor of Medicine
The Emory Clinic
1365 Clifton Road, NE
Atlanta, GA 30322
USA
Phone: +1 (404) 686-7878
anurag.sahu@emory.edu

MRI of Giant Cell (Temporal) Arteritis, GCA

Thorsten Alexander Bley[1], Julia Geiger[2], Oliver Wieben[3], Michael Markl[4]

[1]Department of Diagnostic and Interventional Radiology, University Medical Center Hamburg-Eppendorf, Hamburg, Germany
[2]Department of Radiology, University Hospital Freiburg, Freiburg, Germany
[3]Departments of Radiology and Medical Physics, University of Wisconsin-Madison, Madison, USA
[4]Departments of Radiology and Biomedical Engineering, Northwestern University, Chicago, IL, USA

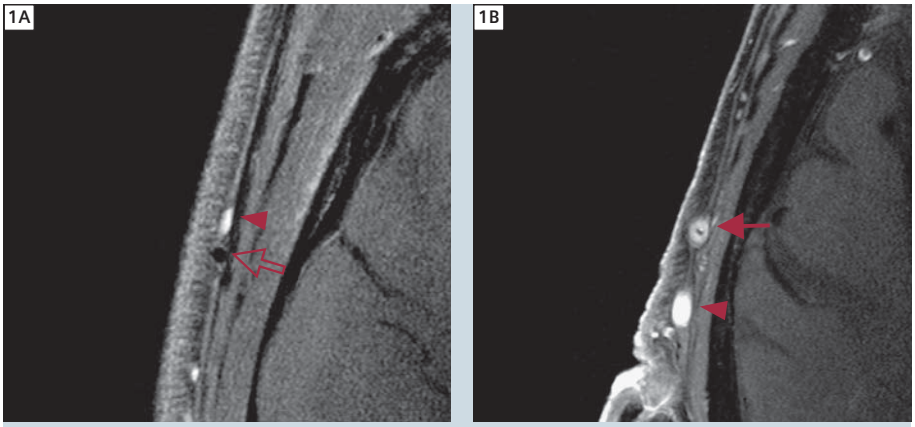

1 High-resolution MRI of the superficial temporal arteries: enlargement of contrast enhanced T1 weighted Spin Echo imaging with 197 x 260 µm² in plane resolution. The vessel wall of unaffected segments of the superficial temporal artery is very thin (open arrow in **1A**). Due to high arterial flow no intraluminal signal is visible ('flow void'). Slower flow in the concomittant vein renders homogeneous intraluminal signal (arrowhead in **1A** and **1B**). Mural inflammatory changes of the affected superficial temporal artery include mural thickening and contrast enhancement (arrow in **1B**).

Introduction

Giant cell (temporal) arteritis (GCA), is a chronic, granulomatous vasculitis, which primarily affects large-to-medium size arteries and is often associated with polymyalgia rheumatica [1]. It occurs more frequently in women than in men with a gender ratio of up to 2-4:1. The maximum incidence occurs in those aged between 70 and 80. The annual rate of new cases is rising and ranges between 15 and 25 per 100.000 for those aged 50 and older [2]. Interestingly, the rate of occurrence is 2.25 times higher in urban compared to rural regions [3].

The classic leading symptom of GCA is new onset of headaches with tender temporal arteries. In addition, the masticatory muscles and scalp may demonstrate enhanced sensitivity associated with pain. Visual symptoms include amaurosis fugax and diplopia. Loss of sight is a severe complication as a consequence of inflammatory involvement of the posterior ciliar arteries (anterior ischaemic optic neuropathy, AION) [4]. The American College of Rheumatology (ACR) has drafted classification criteria to facilitate the difficult clinical diagnosis of GCA [5]. To date, a biopsy of the superficial temporal artery is considered the diagnostic gold standard. However, a segmental affliction pattern is typical for GCA. As a result, even negative biopsy results may erroneously indicate the absence of the disease if the biopsy was taken from a non-affected segment of the superficial temporal artery [1, 6]. In addition to or instead of the superficial temporal artery, other superficial cranial arteries may be affected. Modern imaging techniques such as CT, MRI, and FDG PET have recently demonstrated that extracranial manifestation of GCA was present in up to 70% of cases [7]. In this context, the following vessels may be affected in decreasing order of occurrence: Aorta, subclavian and axillary arteries, vertebral arteries, visceral branches of the aorta including renal and mesenterial arteries, coronary and pulmonary arteries, and the arteries of the extremities.

At least 1 mg prednisone equivalent per kg bodyweight per day is recommended for initial treatment of GCA. In most cases, clinical and serological remission occurs within the very first week of treatment, which permits tapering of the corticoid dosage. However, the period of illness is likely to vary from one individual to another and often spans several years. Disease may recur in phases over a period of up to ten years.

Imaging

Signs of vascular inflammatory involvement such as a dark halo that may be caused by an edema of the arterial wall can be identified with the help of color-coded duplex sonography (CCDS) of the

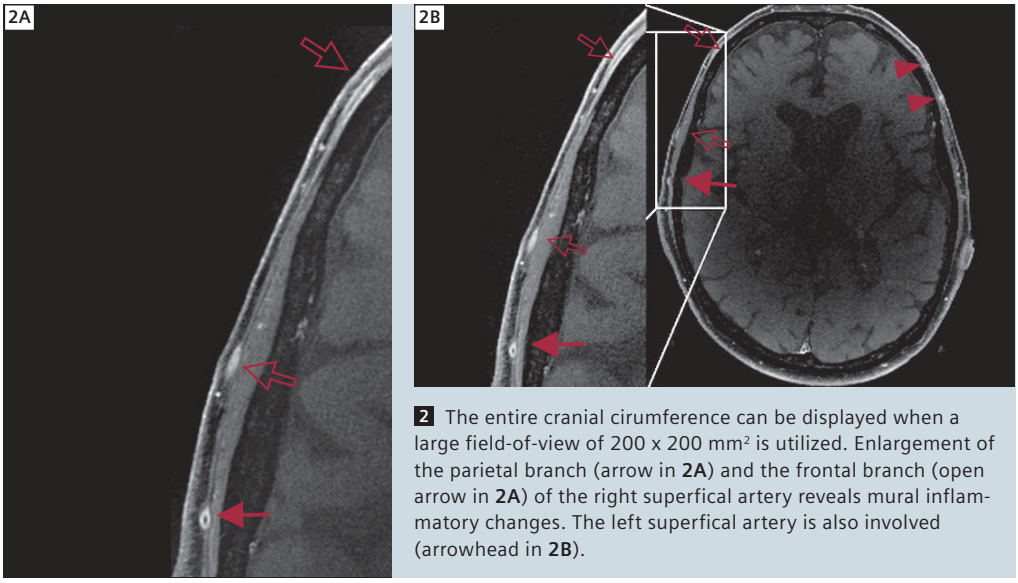

2 The entire cranial circumference can be displayed when a large field-of-view of 200 x 200 mm² is utilized. Enlargement of the parietal branch (arrow in **2A**) and the frontal branch (open arrow in **2A**) of the right superfical artery reveals mural inflammatory changes. The left superfical artery is also involved (arrowhead in **2B**).

superficial temporal artery. Sensitivities of 73–93% and specifities of 89–93% can be achieved with this method [8]. In the hands of an experienced observer CCDS is considered the non-invasive imaging modality of first choice. However, the clinical significance of CCDS is still debated and its operator dependency may limit its diagnostic accuracy. As alternative imaging modalites, CT and MRI/angiography are suitable for non-invasive assessment of extracranial manifestation, particularly to rule out aortitis and inflammation of the supra-aortic branches. FDG-PET represents a valuable and highly sensitive tool for assessment the extracranial manifestation pattern.

High-resolution MRI

Recently, high-resolution post-contrast MRI has been developed as an alternative diagnostic imaging technique for the detailed assessment of segmental inflammation patterns associated with GCA [9]. For the successful evaluation of the small extra-cranial arteries high spatial resolution in the sub-millimeter range is needed. In addition, sufficiently high signal-to-noise (SNR) is necessary to detect contrast agent accumulation (i.e. T1 shortening and bright signal) as a sign of mural inflammatory changes in the very small superficial temporal arteries.

We have developed an imaging protocol for the complete assessment of all superficial cranial arteries based on high-resolution, fat-saturated, contrast enhanced multi-slice T1-weighted spin echo imaging with a spatial resolution of 195 µm x 260 µm [9].

The sequence parameters for data acquisition at 1.5 and at 3 Tesla (T) are listed below.

Sequence parameters at 1.5T

- TR/TE 500/22 ms
- Acquisition matrix of 1024 x 768 voxels
- Field-of-view (FOV) = 200 x 200 mm²
- Spatial resolution: 195 x 260 µm²
- Slice thickness = 3 mm
- Number of excitations = 1
- Bandwidth 65 Hz/pixel
- Acquisition time 6:55 min
- Fat saturation

Sequence parameters at 3T

- TR/TE 500/22 ms
- Acquisition matrix of 1024 x 768 voxels
- FOV 200 x 200 mm²
- Spatial resolution 195 x 260 µm²
- Slice thickness = 3 mm
- Number of excitations = 1
- Bandwidth 76 Hz/pixel
- Partial Fourier acquisition along the phase encoding direction
- (Half Fourier factor) = 6/8
- Acquisition time 4:52 min
- Fat saturation

Ten slices of 3 mm thickness spaced at 3 mm intervals cover a total distance of 63 mm of the temporal artery. Data acquisition using 3 slice packages allows assessment of the complete course of the temporal arteries as needed for GCA. The complete coverage makes it possible to assess the frontal and the parietal branches of the superficial temporal arteries as well as the occipital arteries bilaterally. Increased SNR at 3 Tesla can successfully be used to reduce the measurement time (partial Fourier acquisition along the phase encoding direction). In addition, the contrast agent effect (T1 shortening) is increased at higher field strength and an enhanced blood background contrast can be achieved. We have shown in a number of studies that this protocol allows displaying the arterial wall and lumen of the superficial temporal arteries accurately [9–15]. Mural inflammation is graded on a four-point scale according to mural thickening and contrast enhancement

of the arterial wall and perivascular tissue:

– = No wall thickening (< 0.6 mm), no mural contrast enhancement.
\+ = No wall thickening (< 0.6 mm), barely detectable mural contrast enhancement.
++ = Wall thickening (≥ 0.6 mm) and clearly visible mural contrast enhancement.
+++ = Substantial wall thickening (≥ 0.6 mm) and pronounced mural contrast enhancement.

Arteries can be differentiated from the accompanying veins by their flow characteristics: Blood flows considerably faster in arteries than in veins. In spin echo imaging, fast arterial flow results in the flow of blood prior to spin echo generation and signal reception and thus dark signal in the vessel lumen or 'flow void'. In contrast, slower venous flow contributes to a bright intraluminal venous signal. Furthermore, as a result of the high spatial resolution, the thicker arterial walls can be distinguished from the thin venous walls in most cases.

MR angiography

For assessment of the extracranial involvement in GCA the MR protocol can be extended to include an examination of the thoracic, cervical, and cranial arteries. The contrast agent administration used for post-contrast analysis of the temporal arteries can be used for large FOV time-resolved MR angiography (MRA) prior to high-resolution cranial MRI. As a result, a single dose contrast agent administration can efficiently be used to provide both high-resolution images of the inflamed vessel wall and information on additional stenosis or wall inflammation in the neck and thorax.

Sample protocol for time-resolved MRA

- TE 1.11 ms
- TR 3.15 ms
- FOV 400-500 x 320 mm²
- 3D volume thickness (slab thickness) 120 mm
- Acquisition matrix 640 x 384
- Parallel imaging with up to 3 times the acceleration factor
- 96 slices
- Partial Fourier acquisition along the phase encoded direction (partial Fourier factor 6/8)
- Spatial resolution = 0.63 x 0.83 x 1.25 mm

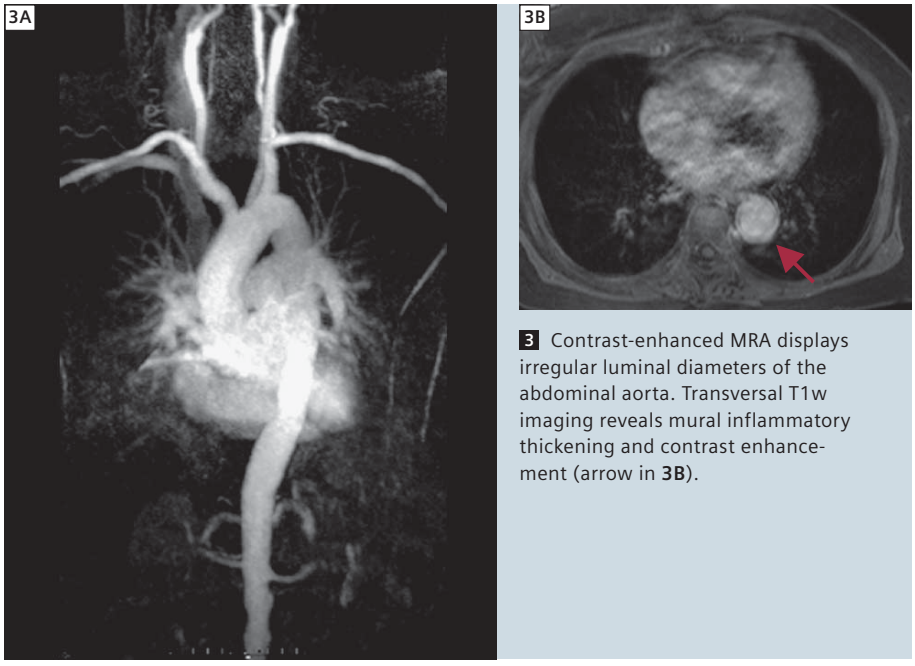

3 Contrast-enhanced MRA displays irregular luminal diameters of the abdominal aorta. Transversal T1w imaging reveals mural inflammatory thickening and contrast enhancement (arrow in **3B**).

The MRA volume should cover the thoracic aorta, the subclavian and axillary arteries and the carotid and vertebral arteries. Ideally, a whole-body MRA covering the entire vasculature from head to toe is performed prior to high-resolution vessel wall imaging of the superficial cranial arteries. It is known that mural inflammatory contrast enhancement persists for several minutes. Sufficient time for repositioning of the patient and planning of the high-resolution images is therefore available.
Of note, axial images of the aortic wall should also be acquired to detect aortitis. An axial gradient echo sequence may be used, for example, to assess mural thickening and contrast enhancement of the aortic wall. The inflammatory edema can also be displayed with a TIRM sequence. High contrast between the intra-luminal and mural signal is favored so that mural thickness and inflammatory changes such as edema and contrast agent enhancement can be revealed.
The non-invasive high-resolution MRI protocol was evaluated in a number of studies in patients with proven GCA and inflammation of the superficial cranial arteries. The sensitivity and specificity of this method was 80.6% and 97.0%. In a subgroup of patients who received their MRI within the first 10 days of treatment, the sensitivity was 85.5% [14]. In a retrospective, intra-individual comparison high-resolution MRI and CCDS revealed similar results. Sensitivity of the MRI was slightly higher but did not reach the level of significance [12].

Discussion

In GCA, steroid treatment has high priority due to severe complications such as blindness. Patients suffering from GCA typically show rapid improvement under steroid treatment. However, temporal artery biopsy may still show signs of GCA even after two weeks of treatment. Our experience has shown that mural contrast enhancement and wall thickening is reduced considerably under treatment. Hence, patients should be scanned prior to or soon after onset of treatment. After a few weeks

of successful treatment, the signs of inflammation recede considerably and can no longer be detected after long term treatment.
High-resolution post-contrast T1-weigted spin echo MRI can be employed to precisely assess the cranial distribution pattern of this inflammatory disease, which is known to occur in a segmental manner. This is particularly important, since negative biopsy results may occur erroneously if, for example, a non-affected segment has been chosen for biopsy. Imaging guided biopsy may have the potential to reduce the rate of false negative biopsy results.
The highest achievable spatial resolution and contrast-to-noise ratio should be selected for imaging small structures such as the wall of the superficial cranial arteries. Hence, imaging at 3T is preferred. To permit imaging with high spatial resolution and SNR, parallel imaging techniques, which could be used to reduce total scan time but are associated with SNR loss, have not been applied. In a comparison of image quality for both 1.5T and 3T, imaging at high field was clearly superior. Nonetheless, examinations at 1.5T demonstrated good image quality and were found to be highly suitable for diagnostic purposes.

Summary

GCA is a diagnostic challenge. Early high-dose steroid treatment is needed to reduce the risk of blindness. The proposed MRI protocol represents a valid and non-invasive method for diagnosing giant cell arteritis. With a high spatial resolution of 195 x 260 µm, the superficial cranial arteries and their inflammatory mural enhancement pattern can be visualized. In a single, non-invasive examination, the cranial inflammation pattern associated with GCA can be displayed.
The high-resolution MRI examination of the superficial cranial arteries should be combined with an MRA of the aorta and the supra-aortic branches. This is particularly useful, since GCA affects also the extracranial arteries in up to 70% of patients. Inflammatory changes of the aorta, the carotid, vertebral, subclavian and axillary arteries can be displayed in a single examination of 30 to 40 minutes.

Conclusions

1. The superficial cranial arteries along with the mural and luminal properties can be displayed in detail using high-resolution MRI.
2. Inflamed arterial segments can be differentiated from non-affected segments.
3. Steroid treatment leads to a rapid reduction in inflammatory mural contrast enhancement. After successful long term steroid treatment mural inflammatory changes vanish entirely.
4. 3T image quality is superior to 1.5T. Nonetheless, imaging at 1.5T provides sufficient diagnostic image quality.
5. High-resolution MRI should be combined with thoracic and cervical MRA to assess the aortic and supraaortic arteries' involvement pattern within one integrated MRI/MRA study.

Thorsten A. Bley, M.D.

Contact
Thorsten Alexander Bley, M.D.
Assistant Professor of
Radiology
University Medical Center
Hamburg-Eppendorf
Department of Diagnostic
and Interventional Radiology
Martinistrasse 52
20246 Hamburg
Germany
Phone.: +49 1522 2816990
Fax: +49 40 7410 53802
t.bley@uke.de

References
1 Weyand CM, Goronzy JJ. Medium- and large-vessel vasculitis. N Engl J Med 2003;349(2):160-9.
2 Salvarani C, Crowson CS, O'Fallon WM, Hunder GG, Gabriel SE. Reappraisal of the epidemiology of giant cell arteritis in Olmsted County, Minnesota, over a fifty-year period. Arthritis Rheum 2004;51(2):264-8.
3 Reinhold-Keller E, Zeidler A, Gutfleisch J, Peter HH, Raspe HH, Gross WL. Giant cell arteritis is more prevalent in urban than in rural populations: results of an epidemiological study of primary systemic vasculitides in Germany. Rheumatology (Oxford) 2000;39(12):1396-402.
4 Schmidt D. Arteriitis temporalis Horton. Diagnose, Differentialdiagnose, Therapie. St. Gallen: Elephas; 1995.
5 Hunder GG, Bloch DA, Michel BA, et al. The American College of Rheumatology 1990 criteria for the classification of giant cell arteritis. Arthritis Rheum 1990;33(8):1122-8.
6 Klein RG, Campbell RJ, Hunder GG, Carney JA. Skip lesions in temporal arteritis. Mayo Clin Proc 1976;51(8):504-10.
7 Maksimowicz-McKinnon K, Clark TM, Hoffman GS.Takayasu arteritis and giant cell arteritis: a spectrum within the same disease? Medicine 2009 Jul;88(4):221-6.
8 Karassa FB, Matsagas MI, Schmidt WA, Ioannidis JP. Meta-analysis: test performance of ultrasonography for giant-cell arteritis. Ann Intern Med 2005;142(5):359-69.
9 Bley TA, Wieben O, Uhl M, Thiel J, Schmidt D, Langer M. High-resolution MRI in giant cell arteritis: imaging of the wall of the superficial temporal artery. AJR Am J Roentgenol 2005;184(1):283-7.
10 Bley TA, Wieben O, Leupold J, Uhl M. MRI findings in Temporal Arteritis. Circulation 2005;111:e260.
11 Bley TA, Wieben O, Vaith P, Schmidt D, Ghanem NA, Langer M. Magnetic resonance imaging depicts mural inflammation of the temporal artery in giant cell arteritis. Arthritis Rheum 2004;51(6):1062-3.
12 Bley TA, Reinhard M, Hauenstein C, Markl M, Warnatz K, Hetzel A, Uhl M, Vaith P, Langer M. Comparison of duplex sonography and high-resolution magnetic resonance imaging in the diagnosis of giant cell (temporal) arteritis. Arthritis Rheum. 2008 Aug;58(8):2574-8.
13 Bley TA, Markl M, Schelp M, Uhl M, Frydrychowicz A, Vaith P, Peter HH, Langer M, Warnatz K. Mural inflammatory hyperenhancement in MRI of giant cell (temporal) arteritis resolves under corticosteroid treatment. Rheumatology (Oxford). 2008 Jan;47(1):65-7.
14 Bley TA, Uhl M, Carew J, Markl M, Schmidt D, Peter HH, Langer M, Wieben O. Diagnostic value of high-resolution MR imaging in giant cell arteritis. AJNR Am J Neuroradiol. 2007 Oct;28(9):1722-7.
15 Markl M, Uhl M, Wieben O, Ness T, Langer M, Hennig J, Bley TA. High resolution 3T MRI for the assessment of cervical and superficial cranial arteries in giant cell arteritis. J Magn Reson Imaging. 2006 Aug;24(2):423-7.

Assessment of Peripheral Arterial Disease Using High Resolution Dynamic MR Angiography and 4D Visualization Software

Edward T. Martin, M.D., FACC, FACP, FAHA[1]; Gary R. McNeal, MS BME, BS EE[2]

[1]Director, Cardiovascular MRI, Oklahoma Heart Institute at Hillcrest Medical Center, Tulsa, OK, USA
[2]Senior Clinical Specialist, Cardiovascular MR R&D, Siemens Healthcare, Chicago, IL, USA

Introduction

Peripheral Arterial Disease (PAD) is quite prevalent affecting approximately 8 million Americans. Patients with PAD are at a 6-7 times greater risk of developing coronary artery disease, myocardial infarction and strokes. PAD is also significantly under-diagnosed. The ankle brachial index (ABI) is an easy and important starting point for evaluating leg pain in the at risk population. Subsequently, if the ABI is less than 0.9, this would suggest significant PAD and requires additional studies. Invasive angiography has its own attendant risks such as vascular damage, contrast reactions and renal dysfunction. Catheter based angiography also requires laboratory testing and usually an investment of almost an entire day of the patient's time. Magnetic resonance angiography (MRA) requires only an IV and rarely blood testing. A typical procedure takes about one half hour and there is no ionizing radiation involved in the acquisition of the images. The *American College of Cardiology (ACC) / American Heart Association (AHA)* task force on PAD has also found MRA to be a class I indication for the assessment of PAD [1].

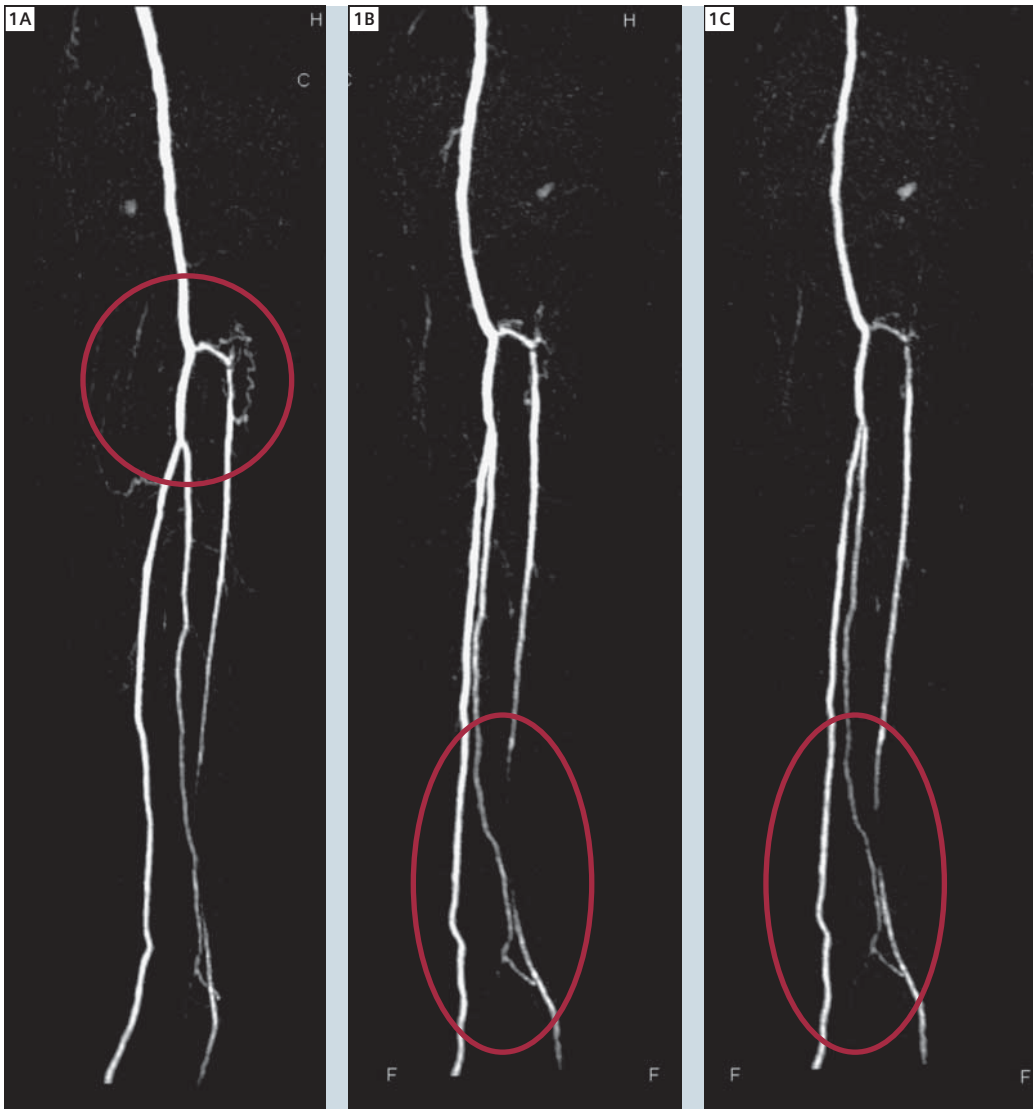

In addition to the ability of PAD assessment, there are a variety of clinical indications for MR assessment of other vascular structures [1].

- Aortic dissection, aneurysm, and intramural hematoma
- Aortic arch anomalies
- Aortic branch vessel disease
- Carotid artery disease
- Subclavian artery disease
- Renal artery disease
- Iliofemoral disease
- Popliteal and infrapopliteal disease
- Anomalous coronary arteries
- Coronary artery bypass graft patency
- Pulmonary emboli

There are also a variety of contrast-enhanced and non-contrast techniques for vascular MR Angiography of Peripheral Arterial Disease (PAD).

- Static high-spatial resolution contrastenhanced MRA
- Dynamic high-temporal resolution contrast-enhanced MRA
- Gated 2D time-of-flight (2D TOF) non-contrast MRA
- Gated 3D phase-contrast (PC) non-contrast MRA

This work explores the assessment of PAD using contrast-enhanced high-temporal resolution dynamic MR angiographic technique for data acquisition (*syngo* TWIST, Siemens Healthcare) and using 4D display software for data visualization (4D INSPACE, Siemens Healthcare). Although TWIST has been applied for this application previously, this work demonstrates the advantages of combining *syngo* TWIST with advanced 4D display techniques.

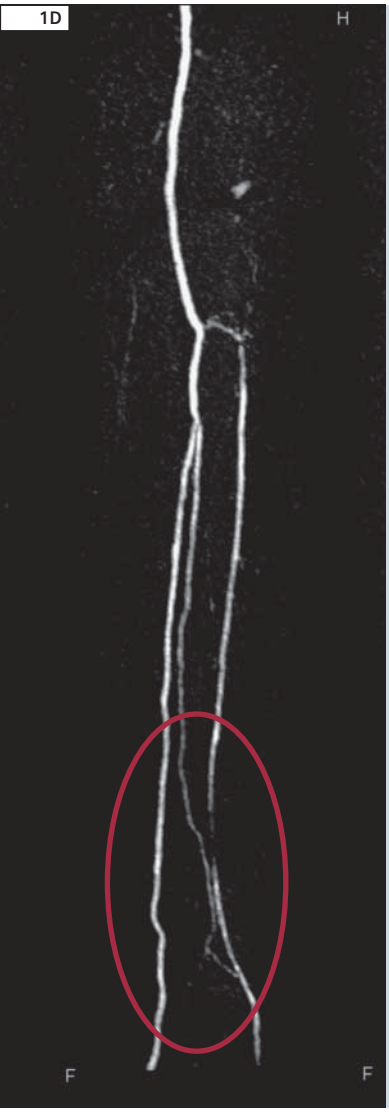

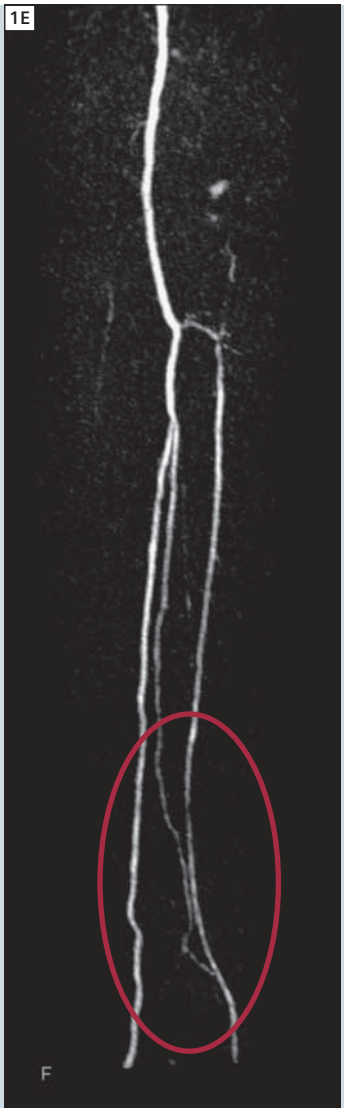

1 In patient #1, MIP reconstructions of lower left extremity of patient with atherosclerotic disease. In coronal view **(1A)** tight stenosis of the proximal segment with early collateral filling is demonstrated, but the distal left anterior tibial artery is overlaid by other infrapopliteal vessels. In RAO view **(1B–E)** the time progression of collateral filling of the distal segment of the left anterior tibial artery is demonstrated.

Methods

- Lower extremities of three patients with atherosclerotic disease were imaged on a 1.5T MR system (MAGNETOM Avanto, Siemens Healthcare).
- Patients were positioned feet-first supine in the bore, and the Peripheral Array Coil was positioned to cover from knees to toes bilaterally.
- Multihance contrast agent (Bracco) was injected (8 ml @ 2.5 ml/s) followed by normal saline flush (20 ml @ 2.5 ml/s).
- Dynamic MR angiography was performed with TWIST pulse sequence at temporal resolution 6.2 s/frame, spatial resolution 1.0 mm isotropic, 15 consecutive measurements, coronal plane.
- First measurement was automatically subtracted from remaining measurements during image reconstruction.
- Load all subtracted datasets into 4D INSPACE visualization software.
- Select maximum intensity projection (MIP) or volume rendering technique (VRT) display mode, crop out overlaid soft tissues and bone.
- Play 4D data in cine loop, rotate volume to expose overlaid vessels.
- Save output jpg images and avi movie files.

Imaging findings

In two of the patients occlusion of the distal anterior tibial artery with collateral retrograde flow was demonstrated, and in one of these patients high grade stenosis of the proximal anterior tibial artery with collateralization was demonstrated. In a third patient infrapopliteal vasculature was obscured by overlying skin artifact due to incomplete background subtraction.

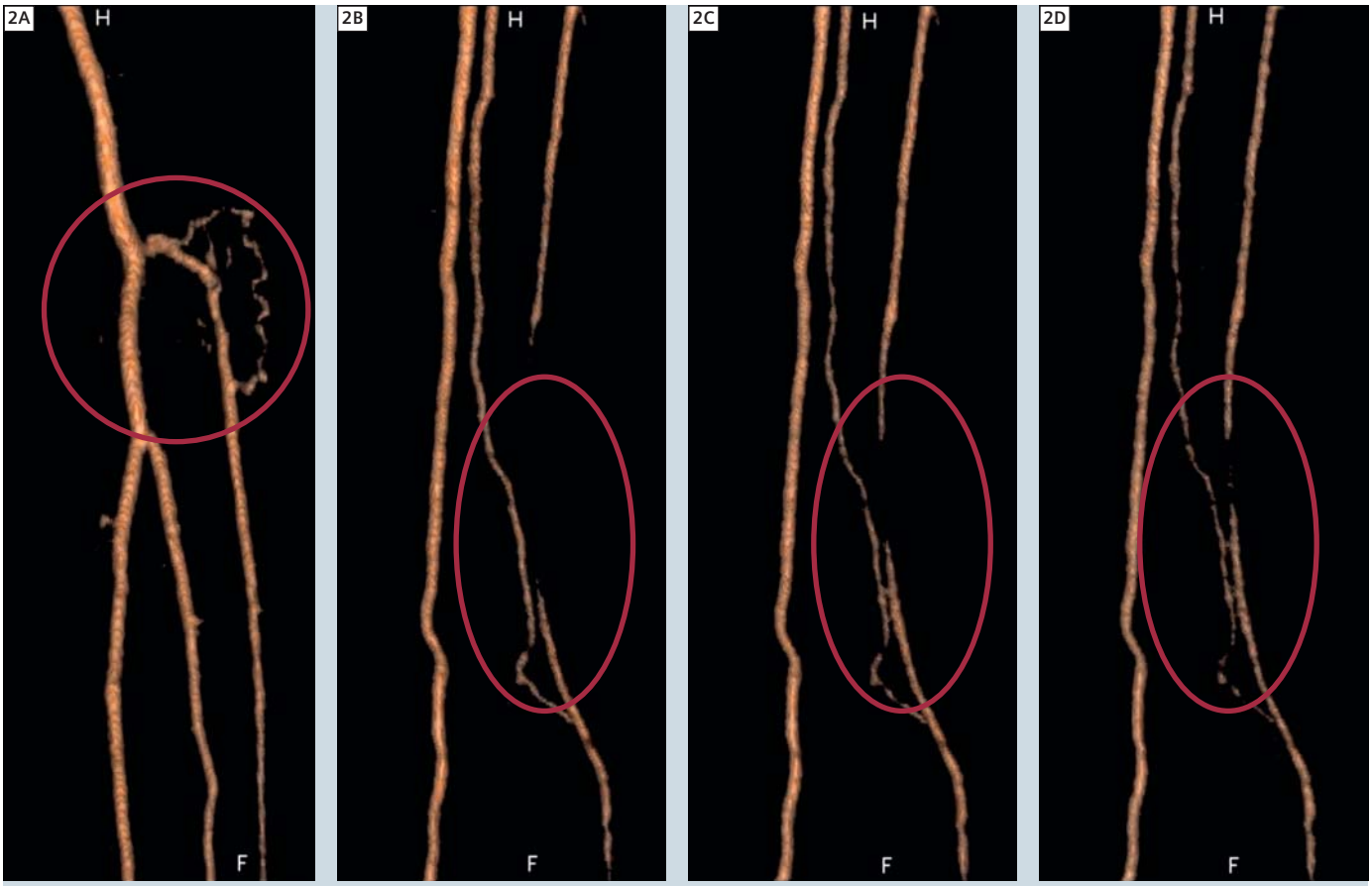

2 In patient #1, VRT reconstructions of lower left extremity of patient with atherosclerotic disease. In coronal view **(2A)** tight stenosis of the proximal segment with early collateral filling is demonstrated, but the distal left anterior tibial artery is overlaid by other infrapopliteal vessels. In RAO view **(2B–D)** the time progression of collateral filling of the distal segment of the left anterior tibial artery is demonstrated.

In patient #1 when the dynamic MIP (Fig. 1) or VRT (Fig. 2) reconstructions from the *syngo* TWIST measurement are displayed solely in the coronal view (as acquired) the anterior tibial arteries are obscured by other overlaid infrapopliteal arteries (Fig. 1A). Right anterior oblique (RAO) rotation of the dynamic MIPs in the 4D INSPACE software helps to visualize the left anterior tibial artery (Fig. 1B), and conversely left anterior oblique (LAO) rotation helps to visualize the right anterior tibial artery. Playing the 4D data sets in cine loop mode while rotating the image volume into oblique views demonstrates filling of the distal segment of the left anterior tibial artery with retrograde collateral flow distal to the occlusion (Figures 1B–E).
In patient #3, the infrapopliteal vasculature was obscured by overlying skin artifact due to incomplete background subtraction. The 4D INSPACE software was used to quickly crop out the skin artifact using a rotational technique, thereby allowing complete visualization of the vessels. Rotating the MIP view allows optimal visualization of the obscured infrapopliteal vessels.

Clinical discussion

Previously, non-invasive assessment of PAD was limited to static imaging. In fact, CT Angiography (CTA) continues to be limited to static assessment of PAD. The TWIST technique enables dynamic vascular assessment which is similar to catheter-based angiography. This advantage allows one to specifically assess retrograde filling vessels, the origin of collateral vessels, length of occlusion, and removes the potential for venous contamination in patients with non-uniform lower extremity PAD. Since speed of retrograde or collateral peripheral flow is secondary to vessel identification, we used a protocol which emphasized spatial resolution at the expense of temporal resolution.
However the advantages of *syngo* TWIST are not useful if the vessels of interest are obscured by overlaying anatomy. The 4D INSPACE technique allows one to rotate the volume into off-axis views, thus allowing unobstructed visualization of vessel anatomy. Additionally, 4D INSPACE rotational function allows one to crop unwanted structures.

Conclusion

These cases have shown the power of combining dynamic vascular imaging (*syngo* TWIST) with the rotational visualization tool (4D INSPACE) for assessment of complex peripheral arterial disease.

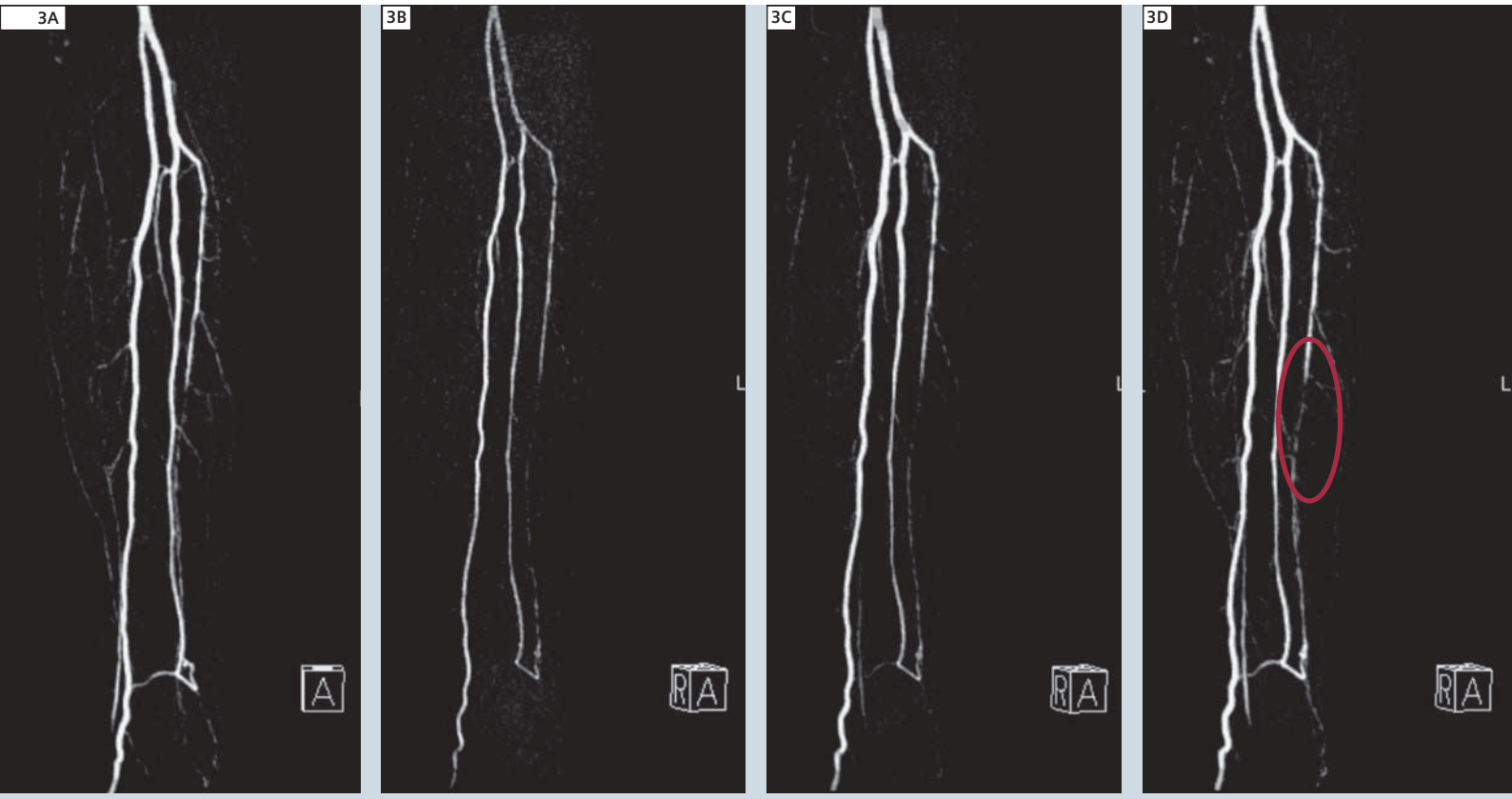

3 In patient #2, MIP reconstructions of lower left extremity of patient with atherosclerotic disease. In coronal view **(3A)** the left anterior tibial artery is overlying the peroneal artery, making an accurate vascular assessment impossible. In RAO views **(3B–D)** the time progression of collateral filling of the mid and distal segment of the left anterior tibial artery is demonstrated. In the last frame the length of the occlusion can be appreciated and measured.

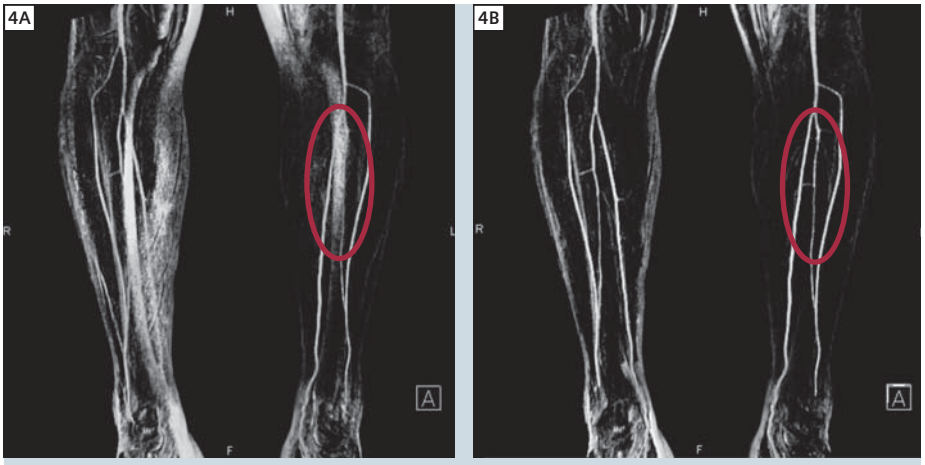

4 In patient #3, MIP reconstructions of lower left extremities. Before cropping of skin artifacts the infrapopliteal vasculature was obscured **(4A)**. The 4D INSPACE software allows to quickly crop out skin artifacts to reveal underlying vasculature **(4B)**.

Contact
Edward T. Martin, MD, FACC, FACP, FAHA
Director, Cardiovascular MRI
Oklahoma Heart Institute at Hillcrest Medical Center
9228 South Mingo Road
Tulsa, OK, 74133
USA
martin@oklahomaheart.com

References

1 ACC/AHA Guidelines for the Management of PAD, JACC 2006; 47:1239-312.

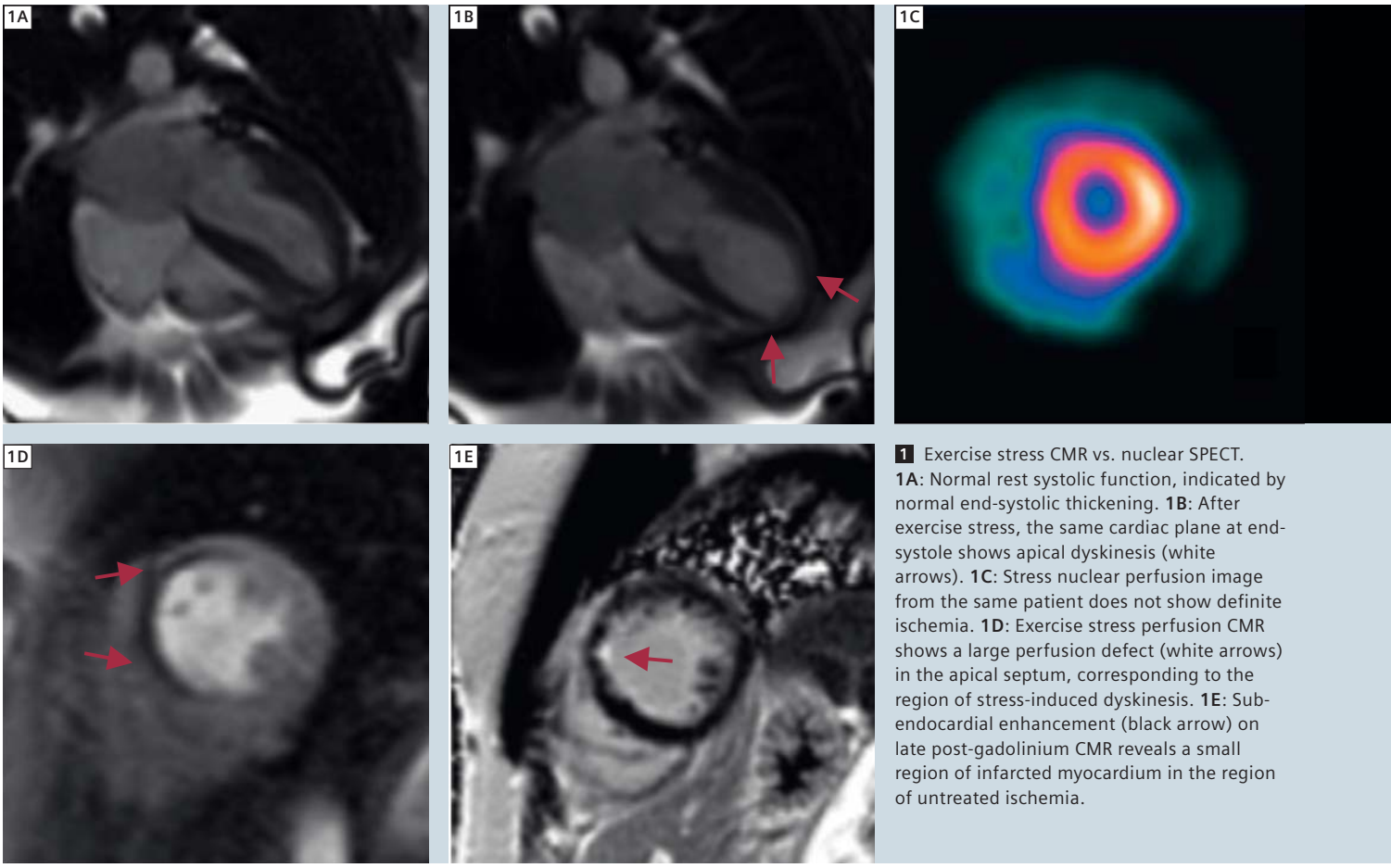

1 Exercise stress CMR vs. nuclear SPECT. **1A**: Normal rest systolic function, indicated by normal end-systolic thickening. **1B**: After exercise stress, the same cardiac plane at end-systole shows apical dyskinesis (white arrows). **1C**: Stress nuclear perfusion image from the same patient does not show definite ischemia. **1D**: Exercise stress perfusion CMR shows a large perfusion defect (white arrows) in the apical septum, corresponding to the region of stress-induced dyskinesis. **1E**: Sub-endocardial enhancement (black arrow) on late post-gadolinium CMR reveals a small region of infarcted myocardium in the region of untreated ischemia.

Treadmill Exercise Stress CMR

Orlando P. Simonetti, Ph.D.; Eric L. Foster, MSME; John W. Arnold, MSAgE; Subha V. Raman, M.D., MSEE

The Ohio State University and EXCMR, Inc., Columbus, Ohio, USA

1. Introduction

Combining exercise testing with Cardiac Magnetic Resonance Imaging (CMR) has the potential to safely, accurately, and non-invasively provide valuable clinical information not available with other existing stress imaging modalities. This approach affords for the first time measurement of myocardial perfusion, diastolic function, systolic function, electrocardiography, myocardial edema, myocardial infarction, and exertional symptoms all in a single test. We expect that by improving both diagnostic accuracy and prognostic information, this new approach to the cardiac stress test may make a significant contribution toward improving outcomes in patients with Ischemic Heart Disease (IHD).

To date, the lack of MRI-compatible exercise equipment, and the lack of imaging techniques that can perform reliably under conditions of high heart rate and rapid breathing have prevented the realization of exercise stress CMR. At The Ohio State University Richard M. Ross Heart Hospital we have developed an MRI-compatible treadmill that can be safely positioned inside the MRI room to minimize the distance a patient has to move between the treadmill and the MRI table, and we have applied improved real-time imaging methods that enable imaging of exercise-induced wall motion, perfusion, and blood flow abnormalities immediately after exercise [1-3]. The success of preliminary studies in coronary artery disease patients (example shown in Fig. 1) has provided the motivation to pursue further development of this

technology and expanded clinical testing in an upcoming multi-center trial. In this article we report on the first experience with treadmill exercise stress CMR using a prototype MRI-compatible treadmill together with rapid techniques for real-time cine and first-pass perfusion imaging accelerated using TPAT (Temporal Parallel Acquisition Technique). After a brief introduction to provide the motivation for this effort, we present a description of the equipment, imaging sequences, the exam protocol, and case examples.

1.1 Importance of exercise stress imaging

The burden of ischemic heart disease (IHD) – in both lives lost and dollars expended – is staggering. Since 1990, more people worldwide have died from coronary artery disease (CAD) than from any other cause; in 2002 approximately 3.8 million men and 3.4 million women died from CAD. In the United States alone, CAD affects approximately 16.8 million people with an estimated annual economic burden of over $165 billion [4]. Stress cardiac imaging is the most common means of defining the presence and extent of IHD, and as many as 7.5 million stress SPECT and 2.5 million stress echocardiography studies are performed each year in the U.S.[5]. Exercise stress with imaging identifies both location and extent of disease, resulting in greater diagnostic accuracy than exercise ECG testing alone [6-10]. However, the rate of false-positive and false-negative stress imaging using standard modalities averages 15% [9]; this uncertainty in diagnosis increases costs by having to treat the sequelae of missed disease or having to perform additional, often invasive testing with attendant risks and cost.

1.2 Exercise vs pharmacological stress

Pharmacologic stress (vasodilator stress perfusion imaging or dobutamine stress cine imaging) has been the only viable option for stress CMR due to lack of magnetic resonance-compatible exercise equipment. However, pharmacological stress testing does not supply the important physiological data provided by treadmill exercise. Exercise links physical activity to symptoms and ischemia [11] and offers information on exercise capacity, blood pressure response, arrhythmias, and the presence or absence of symptoms such as chest pain during exercise [12]. The Bruce Treadmill Test, first published in 1963 [13], is the most commonly used exercise test protocol in the US [14, 15], and has been shown to have high diagnostic and prognostic value [6, 16]. Certain exercise parameters such as inability to complete 6 minutes of the Bruce treadmill protocol [17] and inability to reach 85% of age-predicted maximum heart-rate indicate significant risk of coronary events [18], adding to the prognostic value of a stress imaging test. Undesirable side-effects are another disadvantage of pharmacological stress agents. For these reasons, pharmacologic stress is typically only advised for patients unable to undergo exercise stress due to de-conditioning, peripheral vascular disease, or orthopedic disabilities [7, 19].

1.3 CMR vs Echo and Nuclear

Echocardiography and nuclear SPECT are most commonly combined with treadmill exercise for evaluation of patients with known or suspected CAD, but both modalities have significant limitations. Echocardiography, primarily used to assess cardiac wall motion, can suffer from poor acoustic windows due to obesity, prior surgery, or lung disease [20]. Quality is highly dependent on the skill of the sonographer to repeatedly and rapidly acquire proper views, and complete visualization of all LV segments is often poor [20]. SPECT myocardial perfusion imaging exposes patients to 10-28 mSv of ionizing radiation [21]. In this range, harmful effects must be considered in a patient population likely to undergo other tests involving radiation exposure. SPECT images are of significantly lower spatial resolution than CMR, and image quality is frequently degraded by photon scatter and attenuation artifacts [22]. Women may be particularly prone to false positive stress SPECT results due to breast tissue attenuation. A comprehensive exercise CMR study that demonstrates both wall motion and perfusion with high resolution, plus information on exercise capacity and viability is expected to provide far greater diagnostic information than wall motion stress echocardiography or stress SPECT perfusion alone.

2. Treadmill exercise CMR technology

Two types of exercise devices most commonly used in exercise stress testing are the treadmill and the bicycle ergometer. Attempts at exercise CMR using both devices have had limited success due to technical and clinical challenges. A supine bicycle ergometer that allows exercise imaging inside a closed-bore magnet is commercially available (Lode BV, The Netherlands). While this device has been used to measure blood flow at sub-maximal exercise [23], there are no reports of its use in IHD. Flat supine cycling is an unorthodox form of exercise making it very difficult for patients to achieve the maximal cardiovascular stress required for diagnosis of ischemia. While upright treadmill exercise is the physiologically preferred method of cardiovascular stress testing, it presents significant challenges with MRI. Standard treadmills are made from ferromagnetic components and powered by electromagnetic motors, preventing their safe use in close proximity to any MRI magnet. Accurate diagnosis, especially in patients with less severe single-vessel disease, requires imaging to be performed as close as possible to peak exercise, with as little delay as possible. American Heart Association (AHA) guidelines recommend that function imaging be completed within 60-120 s following peak stress; ideally within 60 s [24]. Requiring the patient to walk from a treadmill immediately following maximal exercise on a treadmill positioned any distance from the MRI table, whether inside or outside the room, may produce dizziness and risk of falling even in relatively healthy patients.

2.1 The MRI-compatible treadmill*

We have made efforts to minimize the time between end of exercise and imaging to maximize both safety as well as sensitivity of the test by designing and constructing a fully MRI-compatible treadmill (Fig. 2). Commonly used treadmill components (such as a steel frame and electric motors) are not suitable for use in the strong magnetic field of the MR environment. To ensure MR compatibility, in-room treadmill components were constructed of non-ferromagnetic structural materials such as plastics, 316-series stainless steel, and aluminum.

The primary challenge in MRI-compatible treadmill design is the drive system. Traditional electrical treadmill motors use ferromagnetic components with significant mass and can pose a severe hazard if brought into close proximity to the MRI magnet. By its nature, an electromagnetic motor cannot be made non-magnetic. For this reason, non-ferromagnetic hydraulic actuators (motor and lift cylinder) were used to power the treadmill belt and elevation mechanism, and optical fiber sensors used for feedback control of speed and elevation. The treadmill was designed to execute the standard Bruce stress test protocol up to Stage 7 (6 mph and 22% incline) in subjects up to 181 kg (400 lbs) in body weight.

The power unit, consisting of an electrical motor driven pump, is located outside the MRI magnet room in the adjacent equipment room. Hydraulic hoses running through a waveguide from the equipment room to the magnet room provide the fluid pressure needed to drive the treadmill belt motor and lift cylinder (Fig. 3). Since the treadmill is intended to be used in healthcare facilities, the hydraulic systems use normal tap water rather than traditional oil-based hydraulic fluids. This ensures simple cleanup of any accidental fluid leakage from the system and also eliminates the need for special hydraulic fluid. The treadmill is connected to the power unit and control computer located in the equipment room via three flexible hydraulic hoses and three fiber optic cables, all of which are routed through a waveguide in the wall of the MRI room. An MRI-compatible keyboard/touchpad and a standard LCD computer monitor mounted to the wall are connected to the control computer via fiber-optic cables run through the waveguide. A LabView (National Instruments, Austin, TX) application was written to control the speed and elevation of the treadmill, as well as to monitor safety parameters. The control program runs the treadmill speed and elevation through the Bruce, or other similar exercise stress protocols using the optical speed and elevation sensors to ensure accuracy. An optical emergency stop button is located on the treadmill that allows the operator to immediately halt the treadmill without computer interaction.

*Currently there are not any MR-compatible treadmills marketed in the US, thus the use described in this article is investigational only.

2

2 MRI-compatible treadmill positioned for stess test adjacent to 1.5T MAGNETOM Avanto. Placement next to MRI facilitates rapid and safe transfer of patient from treadmill to MRI table.

2.2 Patient monitoring

We have configured a PC-based stress testing system (GE Cardiosoft, GE Healthcare) to provide 12-lead ECG monitoring inside the MRI scan room during and after the treadmill test. The 12-lead ECG is non-diagnostic while the patient is inside the magnet bore, but can be effectively used while the patient is on the treadmill and recovering on the MRI table [25]. The Cardiosoft software runs on the treadmill control computer to display and record the 12-lead ECG, as well as to send speed and elevation commands to the treadmill. The ECG acquisition module is connected to the computer in the equipment room via a standard cable that passes through a low-pass filter on the penetration panel to avoid introducing any RF interference into the magnet room. The ECG module has been found to contain only minimal metallic components and can be quickly disconnected and placed on the table at the feet of the patient during MRI without safety risk or generation of image artifacts. Blood pressure is monitored at regular intervals throughout the exercise

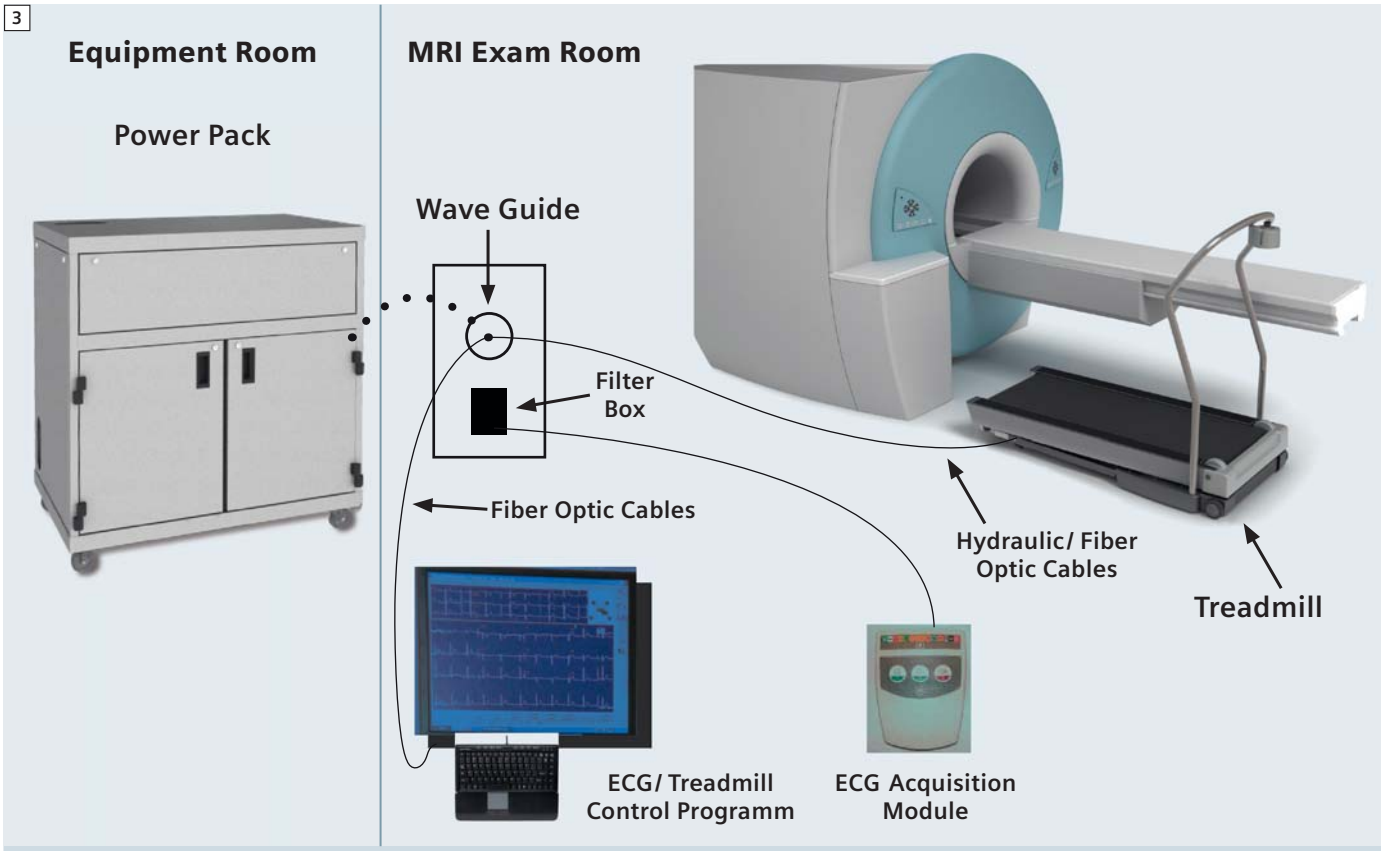

3 Powerpack consisting of electric motor driven pump is located in the MR equipment room and connected to the treadmill in the MRI room via hydraulic hoses and fiber optic cables passed through a waveguide. 12-lead ECG is displayed and treadmill is controlled via Cardiosoft® software.

test using an MRI-compatible manual sphygmomanometer and stethoscope. By positioning the MRI-compatible treadmill directly adjacent to the MRI scan table we are essentially configuring the MRI scanner room exactly like a stress-echocardiography lab (Fig. 4). This configuration facilitates rapid, safe transfer of the patient from the treadmill onto the MRI table, enabling completion of both function and perfusion imaging before ischemic changes dissipate and thereby providing a high level of accuracy and safety. With MRI-compatible equipment allowing positioning of the exercise stress system immediately adjacent to the MRI system, and the use of rapid real-time imaging techniques eliminating breathhold requirements, exercise stress MRI can be successfully performed in cardiac patients, and may potentially achieve higher levels of diagnostic accuracy than previously shown

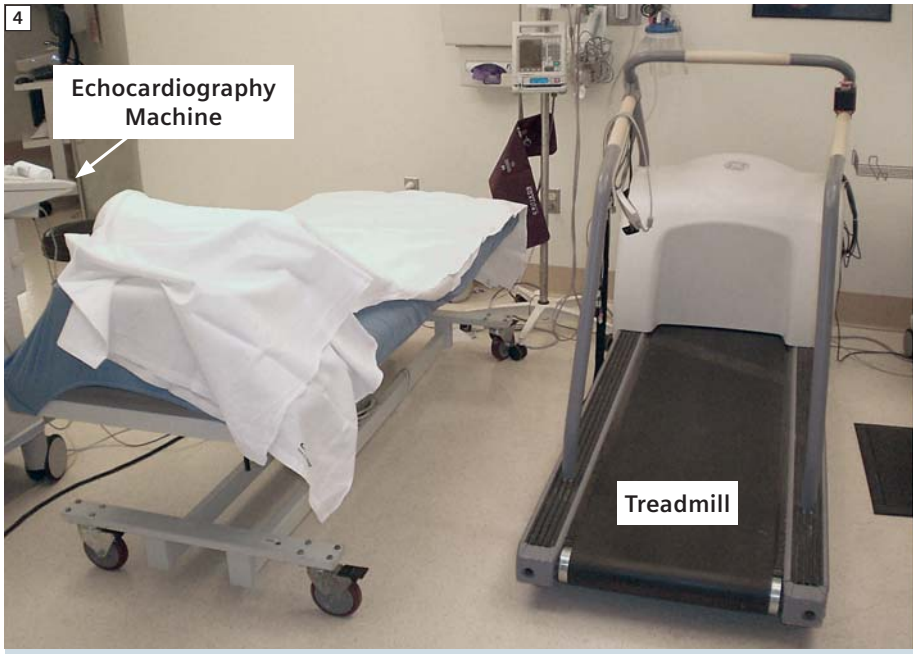

4 Typical layout for exercise stress echocardiography test with patient bed adjacent to the treadmill to minimize both time to post-exercise imaging and risk of patient injury.

for pharmacological stress MRI or other stress imaging modalities.

2.3 Imaging techniques

Real-time and single-shot imaging techniques significantly shorten scan time and eliminate need for regular cardiac rhythm and patient breathhold. These factors are especially critical in imaging patients immediately after exercise. Imaging must be completed rapidly post-exercise due to resolution of stress-induced abnormalities as heart rate recovers [7]; inevitable exercise-induced shortness of breath makes post-stress breath-holding impractical and prevents the use of segmented k-space acquisitions. Temporal resolution requirements are even higher for stress vs. resting cine imaging due to elevated heart rates and rapid, heavy breathing. Recent advances in MRI hardware and advanced techniques such as the TSENSE [26] and TGRAPPA [27] methods of dynamic parallel imaging have resulted in significant improvements in the temporal and spatial resolution of real-time and single-shot imaging methods. The combination of TGRAPPA parallel imaging with advanced 32-channel receiver array technology enables real-time imaging with sufficient spatial and temporal resolution for high heart-rate imaging, impervious to irregularities of cardiac rhythm or patient inability to breathhold. Real-time TrueFISP cine images are acquired at rest and stress using TGRAPPA parallel acceleration rate 4, TR/TE 2.3/1.0 ms, temporal resolution 47.6 ms, matrix 84 x 160, slices: 5 short-axis (SAX), 3 vertical long-axis (VLA), 1 horizontal long-axis (HLA)) without ECG synchronization or breathholding. First-pass perfusion images are acquired at rest and stress using a hybrid gradient echo, echo-planar imaging sequence (GRE-EPI) with TGRAPPA parallel acceleration rate 2, 3 SAX slices, echo train length = 4, matrix 96 x 160, TR/TE 5.6/1.1 ms, FA 25°, BW 1955 Hz/pixel, slice thickness 10 mm, in-plane spatial resolution 3 mm, and temporal resolution (readout only) of 68 ms. The perfusion sequence is ECG triggered but does not require breathhold. Delayed enhancement viability imaging is performed following recovery from exercise using a single-shot non-breathheld inversion-recover TrueFISP sequence (TR/TE 2.5/1.2 ms, FA 50°, BW 790 Hz/pixel, slice thickness 8 mm, in-plane spatial resolution 2–3 mm).

3. The Treadmill exercise CMR protocol

3.1 The procedure

The exercise stress CMR protocol is outlined in figure 5. Images are acquired first at rest prior to treadmill exercise, at stress immediately following maximal exercise, and then again after recovery.

5

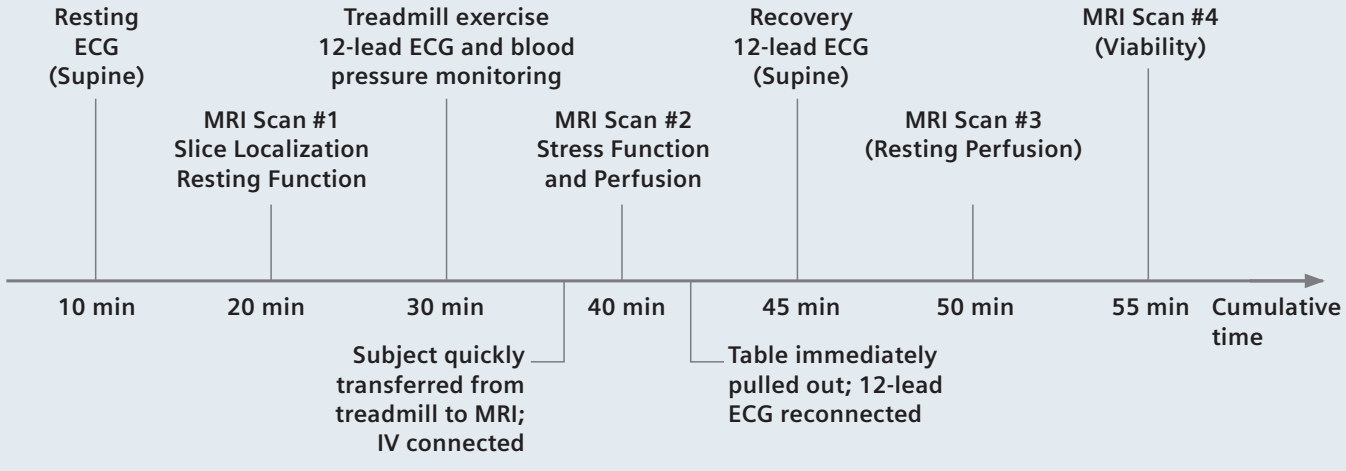

5 Timeline for the treadmill MRI test, including slice localization, rest and stress function, rest and stress perfusion, and viability. The estimated cumulative time for the entire procedure is shown. *Modified with permission from Journal of Cardiovascular Magnetic Resonance [1].*

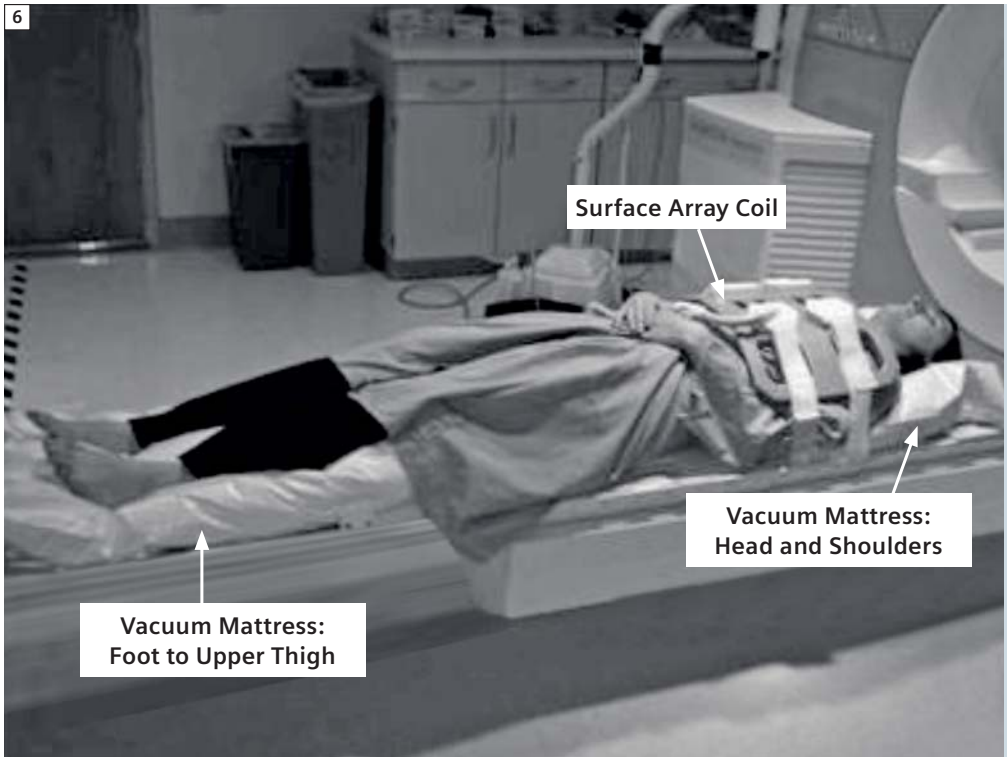

6 Vacuum mattresses placed under shoulders and legs of patient ensure that they return to the same position following exercise. Stress imaging scans are prescribed and queued up in advance for rapid execution post-exercise. *Reprinted with permission from J. Cardiovascular Magnetic Resonance [1].*

Patients are first positioned on the MRI table using vacuum mattress positioning devices (Vac-Lok Cushions, MEDTEC, Orange City, IA, USA) under the head/shoulders and legs to form a cast of their body as shown in figure 6. This facilitates accurate repositioning and eliminates the need to repeat localizer scans after exercise. Slice positions can be defined at rest prior to exercise and imaging sequences for both real-time cine and first-pass perfusion queued up for immediate execution following exercise. After completion of resting cine images and setup of post-exercise scans, the patient is removed from the MRI machine, resting 12-lead ECG is recorded in the supine position while lying on the fully-extended MRI table, and also upright with the patient standing on the treadmill. Patients typically perform the standard Bruce Treadmill Protocol [13] to peak stress as determined by age-predicted maximal heart rate (APMHR = 220 – Age), although other exercise protocols can be used. The goal is to commence imaging with the subject's heart rate at the target of 85% of APMHR. Upon reaching maximal exercise stress as determined by heart rate, the blood pressure cuff and ECG cable are removed and the subject lies back into position on the vacuum mattresses on the MRI examination table. The anterior array coil is positioned on the chest, the IV line connected to the arm for contrast agent injection, and the ECG module is disconnected from the computer before moving the table to magnet isocenter. Imaging can be started from inside the MRI room by pressing the "Start" button located on the MRI scanner housing. Images of cardiac function at peak stress are then immediately acquired using the previously queued cine sequence. The GRE-EPI perfusion sequence is queued to start automatically following the cine scan. Contrast agent injection is administered by the technologist in the MRI room using a pre-armed power injector. The technologist starts the injector as soon as they hear the real-time cine sequence end. Immediately following stress imaging, the patient is removed from the magnet bore and remains on the table for 8–10 minutes of recovery with 12-lead ECG and blood pressure monitoring. The patient is then moved back into the MRI system for recovery cine images as well as resting perfusion and delayed enhancement viability imaging using a single-shot non-breath-hold scan covering the same slice positions used for cine imaging.

3.2 Timing results

While there are no existing clearances or guidelines for exercise CMR, the physiol-

Table 1: Time to complete cine imaging (9 slice positions) and perfusion imaging (3 slice positions) from the end of exercise. Sub-group of older patients showed similar results.

Time from exercise to completion of imaging				
	All patients		66 or older	
	N	median	N	median
CINE	38	47 sec	9	47 sec
PERFUSION	36	80 sec	9	82 sec

Table 2: Mean heart rate shows that on average patients were at target heart rate at start of cine imaging.

Heart Rate (% age predicted max)				
	All patients		66 or older	
	N	mean	N	median
START CINE	38	85.2	9	91.8
END CINE	38	76.9	9	84.3
END PERF	31	69.1	8	72.8

ogy of exercise-induced ischemia and extensive experience with echocardiography has established the need to acquire images as rapidly as possible after the end of exercise before the effects of ischemia resolve. Maximum sensitivity is achieved if imaging commences with the patient's heart rate at 85% of age predicted maximum and completed within 60 seconds of end of exercise. Table 1 and Table 2 show the timing of post-exercise CMR in 38 patients referred for evaluation and diagnosis of known or suspected CAD; this cohort included nine patients age 66 years or older. Using the MRI-compatible treadmill and configuration shown in figure 3 we were able to successfully commence imaging with heart rate at target and to complete cine imaging of cardiac function within the recommended 60 seconds. It took an average of 25 seconds for transfer from treadmill to table, coil and IV positioning, and movement of table to isocenter. The older group of subjects were transferred just as quickly, and their heart rate stayed elevated longer than the younger subjects. These results demonstrate the feasibility of performing post-exercise CMR within the guidelines established for stress echocardiography.

4. Case examples

Three examples are show here of treadmill exercise CMR results in patients referred for exercise stress SPECT exams. These show the image quality possible using rapid real-time imaging techniques even with the high heart rates and rapid breathing encountered immediately post-exercise. In two of the cases, SPECT images acquired at the same time are shown for comparison.

4.1. Normal treadmill stress CMR

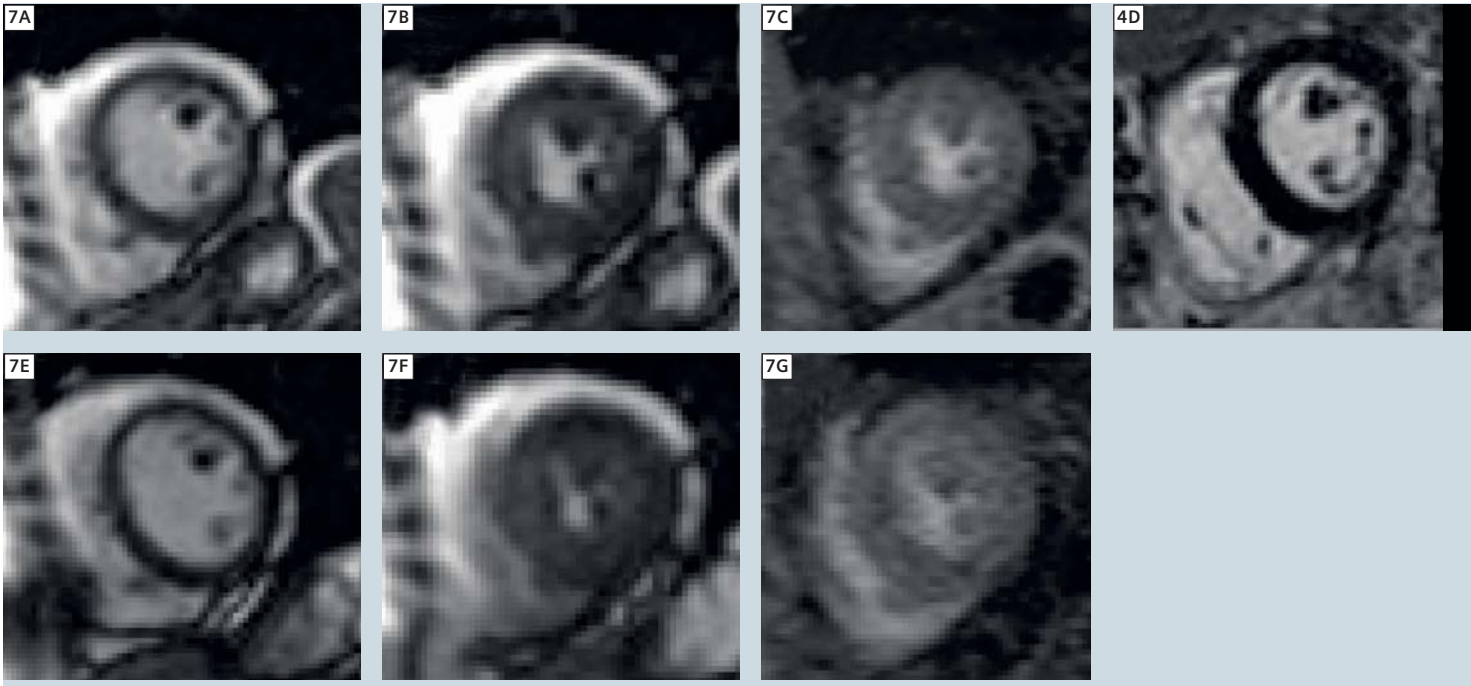

7 Normal Treadmill Stress CMR. End-diastolic **(7A, E)** and end-systolic **(7B, F)** frames of cine imaging at rest (top row) and immediately post-stress (bottom row) plus stress myocardial perfusion imaging **(7C, G)** are shown in a 52-year-old postmenopausal female referred for stress SPECT to evaluate dyspnea; both stress modalities were negative for ischemia. In addition, late post-gadolinium enhancement (LGE) CMR imaging **(7D)** showed no myocardial enhancement. *Reprinted with permission from J. Cardiovascular Magnetic Resonance [3].*

4.2. Ischemia by treadmill stress CMR and SPECT

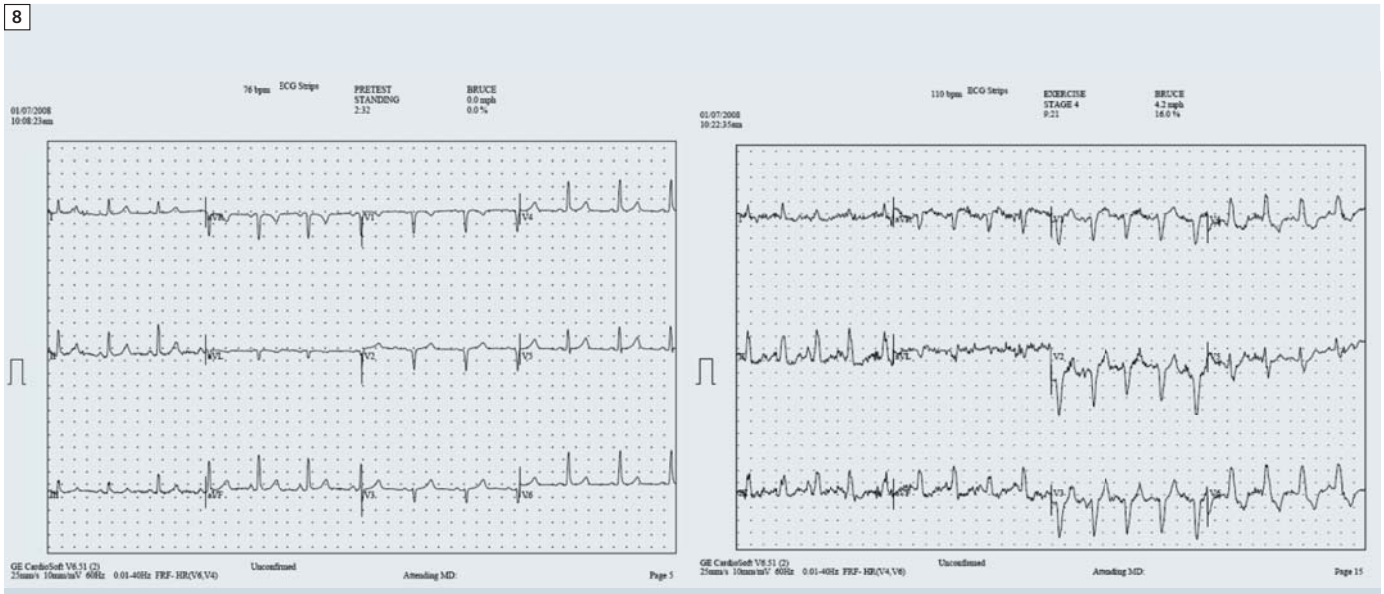

8 Electrocardiography during Treadmill Stress CMR. Rest (left) and stress (right) electrocardiography obtained in a 64-year-old male with exertional chest pain and remote anteroseptal myocardial infarction demonstrates exercise-induced left bundle branch block with reproduction of symptoms at stage 4 of the Bruce treadmill protocol. *Reprinted with permission from J. Cardiovascular Magnetic Resonance [3].*

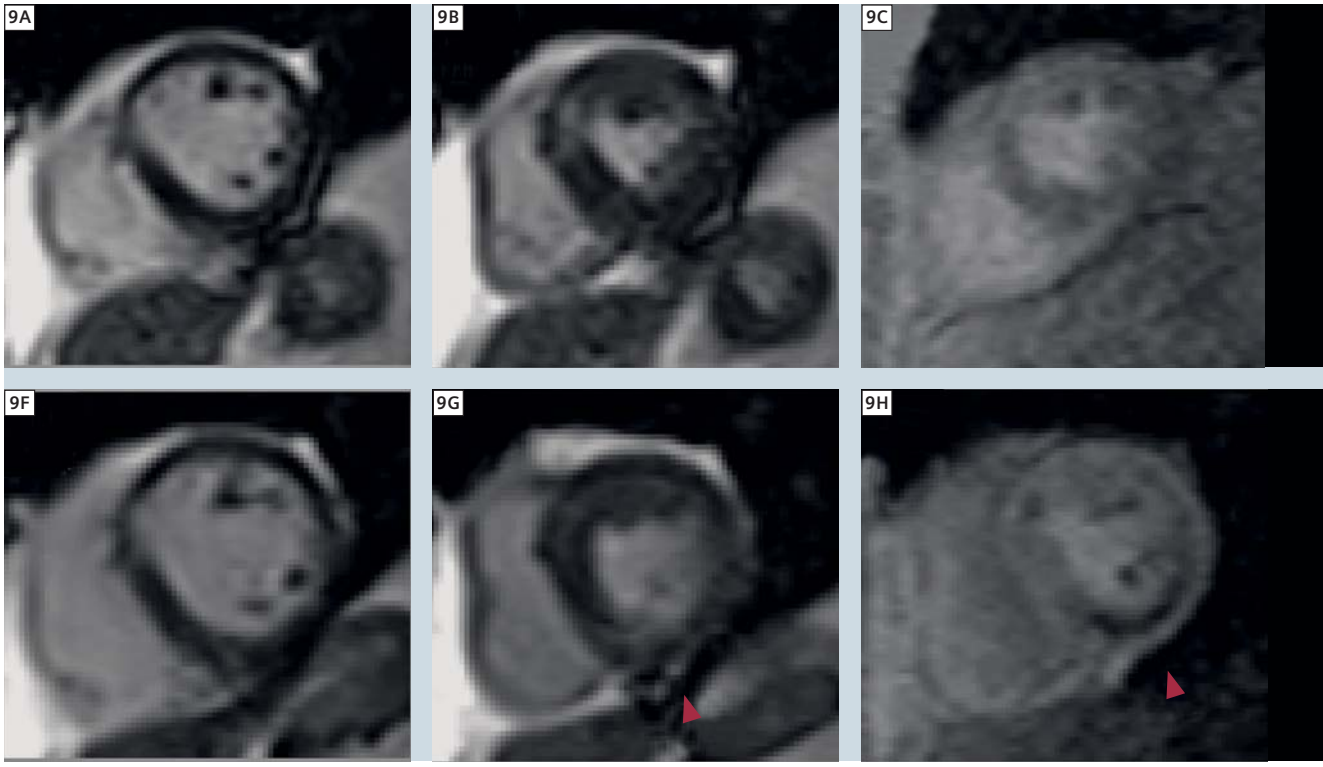

4.3. Ischemia by treadmill stress CMR not evident by SPECT

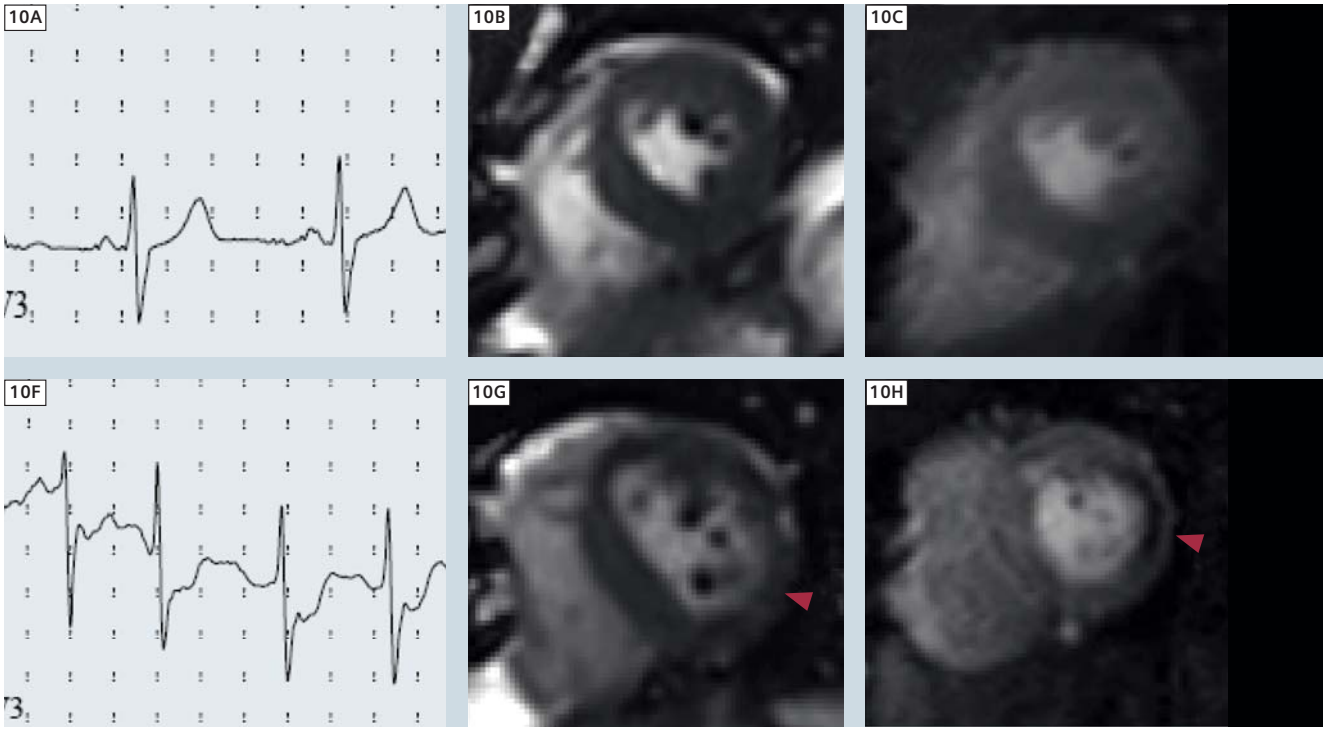

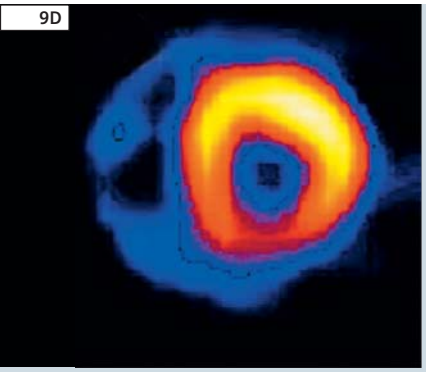

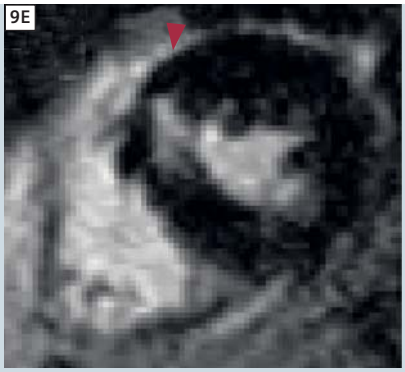

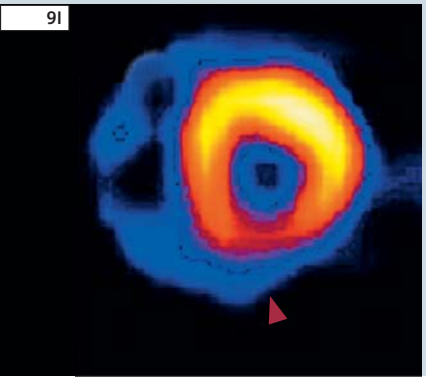

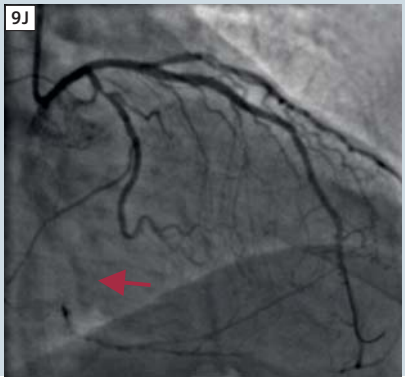

9 Rest and stress CMR and SPECT images in the same patient; both demonstrate myocardial ischemia, with corresponding obstructive coronary artery disease by angiography. Resting diastolic **(9A)** and systolic **(9B)** cine frames vs. comparable post-exercise cine frames **(9F, G)** show stress-induced inferior wall contractile dysfunction (**9G**, arrowhead). Inferior ischemia is also demonstrated by CMR perfusion imaging (**9C**-rest perfusion vs. **9H**-stress perfusion, arrowhead). Prior MI in the anteroseptum can be seen on late post-gadolinium imaging **(9E)**; note some fatty replacement in the infarct region evident as bright intramyocardial signal on non-contrast gradient echo cine frame in panel B. Rest Tc-99 m perfusion SPECT **(9D)** suggests normal perfusion, though somewhat obscured by adjacent bowel uptake; stress Tc-99m perfusion SPECT shows inferior wall defect (**9I**, arrowhead). The patient went on to invasive angiography that showed an occluded right coronary artery (**9J**, arrow) with some left-to-right collateral flow. *Reprinted with permission from J. Cardiovascular Magnetic Resonance [3].*

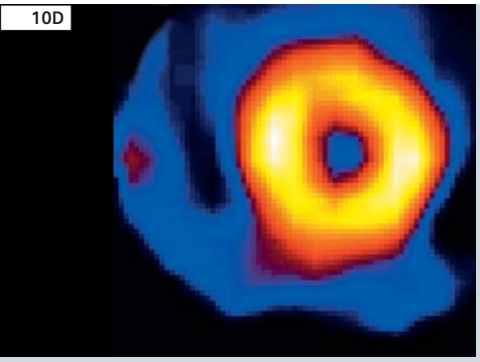

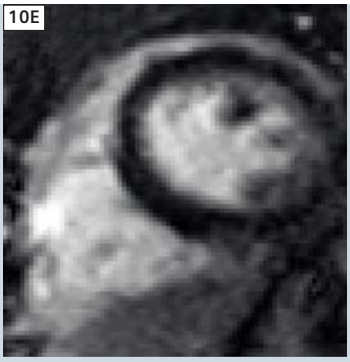

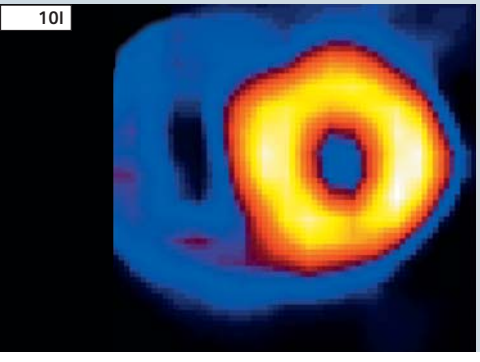

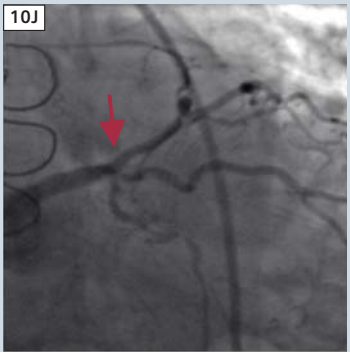

10 Rest and stress images show ischemia by CMR not evident by SPECT in a 56-year-old male with known coronary artery disease was referred for stress testing to evaluate abnormal stress ECG done prior to starting a supervised exercise program. Exercise-induced ischemia is evident by ST depression on electrocardiography (**10A** rest, **10F** stress), lateral wall motion abnormality on end-systolic frames from cine CMR (**10B** rest, **10G** stress) and lateral perfusion abnormality on first-pass contrast enhanced CMR (**10C** rest, **10H** stress). No myocardial infarct scar was seen by LGE CMR (**10E**). SPECT images obtained during the same stress examination suggest normal myocardial perfusion (**10D** rest, **10I** stress). Invasive angiography **(10J)** identified high-grade ostial stenosis of a large ramus intermedius coronary artery leading to percutaneous coronary intervention. *Reprinted with permission from J. Cardiovascular Magnetic Resonance [3].*

5. Summary and future directions

An exercise stress CMR exam can potentially provide a wealth of information not available from any other single diagnostic test. While perfusion defects suggest ischemia, the additional information provided by wall motion assessment with stress provides important insights into the functional effects of perfusion abnormalities on systolic performance. Encouraging initial results have led to the formation of a startup venture, EXCMR, Inc., to pursue commercialization of this technology. EXCMR has partnered with Siemens and Ohio State University in a multi-center trial funded by the State of Ohio Third Frontier program to evaluate treadmill exercise CMR in patients with known or suspected coronary artery disease. MRI-compatible treadmills are being installed at Case Western Reserve University in Cleveland, The Christ Hospital in Cincinnati, and University of Pittsburgh Medical Center. This trial will enroll over 200 patients in a direct comparison with nuclear SPECT imaging. Ohio State University is also collaborating with Siemens Healthcare and Siemens Corporate Research with support from the National Heart Lung and Blood Institute (R01HL102450) on the development of new methods for real-time imaging with improved temporal and spatial resolution, as well as advanced methods for quantification of systolic and diastolic cardiac function at rest and stress. Through these collaborative efforts it is hoped that exercise stress CMR will become an important tool in the diagnosis and guidance of therapy for heart disease patients in the near future.

Contact
Orlando P. Simonetti, Ph.D.
The Ohio State University
Cardiovascular Imaging Research Center
410 West 10th Ave
527 Doan Hall
Columbus, OH 43210
USA
Phone: +1 614- 293-0739
Fax: +1 614-293-2561.
Orlando.Simonetti@osumc.edu

References

1 Jekic M, Foster EL, Ballinger MR, Raman SV, Simonetti OP. Cardiac function and myocardial perfusion immediately following maximal treadmill exercise inside the MRI room. J Cardiovasc Magn Reson. 2008;10(1):3.
2 Foster EL, Arnold JW, Jekic M, Bender JA, Balasubramanian V, Thavendiranathan P, Dickerson JA, Raman SV, Simonetti OP. MR-compatible treadmill for exercise stress cardiac magnetic resonance imaging. Magnetic Resonance in Medicine. 2011.
3 Raman SV, Dickerson JA, Jekic M, Foster EL, Pennell ML, McCarthy B, Simonetti OP. Real-time cine and myocardial perfusion with treadmill exercise stress cardiovascular magnetic resonance in patients referred for stress SPECT. J Cardiovasc Magn Reson. 2010;12:41.
4 Lloyd-Jones D, Adams R, Carnethon M, De Simone G, Ferguson TB, Flegal K, Ford E, Furie K, Go A, Greenlund K, Haase N, Hailpern S, Ho M, Howard V, Kissela B, Kittner S, Lackland D, Lisabeth L, Marelli A, McDermott M, Meigs J, Mozaffarian D, Nichol G, O'Donnell C, Roger V, Rosamond W, Sacco R, Sorlie P, Stafford R, Steinberger J, Thom T, Wasserthiel-Smoller S, Wong N, Wylie-Rosett J, Hong Y. Heart disease and stroke statistics--2009 update: a report from the American Heart Association Statistics Committee and Stroke Statistics Subcommittee. Circulation. 2009;119(3):480-486.
5 Klem I, Heitner JF, Shah DJ, Sketch MH, Jr., Behar V, Weinsaft J, Cawley P, Parker M, Elliott M, Judd RM, Kim RJ. Improved detection of coronary artery disease by stress perfusion cardiovascular magnetic resonance with the use of delayed enhancement infarction imaging. J Am Coll Cardiol. 2006;47(8):1630-1638.
6 Ashley EA, Myers J, Froelicher V. Exercise testing in clinical medicine. Lancet. 2000;356(9241):1592-1597.
7 Fletcher GF, Balady GJ, Amsterdam EA, Chaitman B, Eckel R, Fleg J, Froelicher VF, Leon AS, Pina IL, Rodney R, Simons-Morton DA, Williams MA, Bazzarre T. Exercise standards for testing and training: a statement for healthcare professionals from the American Heart Association. Circulation. 2001;104(14):1694-1740.
8 Gibbons RJ, Balady GJ, Bricker JT, Chaitman BR, Fletcher GF, Froelicher VF, Mark DB, McCallister BD, Mooss AN, O'Reilly MG, Winters WL, Antman EM, Alpert JS, Faxon DP, Fuster V, Gregoratos G, Hiratzka LF, Jacobs AK, Russell RO, Smith SC. ACC/AHA 2002 guideline update for exercise testing: summary article. A report of the American College of Cardiology/American Heart Association Task Force on Practice Guidelines (Committee to Update the 1997 Exercise Testing Guidelines). J Am Coll Cardiol. 2002;40(8):1531-1540.
9 Lee TH, Boucher CA. Clinical practice. Noninvasive tests in patients with stable coronary artery disease. N Engl J Med. 2001;344(24):1840-1845.
10 Bouzas-Mosquera A, Peteiro J, Alvarez-Garcia N, Broullon FJ, Mosquera VX, Garcia-Bueno L, Ferro L, Castro-Beiras A. Prediction of mortality and major cardiac events by exercise echocardiography in patients with normal exercise electrocardiographic testing. J Am Coll Cardiol. 2009;53(21):1981-1990.
11 Armstrong WF, Zoghbi WA. Stress echocardiography: current methodology and clinical applications. J Am Coll Cardiol. 2005;45(11):1739-1747.
12 Tavel ME. Stress Testing in Cardiac Evaluation: Current Concepts With Emphasis on the ECGn 1378/chest.119.3.907. Chest. 2001;119(3):907-925.
13 Bruce RA, Blackmon JR, Jones JW, Strait G. Exercising testing in adult normal subjects and cardiac patients. Pediatrics. 1963;32:SUPPL 742-756.
14 Lear SA, Brozic A, Myers JN, Ignaszewski A. Exercise stress testing. An overview of current guidelines. Sports Med. 1999;27(5):285-312.
15 Myers J, Voodi L, Umann T, Froelicher VF. A survey of exercise testing: methods, utilization, interpretation, and safety in the VAHCS. J Cardiopulm Rehabil. 2000;20(4):251-258.
16 Tavel ME, Shaar C. Relation between the electrocardiographic stress test and degree and location of myocardial ischemia. Am J Cardiol. 1999;84(2):119-124.
17 Bruce RA, Hornsten TR. Exercise stress testing in evaluation of patients with ischemic heart disease. Prog Cardiovasc Dis. 1969;11(5):371-390.
18 Roger VL, Jacobsen SJ, Pellikka PA, Miller TD, Bailey KR, Gersh BJ. Prognostic value of treadmill exercise testing: a population-based study in Olmsted County, Minnesota. Circulation. 1998;98(25):2836-2841.
19 Marwick TH. Stress echocardiography. Heart. 2003;89(1):113-118.
20 Mandapaka S, Hundley WG. Dobutamine cardiovascular magnetic resonance: a review. J Magn Reson Imaging. 2006;24(3):499-512.
21 Thompson RC, Cullom SJ. Issues regarding radiation dosage of cardiac nuclear and radiography procedures. J Nucl Cardiol. 2006;13(1):19-23.
22 Underwood SR, Anagnostopoulos C, Cerqueira M, Ell PJ, Flint EJ, Harbinson M, Kelion AD, Al-Mohammad A, Prvulovich EM, Shaw LJ, Tweddel AC. Myocardial perfusion scintigraphy: the evidence. Eur J Nucl Med Mol Imaging. 2004;31(2):261-291.
23 Niezen RA, Doornbos J, van der Wall EE, de Roos A. Measurement of aortic and pulmonary flow with MRI at rest and during physical exercise. J Comput Assist Tomogr. 1998;22(2):194-201.
24 Gibbons RJ, Balady GJ, Beasley JW, Bricker JT, Duvernoy WF, Froelicher VF, Mark DB, Marwick TH, McCallister BD, Thompson PD, Jr., Winters WL, Yanowitz FG, Ritchie JL, Cheitlin MD, Eagle KA, Gardner TJ, Garson A, Jr., Lewis RP, O'Rourke RA, Ryan TJ. ACC/AHA Guidelines for Exercise Testing. A report of the American College of Cardiology/American Heart Association Task Force on Practice Guidelines (Committee on Exercise Testing). J Am Coll Cardiol. 1997;30(1):260-311.
25 Jekic M, Ding Y, Dzwonczyk R, Burns P, Raman SV, Simonetti OP. Magnetic field threshold for accurate electrocardiography in the MRI environment. Magn Reson Med. 2010;64(6):1586-1591.
26 Kellman P, Epstein FH, McVeigh ER. Adaptive sensitivity encoding incorporating temporal filtering (TSENSE). Magn Reson Med. 2001;45(5):846-852.
27 Griswold MA, Jakob PM, Heidemann RM, Nittka M, Jellus V, Wang J, Kiefer B, Haase A. Generalized autocalibrating partially parallel acquisitions (GRAPPA). Magn Reson Med. 2002;47(6):1202-1210.

Missing information?

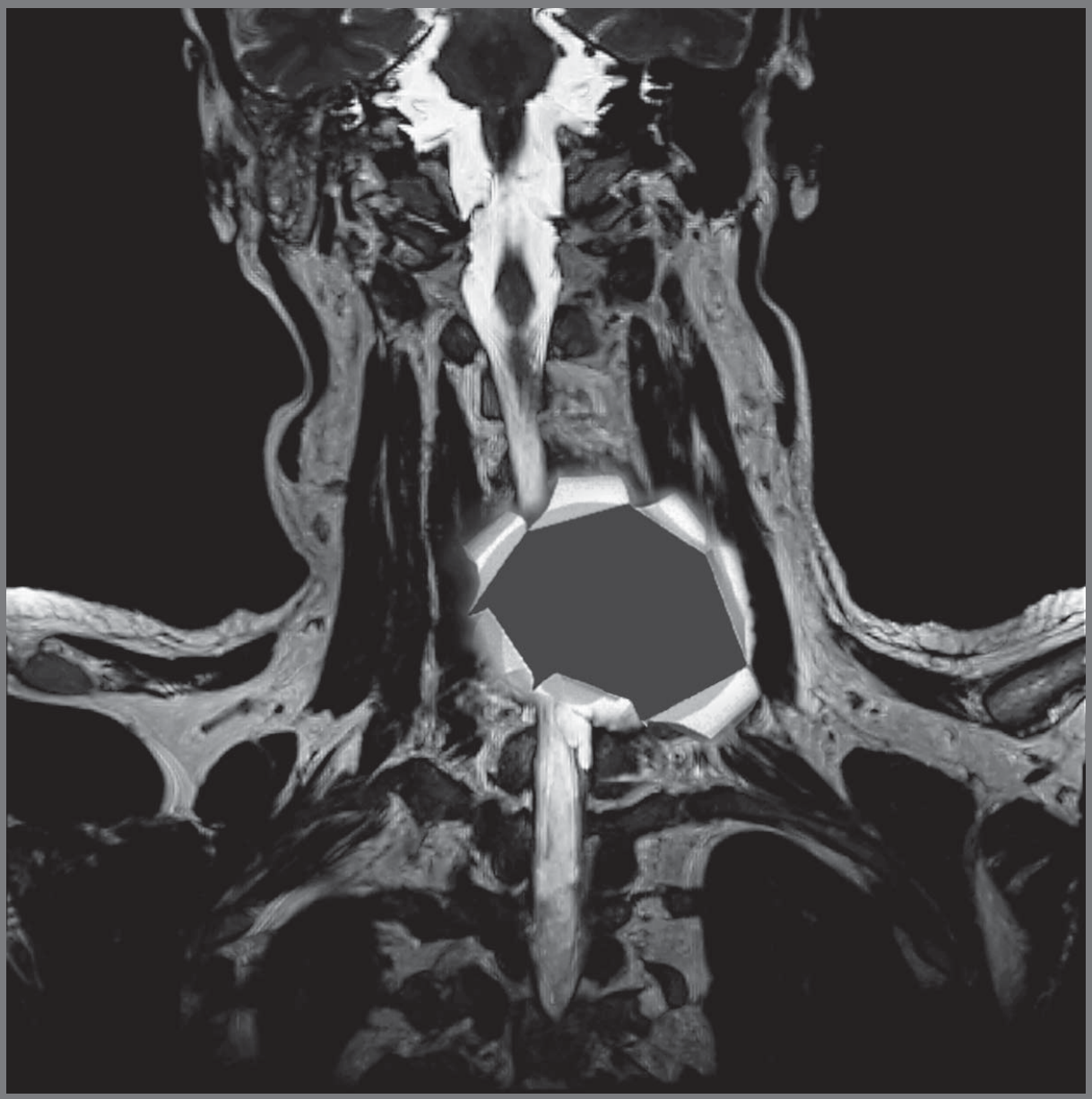

To make sure you have all the information you need, register for our free monthly newsletter on clinical MRI information.
Check out case reports from MAGNETOM users around the world and stay up-to-date with Siemens software applications.

Register at
www.siemens.com/magnetom-world
Go to
Publications > Subscriptions

1

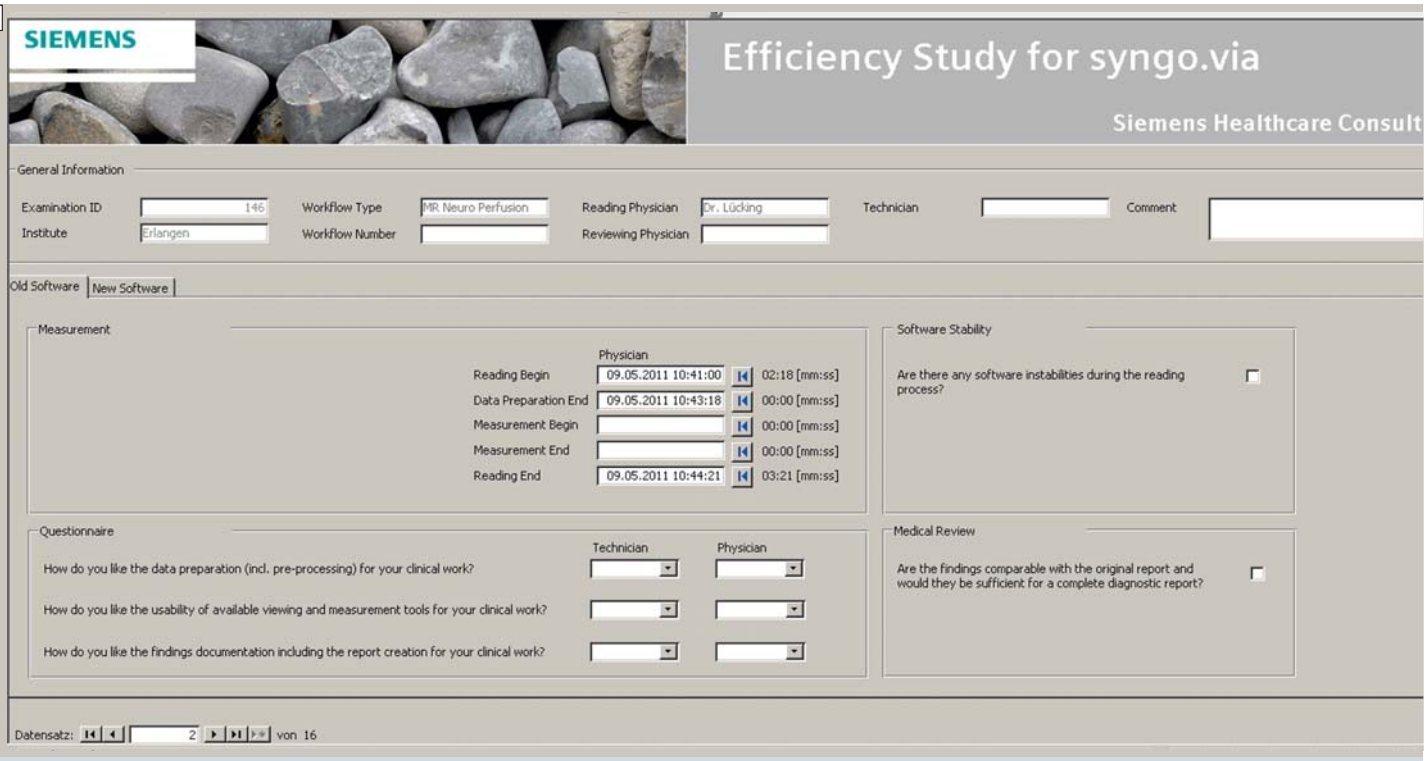

1 User interface for the Microsoft Access® based data collection tool.

Productivity Gains in Neurological and Oncological Reading

Hannes Lücking, M.D.[1]; Markus Lentschig, M.D.[2]; Martin Bünning, M.D.[2]; Arnd Dörfler, M.D.[1]; Scott McCuen Koytek, MHA[3]

[1] *University Medical Center of Erlangen, Department of Neuroradiology, Erlangen, Germany*
[2] *ZEMODI, Zentrum für Moderne Diagnostik, Bremen, Germany*
[3] *Siemens Healthcare, Erlangen, Germany*

The demand for MR scanning continues to grow. As a 'no dose' alternative to other imaging techniques, MR imaging is entering into new fields and is becoming more and more the imaging technology of choice. In many countries this increase is coupled with restraints, such as decreases in reimbursement and or personnel shortages which combine to make an increase in staffing impossible. As a result, imaging departments must produce and read more images in the same amount of time with the same amount of personnel (or even less of both). In a previous Flash article, Horvath et al. examined the benefits of a *syngo*.via reading prototype for whole body reading. The authors found significant productivity gains in the reading process. But what about cases less complex than whole body reading? Can *syngo*.via provide similar gains? In order to answer this question the authors set up a study looking at two separate clinical workflows – oncology evaluation* in the abdomen and neuro perfusion evaluation*. In both instances we were able to find significant productivity gains in comparison to traditional workstation reading.

*These functionalities are still under development and not yet commercially available.

Comparison methodology

Using a database built in Microsoft Access® (Fig.1), observers timed radiologists in interpreting images in their normal reading environment at two different sites. The oncology cases were read in an independent imaging center, while the neuro perfusion cases were read at a university medical center.
We selected 11 to 12 cases at both sites. Each site then chose a radiologist to read the same set of images on their previous workstation solution and on their *syngo*.via client. The workstations used were Siemens Multimodality Work Places (MMWPs, also known as 'Leonardos'). Images were supplied by MAGNETOM Avanto, MAGNETOM Verio and MAGNETOM Espree systems.
In order to prevent bias we built in at least a week's time between the reading sessions. At one site, the radiologist read the images on their workstation solution, and then a week later in *syngo*.via. At the other site we reversed the order. The same person was also used to measure both sessions at each site in order to ensure consistency. In addition to speed we also checked accuracy by comparing the study results to the diagnoses actually recorded for the cases in the RIS. Finally we also collected reader comments regarding the reading experience with both software platforms in order to capture the qualitative differences in the reading process.

Comparison results

As one can clearly see in table 1, *syngo*.via provided significant productivity benefits in the reading process.

Table 1: Comparison of results for MR Oncology reading

MMWP (min:s)	*syngo*.via (min:s)	Difference (%)	Diagnosis
07:53	05:35	29%	colon carcinoma with liver metastasis
07:02	07:05	–1%	suspected pancreas carcinoma
05:07	02:43	47%	pancreatic head carcinoma
06:45	03:10	53%	colon carcinoma and adrenal adenoma
07:53	05:09	35%	nerve sheath tumor left femoral
06:42	04:17	36%	lymphoma with tumors in spleen and liver
07:09	06:36	8%	liver carcinoma with multilocular masses
04:51	03:19	32%	cholezystolithiasis and -docholithiasis, no sign for tumor
06:50	02:48	59%	pancreatic head carcinoma
07:16	03:53	47%	rectum carcinoma
05:14	05:04	3%	liver cirrhosis with suspected liver carcinoma
06:37	**04:31**	**32%**	**average**

Table 2: Comparison of Neuro Perfusion reading results**

MMWP (min:s)	*syngo*.via (min:s)	Difference (%)	Diagnosis
05:06	03:40	28,10%	several vascular stenoses
04:35	03:21	26,91%	stenosis of right internal carotid artery
04:47	03:52	19,16%	no pathology
04:22	04:17	1,91%	low grade stenosis of internal carotid artery
04:04	02:55	28,28%	occlusion of right middle cerebral artery
05:00	03:20	33,33%	diffuse microhemorrhages
04:19	03:24	21,24%	occlusion of middle cerebral artery and high grade stenosis of proximal internal carotid
04:46	02:56	38,46%	proximal occlusion of middle cerebral artery
04:02	03:31	12,81%	infarct in the corona radiata without vascular pathology
04:21	03:02	30,27%	stenosis of bifurcation of middle cerebral artery
04:39	05:09	–10,75%	no pathology
04:32	02:26	46,32%	cortical infarct, left side
04:33	**03:29**	**23,22%**	**average**

In the case of Onco Reading the decrease in reading time was as high as 59% with an average improvement of 32% (95% confidence interval +/– 14%). A single tailed t-test for significance of the paired difference yields a p<.0005. In the case of Neuro perfusion we also saw similar results, with the highest improvement being a 46% reduction in reading time and an average of 23% across the 12 cases selected (95% confidence interval +/– 10%) (Table 2). A single tailed t-test for significance of the paired difference yields a p<.0005.

Discussion

In both an ambulatory imaging practice and in a university clinical setting *syngo*.via was able to provide significant gains in the reading process. Winning anywhere from 3.5 to 4.5 minutes per case in a case group that takes anywhere from 4.5 to 7.5 minutes can make significant differences to the number of cases able to be viewed in day. Another important factor to understand is the fact that the reading physicians had had much more experience with the standard workstations as opposed to *syngo*.via (perhaps a reason for the larger standard deviation in the *syngo*.via reading sessions than in the standard workstation sessions). Furthermore, reading quality in terms of the diagnosis was also maintained and in one case a reader found additional information, which was

2

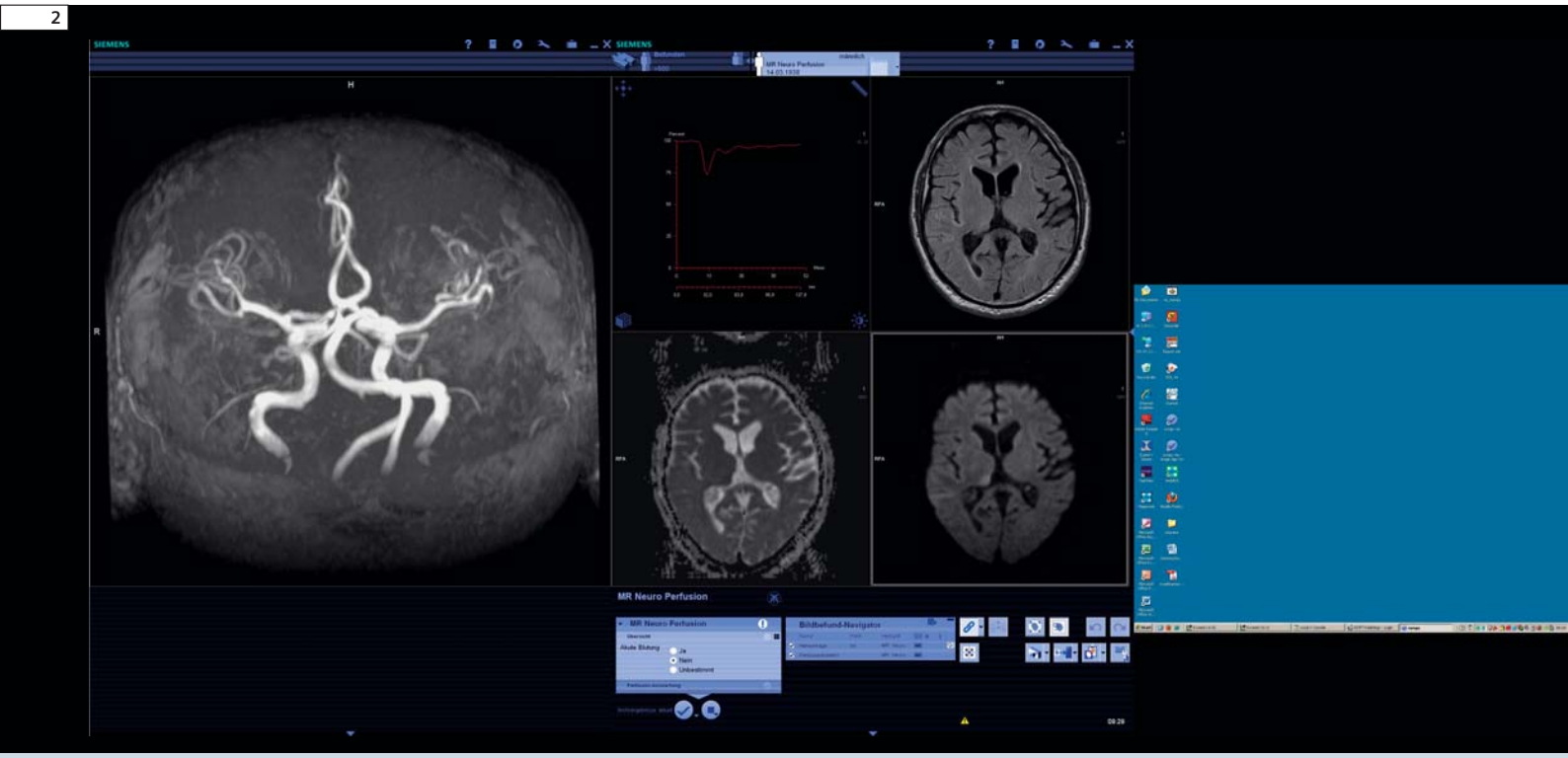

2 *syngo*.via user interface.

missed in a previous reading. Similar to Horvath et al.'s study, the radiologists here also reported being fresher after reading and believed that they had qualitatively done a better job in less time in comparison with their old workstations. Therefore, over the course of a day readers may also be less subject to fatigue.

What were some of the reasons for the improvement with *syngo*.via?

- The preconfigured layouts in *syngo*.via enabeled the radiologists to start reading a case immediately when it is was opened as opposed to first hanging the information.
- An additional time saver is the fact that in every case, the reader looks at exactly the same place within the user interface in order to make his or her image comparison. Knowing that the images will appear in the same place also enables the reader to "automate" his or her reading style.
- In the case of Neuro Perfusion, the automatic calculation of the Perfusion Diffusion Mismatch made a significant difference in the process, as opposed to calculating the mismatch with a calculator**.
- Mouse over corner menus allowed the reader to stay focused within the image, as opposed to having to move his view away from the image in order to access a tool menu.

Conclusion

As the pressure to do more with less continues to grow in radiology, vendors will need to continue to focus their innovation efforts on develping the tools that allow for better diagnosis in less time. Based on the results of this comparison, *syngo*.via is a big step forward in this direction.

Contact
Hannes Lücking, M.D.
University Medical Center of Erlangen
Department of Neuroradiology
Schwabachanlage 6
91054 Erlangen
Germany
Phone: +49 (0)9131 85-44834
hannes.luecking@uk-erlangen.de

Martin Bünning, M.D.
ZEMODI, Zentrum für Moderne Diagnostik
Schwachhauser Herrstr. 63a
28211 Bremen
Germany
Phone +49 421 69641-600
Fax +49 421 69641-649

**The statements by Siemens' customers described herein are based on results that were achieved in the customer's unique setting. Since there is no 'typical' setting and many variables exist, there can be no guarantee that other customers will achieve the same results.

The Networked Scanner Workflow

Anja Fernandez Carmona; Klaus Mayer

Siemens Healthcare, Erlangen, Germany

Introduction

With a Networked Scanner* *syngo*.via is integrated directly into the scanner workspace. With one mouse and one keyboard, the user can easily move from the acquisition workplace to a second monitor that runs *syngo*.via. (Figure 1) The technology provides the opportunity to optimize the radiological workflow in the hospital in several ways:

- Planning MR protocols:
  The Networked Scanner allows to plan a scheduled examination before the patient arrives. The radiologist can adjust the scan and ensure that the patient receives the examination needed. On the other hand, the user can configure the system such that specific scan requests automatically receive the same exam protocol every time, and thereby automate the planning step.
- Pushing MR protocols to the scanner:
  The MRI scanner automatically receives the planned MRI protocols that are loaded immediately into the measurement queue, thereby eliminating the need for paper communication between the radiologist and the technologist.
- Accessing processing and reading:
  Because *syngo*.via runs on the second monitor at the MRI scanners workplace, the technologist can prepare and scan different patients in parallel without screen overlays.
- Managing MRI protocols:
  The client server technology, allows the user to upload their protocol trees to a single database on the *syngo*.via server. Therefore, all MRI protocols can be easily managed and distributed across the scanners – with just one tool, from anywhere in the radiological department. The technologist has a complete overview of all MRI protocols on all MRI systems from any *syngo*.via workplace.

The Networked Scanner offers all of these functionalities and helps to improve the radiological workflow in your department.

1 Simultaneously work with MAGNETOM Skyra/Aera and *syngo*.via on two screens.

*Networked Scanner is only available for MAGNETOM Aera and Skyra in the US.

Note: All patient and physician names mentioned in this article are not actual patients or physicians.

The Networked Scanner workflow comprises the following steps:

1 Schedule → 2 Assign → 3 Plan → 4 Scan → 5 Prepare → 6 Read

1. Schedule the patient at the RIS workplace

The registration of a patient typically is performed by a medical secretary or a technician at a Radiology Information System (RIS) from somewhere within the clinic.

The important entries for networked scanning are the **Requested Procedure** and the **MRI Scanner** intended for the examination. The Medical Information (e.g. *Special Needs, Contrast Allergies, Medical Alert and Pregnancy*) are optional and can be filled out as necessary. Figure 2 shows the registration of a **Brain Dot Engine** examination for the MAGNETOM Skyra system.

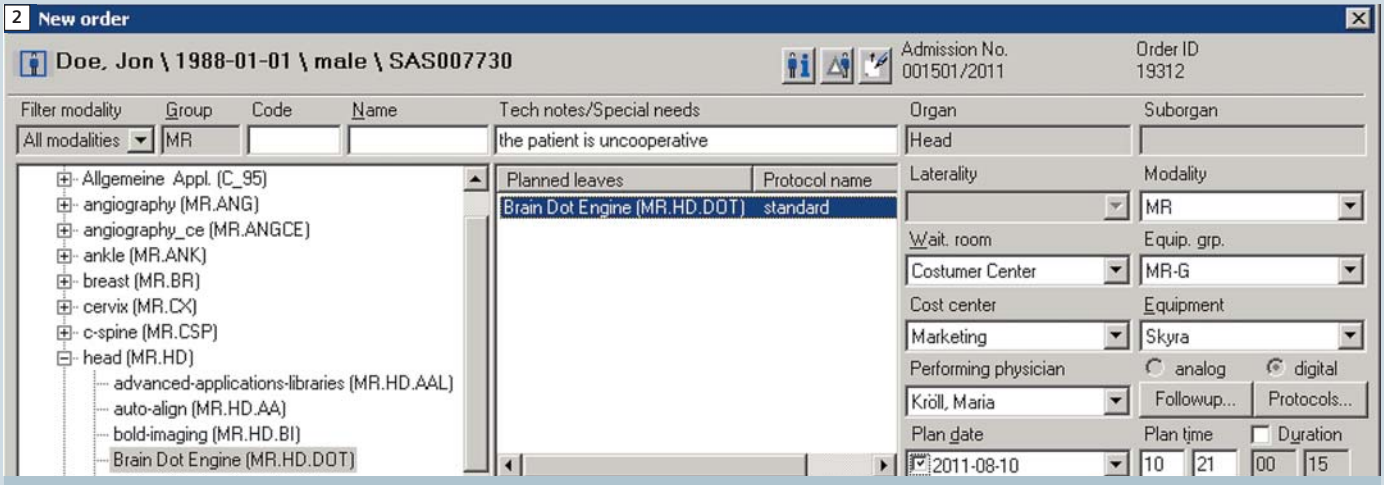

2 Set up a brain examination at the Siemens RIS workplace.

2. Assign the scheduled examination to a specific workflow

After the *syngo*.via system has retrieved the order to examine the new patient, the planned **Requested Procedure** is automatically assigned to a specific *syngo*.via workflow that provides all workflow steps needed to efficiently process and interpret the case. Figure 3 shows the **Workflow Assigned** icon that is displayed as soon as a workflow is assigned in the patient browser. Move the mouse over the icon to see which workflow is assigned to the procedure.

3 Workflow Assigned icon.

If no workflow is assigned to the procedure, the unassigned procedures are shown in the **Assign** worklist and need to be assigned manually. In this case the number next to the **Assign** icon will be increased in the Access Bar (Fig. 5). Figure 4 demonstrates the manual assignment of workflows to procedures from the Patient Folder of *syngo*.via. In the upper area you find the **Request**

Information that you have entered in the RIS system. In the **Workflow** area you can choose a workflow from the **Workflow Description** list. Select the **Learn this manual assignment for all future automatic assignments** check box to add your assignment to the automatic assignment rules.
After the successful assignment, you find the **MR Protocol Planning**, **MR Scanning** and **MR Reading** workitem, which are typical for the Networked Scanner workflow, in the **Workflow** tab of the patient (Fig. 5).

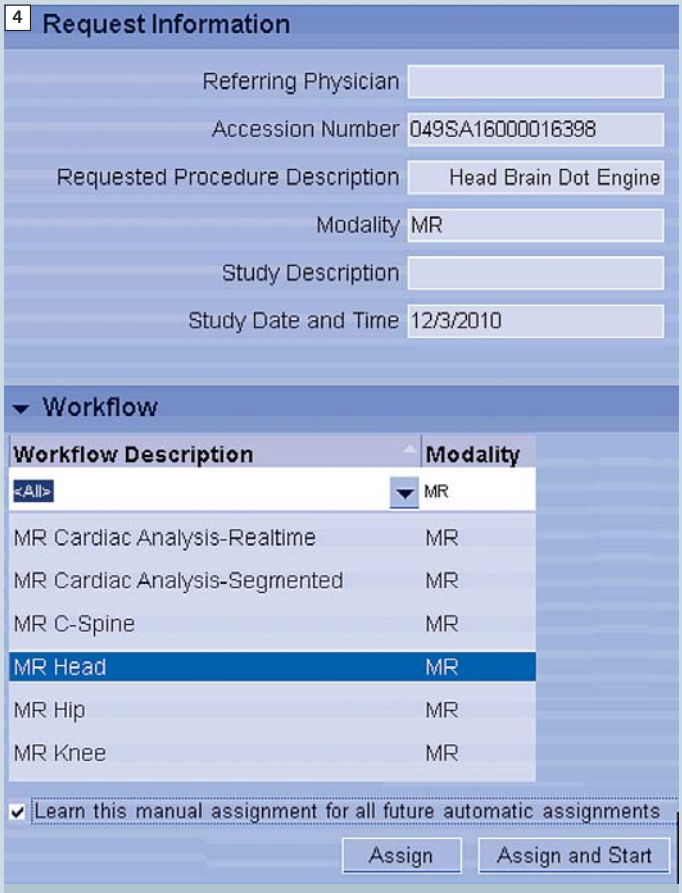

4 Patient Folder assignment.

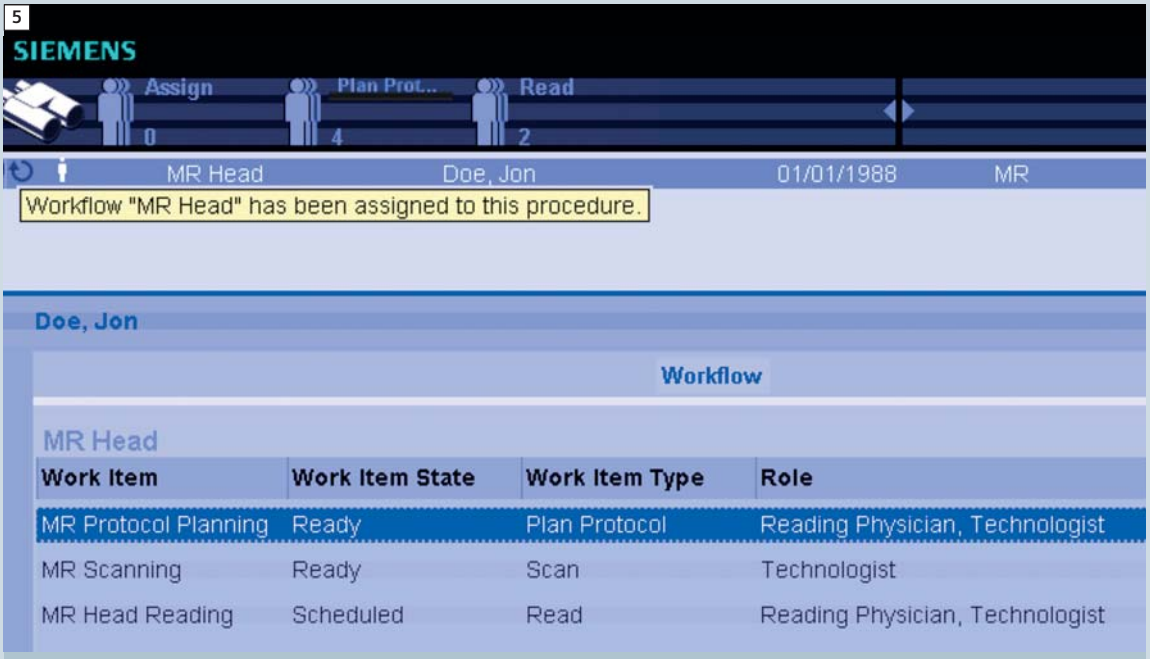

5 Workitems needed for networked scanning.

6

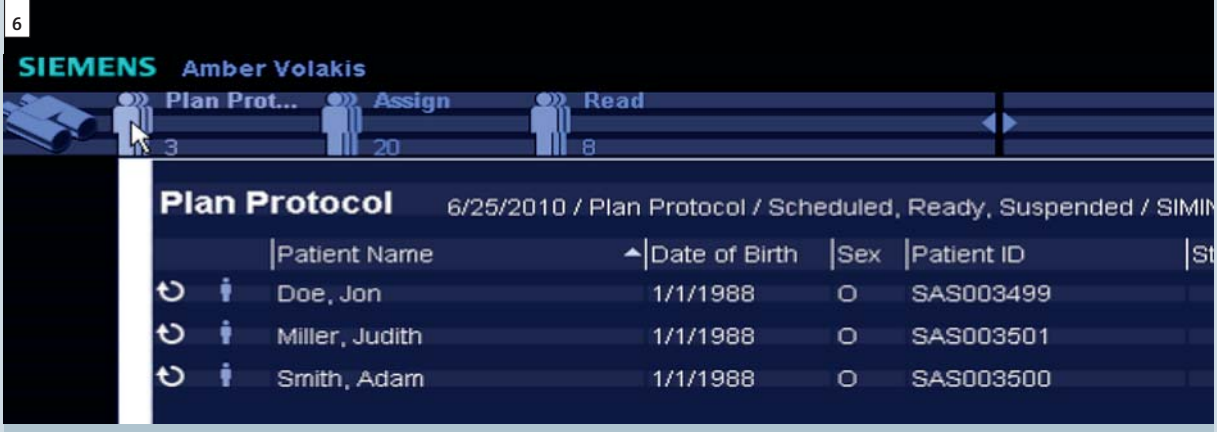

6 Plan Protocol worklist.

3. Plan the examination at the radiologist workplace

The planning of protocols can be performed by the radiologist at any *syngo*.via client in the department. The radiologist selects one patient out of the **Plan Protocol** worklist (Fig. 6).

For this he simply moves his mouse over the **Plan Protocol** icon in the **Access Bar**. The number below the worklist name indicates the number of patients in the worklist.

To speed up the planning with the **Select for Next Patient** option right click on the **Plan Protocol** icon and chose the option in order to move automatically through the worklist (Fig. 7). After the patient has been selected, the **Plan Protocol** step (Fig. 8) is opened in order to perform the protocol planning.

7

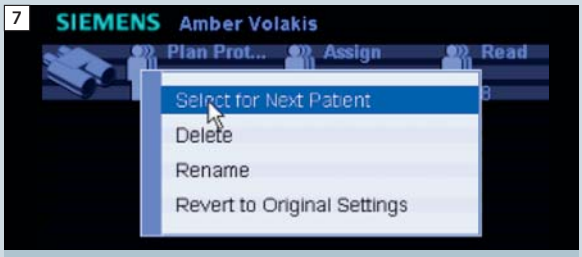

7 Speed up the planning.

8

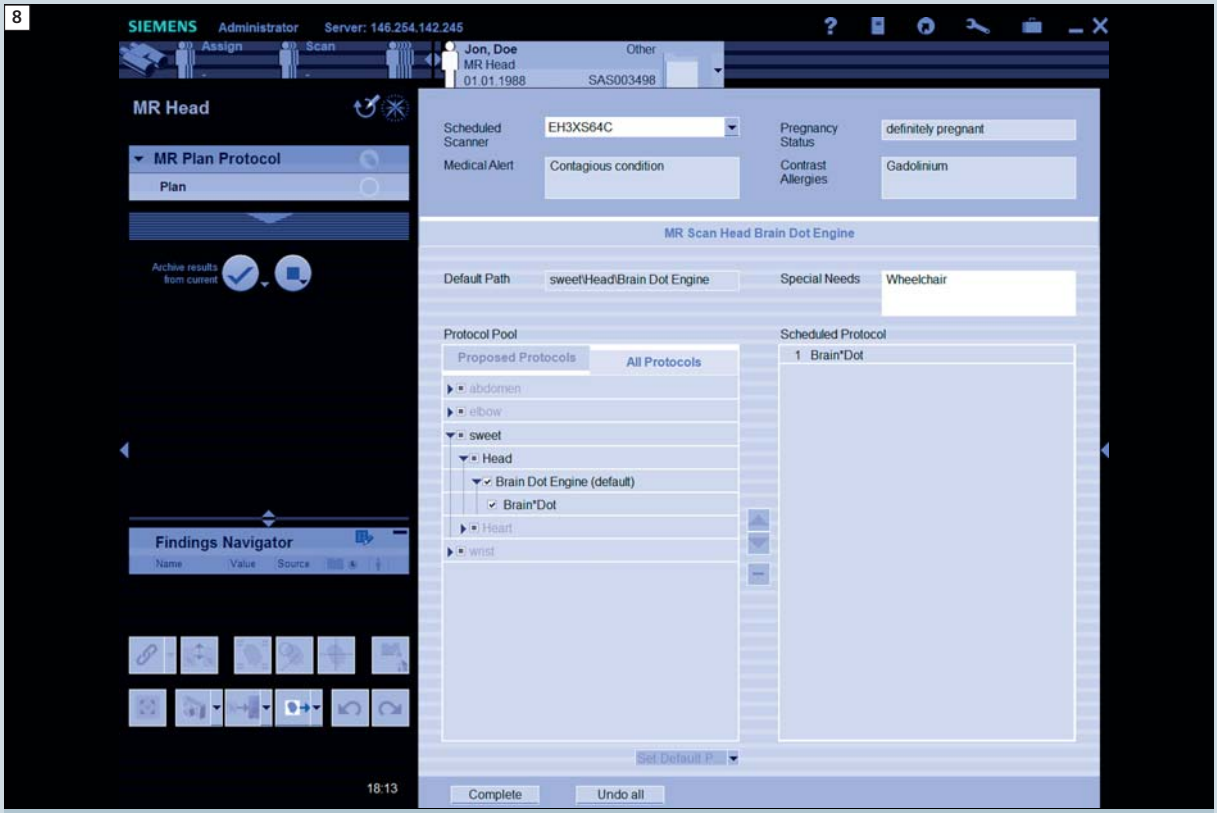

8 Plan Protocol step.

The following items can be adjusted:

Scheduled scanner:
The radiologist is able to change the planned scanner – e.g. if the patient has special needs or if the scanner is busy.

Special Needs:
Allows to enter information about patient's special needs.

9

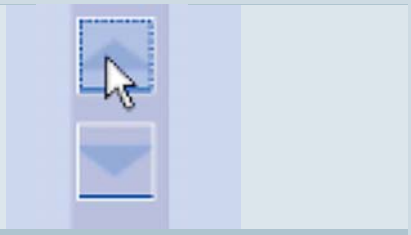

9 Move protocol icon.

10

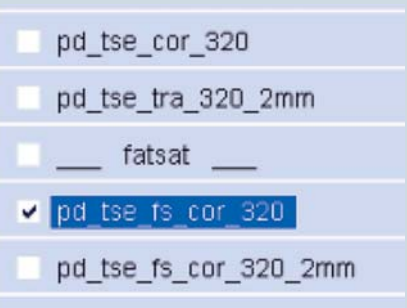

10 Removing a protocol.

Set Default Path:
Select this path as default for upcoming examinations with the same planned **Requested Procedure**. All future patients with the same **Requested Procedure** will receive automatically the same examination protocols. In this case the protocol planning has been done automatically by the system. The result of the automatic planning will be shown in the **Scheduled Protocol** area.

- Choose a protocol that you want to use as default protocol for the next examinations.
- Check the checkbox to select the chosen protocol.
- Push the **Set Default Path** button.
- Check the correct path in the **Default Path** field.

Scheduled Protocol
All planned protocol items are listed in the **Scheduled Protocol** area. As already mentioned, the list is filled automatically if you have set the **Default Path**.

- To move a protocol to another position, you have to select the protocol and press the upward or downward arrow (Fig. 9).
- To delete an item from the list, you have to select it and press the **minus** button.

All items listed in the **Scheduled Protocol** area have been selected automatically in the **Protocol Pool** area on the left. After selecting or deselecting a protocol in the **Protocol Pool** area, the corresponding items are automatically added or deleted to the **Scheduled Protocol** area (Fig. 8). You are able to change the proposed planning at any time.

Protocol Pool:
All protocols available on the scanner are in the **Protocol Pool** area.

- To add a protocol to the scheduled list, choose the anatomical region and check the checkbox next to the protocol.
- To delete a protocol from the scheduled list, 'uncheck' this protocol item (Fig. 10).

Once you have planned the optimal protocol for this examination, finish the protocol planning by pressing the **Complete** button.

4. Scan the planned examination at the technologist workplace

A typical workplace for networked scanning consists of two monitors at the MRI scanner console. The scanner software is displayed on the left monitor. The user interface of *syngo*.via is displayed on the right monitor. Both are controlled with a single keyboard and mouse. With this, the technologist can prepare and scan different patients at the same time without screen overlays (Fig. 11).

To perform the examination, the technologist selects the planned patient from the Scan worklist in *syngo*.via on the second monitor (Fig. 12).
After the patient has been selected, the **Scan** step is opened in order to check the planned protocol and to perform the examination by pressing the **Perform Exam** button (Fig. 13).

Besides the **Plan Protocol** step used by the radiologist, there is a **Protocol Planning** step which can be used by the technologist. The **Check Protocol** step for the technologist has the same functionality as the **Plan Protocol** step for the radiologist, ensuring that the technologist is able to plan the examination as well.

11

11 Simultaneously work with MAGNETOM Skyra/Aera and *syngo*.via.

12

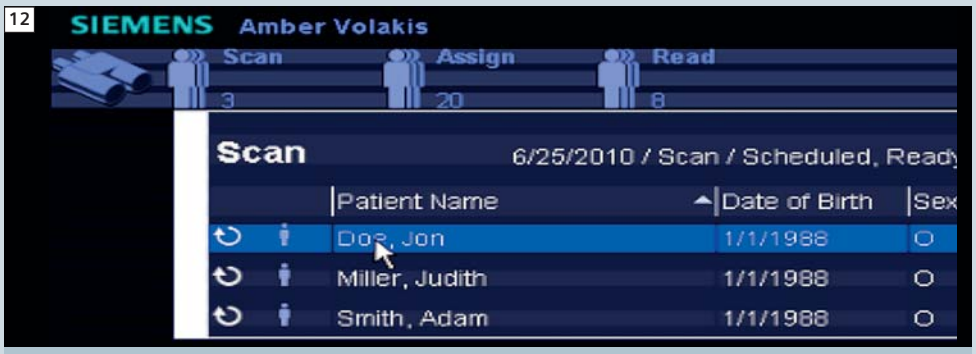

12 Scan Worklist.

13

13 Scan step.

The handling of **Dot Engine** workflows is very easy with the Networked Scanner. It is not necessary to add a single sequence to the **Dot Engines**. They are represented by the suffix ***Dot** (Fig. 13, **Scan Protocol** area on the right side). After pressing the **Perform Exam** button, the technologist has to pay attention to the acquisition monitor on the left hand side. There, the **Patient Registration** platform is opened and has to be confirmed by the technologist. Afterwards the MRI scanner receives automatically the planned MRI protocols that are loaded immediately into the measurement queue (Fig. 14).

Notes:

- The scanner receives the planned order through the DICOM Modality Worklist from the *syngo*.via server, which is usually configured by your service engineer.
- If the *syngo*.via application does not start automatically, you can start it from the windows start menu (Fig. 15).
- Because you can use *syngo*.via for viewing and processing images on the second monitor, The Viewing and other tab cards will not be started automatically on the scanner. You are able to start them manually if you need those cards (Fig. 16).

14 Protocols are loaded automatically.

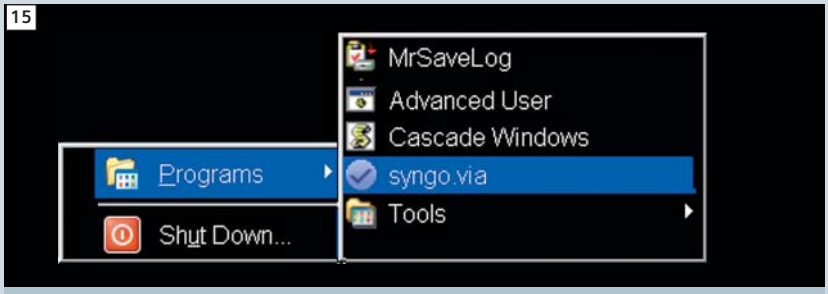

15 Start *syngo*.via

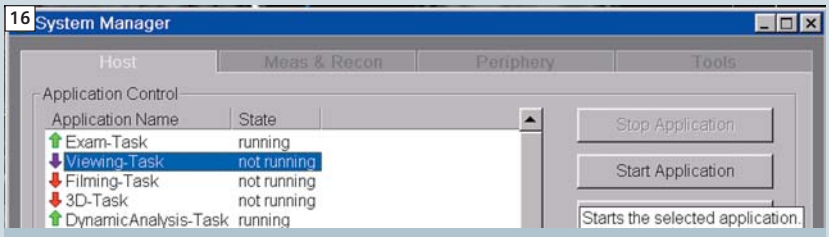

16 Applications can be started manually.

5. Prepare the examination for reading at the technologist workplace

During the scan, the technologist is able to select the patient from the **Read** worklist to open the **Read** workflow for preparing the images (Fig. 17).

HINT: To open a workitem choose the patient from the worklist (Fig. 17). Do not open the workitems via the triangle in the patient access area (Fig. 18) since this would start more than one workitem. All scanned images are loaded automatically into the *syngo*.via segments on the right monitor (Fig. 19).

17

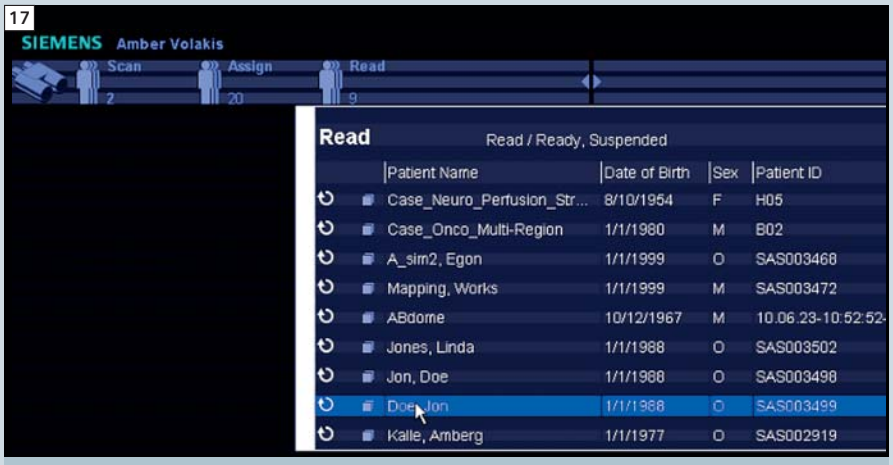

17 Open the workflow via the Reading worklist.

18

18 Do not use the triangle to open workitems.

19

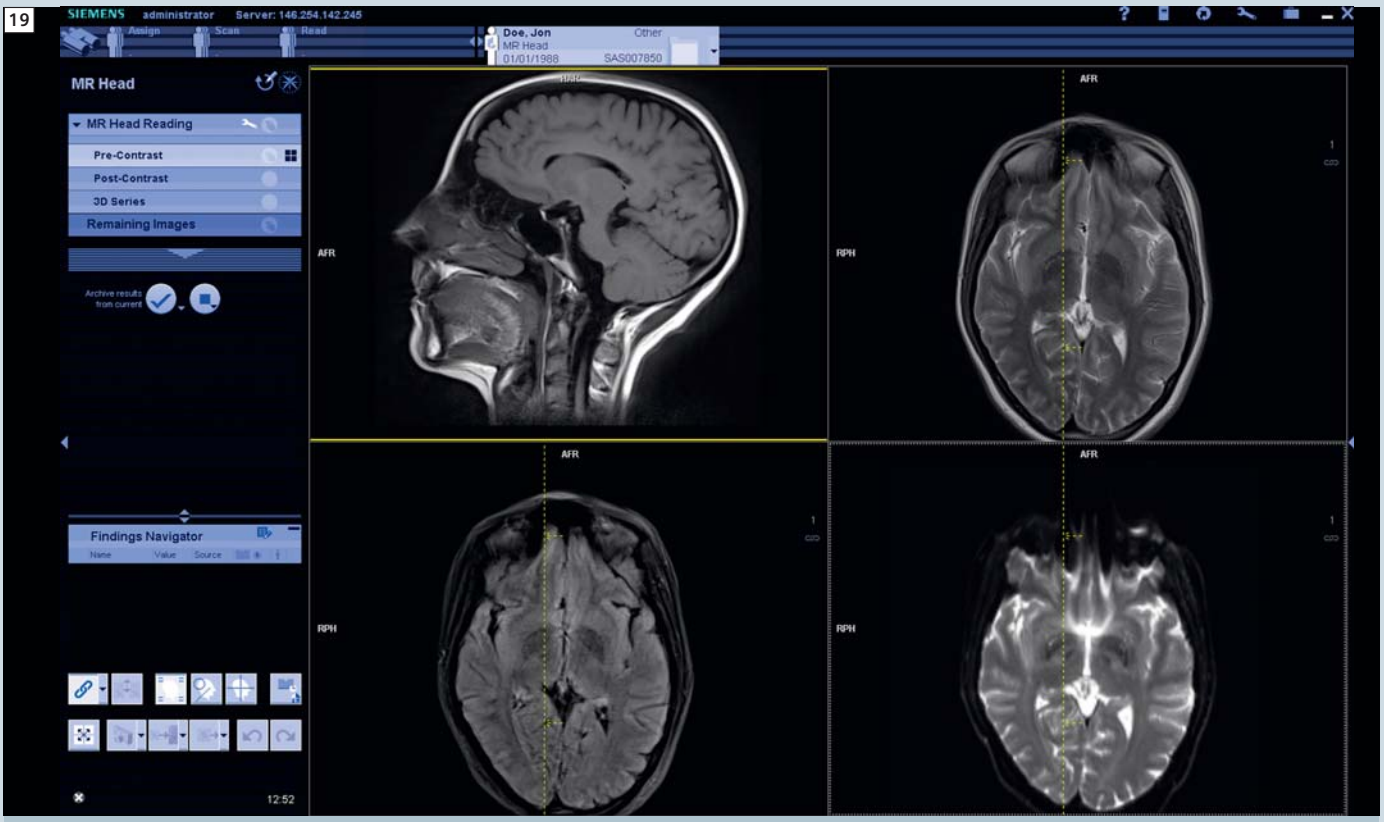

19 Prepare for reading.

Now the technician is able to prepare the case for reading and processing by selecting the **Corner Menus**. Fig. 20 gives some examples. The following steps can be prepared:

- Zoom and Pan
- Windowing
- Create MPRs ,MIPs or VRTs
- Measurements (ROI, distance line etc.)
- Composing*
- Basic Evaluation (mean curve, subtraction)

Furthermore, the technologist has access to all of the advanced applications in the *syngo*.via spectrum, such as *syngo*.MR cardiac 4D Ventricular Function, or the *syngo*.MR Neuro Perfusion Engine**.
Once the technologist has prepared the images, they will close the workflow and send the results to the radiologist for reading. The best way to do this is to select the **Close and send workitem(s) to...** menu (Fig. 21).

* This feature is not currently available for *syngo*.via in the US.
**This product is under development and is not available for sale in the US.

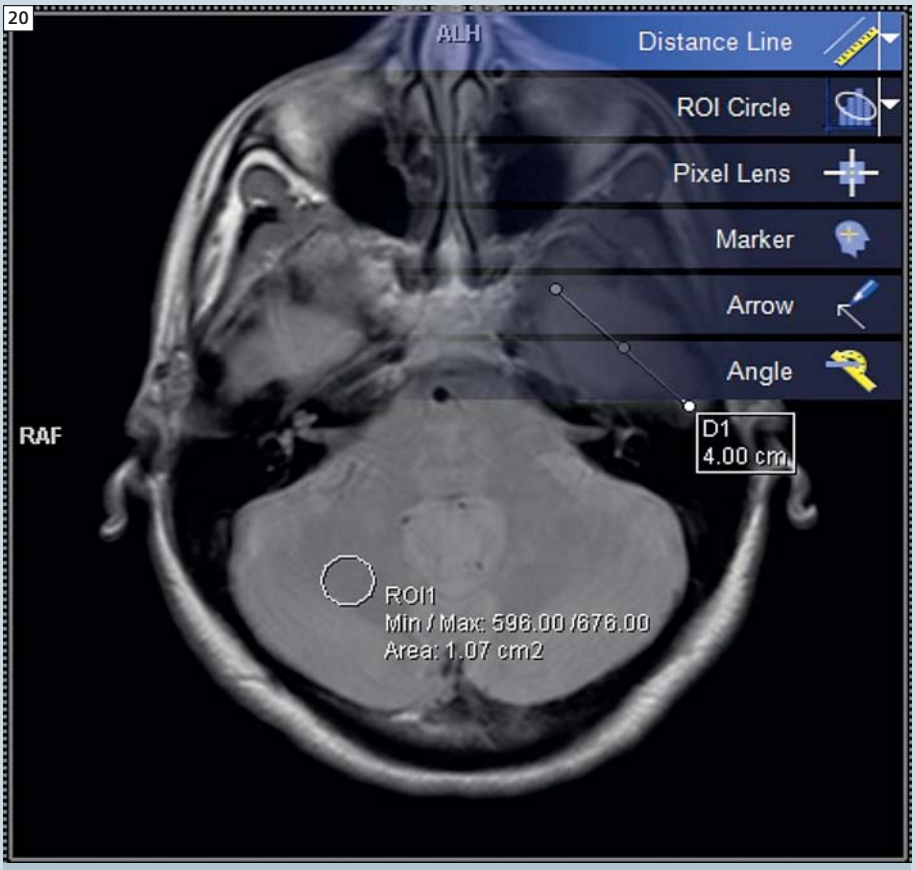

20 *syngo*.via tools.

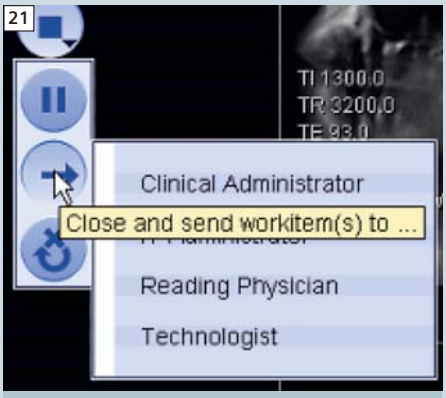

21 Close and send workitem to...

6. Read the examination at the radiologist workplace

Figure 19 shows the layout for the **Reading** task. The radiologist can scroll through the different series and steps and can perform measurements or evaluations. All the prepared work from the technologist is visible and adjustable for the radiologist. Findings can be created and saved in the report. After completing the case, the data is saved in the PACS system (depending on system set-up).

MR protocol management with the Networked Scanner

Protocol Management is used to handle the scan protocols within *syngo*.via and its networked scanners. You can share the protocols across multiple scanners and have a complete overview of all protocols on all scanners from any *syngo*.via workplace. **Protocol Management** ensures standardized protocol planning and thereby enables high quality scanning results across all scanners in your department.

To start the **Protocol Management**, you move the mouse over the **Wrench** icon in the access bar and choose the **Examination Protocol Management** menu (Fig. 22). Note: the **Protocol Management** is password protected.

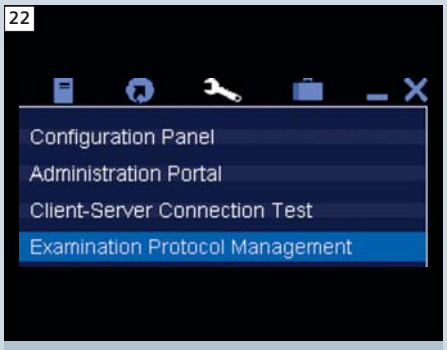

22 Wrench and Protocol Management menu.

23 Protocol Manager.

The **Protocol Manager** allows to upload protocols from a scanner to ***syngo*.via**, distribute protocols to other networked scanners or delete protocols from scanners. Figure 23 shows the opened **Protocol Manager** with its three tab cards: **Approve Upload, Distribute** and **Delete**.

Upload protocols from scanners to *syngo*.via

Before you can use the scan protocols for planning at *syngo*.via, the protocols need to be available on the *syngo*.via server. All protocols, which are available in the USER tree of the **Exam Explorer**, can be uploaded from the scanner to the *syngo*.via server.

- Right mouse click on the protocol that you want to upload,
- Choose the **Upload protocols...** menu from the context menu to start the upload.

You can upload single protocols as well as groups of them. Protocols, which are already uploaded, are displayed in italics in the **Exam Explorer** (Fig. 24).

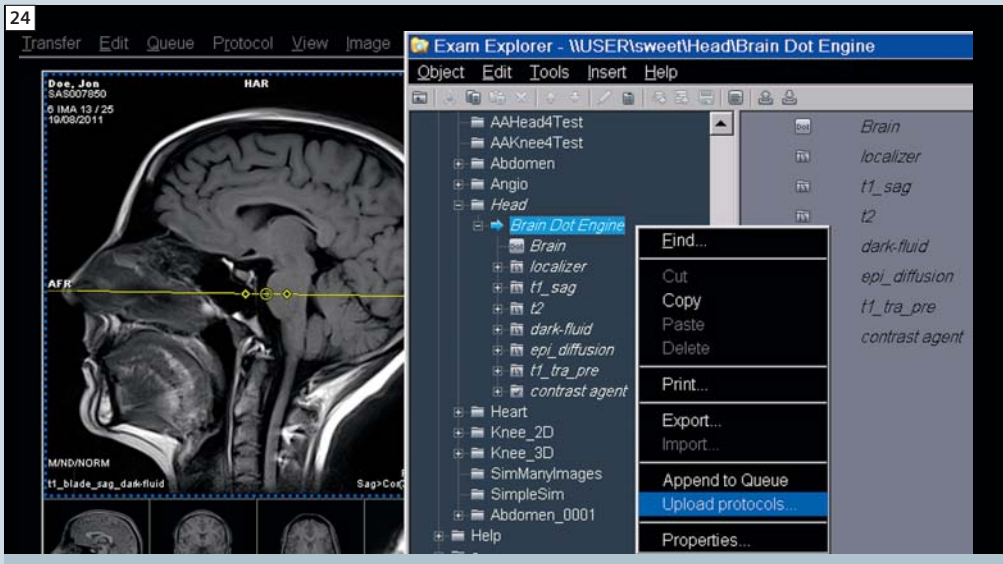

24 Upload protocols... menu.

After the upload has been started, a progress bar is shown (Fig. 25) and remains on the modality screen until you approve the uploaded protocols on the *syngo*.via client in the Approve Upload tab (Fig. 26).

Now go to the **Approve Upload** tab on the right monitor:

- Select the **Approve Upload** tab to accept the protocols.
- Check the displayed protocols.
- Select all of the protocols to be uploaded by using the check box.
- Press the **Load** button to copy the protocols to the *syngo*.via **Protocol Manger**.

After the approval, the transferred protocols are displayed on the right side of the **Approve Upload** tab card.

- Confirm the approval with **OK**.

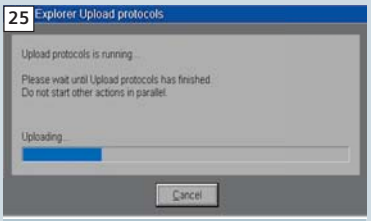

25 Upload protocols progress bar.

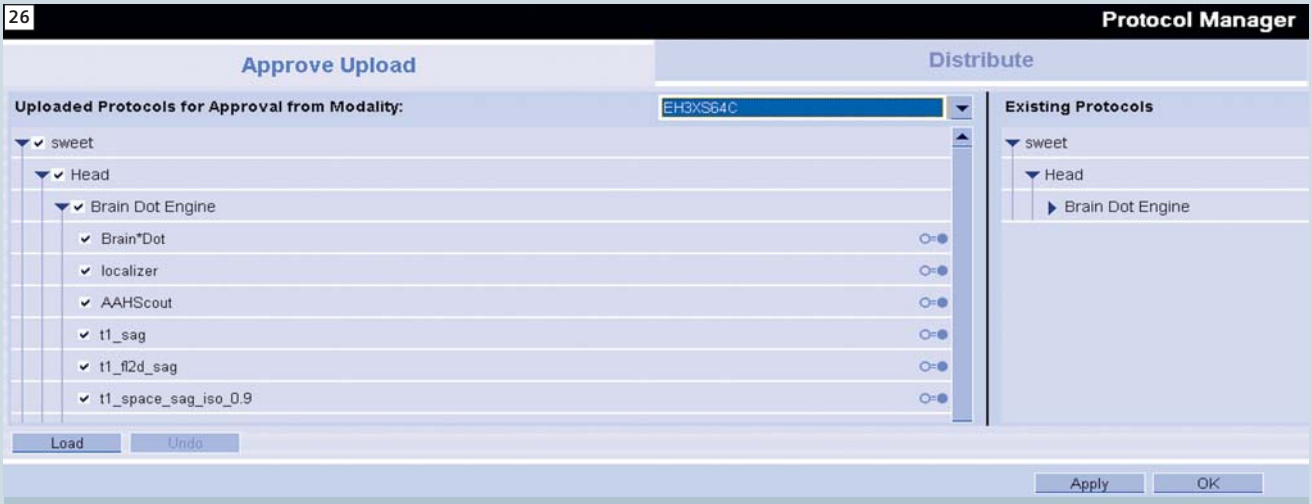

26 Approve Upload tab.

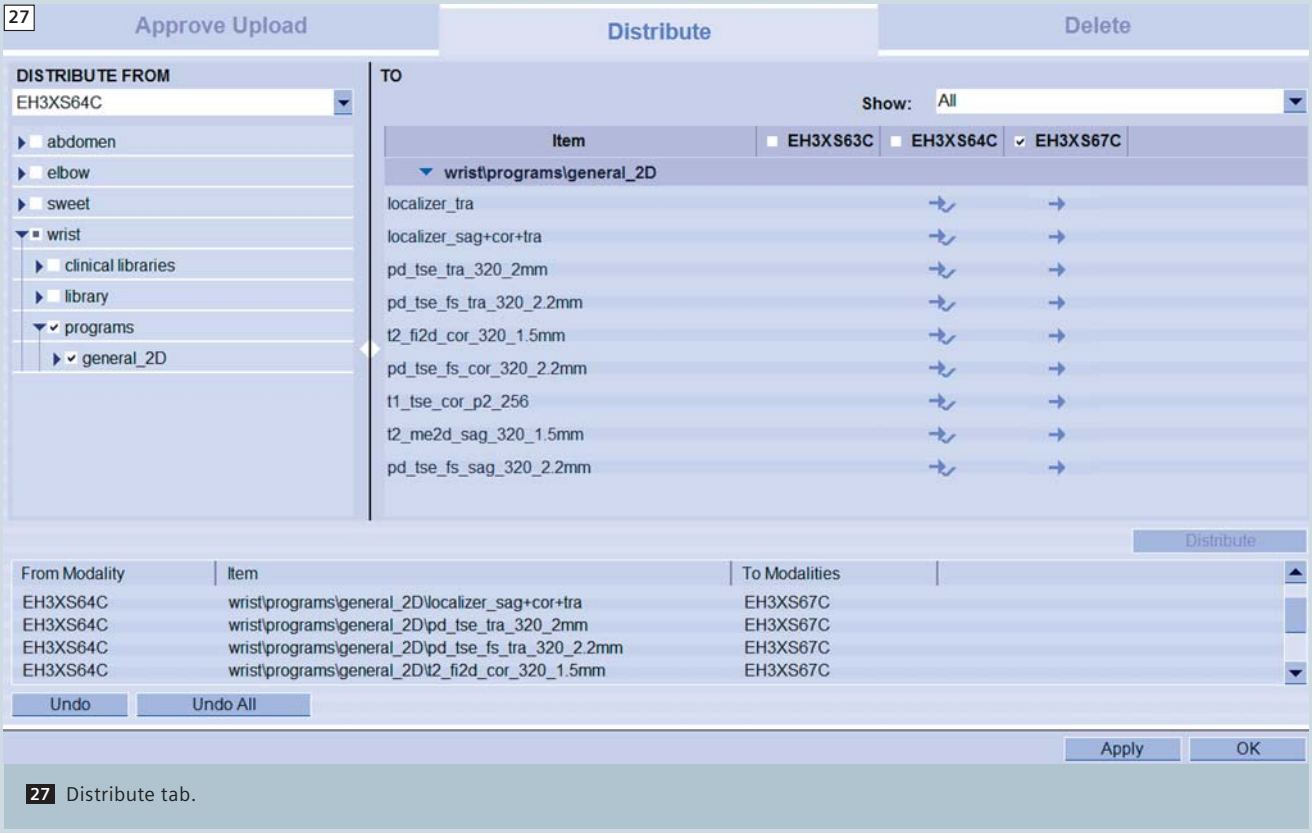

27 Distribute tab.

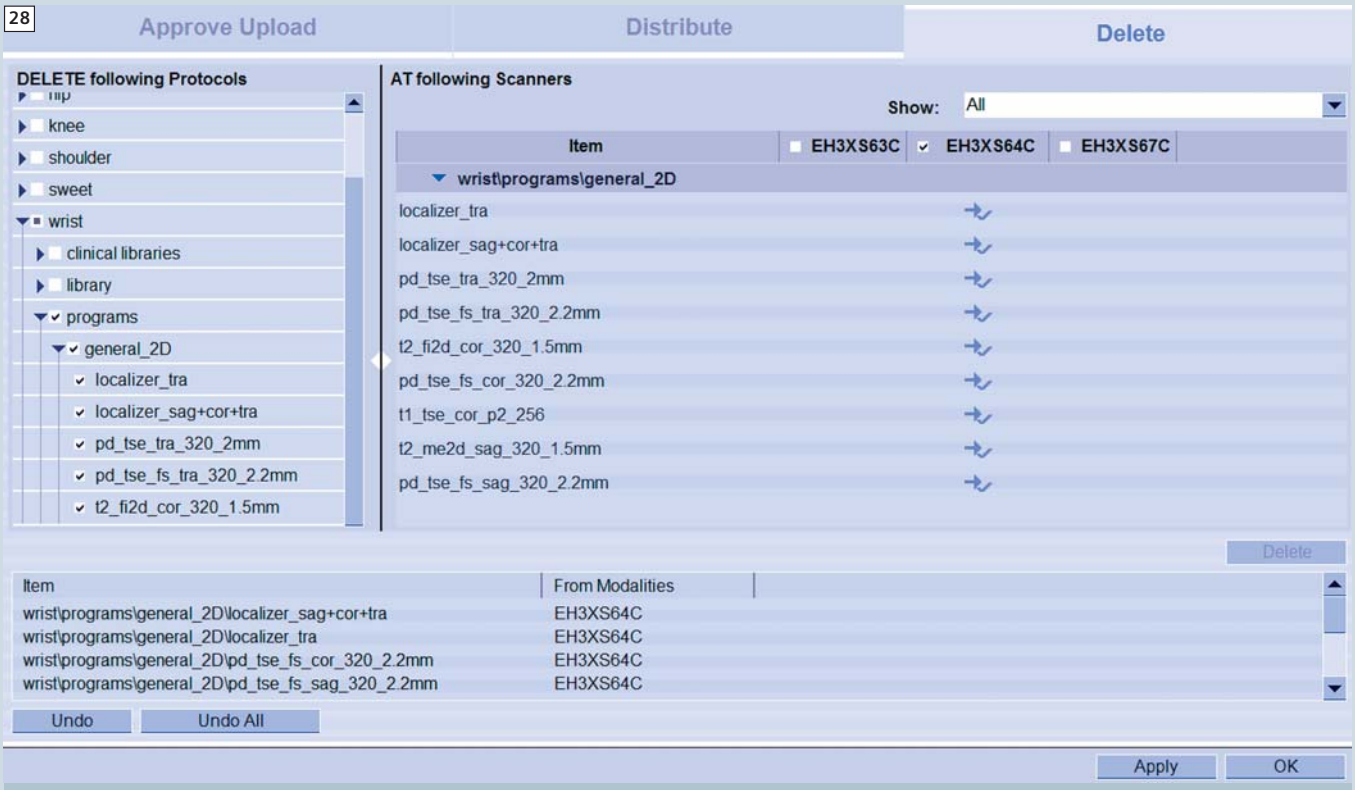

28 Delete tab.

Distribute protocols across scanners

Protocols installed on *syngo*.via can be distributed among the networked scanner pool (Fig. 27).

- Select the **Distribute** tab to distribute the protocols.
- From the **DISTRIBUTE FROM** list, select the source scanner.
- Choose the protocols which are to be copied by checking the box.
- In the **TO** area, select the target scanner.
- Press the **Distribute** button to send the protocols to the selected scanner.

The protocols are listed in the **Action** list in the lower area. If necessary, they can be selected and removed from the distribution list.

- Confirm the distribution with **OK**.

Delete scan protocols from the scanner

Protocols installed on *syngo*.via can be deleted. They are removed from *syngo*.via which means they are no longer available for protocol planning and they are permanently removed from the corresponding scanner (Fig. 28).

Note: The protocols are deleted immediately without further warning on the MR scanner.

- Select the **Delete** tab to delete the protocols.
- In the **DELETE following protocols** area, select the protocols.
- In the **AT following Scanners** area, select the scanner for which the protocols should not be available any longer.
- Press the **Delete** button to delete the selected protocols.

The protocols, which are to be deleted, are listed in the **Action** list. If necessary, they can be selected and removed from the deletion list.

- Confirm the deletion with **OK**.

Conclusion

The Networked Scanner integrates Siemens MR scanners with *syngo*.via and your radiology information system (RIS). It provides a platform for radiology workflow support and protocol management to optimize your daily workflow.

Note: All patient names mentioned above are not actual patients.

Contact
Anja Fernandez Carmona
Siemens Healthcare
IM MR PLM-AW SWT CAS
91050 Erlangen
Germany
Phone: +49 (9131) 84-3566
anja.fernandez_carmona@siemens.com

Klaus Mayer
Siemens Healthcare
IM MR PLM-AW SWT WF
91050 Erlangen
Germany
Phone: +49 (9131) 84-2728
klaus.mayer@siemens.com

Siemens Healthcare Publications

Our publications offer the latest information and background for every healthcare field. From the hospital director to the radiological assistant – here, you can quickly find information relevant to your needs.

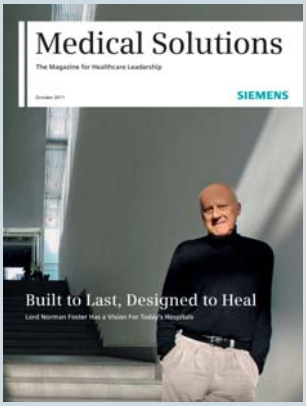

Medical Solutions
Innovations and trends in healthcare. The magazine is designed especially for members of hospital management, administration personnel, and heads of medical departments.

eNews
Register for the global Siemens Healthcare Newsletter at www.siemens.com/healthcare-eNews to receive monthly updates on topics that interest you.

AXIOM Innovations
Everything from the worlds of interventional radiology, cardiology, fluoroscopy, and radiography. This semiannual magazine is primarily designed for physicians, physicists, researchers, and medical technical personnel.

MAGNETOM Flash
Everything from the world of magnetic resonance imaging. The magazine presents case reports, technology, product news, and how-to articles. It is primarily designed for physicians, physicists, and medical technical personnel.

SOMATOM Sessions
Everything from the world of computed tomography. With its innovations, clinical applications, and visions, this semiannual magazine is primarily designed for physicians, physicists, researchers, and medical technical personnel.

Imaging Life
Everything from the world of molecular imaging innovations. This bi-annual magazine presents clinical case reports, customer experiences, and product news and is primarily designed for physicians, hospital management and researches.

For current and past issues and to order the magazines, please visit **www.siemens.com/healthcare-magazine.**



Listen – Discuss – Share
8th MAGNETOM World Summit

May 31 – June 3, 2012, Paris, France

The MAGNETOM World Summit is an excellent platform to establish personal contacts, exchange valuable information, learn from the experience of other users and to share your own expertise.

Lectures and presentations from experts in the field will allow you to be exposed to new ideas and alternative clinical approaches that might help you to improve your clinical and financial outcomes.

For details on the agenda and registration, please visit **www.siemens.com/magnetom-world**

MAGNETOM Flash – Imprint

Publisher:
Siemens AG
Medical Solutions
Business Unit Magnetic Resonance,
Karl-Schall-Straße 6, D-91052 Erlangen,
Germany

Editor-in-Chief: Dr. Matthias Lichy, M.D.
(matthias.lichy@siemens.com)

Associate Editor: Antje Hellwich
(antje.hellwich@siemens.com)

Editorial Board: Christiane Bernhardt;
Peter Kreisler, Ph.D.; Wellesley Were;
Milind Dhamankar, M.D.; Michelle Kessler;
Gary McNeal; Sunil Kumar, M.D.

Production: Norbert Moser, Siemens AG,
Medical Solutions

Layout: independent Medien-Design
Widenmayerstrasse 16, D-80538 Munich

Printer: Mediahaus Biering GmbH,
Freisinger Landstr. 21, 80939 Munich, Germany

MAGNETOM Flash is also available on the internet:
www.siemens.com/magnetom-world

MAGNETOM Flash with a total circulation of 35,000 copies is sent free of charge to Siemens MR customers, qualified physicians, technologists, physicists and radiology departments throughout the world. It includes reports in the English language on magnetic resonance: diagnostic and therapeutic methods and their application as well as results and experience gained with corresponding systems and solutions. It introduces from case to case new principles and procedures and discusses their clinical potential.

We welcome your questions and comments about the editorial content of MAGNETOM Flash. Please contact us at magnetomworld.med@siemens.com. Manuscripts as well as suggestions, proposals and information are always welcome; they are carefully examined and submitted to the editorial board for attention. MAGNETOM Flash is not responsible for loss, damage, or any other injury to unsolicited manuscripts or other materials. We reserve the right to edit for clarity, accuracy, and space. Include your name, address, and phone number and send to the editors, address above.

Global Siemens Headquarters

Siemens AG
Wittelsbacherplatz 2
80333 Muenchen
Germany

Global Siemens Healthcare Headquarters

Siemens AG
Healthcare Sector
Henkestrasse 127
91052 Erlangen
Germany
Phone: +49 9131 84-0
www.siemens.com/healthcare

www.siemens.com/healthcare-magazine

Order No. A91MR-1000-84C-7600 | Printed in Germany | CC MR 01000 ZS 111130. |

Global Business Unit

Siemens AG
Medical Solutions
Magnetic Resonance
Henkestr. 127
DE-91052 Erlangen
Germany
Phone: +49 9131 84-0
www.siemens.com/healthcare

Local Contact Information

Asia
Siemens Pte Ltd
The Siemens Center
60 MacPherson Road
Singapore 348615
Phone: +65 6490-8096

Canada
Siemens Canada Limited
Medical Solutions
2185 Derry Road West
Mississauga ON L5N 7A6
Canada
Phone: +1 905 819-5800

Europe/Africa/Middle East
Siemens AG
Medical Solutions
Henkestr. 127
91052 Erlangen
Germany
Phone: +49 9131 84-0

Latin America
Siemens S.A.
Medical Solutions
Avenida de Pte. Julio A. Roca No 516,
Piso 7
C1067ABN Buenos Aires
Argentina
Phone: +54 11 4340-8400

USA
Siemens Medical Solutions U.S.A., Inc.
51 Valley Stream Parkway
Malvern, PA 19355-1406
USA
Phone: +1-888-826-9702